D 2022

U.PORTO
FEUP FACULDADE DE ENGENHARIA
UNIVERSIDADE DO PORTO

THE RELEVANCE OF BIOMEMBRANES IN ALZHEIMER'S DISEASE: FROM THE IDENTIFICATION OF THERAPEUTIC COMPOUNDS TO THE USE OF NANOCARRIERS

STÉPHANIE MACHADO ANDRADE

TESE DE DOUTORAMENTO APRESENTADA
À FACULDADE DE ENGENHARIA DA UNIVERSIDADE DO PORTO EM
PROGRAMA DOUTORAL EM ENGENHARIA QUÍMICA E BIOLÓGICA

U.PORTO
FEUP FACULDADE DE ENGENHARIA
UNIVERSIDADE DO PORTO

The Relevance of Biomembranes in Alzheimer's Disease:

From the Identification of Therapeutic Compounds to the Use of Nanocarriers

Stéphanie Machado Andrade

Dissertation for the degree:

Doctor in of Philosophy in Chemical and Biological Engineering

Supervisor: Prof. Dr. Maria do Carmo Pereira

Co-Supervisor: Dr. Joana Angélica Loureiro

Co-Supervisor: Prof. Dr. Rodrigo Morales

Porto, December 2022

ALiCE

lepabe
Laboratory for Process Engineering, Environment, Biotechnology and Energy

NANO4MED

UTHealth
The University of Texas Health Science Center at Houston

“What is research but a blind date with knowledge?”

Will Harvey

Financial Support

This work was supported by national funding with a PhD fellowship (SFRH/BD/129312/2017 and COVID/BD/151869/2021) from Fundação para a Ciência e a Tecnologia (FCT). This work was also financially supported by: Base Funding-LA/P/0045/2020 (ALiCE), UIDB/00511/2020, and UIDP/00511/2020 (LEPABE), funded by national funds through the FCT/MCTES (PIDDAC); Project 2SMART-engineered Smart materials for Smart citizens, with reference NORTE-01-0145-FEDER-000054, supported by Norte Portugal Regional Operational Program (NORTE 2020), under the PORTUGAL 2020 Partnership Agreement, through the European Regional Development Fund (ERDF).

Acknowledgments

Several people contributed to this thesis, to whom I would like to express my gratitude. I want to start by expressing my sincere gratitude to my supervisor, Prof. Dr. Maria do Carmo Pereira, for all her assistance and scientific guidance during these years. I appreciate her support and availability all the time as well. To my co-supervisors, Dr. Joana Angélica Loureiro and Prof. Dr. Rodrigo Morales I would also like to thank all the valuable scientific discussions, advice, suggestions, and tireless guidance.

I also want to thank all of my lab colleagues for their assistance, productive conversations, and, not less important, for all the company and enjoyable times we shared in the lab, which made this journey much happier. A special thanks to Dr. Maria João Ramalho, who has been promoted from colleague to friend over the years.

To the members and staff of LEPABE, DEQ, and The University of Texas Health Science Center at Houston (UTHealth), a special thank for their help and contribution.

I am grateful to Dr. Frederico Silva and Dr. Fátima Fonseca from i3S for their training, guidance, and helpful suggestions in circular dichroism experiments. I am also thankful to Dr. Rui Fernandes from i3S for his support in transmission electron microscopy experiments.

Last but not least, I am grateful to my parents for their continuous support, encouragement words, wise advice, and for all the efforts they made for me.

Thesis output

The research work for this thesis was developed at the Laboratory for Process Engineering Environment, Biotechnology and Energy (LEPABE) at the Faculty of Engineering of University of Porto (FEUP) (Portugal) and at University of Texas Health Science Center at Houston (UTHealth) (USA), between 2017 and 2022. From this work, the following publications are published or submitted for publication.

- ***Papers in international scientific periodicals with referees***

1) Andrade, S., Loureiro, J. A., Pereira, M. C. (2022). Transferrin-Functionalized Liposomes for the Delivery of Gallic Acid: A Therapeutic Approach for Alzheimer's Disease. Pharmaceutics, 14(10), 2163. doi: 10.3390/pharmaceutics14102163

2) Andrade, S., Ramalho, M. J., Loureiro, J. A., Pereira, M. C. (2022). Transferrin-Functionalized Liposomes Loaded with Vitamin VB12 for Alzheimer's Disease Therapy. International Journal of Pharmaceutics, 122167. doi: 10.1016/j.ijpharm.2022.122167

3) Andrade, S., Loureiro, J. A., Ramirez, S., Catumbela, C. S. G., Soto, C., Morales, R., Pereira, M. C. (2022). Multi-Dose Intravenous Administration of Neutral and Cationic Liposomes in Mice: An Extensive Toxicity Study. Pharmaceuticals. 15, 761. doi: 10.3390/ph15060761

4) Andrade, S., Loureiro, J. A., Pereira, M. C. (2021). Caffeic acid for the prevention and treatment of Alzheimer's disease: The effect of lipid membranes on the inhibition of aggregation and disruption of Aβ fibrils. International Journal of Biological Macromolecules. 190, 853-861. doi: 10.1016/j.ijbiomac.2021.08.198

5) Andrade, S., Loureiro, J. A., Pereira, M. C. (2021). Influence of *in vitro* neuronal membranes on the anti-amyloidogenic activity of gallic acid: Implication for the therapy of Alzheimer's disease. Archives of Biochemistry and Biophysics, 711, 109022. doi: 10.1016/j.abb.2021.109022

6) Andrade, S., Loureiro, J. A., Pereira, M. C. (2021). The Role of Amyloid β-Biomembrane Interactions in the Pathogenesis of Alzheimer's Disease: Insights from Liposomes as Membrane Models. ChemPhysChem, 22, 1547. doi: 10.1002/cphc.202100124

7) Andrade, S., Ramalho, M. J., Loureiro, J. A., Pereira, M. C. (2021). Liposomes as Biomembrane Models: Biophysical techniques for Drug-Membrane Interaction Studies. Journal of Molecular Liquids, 116141. doi: 10.1016/j.molliq.2021.116141

8) Andrade, S., Loureiro, J. A., Pereira, M. C. (2021). Vitamin B12 Inhibits Aβ Fibrillation and Disaggregates Preformed Fibrils in the Presence of Synthetic Neuronal Membranes. ACS Chemical Neuroscience, 12, 2491–2502. doi: 10.1021/acschemneuro.1c00210

9) Andrade, S., Ramalho, M. J., Loureiro, J. A., Pereira, M. C. (2021). The biophysical interaction of ferulic acid with liposomes as biological membrane model: The effect of the lipid bilayer composition. Journal of Molecular Liquids, 114689. doi: 10.1016/j.molliq.2020.114689

10) Andrade, S., Loureiro, J. A., Pereira, M. C. (2021) Green tea extract-biomembrane interaction study: The role of its two major components,(−)-epigallocatechin gallate and (−)-epigallocatechin. Biochimica et Biophysica Acta (BBA)-Biomembranes, 1863(1), 183476. doi: 10.1016/j.bbamem.2020.183476

11) Ramalho, M. J.*, **Andrade, S.***, Loureiro, J. A., Pereira, M. C. (2020). Nanotechnology to improve the Alzheimer's disease therapy with natural compounds. Drug Delivery and Translational Research, 1-23. doi:10.1007/s13346-019-00694-3

*The authors contributed equally to this work.

12) Andrade, S., Ramalho, M. J., Loureiro, J. A., Pereira, M. C. (2020). Natural Compounds for Alzheimer's Disease Therapy: A Systematic Review of Preclinical and Clinical Studies. Internation Journal of Molecular Sciences, 20(9), 2313. doi: 10.3390/ijms20092313

13) Andrade, S., Ramalho, M. J., Loureiro, J. A., Pereira, M. C. (2019) Interaction of natural compounds with biomembrane models: A biophysical approach for the Alzheimer's disease therapy. Colloids and Surfaces B: Biointerfaces, 180, 83-92. doi: 10.1016/j.colsurfb.2019.04.019

14) Andrade, S., Ramalho, M. J., Pereira, M. C., Loureiro, J. A. (2018) Resveratrol brain delivery for neurological disorders prevention and treatment. Frontiers in Pharmacology. 9, 1261. doi: 10.3389/fphar.2018.01261

- ***Book Chapters***

1) Ramalho, M. J., **Andrade, S.**, Dabur, M., Loureiro, J. A., Pereira, M. C. (2021). Current vs Emerging Natural Compounds-Based Treatments for Alzheimer's Disease (pp. 26-30). In Alzheimer's Disease and Treatment. Volume 3. MedDocs Publishers.

2) Andrade, S., Ramalho, M. J., Loureiro, J. A., Pereira, M. C. (2020). Techniques to produce liposomes for the emerging market of nano-based formulations (pp. 26-31). In Importance & Applications of Nanotechnology. Volume 5. MedDocs Publishers.

Also, from this work resulted the following presentations at international conferences:

1) Andrade, S., Loureiro, J. A., Pereira, M. C. Transferrin-modified nanoparticles for Alzheimer's disease therapy with natural compounds. 5th Edition of World Nanotechnology Conference (Nanotechnology 2022). Online, September 2022. Oral presentation - *Invited speaker*

2) Ramalho, M. J., **Andrade, S.**, Loureiro, J. A., Coelho, M. A. N., Pereira, M. C. Nanoparticles for biomedical applications: Nanocarriers and biomembranes for cancer and neurodegeneration. ETPN 2022, June 2022, Braga, Portugal. Poster presentation

3) Loureiro, J. A., **Andrade, S.**, Ramalho, M. J., Pereira, M. C. Biomembranes as cell models for drug screening based on the drug partitions coefficients. 11th International Colloids Conference, June 2022, Lisbon, Portugal. Poster presentation

4) Andrade, S., Ramalho, M. J., Loureiro, J. A., Pereira, M. C. The anti-amyloidogenic activity of caffeic acid in a neuronal membrane-like environment: Relevance for Alzheimer's disease. AD/PD 2022: 16th International Conference on Alzheimer's and Parkinson's Diseases. March 2022, Barcelona, Spain. Oral presentation

5) Andrade, S., Loureiro, J. A., Pereira, M. C. Anti-amyloidogenic activity of vitamin B12: A promising nutrient for the prevention and treatment of Alzheimer's disease. 4th Doctoral Congress of Engineering (DCE21). Online, June 2021. Oral presentation

6) Andrade, S., Loureiro, J. A., Pereira, M. C. Interaction of Aβ peptide with vitamin B12: Implication for the therapy of Alzheimer's disease. Translating Ideas into Therapies. Online, June-July 2021. Poster presentation

7) Andrade, S., Loureiro, J. A., Coelho, M. A. N., Pereira, M. C., Effects of gallic acid on membrane biophysical properties: relevance for its biophysical effects. 2nd Doctoral Congress of Engineering (DCE17). Porto, Portugal, June 2017. Oral presentation

Abstract

Alzheimer's Disease (AD) is an age-related neurodegenerative disorder and the leading cause of dementia worldwide. AD affects cognitive functions with an intensity that leads to several functional losses. The aggregation of amyloid β (Aβ) peptides with subsequent formation of fibrils that deposit in senile plaques is considered one of the key triggers of the disease. The continuous increase in AD incidence demands the urgent development of effective therapeutic strategies. Despite extensive research, currently available medicines only focus on controlling the symptoms but do not cure the disease. Regarding the advances in the discovery of new treatments for this devastating disease, natural compounds are gaining increasing relevance.

In this work, the ability of eight natural compounds – ferulic acid (FA), nicotine (NIC), caffeine (CAF), caffeic acid (CA), ascorbic acid (AA), vanillic acid (VA), gallic acid (GA) and vitamin B12 (VB12) - to inhibit the $A\beta_{1-42}$ aggregation as well as to disrupt mature fibrils was evaluated. To this end, a thioflavin T (ThT) fluorescence assay was employed to quantify the content of Aβ fibrils. The attained results revealed that CA, GA, and VB12 are the most promising molecules for AD therapy by inhibiting the $A\beta_{1-42}$ fibrillation and disaggregating mature fibrils.

As the *in vivo* environment may affect the drugs' efficacy in inhibiting the amyloid aggregation or disrupting mature fibrils, it is critical to evaluate their anti-amyloidogenic activity in the presence of specific cellular components. Thus, this study also assesses the ability of CA, GA, and VB12 to prevent $A\beta_{1-42}$ aggregation and/or to disrupt mature fibrils in a cellular membrane-like environment. To this end, liposomes made of 1,2-dimyristoyl-*sn*-glycero-3-phosphocholine (DMPC), cholesterol (CHOL), sphingomyelin (SM), and l-α-phosphatidylserine (PS) - the major lipid components of neurons - were used as an *in vitro* model of neuronal membranes. The anti-amyloidogenic activity of CA, GA, and VB12 in the cell membrane-like environment was compared to the bulk solution and discussed based on their lipophilicity. The results suggest that lipid membranes affect the natural compounds' anti-amyloidogenic properties due to the partition of the molecules to the lipid membrane, which prevents them from interacting with Aβ. Even so, CA, GA, and VB12 showed strong anti-amyloidogenic properties in the cell membrane-like environment, supporting the view that these compounds could be a promising approach for preventing and curing AD.

Knowing the limiting characteristics of natural compounds, the encapsulation of CA, GA, and VB12 into liposomes composed of 1,2-distearoyl-sn-glycero-3-phosphocholine (DSPC), CHOL, 1,2-distearoyl-sn-glycero-3-phosphoethanolamine-N-[methoxy(polyethylene glycol)-2000] (18:0 PEG2000 PE), and 1,2-distearoyl-sn-glycero-3-phosphoethanolamine-N-[amino(polyethylene glycol)-2000] (DSPE-PEG2000 amine) is proposed in this work. CA, GA or VB12-loaded liposomes functionalized with transferrin (Tf) were produced, envisaging the dual-targeting of the natural compounds to the blood-brain barrier (BBB) and neuronal cells due to the overexpression of Tf receptors in these cells. The produced liposomes presented sizes smaller than 200 nm, with low polydispersity and neutral zeta potential, being suitable for brain delivery. The nanoparticles exhibited adequate encapsulation efficiencies, sustained release of natural compounds, and physical stability under storage conditions for up to 2 months. The developed drug delivery systems (DDSs) were capable of delaying the formation of Aβ fibrils and disrupting mature fibrils, highlighting their great potential for the prevention and treatment of AD.

Since AD is a chronic illness, the long-term administration of therapeutic molecules is needed. Therefore, the toxicity of the prolonged administration of liposomes composed of DSPC, CHOL, and DSPE-PEG2000 amine was evaluated in adult wild-type mice (C57Bl6). These animals were subjected to 10 doses administered intravenously over 3 weeks. The obtained results highlight the safety of the developed neutral liposomes and support their use as safe nanocarriers, even when repeated doses are needed.

Keywords: Neurodegenerative disease, Amyloid β peptide, Fibrillation, Fibril disaggregation, Natural compound, Anti-amyloidogenic properties, Lipid membrane model, Liposomes, Drug delivery, Brain delivery, Blood-brain barrier, Nanocarrier, Nanoparticles, Transferrin

Resumo

A Doença de Alzheimer (DA) é uma doença neurodegenerativa relacionada com o aumento da idade e é a principal causa de demência no mundo. A DA afeta as funções cognitivas com uma intensidade que leva a diversas perdas funcionais. A agregação do peptido β amilóide (Aβ) com posterior formação de fibras que se depositam em placas senis é considerada um dos principais desencadeadores da doença. O aumento contínuo da incidência de AD exige o desenvolvimento urgente de estratégias terapêuticas eficazes. Apesar da extensa pesquisa, os medicamentos convencionais focam apenas no controle dos sintomas e não curam a doença. Com os avanços na descoberta de novos tratamentos para esta doença devastadora, os compostos naturais ganham cada vez mais relevância.

Neste trabalho, a capacidade de oito compostos naturais – ácido ferúlico (FA), nicotina (NIC), cafeína (CAF), ácido cafeico (CA), ácido ascórbico (AA), ácido vanílico (VA), ácido gálico (GA) e vitamina B12 (VB12) - para inibir a agregação de $A\beta_{1-42}$, bem como para desagregar fibras foi avaliada. Para este fim, um ensaio de fluorescência de tioflavina T (ThT) foi usado para quantificar o conteúdo de fibras Aβ. Os resultados obtidos revelaram que CA, GA e VB12 são as moléculas mais promissoras para a terapia da DA por inibir a agregação e desagregar fibrilas.

Como o ambiente *in vivo* pode afetar a eficácia das drogas em inibir a agregação ou desagregar fibras, é fundamental avaliar a atividade anti-amiloidogénica na presença de componentes celulares específicos. Assim, este estudo também avalia a capacidade de CA, GA e VB12 para prevenir a agregação de Aβ e/ou desagregar fibras num ambiente semelhante à membrana celular. Para isso, lipossomas compostos por 1,2-dimiristoil-sn-glicero-3-fosfocolina (DMPC), colesterol (CHOL), esfingomielina (SM) e l-α-fosfatidilserina (PS) - os principais componentes lipídicos dos neurónios - foram usados como modelo *in vitro* de membranas neuronais. A atividade anti-amiloidogénica de CA, GA e VB12 no ambiente semelhante à membrana celular foi comparada com o ambiente aquoso e discutida com base nas lipofilicidades dos compostos. Os resultados sugerem que as membranas lipídicas afetam as propriedades anti-amiloidogénicas dos compostos naturais devido à afinidade das moléculas para a membrana lipídica, o que as impede de interagir com Aβ. Mesmo assim, CA, GA e VB12 mostraram fortes propriedades anti-amiloidogénicas no ambiente semelhante à membrana celular, apoiando a visão de que estes compostos podem ser uma abordagem promissora para prevenir e curar a DA.

Conhecendo as características limitantes dos compostos naturais, a encapsulação de CA, GA e VB12 em lipossomas compostos por 1,2-diestearoil-sn-glicero-3-fosfocolina (DSPC), CHOL, 1,2-diestearoil-sn-glicero- 3-fosfoetanolamina-N-[metoxi(polietilenoglicol)-2000] (18:0 PEG2000 PE) e 1,2-diestearoil-sn-glicero-3-fosfoetanolamina-N-[amino(polietilenoglicol)-2000] (amina DSPE-PEG2000) é proposta neste trabalho. Foram produzidos lipossomas carregados com CA, GA ou VB12 e funcionalizados com transferrina (Tf), visando o direcionamento duplo dos compostos naturais para a barreira hematoencefálica (BHE) e células neuronais devido à sobre-expressão de receptores de Tf nessas células. Os lipossomas produzidos apresentaram tamanhos inferiores a 200 nm, com baixa polidispersidade e potencial zeta neutro, sendo adequados para entrega cerebral. As nanopartículas apresentaram eficiências de encapsulação adequadas, libertação sustentada dos compostos naturais e estabilidade física sob condições de armazenamento até dois meses. Os sistemas de entrega de drogas (SEDs) desenvolvidos foram capazes de retardar a formação de fibras Aβ e desagregar fibras, destacando o seu grande potencial para a prevenção e tratamento da DA.

Como a DA é uma doença crónica, é necessária a administração contínua de moléculas terapêuticas. Portanto, a toxicidade da administração prolongada de lipossomas compostos por DSPC, CHOL e DSPE-PEG2000 amina foi avaliada. Ratos adultos (C57Bl6) foram submetidos a 10 doses administradas por via intravenosa ao longo de 3 semanas. Os resultados demonstram que os lipossomas não apresentam toxicidade para administração repetida. Os resultados obtidos destacam a segurança dos lipossomas neutros desenvolvidos e confirmam que podem ser utilizados como nanotransportadores seguros, mesmo quando doses repetidas são necessárias.

Palavras-chave: Doença neurodegenerativa, Peptído β amilóide, Fibrilação, Desagregação de fibras, Composto natural, Propriedades anti-amiloidogénicas, Modelo de membrana lipídica, Lipossomas, Entrega de droga, Entrega no cérebro, Barreira hematoencefálica, Nanotransportador, Nanopartículas, Transferrina

Content

List of Figures

Chapter 2

Chapter 3

Chapter 4

Chapter 5

List of Tables

Chapter 2

Chapter 3

Chapter 4

Chapter 5

List of Abbreviations

18:0 PEG2000 PE	1,2-distearoyl-sn-glycero-3-phosphoethanolamine-N-[methoxy(polyethylene glycol)-2000]
AA	Ascorbic acid
Aβ	Amyloid-β peptide
ACH	Amyloid cascade hypothesis
AD	Alzheimer's disease
ALT	Alanine aminotransferase
AMT	Adsorptive-mediated transcytosis
ApoE	Apolipoprotein E
APP	Amyloid precursor protein
AST	Aspartate aminotransferase
ATP	Adenosine triphosphate
ATR-FTIR	Attenuated total reflectance - Fourier transform infrared
AWC	Animal Welfare Committee
BBB	Blood-brain barrier
BW	Bodyweight
CA	Caffeic acid
CAF	Caffeine
CD	Circular dichroism
CE	Conjugation efficiency
CHOL	Cholesterol
CLAMC	Center for Laboratory Animal Medicine and Care
CNS	Central nervous system
[C]/[P]	Compound-to-peptide molar ratio
DDS	Drug delivery system
DHA	Docosahexaenoic Acid
DLS	Dynamic light scattering
DMPC	1,2-dimyristoyl-sn-glycero-3-phosphocholine
DOTAP	1,2-dioleoyl-3-trimethylammonium-propane
DSPC	1,2-distearoyl-sn-glycero-3-phosphocholine

DSPE-PEG2000 amine	1,2-distearoyl-sn-glycero-3-phosphoethanolamine-N-[amino(polyethylene glycol)-2000]
EE	Encapsulation efficiency
EGCG	Epigallocatechin gallate
ELS	Electrophoretic light scattering
FA	Ferulic acid
FDA	Food and Drug Administration
GA	Gallic acid
GUVs	Giant unilamellar vesicles
HFIP	1,1,1,3,3,3-hexafluoro-2-propanol
KP	Partition coefficient
LC	Loading capacity
LDL	Low-density lipoprotein
Lf	Lactoferrin
LNCs	Lipid-core nanocapsules
log D	Distribution coefficient
[L]/[P]	Lipid-to-peptide molar ratio
LUVs	Large unilamellar vesicles
MEs	Microemulsions
MLVs	Multilamellar lipid vesicles
MPs	Microparticles
NEs	Nanoemulsions
NFTs	Neurofibrillary tangles
NGF	Nerve growth factor
NIC	Nicotine
NLCs	Nanostructured lipid carriers
NPs	Nanoparticles
PA	Phosphatidic acid
PBS	Phosphate buffer saline
PC	Phosphatidylcholine
PdI	Polydispersity index
PE	Phosphatidylethanolamine
PEG	Polyethylene glycol
P-gp	P-glycoprotein

PI	Phosphatidylinositol
PLGA	Poly (lactic-co-glycolic acid)
POs	Polymersomes
PS	Phosphatidylserine
PSEN1	Presenilin 1
PSEN2	Presenilin 2
RBCs	Red blood cells
RDW	Red cell distribution width
RES	Reticuloendothelial system
RMT	Receptor-mediated transcytosis
ROS	Reactive oxygen species
ScFv	Single-chain variable fragments
SD	Standard deviation
SLBs	Supported lipid bilayers
SLNs	Solid lipid nanoparticles
SM	Sphingomyelin
SUVs	Small unilamellar vesicles
TEM	Transmission electron microscopy
Tf	Transferrin
TfR	Transferrin receptor
ThT	Thioflavin T
ULVs	Unilamellar lipid vesicles
VA	Vanillic acid
VB12	Vitamin B12
WGA	Wheat germ agglutinin
WHO	World Health Organization

Chapter 1

Introduction

Alzheimer's disease (AD) is a chronic illness caused by an irreversible and progressive brain degeneration, which compromises patients' memory, cognition, and personality, eventually leading to death. AD represents the most common cause of dementia, accounting for over 70% of the cases globally [1]. Statistics by the World Health Organization (WHO) indicate that more than 40 million people are currently diagnosed with AD worldwide, and the incidence of AD is expected to triple in 30 years [2]. Despite the persistent attempts of the pharmaceutical and research sectors, AD continues to be a serious emotional, social and economic burden since the disease remains untreatable. Regrettably, most currently available AD drugs only temporarily improve the disease's symptoms. However, the recent approval of Aduhelm brings hope to AD therapy, although its effectiveness is still a matter of debate. Along this line, new medicines capable of preventing, delaying, or even curing AD are urgently needed.

Although the exact mechanisms that cause AD are still debated, it is widely accepted that senile plaques in patients' brains are associated with the disease. These neuritic plaques comprise misfolded forms of amyloid-β (Aβ) peptides aggregated into fibrils and cause neurotoxicity directly or indirectly by inducing overt inflammation and oxidative stress [3]. Moreover, substantial evidence reveal that biological membranes play a crucial role in the protein misfolding process [4]. Preventing the aggregation of Aβ or disaggregating misfolded Aβ structures are thus viable therapeutic options for preventing

or treating AD, respectively. Aducanumab was recently approved by the U.S. Food and Drug Administration (FDA) for AD therapy, particularly in those with the illness at the early stages. Marketed as Aduhelm, aducanumab is a monoclonal antibody that bind to the senile plaques, enhancing their removal from the brain [5]. Regardless, the effectiveness of aducanumab is debated [6], and more effective therapeutic alternatives are still being evaluated.

Natural compounds were the first molecules used as therapeutic agents. Nowadays, the study of some of these natural compounds revealed that they present neuroprotective effects, arousing an increasing interest in the scientific community and the pharmaceutical industry. A diversity of natural compounds was described as suitable for preventing and attenuating several neurological diseases, including AD [7]. Despite the promising results in preclinical studies, there is still no solid evidence that natural compounds can prevent or treat the disease clinically. This has been connected to some of their characteristics, including low solubility, absorption, and bioavailability, *in vivo* instability, lack of specificity, high systemic clearance, and inability to cross the blood-brain barrier (BBB), which prevent them from reaching the brain [8].

Drug delivery systems (DDSs) targeting the brain seem to be a promising strategy to increase the bioavailability of natural compounds and transport across the BBB. DDSs can protect the natural compounds from biological degradation and transport the molecules to the brain by masking their limiting physicochemical properties. Thus, low doses of natural compounds are slowly released into the brain, increasing the efficiency of the therapeutic effects [8].

The main goals of the present work were: i) to evaluate the natural compounds' ability to inhibit the $A\beta_{1-42}$ fibrillation and disaggregate mature fibrils in a neuronal cell membrane-like environment using liposomes as biomembrane models; ii) to design and produce targeted liposomes as nanocarriers for the brain delivery of natural compounds and evaluate their anti-amyloidogenic properties; and iii) to evaluate the safety of the developed nanocarriers *in vivo*.

This dissertation is organized into six chapters. This chapter – Introduction – presents the subject and main goals of this research work. Chapter 2 – State of the Art – overviews AD and natural compounds-based therapeutics. Nanotechnology is also described as a suitable therapeutic strategy, and a review of the studies that have developed targeted nanoparticles (NPs) for the brain delivery of natural compounds for AD is presented. Part

of the content of this chapter has been published in manuscripts 4, 5, 9, and 10, and in the book chapter 1. Chapter 3 – Anti-Amyloidogenic Activity of Natural Compounds in the Presence of a Neuronal Membrane Model – starts with screening various natural compounds for anti-amyloidogenic properties in a bulk solution. Then, the effect of *in vitro* neuronal cell membranes on natural compounds' therapeutic activity was assessed using liposomes as cell membrane models. The results presented in this chapter have been published in papers 2, 3, and 6. Chapter 4 – Transferrin-Functionalized Liposomes for Alzheimer's Disease Therapy with Natural Compounds – presents the methodology, attained results and respective discussion for the development and therapeutic evaluation of transferrin-functionalized liposomes for natural compounds delivery. The results of this chapter were submitted for publication. Chapter 5 – *in vivo* Toxicity of Liposomes – presents an extensive toxicity study following multi-dose intravenous administration of the developed liposomes in mice, compared with traditional cationic liposomes. The findings from this chapter were published in paper 1. Finally, an overall summary of this project and its main conclusions are presented in Chapter 6 – Concluding Remarks.

References

[1] Zeisel, J., Bennett, K.&Fleming, R. World alzheimer report 2020: Design, dignity, dementia: Dementia-related design and the built environment. 2020,

[2] Organization, W. H., The global dementia observatory reference guide. 2018, World Health Organization.

[3] Hansra, G. K., Popov, G., Banaczek, P. O., Vogiatzis, M., Jegathees, T., Goldsbury, C. S.&Cullen, K. M. The neuritic plaque in alzheimer's disease: Perivascular degeneration of neuronal processes. Neurobiology of Aging 2019, 82, 88-101.

[4] Andrade, S., Loureiro, J. A.&Pereira, M. C. The role of amyloid β-biomembrane interactions in the pathogenesis of alzheimer's disease: Insights from liposomes as membrane models. ChemPhysChem n/a,

[5] Tanzi, R. E. Fda approval of aduhelm paves a new path for alzheimer's disease. ACS Chemical Neuroscience 2021, 12, 2714-2715.

[6] Karlawish, J.&Grill, J. D. The approval of aduhelm risks eroding public trust in alzheimer research and the fda. Nature Reviews Neurology 2021, 17, 523-524.

[7] Andrade, S., Ramalho, M. J., Loureiro, J. A.&Pereira, M. C. Natural compounds for alzheimer's disease therapy: A systematic review of preclinical and clinical studies. Int. J. Mol. Sci. 2019, 20, 1-41.

[8] Ramalho, M. J., Andrade, S., Loureiro, J. A.&Pereira, M. C. Nanotechnology to improve the alzheimer's disease therapy with natural compounds. Drug delivery and translational research 2020, 10, 380-402.

Chapter 2

State of the Art

2.1. Alzheimer's Disease

As people get older, neurodegenerative diseases become more common. Neurodegenerative diseases refer to a group of disorders that predominantly damage the neurons in the brain. These are incurable and severe disorders that cause nerve cells to degenerate or die over time. As neurons are damaged, there is a loss of brain activity leading to movement and mental functioning issues such as thinking, remembering, and reasoning to the extent that it affects the patients' daily lives and activities. The group of symptoms that are caused by brain disorders, promoting that an individual cannot fulfill his/her basic activities independently, is called dementia [1].

Dementia is a serious global health concern affecting around 50 million people worldwide, with nearly 10 million new cases diagnosed annually. The WHO estimates that the incidence will triple by 2050 [2]. AD is the most common neurodegenerative disease and the leading cause of dementia in the elderly, accounting for around 70% of cases globally. AD was first discovered in 1906 by the German neurologist Alois Alzheimer after noticing changes in the brain tissue of a 51-year-old woman who had died of an unusual mental illness [3].

AD is characterized by severe loss of cognitive functions and declarative memory, communication issues, and psychiatric symptoms such as apathy, spatial disorientation, general disinterest, depression, agitation, and aggression [4]. AD patients frequently experience a loss of emotional control, usually accompanied by physical or verbal violence. As the disease progresses, AD patients develop motor problems to such an extent that they disable them from walking and performing daily tasks such as dressing or eating. AD remains a progressive disease and, so far, irreversible [5].

2.1.1. Epidemiology

Increasing age is the most well-known risk factor for AD. The prevalence of AD increases dramatically with age, with less than 1% of people under 65 diagnosed with AD. The disease affects approximately 3% of individuals aged between 65 and 74 years old. AD incidence increases to 17% in people aged between 75 and 84 years old. Individuals 85 or older with AD reach 32%. Almost half of the world's population over the age of 75 was diagnosed with AD. Nevertheless, it is important to emphasize that AD does not represent a normal part of aging, and older age alone is not enough to trigger the disease [6].

Usually, AD remains undiagnosed in the first years. The average period between the onset of the symptoms and the diagnosis of AD is 2.8 years. After that, the average life expectancy is around 8 to 10 years. The life expectancy of AD patients older than 80 significantly decreases to 3.4 years. However, some AD patients can live much longer, often 15 or even 20 years after diagnosis [7].

Following age, the major risk factor for AD is sex. Women are disproportionately affected by AD, accounting for almost two-thirds of the world's population with AD. This can be explained by women's longer life expectancy than men, making them more likely to reach the ages of greater risk. However, recent findings suggest that there may be biological explanations for this disparity beyond longevity [8].

The WHO estimates that more than 40 million people are diagnosed with AD, globally. With the mean life expectancy increasing, it is expected that the AD incidence will increase to 66 million by 2030, 80 million by 2040, and 150 million by 2050 [9]. Because current treatments are merely symptomatic, AD will remain an increasing clinical, social, and economic burden in the following years.

2.1.2. Pathogenesis

AD patients' brains are microscopically characterized by intraneuronal neurofibrillary tangles (NFTs) and extracellular senile plaques. NFTs consist of paired helical filaments formed by hyperphosphorylated tau, a protein responsible for the assembly and stability of microtubules in neuronal cells and axoplasmic transport. NFTs are commonly localized in the hippocampus, entorhinal cortex, amygdala, and perirhinal cortex. Senile plaques are extracellular deposits of Aβ peptides [10]. In an early stage, senile plaques appear in the brain's basal, temporal, and orbitofrontal neocortex areas and spread across the neocortex, hippocampus, amygdala, diencephalon, and basal ganglia in later stages. As AD progresses, Aβ is found in the mesencephalon, lower brain stem, and cerebellar cortex. Hyperphosphorylated tau and insoluble tangles appear first in the limbic system (entorhinal cortex, hippocampus, dentate gyrus) and then in the cortical region. Macroscopically, the AD patients' brain exhibits modified morphology, including enlargement of the ventricular system and atrophy of the frontal, temporal and parietal cortex due to synaptic degeneration and neuron death [11]. Although both NFTs and senile plaques are considered the major players in the AD progression, more importance is given to the amyloid plaques as evidence supports a direct relationship between the disease severity and the concentration of Aβ aggregates.

Aβ is a physiological peptide with a characteristic β-pleated sheet configuration that derives from the proteolytic cleavage of the amyloid precursor protein (APP), a transmembrane protein with cell surface receptor properties. The APP gene codes for multiple isoforms of a glycoprotein that contain a membrane-spanning sequence, a long N-terminal extracellular region, and a short C-terminal cytoplasmic tail. Although the shorter APP695 is the most abundant form of APP in the brain, different APP isoforms are also produced with sizes ranging from 695 to 770 amino acids. APP is highly expressed in neurons, although it can also be found in lower amounts in other tissues [12].

The Aβ sequence is found within the cell surface, with a peptide fragment incorporated into the membrane. The APP can be processed through two main pathways: non-amyloidogenic and amyloidogenic (Figure 2.1). In the non-amyloidogenic pathway, the proteolytic enzyme α-secretase cleaves the APP within the Aβ domain in its transmembrane region to produce the soluble carboxyl-truncated form of APP (SAPPα), which includes the first 16 amino acid residues of Aβ. The remnant C-terminal proteolytic product with 83 amino acids (C83) is cleaved by γ-secretase yielding two non-amyloidogenic fragments, p3

and AICD. In the amyloidogenic pathway, the APP cleavage by β-secretase produces another soluble form of APP (SAPPβ) and a 99-amino-acid C-terminal fragment (C99). Then, γ-secretase cleaves the APP near the N-terminus of Aβ, producing Aβ peptides ranging from 38 to 43 residues [12].

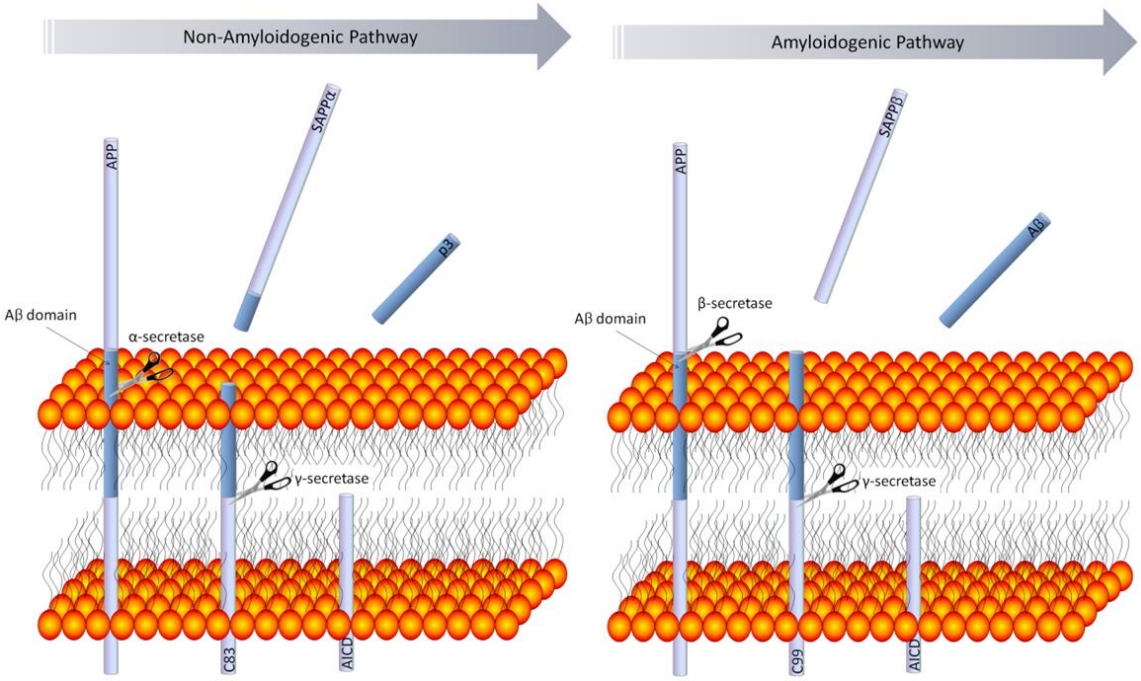

Figure 2.1. Non-amyloidogenic and amyloidogenic processing of the amyloid precursor protein (APP).

Depending on the pattern of cleavage of APP, Aβ can vary in length at the C-terminus. The regulatory activity of the three different proteolytic enzymes, α-, β-, and γ -secretases, in their specific cleavage sites produces various products, including $A\beta_{1\text{-}40}$ and $A\beta_{1\text{-}42}$. $A\beta_{1\text{-}40}$ is the most abundant isoforms of Aβ peptide, accounting for around 90%, and it is mainly produced by the APP cleavage in the trans-Golgi network. However, $A\beta_{1\text{-}42}$ is considered the more amyloidogenic isoforms of Aβ since it aggregates more readily than $A\beta_{1\text{–}40}$. This isoform is mainly produced in the endoplasmic reticulum [13].

After being released from cells in a water-soluble form, Aβ peptides may misfold and gradually aggregate into oligomers, known as the lag phase (Figure 2.2). Elongation then occurs, resulting in the formation of protofibrils. In the last stage, protofibrils assemble into insoluble mature fibrils (stationary phase), which deposit into extracellular senile plaques [14]. It appears that the Aβ aggregation requires the conformational transitions of α-helices

to β-sheets. Initially, soluble monomeric form of Aβ with α-helix conformation aggregated in species-rich antiparallel β-sheet structures. The transition of antiparallel to parallel β-sheet results in converting oligomers into fibrils [15].

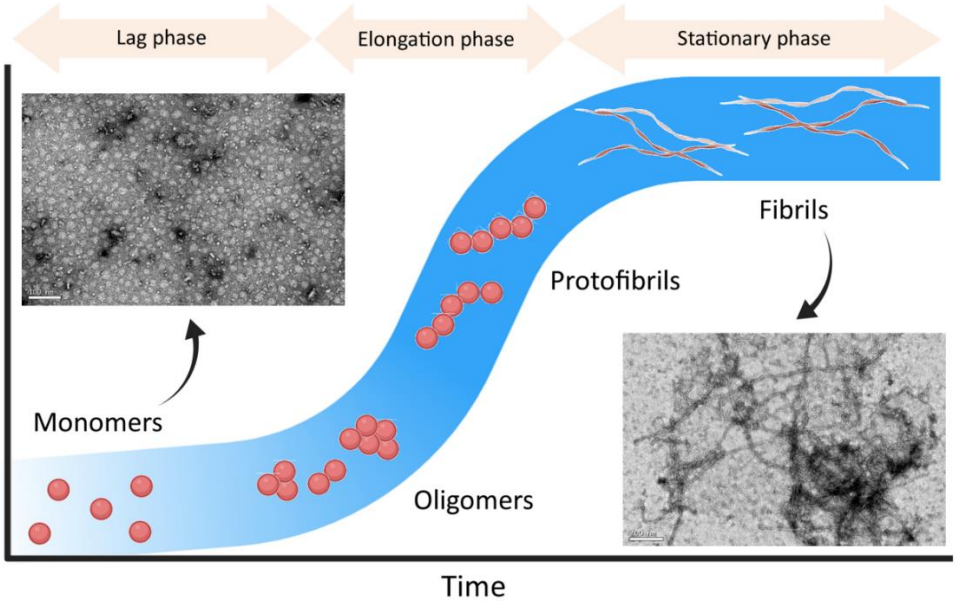

Figure 2.2. Schematic representation of amyloid β (Aβ) fibril formation. Images of $A\beta_{1-42}$ (25 μM) in phosphate buffer saline (PBS) were acquired by transmission electron microscopy (TEM). Scale bars correspond to 100 nm (left) and 200 nm (right).

The aggregation and fibrillation of Aβ have been pointed as the main trigger of the neurotoxicity and pathogenesis of AD. Numerous findings revealed that the toxicity of Aβ depends on its aggregation status. While monomers were shown to be nontoxic, oligomers have been indicated as the most toxic species of Aβ. Protofibrils followed by fibrils also induce some toxicity, although to a lesser extent [16].

2.1.3. Genetic

From a genetic perspective, AD is a heterogeneous pathology with familial (around 15-25% of AD cases) and sporadic variants (approximately 75-85% of AD cases) [17]. Familial AD is an autosomal dominant condition that commonly begins before the age of 65 years. Mutations at the APP gene on chromosome 21 were first found to cause the familial form of the disease. Although several APP mutations have already been identified, they explain a reduced number of familial AD cases. Presenilin 1 (PSEN1) and presenilin 2

(PSEN2) gene mutations are responsible for the majority of cases of familial AD. Currently, 32 APP, 179 PSEN1, and 14 PSEN2 gene mutations have been identified [18].

Mutations in APP or presenilins genes are thought to alter the cleavage site, resulting in increased synthesis of $A\beta_{1-42}$ peptides. PSEN1 and PSEN2 mutations affect the concentrations of $A\beta_{1-42}$ since these genes encode the major component of γ-secretase, which is involved in the APP cleavage and consequent Aβ peptide production. The $A\beta_{1-42}$ oligomerization and plaque deposition in the human brain were found to be enhanced in the presence of presenilin mutation. Moreover, an increased ratio of $A\beta_{1-42}/A\beta_{1-40}$ has been found in transgenic mice and humans' brain [19].

Sporadic AD has a considerable genetic component, ranging from 50% to 70% of total cases. Several risk genes for AD have been identified, with the apolipoprotein E (ApoE) gene, located on chromosome 19, considered the major genetic risk factor for AD. The three majors human ApoE alleles are ApoE ε2, ApoE ε3, and ApoE ε4. The most common allele is the ApoE ε3, which is found in about 77% of the world's population. It is considered to play a neutral role in AD. In turn, ApoE ε2 is the least common allele, accounting for around 8%, and it is thought to play a protective role on AD onset. The ApoE ε4 is roughly 15% in healthy individuals, but it rises to around 40% in AD patients. The presence of one ApoE ε4 allele anticipates the AD onset's age in approximately 5 to 10 years. In the presence of the two alleles, these values rise to 10 to 20 years. The ApoE ε4 allele increases the risk of AD three times in heterozygotes and 15 times in homozygotes. However, this allele is neither necessary nor sufficient for developing AD [20].

The molecular mechanism behind the ApoE ε4 allele-promoted AD incidence results of a cascade of events. ApoE protein acts as a carrier of cholesterol (CHOL) to the brain, which modulates the APP processing by increasing the β-secretase activity, resulting in increased production of Aβ peptide [21].

Rare variants in the triggering receptor expressed on myeloid cells 2 (TREM2) gene, which encodes a receptor expressed in myeloid cells that modulates inflammatory responses – have been demonstrated to triple an individual’s risk of developing AD. TREM2 is a transmembrane receptor expressed in myeloid cells, and its link with AD suggests that immunological and inflammatory pathways are involved in the cause of AD, rather than as a consequence. TREM2 variants associated with AD induce partial loss of function of the TREM2 protein and affect microglial cell activity, especially their response to amyloid plaques {Carmona, 2018 #334}.

2.1.4. Amyloid Cascade Hypothesis

The amyloid cascade hypothesis (ACH) has been the most influential model of AD pathology (Figure 2.3). The ACH postulates that the neurodegeneration observed in AD is initiated by the abnormal accumulation of Aβ plaques in various brain areas [22]. According to this hypothesis, mutations in the APP, PSEN1, and PSEN2 genes induce deregulation in APP processing, causing the increase in the production of Aβ peptides and in the $A\beta_{1-42}/A\beta_{1-40}$ ratio, or the generation of prone-to-misfold mutant Aβ peptides, facilitating their aggregation. In the early stages of the disease, Aβ oligomers (soluble non-fibrillar Aβ assemblies with 2 to 12 peptides) impair synaptic functions and attenuate microglial phagocytic functions through strong proinflammatory responses. As a result, the efficiency of microglia to clear Aβ aggregates decreases, promoting its deposition in the brain as diffuse plaques. While Aβ non-fibrillar species, namely oligomers, have been linked to the onset of AD symptoms, secondary events are related to amyloid plaques [23]. The formation of these diffuse plaques results in microglial and astrocytic activation, altered ionic homeostasis, oxidative stress, and hyperphosphorylation of tau protein with NFTs formation at a later stage of the disease. NFTs accumulate inside the neurons leading to neurotransmitter system deficits, synaptic dysfunction, and neuronal loss in critical areas associated with cognitive functions such as memory. This cascade of events culminates in cell death leading to dementia [24].

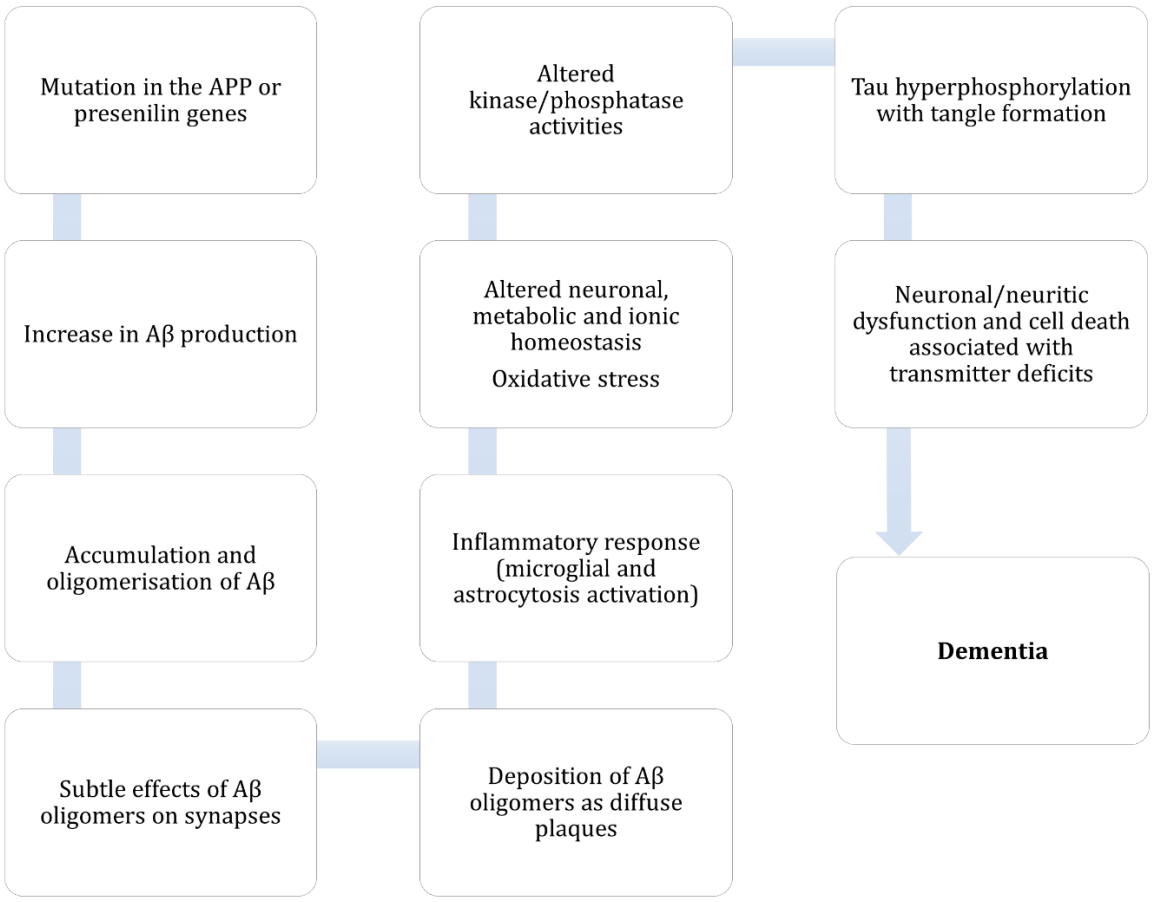

Figure 2.3. Amyloid cascade hypothesis (ACH).

2.2. The Role of Amyloid β-Biomembrane Interactions in Alzheimer's Disease

Although initially considered an abnormal product of the APP cleavage, the Aβ peptide is now established as a regular metabolic product found in healthy peoples' cerebrospinal fluid and serum. Nontoxic soluble Aβ peptides with an unordered structure are found in biological fluids at low concentrations ($<10^{-8}$ M) [25]. However, it is well documented that Aβ only forms fibrils at a concentration above 1 μM *in vitro*, thus suggesting the presence of some mechanism that promotes the abnormal aggregation of Aβ *in vivo*. Although the structural conversion of monomeric Aβ into aggregates has not yet been fully clarified, substantial evidence reveals that cell membranes play a crucial role in enhancing the Aβ aggregation rates. In turn, neuronal membrane damage caused by the

interaction between Aβ and biomembranes has been related to the early impairments observed in AD patients [15]. The disruption of lipid membranes induced by Aβ has been considered one of the major pathological mechanisms of AD. Moreover, increasing evidence indicates the variation of membranes' properties such as fluidity and permeability are possible mechanisms for toxicity mediated by Aβ. Three distinct mechanisms of membrane permeabilization as consequence of Aβ-biomembrane interactions have been proposed so far (Figure 2.4) [26].

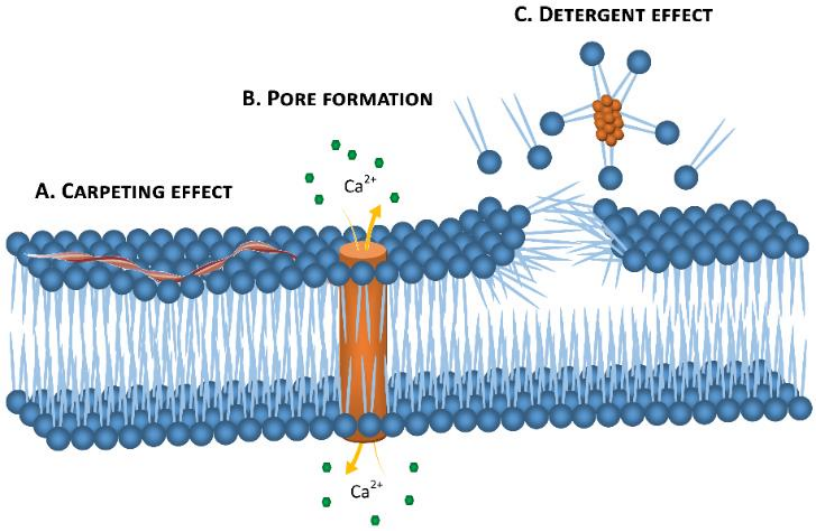

Figure 2.4. Molecular mechanisms of Aβ-induced membrane permeabilization.

The carpeting effect involves the destabilization of the membrane permeability via the direct interaction of Aβ with the membrane's surface, without specific binding sites. This interaction leads to an asymmetric pressure between the two lipid layers of the membrane and consequence deregulation of small molecules' leakage (Figure 2.4 A). According to the pore formation model, oligomeric pores crossing the transmembrane are formed, allowing the exchange of ions through the lipid bilayer with consequent destabilization of the ionic homeostasis (Figure 2.4 B). In the detergent-like model, mature Aβ fibrils adsorbed on the membrane's surface remove lipids from the bilayer producing micelles-like structures that lead to defects in the membrane (Figure 2.4 C) [15].

2.2.1. Cell membranes

Cell membranes are important cellular components involved in most biochemical processes. Considered the shield of animal eukaryotic cells, cell membranes work as

permeable selective barriers between the inside and the outside environments. Thus, by controlling both the influx and the efflux of compounds, cell membranes are involved in the regulation of homeostasis processes and the transport of molecules [27]. Other key functions of cell membranes include the maintenance of chemical and electrical gradients, regulation of membrane-bound enzyme activity, supply of substrates for metabolism, promotion of signal transduction, and protein trafficking [28].

First proposed in 1972 by Singer and Nicolson, the fluid mosaic membrane model describes biological membranes as fluid and complex structures composed of a phospholipid bilayer with embedded proteins able to freely diffuse within the lipid bilayer. This structure is mainly composed of phospholipids, sterols, and sphingolipids (Figure 2.5). Phosphatidylcholine (PC) is the most abundant phospholipid in eukaryotic cell membranes, accounting for approximately 40-60% of the lipid content. Phosphatidylethanolamine (PE) (15-25%), phosphatidylserine (PS) (5-15%), and phosphatidic acid (PA) (1-2%) are found in smaller amounts [29]. Due to the amphipathic nature of phospholipids, biological membranes are relatively impermeable to water-soluble compounds.

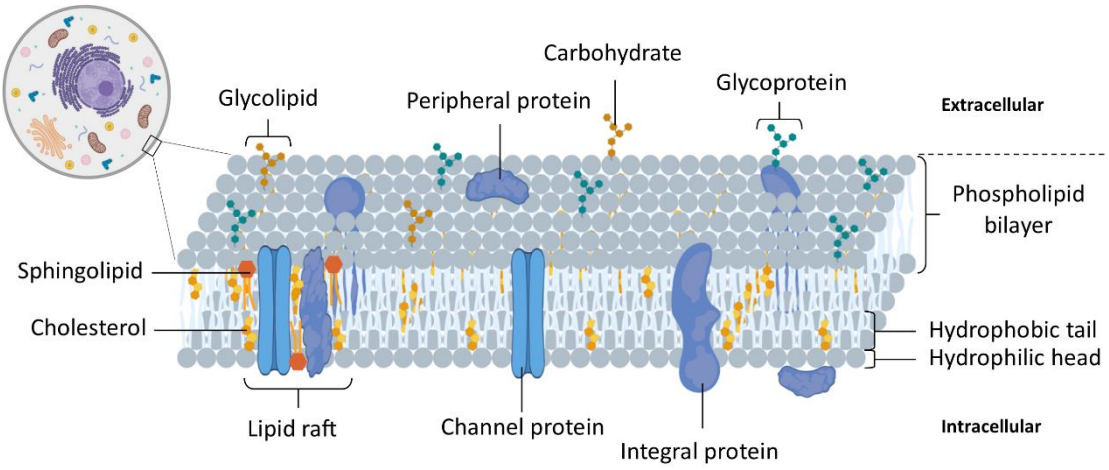

Figure 2.5. Schematic illustration of a cell membrane.

CHOL is another major component of cellular membranes and the most predominant sterol, representing 15 to 50% of the total lipid content [30]. This molecule provides mechanical strength to the bilayer, therefore affecting the structural organization and packing of the surrounding phospholipids. CHOL molecules also regulate the phase behavior of membranes, promoting an ordering and rigidizing effect of the physiologically

fluid state of the membrane, and displaying an opposite impact on gel state membranes. Thus, CHOL has been proposed to reduce membrane permeability [31].

Sphingomyelin (SM) is the main sphingolipid found in animal cell membranes. Its interaction with CHOL and proteins leads to the formation of dynamic lipid rafts that exhibit a more ordered and tightly packing than the surrounding bilayer, typically defined as the liquid-ordered phase of membranes [28]. These microdomains have a relatively short lifetime and are involved in signal transmission and cell recognition [32].

Despite cell membranes exhibiting different compositions and organization depending on the organelles and cell type, there is also an asymmetry in the lipid composition of the two monolayers of the cell membrane. While the most abundant lipids in the outer monolayer are PC, CHOL, and SM, the inner monolayer is mainly composed of phosphatidylinositol (PI), PS, and PE [28]. Such asymmetry contributes to specific functions that include recognition events, regulation of membrane budding, and structural stability [33]. Evidence has highlighted the importance of membrane heterogeneity in maintaining biological membranes functions [34].

2.2.2. Biomembrane models

High-resolution mechanisms of Aβ-membrane interactions remain unclear due, in large part, to the complexity and dynamics of cell membranes [26]. In this context, lipid-based membrane models emerged to offer a simple yet valuable alternative way of studying membrane processes. By simplifying the physiological conditions, *in vitro* membrane models provide the possibility of discriminating the peptide-membrane interactions without the confounding presence of uncontrolled conditions that would occur in *in vivo* studies [35].

Several *in vitro* lipid membrane models have been employed to mimic biological membranes for peptide-membrane interactions studies, including lipid monolayers, supported lipid bilayers (SLBs), micelles and liposomes. These models allow simulating the lipid content of cell membranes under both physiological and pathological conditions by adjusting several biophysical parameters, such as the molecular packing, physical phase, lateral pressure, lipid composition, pH, ionic strength, and temperature [35].

Artificial lipid membranes are valid models with high predictive value and reproducibility, low cost, easy handling, and short experimental times [35]. Each of these

models has advantages and disadvantages and can be prepared with different degrees of complexity to better mimic the composition of biological cell membranes.

2.2.2.1. Lipid monolayers

Lipid monolayers are popular models of cell membranes and include Langmuir monolayers and solid-supported lipid monolayers (Figure 2.6). These monolayers present advantages due to their simplicity and the precise control of the area per molecule at the air/liquid or air/solid interface. These monolayers can be compressed to better regulate their structure and physical state [36]. Solid-supported lipid monolayers offer an advantage over the non-immobilized monolayers since the surface immobilization limits the motion of phospholipids while still allowing the study of drug-lipid interactions. These immobilized monolayers also constitute more realistic models since they better mimic the dynamics of the phospholipids in the biological membranes.

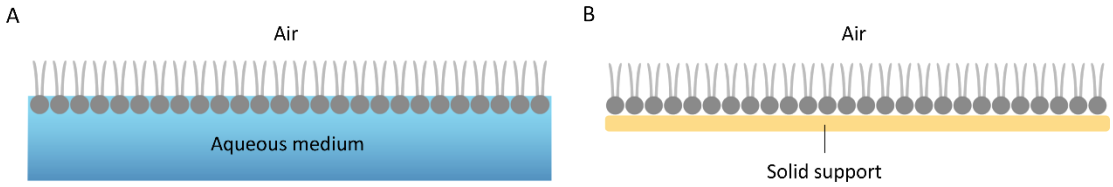

Figure 2.6. Schematic representation of a A) lipid monolayers and B) solid-supported lipid monolayer.

Pieces of evidence state that it is possible to establish a direct relationship between the thermodynamics of monolayer and bilayer membranes. Therefore, simpler monolayer models are often chosen for membrane phenomena studies. However, lipid monolayers only mimic the outer leaflet of cellular membranes. Also, monolayers are less thermodynamically stable than lipid bilayers. Since these models are 2D representations of the 3D biological membranes, 3D monolayer structures such as micelles could offer an advantage over the monolayers [35].

2.2.2.2. Micelles

As represented in Figure 2.7, micelles are the most simple 3D model of cell membranes [37]. Other unique features make micelles attractive tools, such as the

possibility of controlling the resulting size and shape of the micelles by choosing the lipid composition and the aqueous medium [38]. Also, depending on the type of amphiphilic molecules selected for the micelles' design, it is possible to prepare micelles with different surface charges to study the electrostatic forces involved in membrane processes. Although their relatively small size and high curvature are pointed out as advantageous, some studies report that the surface curvature of micelles is significantly higher than those of biological membranes [39]. Additionally, the optical properties of micelles are not ideal for some spectroscopy experimental techniques due to the background noise from the scattered light. Besides, the partition of small molecules into micelles is often ill-defined [37]. Another disadvantage of using micelles as biomimetic membrane models is that micelles are also composed of a monolayer instead of a bilayer, as in biological membranes [39].

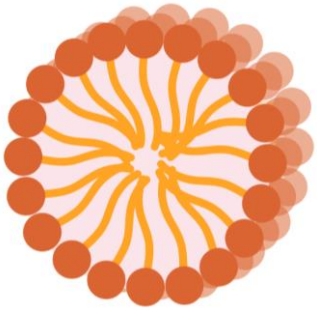

Figure 2.7. Schematic representation of a lipid micelle.

2.2.2.3. Supported Lipid Bilayers

SLBs are biomimetic models where a bilayer is supported onto a hydrophilic surface (Figure 2.8). Depending on the support, SLBs can be prepared with different shapes and curvatures such as planar, spherical, or cylindrical [40]. SLBs as membrane models allow obtaining quicker and more reproducible results than free-floating vesicles [41]. Besides, the use of solid surfaces as a support for the bilayer increases the bilayer's stability when compared with free-standing lipid vesicles by limiting the lipid motion through surface immobilization [39]. This also facilitates the characterization of the membrane, enabling the use of more time-consuming and sensitive methodologies [42]. Moreover, the use of metallic supports allows the characterization of electrochemical features of the membrane [43].

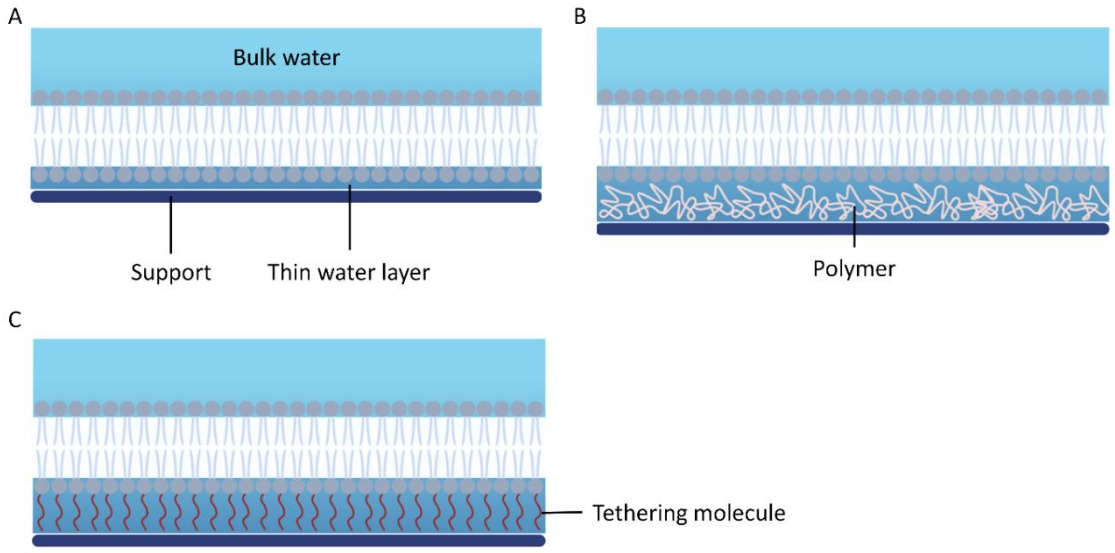

Figure 2.8. Schematic representation of a A) supported lipid bilayer (SLBs), B) polymer-SLBs, and C) tethered lipid bilayer.

Still, SLBs exhibits some drawbacks due to the proximity between the substrate and the lipid bilayer, which hampers the free diffusion of ions and accommodation of transmembrane proteins. To overcome these limitations, new variations of SLBs such as polymer-supported bilayers and tethered bilayers (Figure 2.8) have been proposed in the past. In polymer-supported bilayers, one polymer layer is usually bound to the surface of the support and the lipid bilayer is placed on the polymer [44]. While in tethered bilayer lipid membranes, the inner leaflet of the lipid bilayer is covalently linked to the surface through a spacer group [41].

Although solid supports confer robustness and stability to the model, they also present some limitations. The supported membrane is not truly decoupled from the underlying substrate, and the interaction between the bilayer and the support can lead to shape changes that may alter the system's physiological response. Also, being a 2D model, SLBs are not the most representative models for the membranes' structure and curvature [45].

2.2.2.4. Liposomes

Liposomes appear as a popular model due to their 3D structure representing both cell membranes' inner and outer leaflets. Liposomes are vesicles constituted of one or more

phospholipid bilayers oriented concentrically around an aqueous compartment (Figure 2.9). Liposomes can be prepared with different lipids components that approximate the composition of membranes *in vivo* [46]. Liposomes can be classified by their size and number of bilayers, as shown in Figure 2.9 [47]. Regarding the number of bilayers, liposomes can be divided in two categories, multilamellar lipid vesicles (MLVs) that are composed by many concentric lipid bilayers, and unilamellar lipid vesicles (ULVs). ULVs can then be named by their size as small (SUVs), large (LUVs) and giant (GUVs) unilamellar vesicles [48]. LUVs are the most suitable liposomes for studying peptide and drug-membrane interactions due to their curvature being more similar to that of biological membranes. Despite liposomes' curvature being higher than the one observed in biological membranes, these still present an advantage over the other models by better resembling to biological membranes [35].

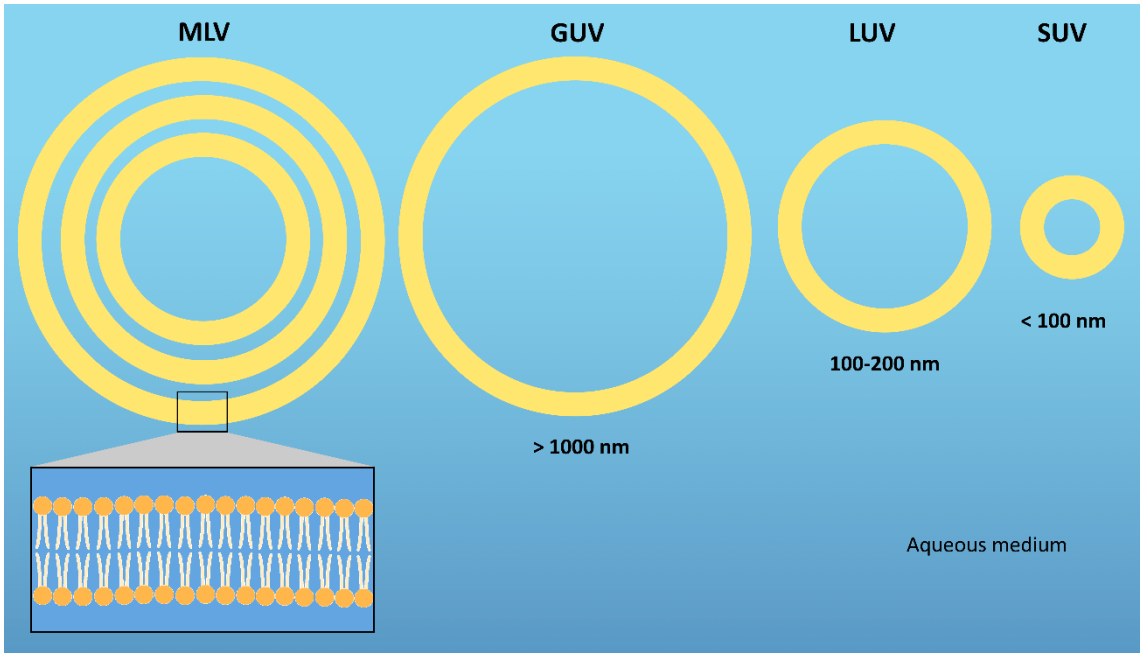

Figure 2.9. Schematic representation of multilamellar lipid vesicles (MLVs) and unilamellar liposomes-based on size: giant unilamellar vesicles (GUVs), large unilamellar vesicles (LUVs), and small unilamellar vesicles (SUVs).

By mimicking both the inner and outer leaflet of cell membranes, liposomes offer an advantage over lipid monolayers and micelles, which only mimic the membranes' outer leaflet. Despite SLBs being more robust than liposomes, lipid vesicles are preferred because of their resemblance to the structure and curvature of natural membranes. Liposomes are

versatile biomimetic models that can be used for various studies, including specific membrane processes such as fusion, membrane trafficking, cell adhesion, molecular recognition, and pore formation [42]. Despite their enormous potential as *in vitro* membrane models, liposomes also exhibit some limitations. Like the other models, liposomes do not fully mimic the complexity of biological membranes [49].

Although each one of the presented membrane models exhibits their advantages and disadvantages, liposomes are the ones that best mimic the entire lipidic assembly of cellular membranes. In fact, various lipid components of biological membranes can be included when producing liposomes. To mimic the inner leaflet of the cell membrane, negatively charged phospholipids can be used such as PS, and to mimic the outer leaflet of the membrane PC, SM and glycosphingolipids are the most appropriates lipids. Therefore, liposomes are being the most used lipid membrane model in peptide-membrane interaction studies [39].

2.3. Natural Compounds for Alzheimer's Disease Therapy

Some medications are prescribed for attenuating the disease's symptoms [50]. So far, three cholinesterase inhibitors are commercially available for AD treatment: galantamine, rivastigmine, and donepezil. These drugs increase the acetylcholine brain levels by inhibiting the acetylcholinesterase enzyme activity. As acetylcholine helps send messages between nerve cells, higher acetylcholine concentrations in the brain lead to cognitive improvement. Memantine, an antagonist at glutamatergic NMDA receptors, is another drug commonly used to treat moderate to severe AD cases. By regulating the activity of glutamate, a molecule involved in information processing, storage, and retrieval, memantine improves the AD symptoms, including memory, attention, and reasoning. In addition to not providing a cure, these drugs induce several side effects, including headache, constipation, confusion, dizziness, nausea, vomiting, loss of appetite, and increased frequency of bowel movements [50]. Therefore, it is fundamental to seek new strategies for AD therapy.

Developing new drugs is a costly and time-consuming process that is often delayed due to the failure of drug candidates in the clinical trials phase. Over the years, natural

compounds have aroused increasing interest as promising alternatives to synthetic drugs due to their presumable safety for human intake since they are widely consumed in daily life, which facilitates their clinical approval. Due to their neuroprotective effects, a diversity of natural compounds from different origins has been proposed for AD therapy [51]. Instead of controlling the disease symptoms, natural compounds have been demonstrated to target the various aspects of the disease pathogenesis (Figure 2.10). These include the inhibition of Aβ production and aggregation or the promotion of Aβ clearance from the brain. Natural compounds have also been proposed for AD therapy by reducing neuroinflammation and oxidative stress and inhibiting NFTs formation.

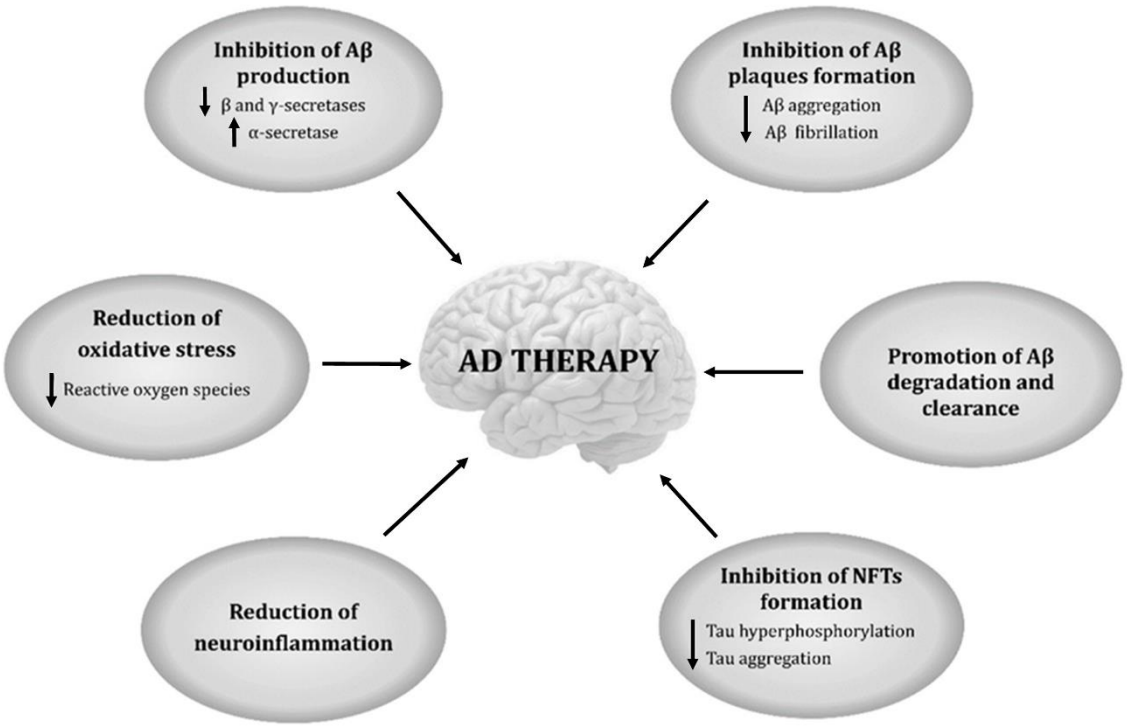

Figure 2.10. Schematic representation of ACH-based therapeutic strategies. Down and up-oriented arrows indicate the decrease and the increase of the phenomena, respectively.

2.3.1. Natural Compounds in Clinical Trials

For the assessment of the natural compounds' therapeutic efficiency and potential side effects, human trials have been performed in the last years. In the first stage, natural compounds are required to be safe for human use and then can further proceed to the other successive phases. Although several natural compounds have shown promising effects in

preclinical studies and proved to be safe in phase I of clinical trials, only a small number have progressed to phase II, III and IV of clinical trials (Table 2.3) [50].

Table 2.1. Natural compounds in phase II, III, and IV of clinical trials for AD therapy.

Bioactive compound	Trial Phase	Trial status	Number of subjects	Duration	Outcomes	Ref.
Nicotine	II	Ongoing	300	2 years	No results yet	
Bryostatin	II	Completed	150	12 weeks	Cognitive functions improved	[52]
Ginkgo biloba	II	Completed	410	24 weeks	Cognitive functions improved	[53]
Homotaurine	III	Completed	1052	78 weeks	Cognitive functions improved	[54]
Docosahexaenoic acid (DHA)	III	Completed	485	24 weeks	Cognitive functions improved	[55]
Vitamin D and memantine	III	Ongoing	90	24 weeks	No results yet	
Vitamin E and memantine	III	Completed	613	5 years	Slowed cognitive decline	[56]
Vitamin E and selegiline	III	Completed	341	2 years	Slowed disease progression	[57]
Huperzine A	IV	Ongoing	300	52 weeks	No results yet	

Nicotine was the first natural compound to be tested in human trials for AD prevention or treatment in 1992. Interesting, although nicotine improved the perceptual and visual attentional deficits in a pilot study conducted for 2 weeks with 70 AD patients, it was not further studied for several years [58]. Nicotine supplementation is controversial due to its association with tobacco consumption and high dependence. However, several *in vitro* studies showed the potential of this natural compound for AD therapy [59]. Only most recently, nicotine has attracted attention in the scientific community and is now currently being studied in an ongoing randomized, placebo-controlled phase II trial with 300 participants with mild cognitive impairment. In this 2-year trial, subjects will be randomized (50:50) and a transdermal patch containing nicotine (21 mg/day) will be used or placebo (ClinicalTrials.gov Identifier: NCT02720445).

Another natural compound, bryostatin, was also studied in a phase II clinical trial for AD therapy. Farlow *et al*. (2018) [52] evaluated the effects on cognitive function of bryostatin on AD patients in a placebo-controlled trial with 150 participants. The subjects were randomly divided into two groups, the placebo group and one group of patients

administered with 20 or 40 μg of bryostatin for 12 weeks. This study showed the ability of the natural compounds in improving the cognitive functions of patients.

Ginkgo biloba (*Ginkgo biloba L*., Ginkgoaceae) has been studied as a therapeutic drug for AD in several clinical trials in the last 10 years. Bachinskaya *et al*. (2011) [53, 60] examined the effect of ginkgo biloba extract EGb 761® on neuropsychiatric symptoms of dementia. Outpatients with mild to moderate dementia (AD with or without cerebrovascular disease or vascular dementia) (n=410) were considered in this study. Patients received 240 mg of extract or placebo once daily for 24 weeks. The treatment with ginkgo biloba was safe and improved the neuropsychiatric symptoms, including apathy, irritability, and depression. With the same conditions, Herrschaft *et al*. (2012) [61] revealed that the treatment with ginkgo biloba improved patients' cognition and life quality.

The administration of natural compounds for AD has also been evaluated in phase III clinical trials. The effects of homotaurine intake were evaluated in a phase III placebo-controlled clinical trial with AD patients from mild to-moderate symptoms. A total of 1052 patients were randomly divided into three groups, one group receiving placebo, and the other two groups treated with 100 or 150 mg of homotaurine for 78 weeks. The obtained results showed that this natural compound has the ability to improve cognitive functions [54].

Other natural compounds have revealed to be more promising for AD therapy and have already been able to reach the phase III of clinical trials, such as docosahexaenoic Acid (DHA). Quinn *et al*. (2010) started a placebo-controlled phase III clinical trial to evaluate the effect of DHA supplementation on cognitive impairment [55]. Here, 485 healthy participants with age-related cognitive decline were randomly divided into two groups and daily administered orally with placebo or 900 mg of DHA orally for 24 weeks. The treated patients showed improved cognitive and memory functions.

The co-administration of memantine with different vitamins also reached phase III of clinical trials. The co-administration of vitamin D and memantine was first evaluated in a pilot study with 43 AD patients for 24 weeks [62]. The subjects were randomized in three groups, being the first treated with a combination of vitamin D and memantine, and the second and the third groups being administered with only vitamin D or only memantine, respectively. The results showed that co-therapy with both compounds is more effective in improving cognitive function than vitamin D or memantine alone. After the promising results obtained in this pilot study, the co-administration of both compounds has been

further studied in human trials. Currently there is an ongoing phase III clinical trial to study their concomitant use in 90 patients with diagnosis of moderate AD. In this 24-week trial, subjects will be randomly divided into two groups (only memantine and vitamin D plus memantine) to assess if co-administration with vitamin D increases the efficacy of memantine (ClinicalTrials.gov Identifier: NCT01409694).

The combination effect of memantine with other natural compound, vitamin E, was also evaluated in a phase III clinical trial. Dysken *et al*. (2014) studied the combination effects of vitamin E and memantine in a placebo-controlled clinical trial with 613 AD patients from mild to moderate symptoms [56]. The subjects were randomized in three groups, being the first treated with a combination of vitamin E and memantine, and the second and the third groups being administered with only vitamin E or only memantine, respectively. Treatment with vitamin E alone has proved to be effective in slowing down the cognitive decline; however, coadministration with vitamin E did not improve memantine effects.

The co-therapy of vitamin E with selegiline was also studied in clinical trials. Selegiline is a monoamine oxidase inhibitor that prevents dopamine degradation [63]. Sano *et al*. (1997) [57] conducted a double-blind, placebo-controlled clinical trial with 341 patients with moderate AD symptoms for 2 years. The patients were randomly divided into four groups, a placebo group, one receiving vitamin E, one receiving selegiline, and another one receiving both drugs. Vitamin E was administered daily at a dose of 2000 IU per day, and 10 mg of selegiline daily. Co-therapy proved to slow efficiently the progression of the disease [57].

Huperzine A is currently the only natural compound in phase IV of clinical trials after being proven to improve cognitive functions in mild to moderate AD patients in a study conducted in 2011 with 177 patients for 16 weeks [64]. This natural compound is now being evaluated in an ongoing phase IV clinical trial. In this placebo-controlled trial, 300 AD patients with mild cognitive impairment were randomized (50:50) and administered with huperzine A (200 ug/day) or placebo for 52 weeks (ClinicalTrials.gov Identifier: NCT02931136).

Other natural compounds can also be a promising approach for AD prevention and therapy in present and near future. For example, curcumin and melatonin have presented promising results in *in vitro* and therefore have been studied in small-scale pilot studies. Despite having a limited size of subjects, pilot studies can provide useful information for the

preparation of further clinical trials [50]. Valuable information can also be obtained from human trials with no positive outcomes. For example, resveratrol has been studied in phase III clinical trials for AD therapy but did not show significant improvement [65]. A similar result was verified in two different phase III clinical trials to study the combination effect of vitamin E with AD drugs (vitamin E/donepezil [66] and vitamin E/selenium [67], respectively), where no positive outcomes were verified.

2.3.2. Limitations of Natural Compounds to their Clinical Application

Despite their promising value for AD therapy, natural compounds have some limiting features that prevent them from reaching the brain in effective concentrations. Among them, the compounds' low solubility, absorption, and bioavailability, *in vivo* instability, lack of specificity, high systemic clearance, and harmful effects stand out. Premature degradation due to the low stability to light, oxygen and temperature also decreases the bioavailability of therapeutic molecules. This was reported for several natural compounds such as resveratrol [68], vitamin E [69] and curcumin [70]. In addition to these limitations, the molecules' difficulty in crossing the BBB and reaching the brain remains the major obstacle for developing effective therapies [71].

2.4. Blood-Brain Barrier

Drug delivery to the brain has been one of the most challenging issues that researchers have faced in developing effective treatments for brain illnesses. Due to the BBB, only a tiny portion of administered drugs can reach the brain. The BBB is an organized interface between the peripheral circulation and the central nervous system (CNS) that acts as a barrier protecting the CNS from damage [72]. It is the primary site for exchanging molecules between the blood and the CNS, being fundamental in ensuring a stable fluid microenvironment required to execute complex neural functions. On the one hand, the BBB blocks the transport of potentially toxic or harmful substances from the bloodstream to the brain. On the other hand, it allows the transport of nutrients, maintaining the CNS homeostasis. Thus, this interface maintains the CNS homeostasis by regulating the ionic balance and metabolites influx/efflux [73].

The BBB's structure is crucial to its functional ability to protect and maintain the brain microenvironment. The BBB is found throughout the brain, except for areas that control the body's autonomic nervous system and endocrine glands. The main functions of the BBB result from the combination of the physical barrier, transport barrier (specific transport mechanisms mediating solute flux), and metabolic barrier (enzymes that metabolize molecules in transit) [74].

2.4.1. Structure and Composition

The BBB is formed by endothelial cells of brain capillaries. Astrocytes and pericytes are positioned close to the capillary endothelium with the primary function of supporting the BBB. The astrocytes' ends are placed over the continuous basal lamina forming a restricted barrier. In turn, the pericytes are mesenchymal cells with smooth muscle properties located in the perivascular space, between the capillary wall and the extremities of astrocytes. They regulate the BBB permeability by releasing vasoactive substances. As they decrease with age, there is an increase in the BBB permeability. In large vessels, the pericytes are replaced by smooth muscle cells. Neurons and microglia also communicate with BBB endothelial cells. The basal lamina comprises type IV collagen, fibronectin, heparin sulfate, and laminin [75].

There are two other sites in the CNS that form a barrier between the blood and cerebrospinal fluid: the arachnoid epithelium forming the middle layer of the meninges and the choroid plexus epithelium. Here, the permeation of ions and other small hydrophilic solutes is significantly reduced through the tight junctions in the intercellular slot that form a physical barrier. Thus, the passive diffusion of molecules through the BBB is limited to high liposoluble molecules with a low molecular weight (<400 Da) [76].

2.4.2. Transport Mechanisms

Numerous transport mechanisms present at the BBB provide the brain with essential nutrients and protect it from toxic substances. The transport of molecules across the BBB can occur through different systems depending on their physicochemical properties, as summarized in Figure 2.11 [77].

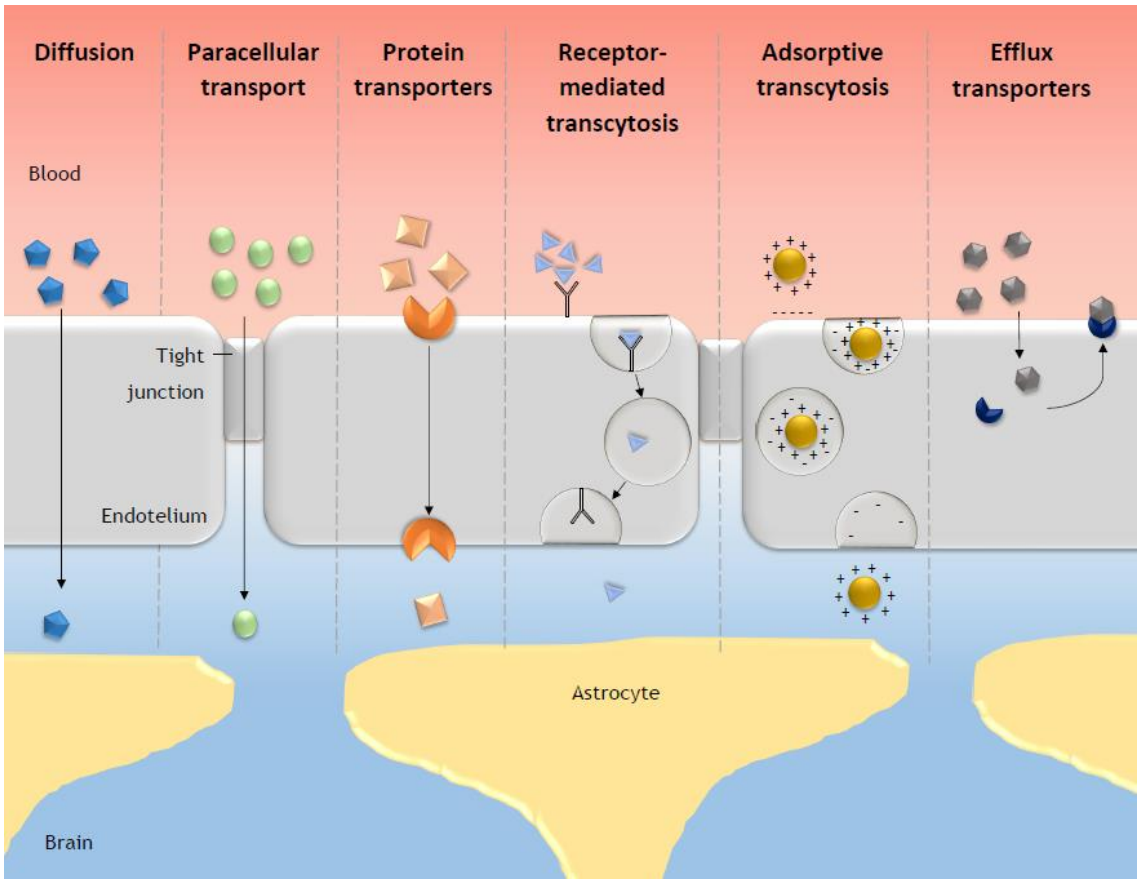

Figure 2.11. Transport mechanisms across the blood-brain barrier (BBB).

- **Tight junction**: Most molecules cross the BBB via paracellular transport due to the tight junction between adjacent endothelial cells. The tight junctions regulate the lateral diffusion between the apical and the basolateral plasma membrane, preserving the plasma membrane protein and the lipid polarity. Thus, they prevent the passage of protein, controlling the traffic from the blood to the CNS. The BBB functions are mainly due to tight junctions [78].

- **Lipid-mediated free diffusion**: As membranes are held together by weak forces, some molecules can move from side to side of the lipid bilayer in a spontaneous transport mechanism known as lipid diffusion. Only gaseous molecules such as oxygen and carbon dioxide and small lipophilic molecules are capable of entering the brain passively by diffusion through the BBB. This ability is connected to the molecule's lipid solubility. Compounds positively charged can cross the BBB by interacting with the membrane's negatively charged glycocalyx and phospholipid head groups. Thus, the molecules' entry into the CNS depends on the molecules' physicochemical properties such as size (<400 Da),

charge, hydrogen bonding potential (<10 hydrogen bonds with water), and lipophilicity [79].

- **Transport proteins**: An array of specific membrane proteins embedded in the apical and basal membranes mediates small solute traffic across the hydrophobic portion of the bilayer. This regulates the entry of ions, nutrients, and essential molecules for CNS metabolism, including glucose, amino acids, nucleosides, and monocarboxylic acids. Membrane transport proteins are divided into carrier proteins that allow the passage of specific molecules; and channel proteins that form thin pores to transport ions. While some carrier proteins allow for passive molecular transport (facilitated diffusion), others can carry molecules against their concentration gradient when joined to an energy source. Channel proteins passively transport ions based on their concentration gradient. Aside from that, membrane transport proteins allow the efflux of waste products [80].

- **Receptor- or adsorptive-mediated transcytosis**: Hydrophilic macromolecules essential for the brain homeostasis, such as hexoses, neuropeptides, and proteins, cross the BBB by endocytosis in vesicles, which can be specific (receptor-mediated transcytosis, or RMT) or less specific (adsorptive-mediated transcytosis, or AMT). On the RMT, molecules bind to their receptors on the luminal side of endothelial cells and endocytosis is initiated. The receptor–ligand complex is invaginated, leading to the formation of intracellular transport vesicles. The vesicles are then subjected to exocytosis to release the ligand to its basolateral side. The receptor is then recycled. On the other hand, AMT relies on electrostatic interaction between the positively charged ligand and the negatively charged endothelial cells to initiate endocytosis and then transcytosis. This process depends on energy, time and concentration [81].

- **Adenosine triphosphate-binding cassette transporters (ABC transporters)**: Efflux transport is essential for the protection of the brain from endogenous substances. The main role of ABC transporters, which are predominantly inserted in the apical membrane, is to act as active flux pumps that consume adenosine triphosphate (ATP) and transport potentially neurotoxic molecules out of the CNS. Thus, these receptors have an important neuroprotective and detoxifying role. Nonetheless, ABC transporters reduce drug penetration into the brain and enhance efflux, transporting medicines from the parenchyma to the luminal membrane and back into the bloodstream [82]. P-glycoprotein (P-gp) is an ATP-dependent protein highly expressed in endothelial cells, that actively carries several molecules out of the brain by acting as an efflux pump. P-gp belongs to the class of multidrug

resistance receptors with capability to efflux drug molecules out of the brain leading to reduced efficiency of drugs [83].

2.5. Nanocarriers for Brain Drug Delivery

Distinct approaches have been explored in the last decades to circumvent the various limitations of natural compounds. Nanocarriers seem to be a proper strategy to overcome these issues by protecting compounds from biological degradation [84] and masking their limiting physicochemical properties without modifying them [85]. NPs are colloidal carriers in the nanoscale range (10^{-9} m) with interesting properties, including small size, larger surface area, high stability, and capacity to interact with receptors present at the BBB [86, 87]. Additionally, the controlled and sustained release provided by nanocarriers allow maintaining active doses of therapeutic agents for long periods [88]. Moreover, nanocarriers reduce the amount of compounds needed to produce therapeutic effects due to the improvement of their pharmacological activity, thus decreasing side effects [89]. Nano-scaled DDSs present numerous beneficial properties such as biodegradability, biocompatibility, nontoxicity, non-immunogenicity, high stability in body fluids, and the ability to interact with specific receptors [90].

NPs can interact with the BBB, allowing them to easily cross it and distribute drugs in a controlled manner [91]. The ability of NPs to cross the BBB is determined by their physicochemical and biomimetic properties, such as surface charges and NPs manufacturing material. Because they interfere with the pattern of proteins adsorbed from plasma, the surface charge and hydrophobicity of NPs impact their absorption and/or rate of transcytosis. NPs with a hydrophobic surface are quickly opsonized and recognized by the reticuloendothelial system (RES) [92]. The final particle size is another major factor influencing the drug delivery to the brain since small carriers (below 100 nm) promote toxicity, and large ones (over 200 nm) do not cross the BBB.

2.5.1. Types and Properties of Nanoparticles

Different NPs can be produced using various materials depending on the drug properties to be encapsulated [93]. The most used NPs are summarized in Figure 2.12 and detailed in the following subsections.

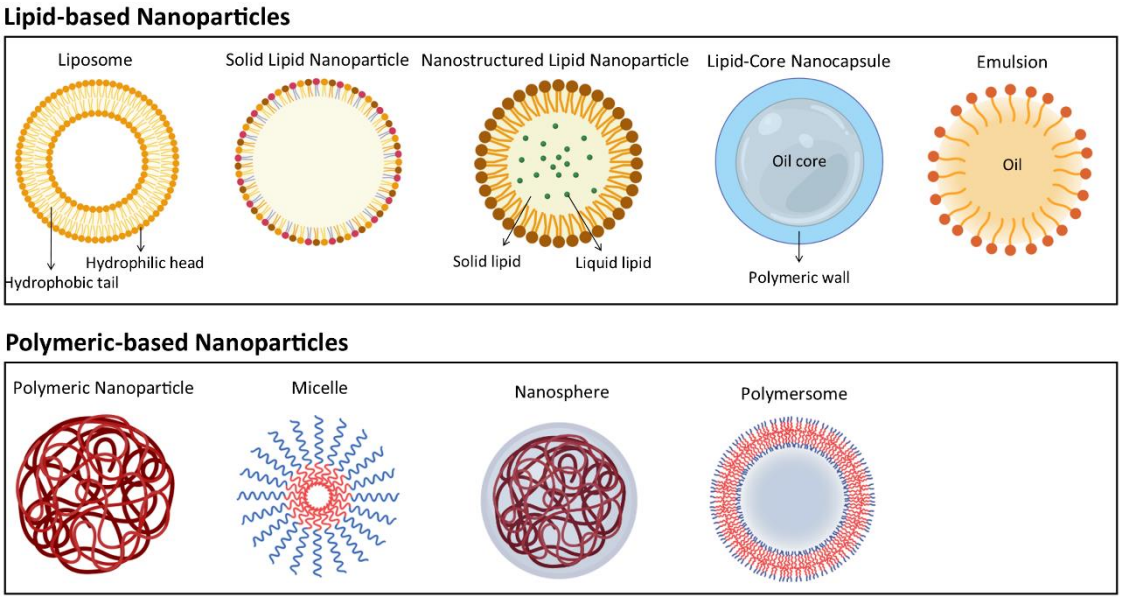

Figure 2.12. Schematic representation of the most used nanoparticles (NPs) for the delivery of natural compounds for Alzheimer's disease (AD) therapy.

2.5.1.1. Liposomes

Liposomes, first described by Bangham in 1964 [94], are among the most popular DDSs. Liposomes are spherical vesicles composed of one or more phospholipid bilayers enclosing aqueous compartments. The amphiphilic property of phospholipids, which display hydrophilic polar heads and lipophilic tails, allows to encapsulate both hydrophilic compounds in the aqueous space and lipophilic compounds in the lipid bilayer [95]. This singular composition makes the structure of liposomes similar to the biological membranes, thereby allowing their fusion with cell membranes and the release of the content into the cytoplasm. The biocompatibility, bioavailability, high loading capacity, and ease of production of liposomes are other properties that stand out [96]. Moreover, these lipid vesicles guarantee the controlled and sustained release of therapeutic agents, ensuring the maintenance of active doses for an extended period. Consequently, the pharmacological

activity of compounds is achieved with reduced doses, thereby decreasing side effects induced by high amounts of therapeutics.

Liposomes can be classified by their size and number of bilayers, as mentioned in section 2.2.2.1. LUVs are often preferred for drug delivery applications due to having a higher trapped volume than SUVs, which allows the loading of higher amounts of drugs. Also, when compared to MLVs, LUVs require fewer lipids to entrap the same amount of drugs. However, SUVs usually have a higher blood-circulation time due to their smaller sizes [97].

Conventional liposomes (Figure 2.13 A) composed of neutral and/or anionic lipids were the first generation of lipid vesicles created and used in the pharmaceutical industry. The most used lipids in the formulation of conventional liposomes are PC and CHOL [46]. However, the rapid uptake by the RES after systemic administration of conventional liposomes represents the major drawback for their therapeutic efficacy *in vivo*. It was in this context that the second generation emerged. To increase the liposomes' stability and their blood circulation time, sterically-stabilized liposomes (Figure 2.13 B) were introduced by adding a coating to the liposomes' surface. The hydrophilic polymer polyethylene glycol (PEG) has proved to be a great strategy by offering an extra surface hydration layer that sterically inhibits both electrostatic and hydrophobic interaction between liposomes and serum components, therefore reducing the clearance of liposomes by RES [98].

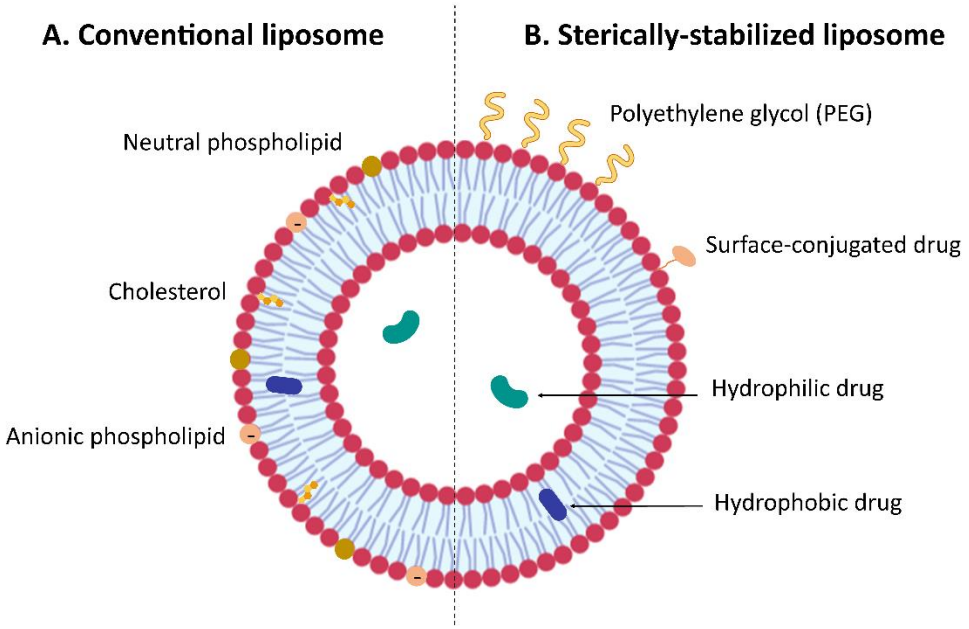

Figure 2.13. Schematic representation of A) conventional and B) sterically-stabilized liposomes.

2.5.1.2. Solid Lipid Nanoparticles

Solid lipid nanoparticles (SLNs) are nanocarriers composed of a solid hydrophobic lipid core that encapsulates hydrophobic drugs. The incorporation of hydrophilic molecules can be achieved at the NP's surface. This type of nanocarrier is produced using an oil/water emulsion with a solid lipid at room temperature [99]. SLNs usually present a mean size between 40 to 200 nm, allowing their transport across the BBB and escape from the RES. SLNs have attractive properties, including a large surface area and high drug loading [100]. Their synthesis is cheap, highly reproducible, and free of organic solvents. SLNs can be stable for about 3 years, and a controlled drug release for several weeks is achievable. Triglycerides, fatty acids, and waxes are examples of lipids used to synthesize SLNs [101].

2.5.1.3. Nanostructured Lipid Carriers

Nanostructured lipid carriers (NLCs) are composed of a solid lipid matrix and a liquid lipid (oil) at room temperature. The mixture of the solid lipid with an incompatible liquid lipid produces NPs with a high drug loading and good release properties. The use of liquid lipids affects the entrapment efficiency due to the numerous crystal defects in solid lipids, causing imperfections in the matrix that provide sufficient space for the successful accommodation of a large amount of drug molecules [99].

The use of NLCs as DDSs allows for controlling the drug release, increasing the drug stability, and incorporating lipophilic and hydrophilic molecules, avoiding using organic solvents. NLCs exhibit a biphasic drug release pattern with an initial burst release followed by a sustained release. The liquid lipid in the outer NPs' layers forms a drug-enriched portion, leading to the burst release. NLCs retain molecules in the solid matrix and protect them from degradation [102].

2.5.1.4. Lipid-Core Nanocapsules

Lipid-core nanocapsules (LNCs) are DDSs composed of an oil core with a polymeric membrane or coating. LNCs can transport drugs in their reservoir or within a cavity enclosed by a polymer wall. A slower drug release is observed with high polymer concentrations. It occurs due to the decrease of the permeability in the polymer membrane

of the vesicular carrier. LNCs are characterized by a lipoprotein-like structure and average size ranging from 20 to 100 nm. LNCs can be considered hybrids between liposomes and polymeric NPs because they have an oily core with a rigid tensioactive membrane [103]. Therefore, this DDS is appropriate for the transport of hydrophobic molecules.

2.5.1.5. Microemulsions and Nanoemulsions

Microemulsions (MEs) are homogeneous isotropic mixtures and can be of two types: oil-in-water (o/w) or water-in-oil (w/o). They are composed of water, oil, and surfactant, commonly mixed with a co-surfactant [104]. Usually, by mixing an oil phase with an aqueous phase containing a surfactant and a co-surfactant, the MEs are spontaneously self-assembling without any relevant energy input. MEs characteristically have a diameter between 5 to 100 nm. These NPs are easily produced, highly soluble, thermodynamic stable, and translucent. MEs present a suitable drug release profile and slow degradation. Furthermore, MEs demonstrate to have high absorption rates and diffusion. Regarding drug transport, MEs accommodate drugs mainly in the oil phase. Nevertheless, at the equilibrium stage, the drug can be entrapped in the continuous phase, in the dispersed phase, and in the surfactant interphases. The drug release from MEs depends on several factors, such as the system's stability on biological conditions and drug location. However, MEs present some disadvantages. It is quite complicated to encapsulate lipophilic molecules with high molecular weight within these nanocarriers. MEs can also present some toxicity since they require large amounts of surfactants to stabilize them [105].

Nanoemulsions (NEs) are emulsions that contain particles with a diameter ranging from 20 to 100 nm [106]. Emulsifiers are essential to produce droplets of small size by decreasing the interfacial tension [106]. NEs present enhanced stability compared with conventional emulsions. However, NEs present some disadvantages, such as their stability which can be disturbed by pH or temperature, and the release profile is usually slow [107].

2.5.1.6. Polymeric Nanoparticles

Several polymers have been extensively used for developing DDSs for being soluble in water, biocompatible and biodegradable [108]. The degradation of polymeric materials can occur due to chemical, photo, mechanical or thermal stimuli [109]. Also, enzymes, acidic pH, and other biological conditions affect polymer degradation. The instability of polymeric

materials in biological scenarios influences the drug release, which allows the release of the encapsulated drug and avoids the accumulation of the material in the body.

Various polymeric materials have been used to develop DDSs for AD therapy with natural compounds such as poly (lactic-co-glycolic acid) (PLGA). PLGA microparticles (MPs) and NPs are the most popular PLGA-based carriers. The size of the PLGA carriers influences the blood circulation time since RES can easily recognize PLGA vehicles if no surface modification strategy is used [110]. The toxicity of PLGA carriers also depends on their size. Small PLGA NPs can promote several inflammatory processes by releasing cytokines and depolarizing the mitochondria [111]. PLGA NPs also can induce oxidative stress by producing reactive oxygen species (ROS) [112]. However, it is reported that PLGA NPs with diameters over 100 nm can be used safely [113].

Despite being widely used for biomedical applications, PLGA NPs exhibit drawbacks such as poor loading capacity, high cost associated with the production techniques, and high burst release. PLGA NPs usually release a large amount of drug once they reach the blood circulation, decreasing the effective drug concentration in the target tissues [114]. Another limitation of these NPs is the low entrapment efficiency of hydrophilic drugs, requiring suitable NPs preparation methods, such as double emulsion [115].

Chitosan has gained attention as a polymeric material for DDSs due to its biodegradability and biocompatibility. Chitosan NPs can enhance the drug aqueous' solubility, systemic absorption, stability, and resistance to enzyme degradation. Furthermore, chitosan allows the controlled release of drugs, reducing their toxicity, and can be produced without using organic solvents [116]. Some studies have suggested using chitosan to coat other types of NPs to reduce their collateral effects on the body and promote their bioavailability [117]. Further, chitosan presents good mucoadhesive properties [118]. However, there are some drawbacks to using chitosan NPs as DDSs, mainly related to its low solubility at physiological pH [119].

2.5.2. Brain Targeting Strategies

Different strategies can be employed for nanocarriers to reach the brain. RMT is the more relevant mechanism to transport NPs across the BBB, followed by AMT [120]. Therefore, the conjugation of specific ligands to the NPs' surface has been widely employed

to enhance their transport across the BBB [121]. Figure 2.14 displays the numerous ligands that can be conjugated at the NPs' surface.

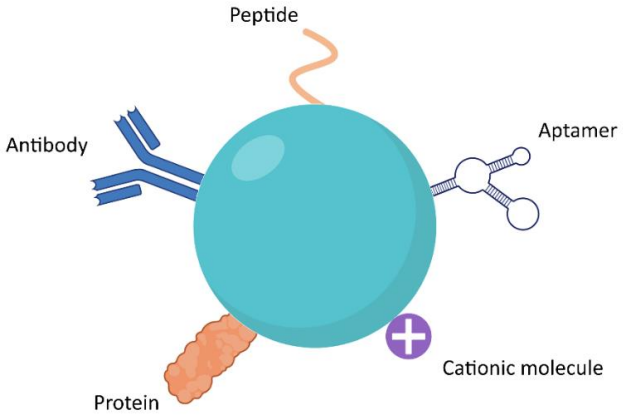

Figure 2.14. Schematic representation of a functionalized NP.

In the case of RMT, the appropriate choice of the ligand is crucial to increase the transport efficiency of the NPs since the receptor needs to be expressed at the target site, in this case, at the BBB. Indeed, receptor saturation needs to be considered to avoid competition with other ligands [122]. Tf receptor (TfR) and insulin receptor are the most expressed receptors by the BBB endothelial cells [123]. Insulin-like growth factor receptor, low-density lipoprotein (LDL) receptor, scavenger receptor class B type I, leptin receptor, and lactoferrin (Lf) receptor are also found at the BBB. More recently, the nicotinic acetylcholine receptor and diphtheria toxin receptor have also been described [81]. The most used ligands are antibodies, peptides, proteins, and aptamers.

Furthermore, the attachment of positively charged molecules has been used to increase the nanocarriers' transport across the BBB by AMR [124]. However, positively charged NPs are usually more toxic than neutral or anionic NPs.

2.5.2.1. Transferrin Receptor

TfR is currently the most relevant target for enhanced drug delivery to the brain since it is present in a more significant amount in BBB's capillary endothelium than in other organs [125]. Various molecules have been used as ligands in nanocarriers functionalization to target the TfR, including Tf itself, antibodies, and targeting peptides [126].

Tf is a 76 KDa blood–plasma glycoprotein generated mainly in the liver that plays a crucial function in iron metabolism by being responsible for ferric-ion delivery. Because Tf is easily obtained from human sources at a high abundance and relatively low cost, it is the most studied targeted ligand for TfR-mediated brain delivery. Tf is also nonimmunogenic, so it can be safely administered without inducing toxicity. However, Tf shows a loss of specificity in the biological environment due to the high amounts of endogenous Tf. Due to the competitive binding, plasmatic Tf molecules can reduce the affinity of Tf-functionalized NPs for the TfR, resulting in diminished therapeutic efficacy [127].

To address this limitation, other approaches using ligands that bind noncompetitively to an alternate location of the TfR have been investigated. These alternative ligands, such as antibodies, do not compete with the Tf present in blood circulation, thus preventing the TfR saturation and increasing specificity [128]. Antibodies, particularly monoclonal antibodies, exhibit high specificity against TfR, which allows achieving high levels of targeting using small amounts. Monoclonal antibodies present other advantages over polyclonal antibodies, including longer half-life, homogeneous structure, and the ability to be mass-produced [129]. So far, different monoclonal antibodies have been described, with particular attention to OX26 [130].

Nonetheless, the difficulty of synthesizing high-quality monoclonal antibodies and their high molecular weight are the main limitations to their application, highlighting the importance of developing more effective targeting strategies. In the last years, single-chain variable fragments (scFv) against the TfR have been investigated as targeting moieties in alternative to antibodies. ScFv are short peptides produced by fusing antibodies' heavy and light chains through a short polypeptide linker. While preserving the binding specificity of antibodies, these fragments exhibit better pharmacokinetic properties due to their higher ability to permeate tissues and faster blood/tissue clearance due to their smaller size [131]. In addition, ScFv bind to an alternative site of the TfR, avoiding the competition with endogenous Tf. These peptides also exhibit higher cost-effectiveness than antibodies [132]. Among the various peptides described for TfR targeting to date, T7 (HAIYPRH) and T12 (THRPPMWSPVWP) are the ones more explored [133].

Other less-explored approaches, such as aptamers, have been described. Aptamers are single-stranded oligonucleotides or peptides that fold into three-dimensional structures and bind to molecular targets like cell receptors. In addition to presenting equal or higher affinity/specificity to the target receptor than antibodies, aptamers offer unique

advantages, including increased stability, smaller sizes, easier modification and immobilization, and improved reproducibility [134].

2.5.3. Functionalized Nanoparticles for the Brain Delivery of Natural Compounds for Alzheimer's Disease Therapy

Numerous efforts have been made to develop suitable natural compounds-loaded DDSs with clinical interest for AD. However, few studies have reported nanocarriers with brain targeting ability for AD therapy. The most relevant information from these studies is summarized in Table 2.2.

Table 2.2. Functionalized NPs for the brain targeted delivery of natural compounds for AD therapy.

Natural compound	Carrier	Targeting ligand	BBB Receptor	Mean diameter (nm)	Zeta potential (mV)	Ref.
Curcumin	Liposomes	Anti-TrF mAb	Tf	153	-8	[135]
	Liposomes	Tf	Tf	101	-21	[136]
	NLCs	Lf	Lf	104	-6	[137]
	PLGA NPs	Tet-1 peptide	GT1b (Neurons)	150 to 200	-30 to -20	[138]
	PLGA NPs	B6 peptide	Tf	50 to 250	4	[139]
	Polymeric NPs	ApoE3	LDL	197	-2	[140]
	POs	Tet-1 and TrF peptides	GT1b (Neurons) and Tf	50 to 60	-6 to -5	[141]
Curcumin and PQVGHL peptide	PLGA NPs	Cyclic CRTIGPSVC peptide	Tf	140	-26	[142]
Curcumin and NGF	Liposomes	Wheat germ agglutinin and cardiolipin	Adsorptive transcytosis	105 to 165	-5 and -15	[143]
Curcumin, NGF, rosmarinic acid and quercetin	SLNs	Tf	Tf	160 to 210	-41 to -30	[144]
Quercetin	SLNs and NLCs	Tf	Tf	200	-30	[145]
	Liposomes	RPM-7 and Lf	Bradykinin B2 and Lf	105 to 165	3 to 37	[146]

Galantamine	Liposomes	Lys-Val-Leu-Phe-Leu-Ser	Serpin-enzyme complex	127 to 165	-36 to -27	[147]
Osthole	Liposomes	Tf	Tf	104	-7	[148]
Epigallocatechin gallate	Selenium NPs	Tet-1 peptide	GT1b (Neurons)	25 to 29	13	[149]
Grape extract	SLNs	OX26 mAb	Tf	182 to 188	0	[150]
Resveratrol	SLNs	OX26 mAb	Tf	254	-4	[150]
Huperzine A	PLGA NPs	Lf	Lf	153	36	[151]

Curcumin is currently the most studied natural compound in terms of targeted delivery to the brain via NPs. Liposomes have been synthetized by Mourtas *et al*. (2014) [135] to encapsulate curcumin and target the Aβ deposits and the BBB. Functionalized liposomes with an antibody for the TfR were produced for this purpose. The prepared NPs showed a negative zeta potential and a mean diameter of less than 160 nm, making them suitable for brain delivery. *Ex vivo* studies on *post-mortem* brains of AD patients have proven that the nanosystem has a great affinity for Aβ deposits, delaying Aβ aggregation. Furthermore, the results showed that the addition of the antibody significantly increased the intake of curcumin-decorated liposomes in an *in vitro* BBB model.

Liu *et al*. (2021) [136] also developed curcumin-loaded liposomes with the surface-modified Tf molecules. Morris water maze and open-field test results revealed that the developed nanosystem improves AD mice's memory and learning ability without inducing toxicity. Furthermore, the liposomes decreased the Aβ levels and oxidative stress in AD mice.

Meng *et al*. (2015) [137] developed LDL-mimic NLCs functionalized with Lf for the brain-targeted delivery of curcumin. The NPs proved to have optimal features for brain targeting, including a mean diameter of around 100 nm and negative zeta potential. Experiments performed in an AD rat model demonstrated that the addition of Lf increased the uptake of the nanosystem in brain capillary endothelial cells. *Ex vivo* images confirmed the ability of this system to cross the BBB and accumulate in the brain. Further, the presence of Lf reduced the AD-induced damage.

Mathew *et al*. (2011) started by proposing the encapsulation of curcumin in PLGA NPs [152]. The *in vitro* effect of the NPs was evaluated using a neuroblastoma cell line. The obtained results proved that the developed NPs were biocompatible, not inducing toxic

effects on the cellular morphology and activity. Encapsulated curcumin retained the ability of Aβ clearance, although to a smaller extent than free curcumin. To address this issue, the group later modified the surface of the developed NPs with Tet-1 peptide to target neuronal receptors, thus increasing the bioavailability in brain tissue [138]. Tet-1 peptide exhibits a high affinity to neurons [149]. *In vitro* studies showed that the NPs uptake by the neuronal cells is enhanced by functionalization with the Tet-1 peptide. This nanosystem can improve the curcumin's Aβ clearance activity compared with the previously developed non-modified NPs. Surface modification of the NPs with Tet-1 peptide did not affect curcumin's therapeutic properties and enhanced the nanocarrier efficiency.

Fan *et al*. (2018) also used PLGA NPs with an active targeting strategy for curcumin delivery for AD therapy [139]. The authors intended to increase its bioavailability on the target tissue and overcome its low solubility issue. The NPs were modified with B6 peptide to target the Tf receptor. The developed PLGA NPs exhibited mean diameters ranging between 50 to 250 nm and positive zeta potential values. *In vitro* studies using a mouse neuronal cell line showed increased cellular uptake of encapsulated curcumin compared with its free form and proved that the NPs are biocompatible, showing no cytotoxicity and good blood compatibility. Bioassays using transgenic AD mice demonstrated that the encapsulation of curcumin in PLGA NPs enhanced its ability to improve the spatial learning and memory of the studied animals. *Ex vivo* studies proved that the entrapped curcumin reduces the Aβ fibrils formation and tau hyperphosphorylation more efficiently in the mice's brains than in its free form.

Mulik *et al*. (2010) [140] used another polymer - poly(butyl) cyanoacrylate - to develop NPs for curcumin delivery, stabilized with poloxamer 188 that showed a negative zeta potential. This group intended to enhance cellular uptake of curcumin by modifying the NPs' surface with apoE3. The encapsulation of curcumin in the prepared NPs increased its stability and *in vitro* cellular internalization in a neuronal cell model of human neuroblastoma cells. Consequently, the NPs enhanced the therapeutic efficacy of curcumin against Aβ-induced cytotoxicity by reducing ROS levels. The synergistic effect of curcumin and ApoE3 was observed due to the antioxidant and anti-amyloidogenic activities of ApoE3 [140].

Jia *et al*. (2016) proposed POs for the targeted delivery of curcumin [141]. The POs were composed of PLGA and PEG block co-polymer, and the nanocarrier's surface was modified with Tet-1 peptide and Tf molecules to enhance the transport across the BBB.

Pharmacokinetic studies with healthy mice showed that the biodistribution of curcumin in brain tissue significantly improved with its encapsulation. Furthermore, POs modified with both targeting moieties showed a significantly higher accumulation in brain tissue than non-modified ones, and POs modified with only one targeting molecule, proving that both molecules have efficient targeting effects. Therefore, the modified nanocarriers ameliorated the cognitive dysfunction induced by Aβ.

The co-delivery of curcumin with other therapeutic molecules was also studied in the last years. Huang *et al*. (2017) proposed PLGA NPs to co-deliver curcumin and PQVGHL peptide for AD therapy [142]. PQVGHL peptide is an Aβ production inhibitor that binds to the cleavage site of β-secretase on APP [153]. These NPs were modified with cyclic CRTIGPSVC peptide that targets TfR to enhance the transport across the BBB. The developed NPs exhibited mean diameters of about 140 nm, negative zeta potential values, and encapsulation efficiency values of around 20% for both curcumin and PQVGHL peptide. Cytotoxicity studies using one human and two mouse neuronal cell lines proved that these NPs are biocompatible, causing no harmful effects to the studied cells. The authors used bEnd.3 mouse brain endothelial cells as an *in vitro* model of the BBB and demonstrated that modification with the targeting peptide increased the permeation of the NPs across the BBB model. Animal studies using transgenic AD mice showed that encapsulation of curcumin improved spatial memory and decreased the Aβ and ROS levels in the treated animals [142].

In turn, Kuo and Lin (2015) developed liposomes for the co-delivery of curcumin and nerve growth factor (NGF) for AD therapy [143]. The surface of the liposomes was conjugated with wheat germ agglutinin (WGA) molecules to enhance the transport across the BBB. Cardiolipin molecules were also used to modify the surface of the nanocarriers to increase the liposomes' affinity to Aβ. The obtained liposomes exhibited mean diameters ranging between 105 to 165 nm, negative zeta potential values, and encapsulation efficiency values of 15 to 35% for NGF and 40 to 65% for curcumin. *In vitro* studies using different human cell lines showed that the developed nanocarriers were biocompatible, inducing no cytotoxicity. *In vitro* studies using a BBB model showed that modification of the liposomes' surface with WGA significantly increased the permeability of the nanocarriers across the monolayer. The developed nanosystem also protected neuronal cells against apoptosis induced by Aβ fibrils.

Kuo *et al*. (2020) [144] designed Tf-functionalized SLNs to co-deliver NGF, curcumin, rosmarinic acid, and quercetin. The SLNs' functionalization with Tf improved their passage

across the BBB. Furthermore, the nanosystem decreased the drug-induced cytotoxicity to BBB cells through sustained release and enhanced the drugs' antioxidant activity.

Pinheiro et al. (2020) [145] developed lipid NPs, including SLNs and NLCs, to enhance quercetin's bioavailability and site-specific delivery into the brain. The NPs' surface was functionalized with Tf to facilitate the passage across the BBB. *In vitro* cytotoxicity studies demonstrated that the NPs are safe. Permeability studies across hCMEC/D3 cell monolayers, a commonly used BBB model system, showed that NLCs exhibit higher permeability than SLNs. The NPs' functionalization did not improve their permeability across the monolayer compared to non-functionalized NPs, due to the saturation of TfR. The ability of the developed nanosystems to inhibit the Aβ fibrillation was studied, and the results demonstrate that quercetin-loaded NLCs (both non-functionalized and functionalized) prevented the fibril formation, unlike SLNs. This difference between the two lipid NPs was attributed to their different crystalline structures, implying an additional capacity for accommodating and releasing quercetin from their lipid matrix.

Kuo et al. (2017) proposed other lipid-based NPs – liposomes - for the brain delivery of quercetin. Liposomes were functionalized with RMP-7 and Lf to permeate a BBB model of human brain microvascular endothelial cells and rescue degenerated human neuroblastoma cells [146]. RPM-7 peptide is an analog of the inflammatory mediator, bradykinin, recognized by its receptors overexpressed at the BBB [154]. The results demonstrated that the functionalization of liposomes increased the transport of NPs across the BBB model without inducing toxicity or damage to the tight junctions. Moreover, the DDS significantly decreased the Aβ-induced neurotoxicity, protecting the neurons against apoptosis and improving the viability of human neuroblastoma cells. Tau phosphorylation was also reduced [146].

Functionalized liposomes were also proposed by Mufamadi et al. (2013) [147] to deliver another natural compound – galantamine – into PC12 cells derived from a pheochromocytoma of the rat adrenal medulla. For this purpose, a synthetic peptide (Lys-Val-Leu-Phe-Leu-Ser) was attached to the liposomes' surface for the targeted delivery of galantamine. The obtained NPs were stable, with a high negative zeta potential and a mean size lower than 165 nm, fundamental features to ensure brain delivery. Further, the results revealed that the nanosystem increased the galantamine uptake by PC12 cells. Furthermore, *ex vivo* results indicated that the peptide enhanced the accumulation of this

compound into PC12 cells, which was not observed with free galantamine and non-functionalized liposomes.

In turn, Kong et al. (2020) [148] designed Tf-modified liposomes to enhance the bioavailability and brain targeting of osthole. *In vitro* studies revealed the liposomes' ability to cross the BBB using an *in vitro* BBB model. Moreover, the functionalized nanosystem was found to protect APP-SH-SY5Y cells against neurotoxicity. *In vivo* studies using an APP/PS1 mouse model of AD indicate that Tf-modified liposomes increased the accumulation of osthole in the mice brain and alleviated the AD-related pathology, including Aβ plaque deposition, apoptosis, oxidative stress, and neuroinflammation.

The encapsulation of another natural compound – epigallocatechin gallate (EGCG) - in functionalized NPs has also been addressed. Selenium was used to formulate NPs for the delivery of EGCG. Zhang et al. (2014) [149] attached EGCG to selenium NPs and functionalized them with Tet-1 peptide. The authors demonstrated that the DDS inhibited the formation of Aβ fibrils and promoted their disaggregation *in vitro*. However, the enhanced cellular uptake efficiency was only observed for the PC12 cells.

Loureiro et al. (2017) [150] developed a targeting DDS using stable SLNs to encapsulate resveratrol and grape extracts. Grape extracts contain several polyphenols, including resveratrol. The authors demonstrated that the grape extracts and resveratrol-loaded SLNs strongly inhibit Aβ fibril formation. An *in vitro* BBB model was used to evaluate the ability of these NPs to cross the BBB. For this purpose, the NPs were functionalized with OX26 (monoclonal antibody for the TfR) and LB509 (non-specific antibody for the BBB). The results suggest that the functionalization of SLNs with OX26 increased the SLNs uptake and transcytosis by human brain-like endothelial cells compared to the SLNs functionalized with LB509 and non-functionalized SLNs [150].

The brain-targeted delivery of huperzine A was addressed by Meng et al. (2018) [151] by developing PLGA NPs. To enhance the intranasal delivery, mucoadhesive properties were added to the NPs by coating their surface with a positively charged derivative of chitosan. The intranasal route was chosen to avoid the BBB. The intranasal route allows NPs to reach directly to the brain from the nasal cavity along the nerves bypassing the BBB [155]. The targeting of neuronal cells was also envisaged by attaching Lf molecules to the NPs' surface. *In vitro* studies showed the NPs were efficiently internalized by human neuroblastoma cells. Lf modification increased the cellular uptake through receptor-mediated transport. *In vivo* studies using Kunming mice (model for age-related decline)

showed a higher accumulation of modified PLGA NPs when compared with non-modified NPs, suggesting that the modification with positively charged chitosan enhanced the nose-to-brain huperzine A delivery due to its mucoadhesive properties [151].

References

[1] Perneczky, R. Dementia prevention and reserve against neurodegenerative disease. Dialogues Clin Neurosci 2019, 21, 53-60.

[2] Organization, W. H. Global action plan on the public health response to dementia 2017–2025. 2017,

[3] Hippius, H.&Neundörfer, G. The discovery of alzheimer's disease. Dialogues Clin Neurosci 2022,

[4] Deardorff, W. J.&Grossberg, G. T., Chapter 2 - behavioral and psychological symptoms in alzheimer's dementia and vascular dementia, in Handbook of clinical neurology, V.I. Reus and D. Lindqvist, Editors. 2019, Elsevier. p. 5-32.

[5] Joe, E.&Ringman, J. M. Cognitive symptoms of alzheimer’s disease: Clinical management and prevention. Bmj 2019, 367,

[6] 2020 alzheimer's disease facts and figures. Alzheimer's & Dementia 2020, 16, 391-460.

[7] Dhana, K., Franco, O. H., Ritz, E. M., Ford, C. N., Desai, P., Krueger, K. R., Holland, T. M., Dhana, A., Liu, X.&Aggarwal, N. T. Healthy lifestyle and life expectancy with and without alzheimer’s dementia: Population based cohort study. bmj 2022, 377,

[8] Nebel, R. A., Aggarwal, N. T., Barnes, L. L., Gallagher, A., Goldstein, J. M., Kantarci, K., Mallampalli, M. P., Mormino, E. C., Scott, L.&Yu, W. H. Understanding the impact of sex and gender in alzheimer's disease: A call to action. Alzheimer's & Dementia 2018, 14, 1171-1183.

[9] Organization, W. H., The global dementia observatory reference guide. 2018, World Health Organization.

[10] Rabbito, A., Dulewicz, M., Kulczyńska-Przybik, A.&Mroczko, B. Biochemical markers in alzheimer’s disease. International journal of molecular sciences 2020, 21, 1989.

[11] Tiwari, S., Atluri, V., Kaushik, A., Yndart, A.&Nair, M. Alzheimer's disease: Pathogenesis, diagnostics, and therapeutics. International journal of nanomedicine 2019, 14, 5541.

[12] Tsatsanis, A., Wong, B. X., Gunn, A. P., Ayton, S., Bush, A. I., Devos, D.&Duce, J. A. Amyloidogenic processing of alzheimer's disease β-amyloid precursor protein induces cellular iron retention. Molecular Psychiatry 2020, 25, 1958-1966.

[13] Chen, G.-f., Xu, T.-h., Yan, Y., Zhou, Y.-r., Jiang, Y., Melcher, K.&Xu, H. E. Amyloid beta: Structure, biology and structure-based therapeutic development. Acta Pharmacologica Sinica 2017, 38, 1205-1235.

[14] Almeida, Z. L.&Brito, R. M. Structure and aggregation mechanisms in amyloids. Molecules 2020, 25, 1195.

[15] Andrade, S., Loureiro, J. A.&Pereira, M. C. The role of amyloid β-biomembrane interactions in the pathogenesis of alzheimer's disease: Insights from liposomes as membrane models. ChemPhysChem n/a,

[16] Korshavn, K. J., Satriano, C., Lin, Y., Zhang, R., Dulchavsky, M., Bhunia, A., Ivanova, M. I., Lee, Y.-H., La Rosa, C.&Lim, M. H. Reduced lipid bilayer thickness regulates the aggregation and cytotoxicity of amyloid-β. Journal of Biological Chemistry 2017, 292, 4638-4650.

[17] D'Argenio, V.&Sarnataro, D. New insights into the molecular bases of familial alzheimer's disease. Journal of Personalized Medicine 2020, 10, 26.

[18] Quan, M., Zhao, T., Tang, Y., Luo, P., Wang, W., Qin, Q., Li, T., Wang, Q., Fang, J.&Jia, J. Effects of gene mutation and disease progression on representative neural circuits in familial alzheimer's disease. Alzheimer's Research & Therapy 2020, 12, 14.

[19] Ohshima, Y., Taguchi, K., Mizuta, I., Tanaka, M., Tomiyama, T., Kametani, F., Yabe-Nishimura, C., Mizuno, T.&Tokuda, T. Mutations in the β-amyloid precursor protein in familial alzheimer's disease increase aβ oligomer production in cellular models. Heliyon 2018, 4, e00511-e00511.

[20] Husain, M. A., Laurent, B.&Plourde, M. Apoe and alzheimer's disease: From lipid transport to physiopathology and therapeutics. Frontiers in Neuroscience 2021, 15,

[21] Troutwine, B. R., Hamid, L., Lysaker, C. R., Strope, T. A.&Wilkins, H. M. Apolipoprotein e and alzheimer's disease. Acta Pharmaceutica Sinica B 2022, 12, 496-510.

[22] Ricciarelli, R.&Fedele, E. The amyloid cascade hypothesis in alzheimer's disease: It's time to change our mind. Curr Neuropharmacol 2017, 15, 926-935.

[23] Uddin, M. S., Kabir, M. T., Rahman, M. S., Behl, T., Jeandet, P., Ashraf, G. M., Najda, A., Bin-Jumah, M. N., El-Seedi, H. R.&Abdel-Daim, M. M. Revisiting the amyloid cascade hypothesis: From anti-aβ therapeutics to auspicious new ways for alzheimer's disease. International Journal of Molecular Sciences 2020, 21, 5858.

[24] Tolar, M., Abushakra, S.&Sabbagh, M. The path forward in alzheimer's disease therapeutics: Reevaluating the amyloid cascade hypothesis. Alzheimer's & Dementia 2019,

[25] Banerjee, S.&Lyubchenko, Y. Interaction of amyloidogenic proteins with membranes and molecular mechanism for the development of alzheimer's disease. Alzheimer's research & therapy open access 2019, 2,

[26] Bharadwaj, P., Solomon, T., Malajczuk, C. J., Mancera, R. L., Howard, M., Arrigan, D. W., Newsholme, P.&Martins, R. N. Role of the cell membrane interface in modulating production and uptake of alzheimer's beta amyloid protein. Biochimica et Biophysica Acta (BBA)-Biomembranes 2018, 1860, 1639-1651.

[27] Clifton, L. A., Campbell, R. A., Sebastiani, F., Campos-Terán, J., Gonzalez-Martinez, J. F., Björklund, S., Sotres, J.&Cárdenas, M. Design and use of model biomembranes to study biomolecular interactions using complementary surface-sensitive techniques. Advances in Colloid and Interface Science 2020, 102118.

[28] Pinheiro, M., Magalhães, J.&Reis, S. Antibiotic interactions using liposomes as model lipid membranes. Chemistry and physics of lipids 2019,

[29] Yeagle, P. L., The membranes of cells. 2016: Academic Press.

[30] Pereira-Leite, C., Nunes, C.&Reis, S. Interaction of nonsteroidal anti-inflammatory drugs with membranes: In vitro assessment and relevance for their biological actions. Progress in Lipid Research 2013, 52, 571-584.

[31] Fernández-Pérez, E. J., Sepúlveda, F. J., Peters, C., Bascuñán, D., Riffo-Lepe, N. O., González-Sanmiguel, J., Sánchez, S. A., Peoples, R. W., Vicente, B.&Aguayo, L. G. Effect of cholesterol on membrane fluidity and association of aβ oligomers and subsequent neuronal damage: A double-edged sword. Frontiers in Aging Neuroscience 2018, 10,

[32] Sezgin, E., Levental, I., Mayor, S.&Eggeling, C. The mystery of membrane organization: Composition, regulation and roles of lipid rafts. Nature Reviews Molecular Cell Biology 2017, 18, 361.

[33] Siontorou, C. G., Nikoleli, G.-P., Nikolelis, D. P.&Karapetis, S. K. Artificial lipid membranes: Past, present, and future. Membranes 2017, 7, 38.

[34] Escribá, P. V., González-Ros, J. M., Goñi, F. M., Kinnunen, P. K. J., Vigh, L., Sánchez-Magraner, L., Fernández, A. M., Busquets, X., Horváth, I.&Barceló-Coblijn, G. Membranes: A meeting point for lipids, proteins and therapies. Journal of Cellular and Molecular Medicine 2008, 12, 829-875.

[35] Andrade, S., Ramalho, M. J., Loureiro, J. A.&Pereira, M. C. Liposomes as biomembrane models: Biophysical techniques for drug-membrane interaction studies. J. Mol. Liq. 2021, 334, 1-16.

[36] Elderdfi, M.&Sikorski, A. F. Langmuir-monolayer methodologies for characterizing protein-lipid interactions. Chemistry and Physics of Lipids 2018, 212, 61-72.

[37] Sebaaly, C., Greige-Gerges, H.&Charcosset, C., Chapter 11 - lipid membrane models for biomembrane properties' investigation, in Current trends and future developments on (bio-) membranes, A. Basile and C. Charcosset, Editors. 2019, Elsevier. p. 311-340.

[38] Oliver, R. C., Lipfert, J., Fox, D. A., Lo, R. H., Doniach, S.&Columbus, L. Dependence of micelle size and shape on detergent alkyl chain length and head group. PLOS ONE 2013, 8, e62488.

[39] Lucio, M., Lima, J.&Reis, S. Drug-membrane interactions: Significance for medicinal chemistry. Current medicinal chemistry 2010, 17, 1795-1809.

[40] Knobloch, J., Suhendro, D. K., Zieleniecki, J. L., Shapter, J. G.&Köper, I. Membrane–drug interactions studied using model membrane systems. Saudi Journal of Biological Sciences 2015, 22, 714-718.

[41] Alghalayini, A., Garcia, A., Berry, T.&Cranfield, C. G. The use of tethered bilayer lipid membranes to identify the mechanisms of antimicrobial peptide interactions with lipid bilayers. Antibiotics 2019, 8, 12.

[42] Deleu, M., Crowet, J.-M., Nasir, M. N.&Lins, L. Complementary biophysical tools to investigate lipid specificity in the interaction between bioactive molecules and the plasma membrane: A review. Biochimica et Biophysica Acta (BBA) - Biomembranes 2014, 1838, 3171-3190.

[43] Juhaniewicz, J.&Sek, S. Interaction of melittin with negatively charged lipid bilayers supported on gold electrodes. Electrochimica Acta 2016, 197, 336-343.

[44] McCabe, I. P.&Forstner, M. B. Polymer supported lipid bilayers. Open Journal of Biophysics 2013, Vol.03No.01, 11.

[45] Khan, M. S., Dosoky, N. S.&Williams, J. D. Engineering lipid bilayer membranes for protein studies. Int J Mol Sci 2013, 14, 21561-21597.

[46] Daraee, H., Etemadi, A., Kouhi, M., Alimirzalu, S.&Akbarzadeh, A. Application of liposomes in medicine and drug delivery. Artificial cells, nanomedicine, and biotechnology 2016, 44, 381-391.

[47] Ramalho, M. J., Andrade, S., Loureiro, J. A.&do Carmo Pereira, M. Nanotechnology to improve the alzheimer's disease therapy with natural compounds. Drug delivery and translational research 2020, 1-23.

[48] Akbarzadeh, A., Rezaei-Sadabady, R., Davaran, S., Joo, S. W., Zarghami, N., Hanifehpour, Y., Samiei, M., Kouhi, M.&Nejati-Koshki, K. Liposome: Classification, preparation, and applications. Nanoscale Research Letters 2013, 8, 102.

[49] Pereira, S. A. M. J. R. J. L. M. C., Techniques to produce liposomes for the emerging market of nano-based formulations, in Importance & applications of nanotechnology. 2020, Meddocs: NV, USA. p. 26-31.

[50] Ramalho, M. J., Andrade, S., Dabur, M., Loureiro, J. A.&Pereira, M. C., Current vs emerging natural com-pounds-based treatments for alzheimer's disease. Alzheimer's disease and treatment. 2021, MedDocs Publishers.

[51] Andrade, S., Ramalho, M. J., Loureiro, J. A.&Pereira, M. C. Natural compounds for alzheimer's disease therapy: A systematic review of preclinical and clinical studies. Int. J. Mol. Sci. 2019, 20, 1-41.

[52] Farlow, M. R., Thompson, R. E., Wei, L.-J., Tuchman, A. J., Grenier, E., Crockford, D., Wilke, S., Benison, J.&Alkon, D. L. A randomized, double-blind, placebo-controlled, phase ii study assessing safety, tolerability, and efficacy of bryostatin in the treatment of moderately severe to severe alzheimer's disease. Journal of Alzheimer's Disease 2019, 67, 555-570.

[53] Bachinskaya, N., Hoerr, R.&Ihl, R. Alleviating neuropsychiatric symptoms in dementia: The effects of ginkgo biloba extract egb 761. Findings from a randomized controlled trial. Neuropsychiatr Dis Treat 2011, 7, 209-215.

[54] Aisen, P. S., Gauthier, S., Ferris, S. H., Saumier, D., Haine, D., Garceau, D., Duong, A., Suhy, J., Oh, J.&Lau, W. C. Tramiprosate in mild-to-moderate alzheimer's disease–a randomized,

double-blind, placebo-controlled, multi-centre study (the alphase study). Archives of medical science: AMS 2011, 7, 102.

[55] Yurko-Mauro, K., McCarthy, D., Rom, D., Nelson, E. B., Ryan, A. S., Blackwell, A., Salem Jr, N., Stedman, M.&Investigators, M. Beneficial effects of docosahexaenoic acid on cognition in age-related cognitive decline. Alzheimer's & Dementia 2010, 6, 456-464.

[56] Dysken, M. W., Sano, M., Asthana, S., Vertrees, J. E., Pallaki, M., Llorente, M., Love, S., Schellenberg, G. D., McCarten, J. R.&Malphurs, J. Effect of vitamin e and memantine on functional decline in alzheimer disease: The team-ad va cooperative randomized trial. Jama 2014, 311, 33-44.

[57] Sano, M., Ernesto, C., Thomas, R. G., Klauber, M. R., Schafer, K., Grundman, M., Woodbury, P., Growdon, J., Cotman, C. W., Pfeiffer, E., Schneider, L. S.&Thal, L. J. A controlled trial of selegiline, alpha-tocopherol, or both as treatment for alzheimer's disease. New England Journal of Medicine 1997, 336, 1216-1222.

[58] Jones, G., Sahakian, B., Levy, R., Warburton, D. M.&Gray, J. Effects of acute subcutaneous nicotine on attention, information processing and short-term memory in alzheimer's disease. Psychopharmacology 1992, 108, 485-494.

[59] Navarro, E., Buendia, I., Parada, E., Leon, R., Jansen-Duerr, P., Pircher, H., Egea, J.&Lopez, M. G. Alpha7 nicotinic receptor activation protects against oxidative stress via heme-oxygenase i induction. Biochemical pharmacology 2015, 97, 473-481.

[60] Ihl, R., Bachinskaya, N., Korczyn, A. D., Vakhapova, V., Tribanek, M., Hoerr, R., Napryeyenko, O.&Group, G. S. Efficacy and safety of a once-daily formulation of ginkgo biloba extract egb 761 in dementia with neuropsychiatric features: A randomized controlled trial. Int J Geriatr Psychiatry 2011, 26, 1186-1194.

[61] Herrschaft, H., Nacu, A., Likhachev, S., Sholomov, I., Hoerr, R.&Schlaefke, S. Ginkgo biloba extract egb 761® in dementia with neuropsychiatric features: A randomised, placebo-controlled trial to confirm the efficacy and safety of a daily dose of 240 mg. Journal of Psychiatric Research 2012, 46, 716-723.

[62] Annweiler, C., Herrmann, F. R., Fantino, B., Brugg, B.&Beauchet, O. Effectiveness of the combination of memantine plus vitamin d on cognition in patients with alzheimer disease: A pre-post pilot study. Cognitive and behavioral neurology 2012, 25, 121-127.

[63] Youdim, M. B. H., Edmondson, D.&Tipton, K. F. The therapeutic potential of monoamine oxidase inhibitors. Nature Reviews Neuroscience 2006, 7, 295.

[64] Rafii, M., Walsh, S., Little, J., Behan, K., Reynolds, B., Ward, C., Jin, S., Thomas, R.&Aisen, P. A phase ii trial of huperzine a in mild to moderate alzheimer disease. Neurology 2011, 76, 1389-1394.

[65] Zhu, C. W., Grossman, H., Neugroschl, J., Parker, S., Burden, A., Luo, X.&Sano, M. A randomized, double-blind, placebo-controlled trial of resveratrol with glucose and malate (rgm) to slow the progression of alzheimer's disease: A pilot study. Alzheimer's & Dementia: Translational Research & Clinical Interventions 2018, 4, 609-616.

[66] Petersen, R. C., Thomas, R. G., Grundman, M., Bennett, D., Doody, R., Ferris, S., Galasko, D., Jin, S., Kaye, J.&Levey, A. Vitamin e and donepezil for the treatment of mild cognitive impairment. New England Journal of Medicine 2005, 352, 2379-2388.

[67] Kryscio, R. J., Abner, E. L., Caban-Holt, A., Lovell, M., Goodman, P., Darke, A. K., Yee, M., Crowley, J.&Schmitt, F. A. Association of antioxidant supplement use and dementia in the prevention of alzheimer's disease by vitamin e and selenium trial (preadvise). JAMA neurology 2017, 74, 567-573.

[68] Zupančič, Š., Lavrič, Z.&Kristl, J. Stability and solubility of trans-resveratrol are strongly influenced by ph and temperature. Eur J Pharm Biopharm 2015, 93, 196-204.

[69] Saberi, A. H., Fang, Y.&McClements, D. J. Effect of glycerol on formation, stability, and properties of vitamin-e enriched nanoemulsions produced using spontaneous emulsification. Journal of colloid and interface science 2013, 411, 105-113.

[70] Shen, L.&Ji, H.-F. Low stability remedies the low bioavailability of curcumin. Trends in molecular medicine 2012, 18, 363-364.

[71] Ramalho, M. J., Andrade, S., Loureiro, J. A.&Pereira, M. C. Nanotechnology to improve the alzheimer's disease therapy with natural compounds. Drug delivery and translational research 2020, 10, 380-402.

[72] Kadry, H., Noorani, B.&Cucullo, L. A blood–brain barrier overview on structure, function, impairment, and biomarkers of integrity. Fluids and Barriers of the CNS 2020, 17, 69.

[73] Segarra, M., Aburto, M. R.&Acker-Palmer, A. Blood–brain barrier dynamics to maintain brain homeostasis. Trends in Neurosciences 2021, 44, 393-405.

[74] Benz, F.&Liebner, S., Structure and function of the blood–brain barrier (bbb). 2020, Springer.

[75] Benz, F.&Liebner, S., Structure and function of the blood–brain barrier (bbb). Springer Berlin Heidelberg: Berlin, Heidelberg. p. 1-29.

[76] Pardridge, W. M. Treatment of alzheimer's disease and blood–brain barrier drug delivery. Pharmaceuticals 2020, 13, 394.

[77] Lalatsa, A.&Butt, A. M., Chapter 3 - physiology of the blood–brain barrier and mechanisms of transport across the bbb, in Nanotechnology-based targeted drug delivery systems for brain tumors, P. Kesharwani and U. Gupta, Editors. 2018, Academic Press. p. 49-74.

[78] Hashimoto, Y.&Campbell, M. Tight junction modulation at the blood-brain barrier: Current and future perspectives. Biochimica et Biophysica Acta (BBA)-Biomembranes 2020, 1862, 183298.

[79] Janicka, M., Sztanke, M.&Sztanke, K. Predicting the blood-brain barrier permeability of new drug-like compounds via hplc with various stationary phases. Molecules 2020, 25, 487.

[80] Fu, B. M. Transport across the blood-brain barrier. Molecular, Cellular, and Tissue Engineering of the Vascular System 2018, 235-259.

[81] Lombardo, S. M., Schneider, M., Türeli, A. E.&Türeli, N. G. Key for crossing the bbb with nanoparticles: The rational design. Beilstein Journal of Nanotechnology 2020, 11, 866-883.

[82] Aykac, A.&Sehirli, A. Ö. The function and expression of atp-binding cassette transporters proteins in the alzheimer's disease. Glob Med Genet 2021, 8, 149-155.

[83] Robinson, K.&Tiriveedhi, V. Perplexing role of p-glycoprotein in tumor microenvironment. Frontiers in Oncology 2020, 10,

[84] Park, K. Drug delivery of the future: Chasing the invisible gorilla. J Control Release 2016, 240, 2-8.

[85] Saraiva, C., Praca, C., Ferreira, R., Santos, T., Ferreira, L.&Bernardino, L. Nanoparticle-mediated brain drug delivery: Overcoming blood-brain barrier to treat neurodegenerative diseases. J Control Release 2016, 235, 34-47.

[86] Chen, Y.&Liu, L. Modern methods for delivery of drugs across the blood-brain barrier. Adv Drug Deliv Rev 2012, 64, 640-665.

[87] Masserini, M. Nanoparticles for brain drug delivery. ISRN Biochem 2013, 2013, 238428.

[88] Rizvi, S. A.&Saleh, A. M. Applications of nanoparticle systems in drug delivery technology. Saudi Pharmaceutical Journal 2018, 26, 64-70.

[89] Wais, U., Jackson, A. W., He, T.&Zhang, H. Nanoformulation and encapsulation approaches for poorly water-soluble drug nanoparticles. Nanoscale 2016, 8, 1746-1769.

[90] Teleanu, D. M., Chircov, C., Grumezescu, A. M., Volceanov, A.&Teleanu, R. I. Impact of nanoparticles on brain health: An up to date overview. Journal of clinical medicine 2018, 7, 490.

[91] Liu, Y., Tan, J., Thomas, A., Ou-Yang, D.&Muzykantov, V. R. The shape of things to come: Importance of design in nanotechnology for drug delivery. Therapeutic delivery 2012, 3, 181-194.

[92] Jo, D. H., Kim, J. H., Lee, T. G.&Kim, J. H. Size, surface charge, and shape determine therapeutic effects of nanoparticles on brain and retinal diseases. Nanomedicine: Nanotechnology, Biology and Medicine 2015, 11, 1603-1611.

[93] Lockman, P. R., Mumper, R. J., Khan, M. A.&Allen, D. D. Nanoparticle technology for drug delivery across the blood-brain barrier. Drug Dev Ind Pharm 2002, 28, 1-13.

[94] Bangham, A. D.&Horne, R. Negative staining of phospholipids and their structural modification by surface-active agents as observed in the electron microscope. Journal of molecular biology 1964, 8, 660-IN610.

[95] Shim, G., Kim, M.-G., Park, J. Y.&Oh, Y.-K. Application of cationic liposomes for delivery of nucleic acids. Asian journal of pharmaceutical sciences 2013, 8, 72-80.

[96] Çağdaş, M., Sezer, A. D.&Bucak, S. Liposomes as potential drug carrier systems for drug delivery. Application of nanotechnology in drug delivery 2014, 1-100.

[97] Sharma, D., Ali, A. A. E.&Trivedi, L. R. An updated review on: Liposomes as drug delivery system. PharmaTutor 2018, 6, 50-62.

[98] Sercombe, L., Veerati, T., Moheimani, F., Wu, S. Y., Sood, A. K.&Hua, S. Advances and challenges of liposome assisted drug delivery. Front Pharmacol 2015, 6, 286-286.

[99] Geszke-Moritz, M.&Moritz, M. Solid lipid nanoparticles as attractive drug vehicles: Composition, properties and therapeutic strategies. Materials Science and Engineering: C 2016, 68, 982-994.

[100] Cavalli, R., Caputo, O.&Gasco, M. R. Solid lipospheres of doxorubicin and idarubicin. International Journal of Pharmaceutics 1993, 89, R9-R12.

[101] Gastaldi, L., Battaglia, L., Peira, E., Chirio, D., Muntoni, E., Solazzi, I., Gallarate, M.&Dosio, F. Solid lipid nanoparticles as vehicles of drugs to the brain: Current state of the art. Eur J Pharm Biopharm 2014, 87, 433-444.

[102] Jaiswal, P., Gidwani, B.&Vyas, A. Nanostructured lipid carriers and their current application in targeted drug delivery. Artificial Cells, Nanomedicine, and Biotechnology 2016, 44, 27-40.

[103] Huynh, N. T., Passirani, C., Saulnier, P.&Benoit, J. P. Lipid nanocapsules: A new platform for nanomedicine. Int J Pharm 2009, 379, 201-209.

[104] Gurpreet, K.&Singh, S. K. Review of nanoemulsion formulation and characterization techniques. Indian J Pharm Sci 2018, 80, 781-789.

[105] Callender, S. P., Mathews, J. A., Kobernyk, K.&Wettig, S. D. Microemulsion utility in pharmaceuticals: Implications for multi-drug delivery. Int J Pharmaceut 2017, 526, 425-442.

[106] Singh, Y., Meher, J. G., Raval, K., Khan, F. A., Chaurasia, M., Jain, N. K.&Chourasia, M. K. Nanoemulsion: Concepts, development and applications in drug delivery. Journal of Controlled Release 2017, 252, 28-49.

[107] McClements, D. J. Edible nanoemulsions: Fabrication, properties, and functional performance. Soft Matter 2011, 7, 2297-2316.

[108] Banik, B. L., Fattahi, P.&Brown, J. L. Polymeric nanoparticles: The future of nanomedicine. Wiley Interdisciplinary Reviews: Nanomedicine and Nanobiotechnology 2016, 8, 271-299.

[109] Kamaly, N., Yameen, B., Wu, J.&Farokhzad, O. C. Degradable controlled-release polymers and polymeric nanoparticles: Mechanisms of controlling drug release. Chemical Reviews 2016, 116, 2602-2663.

[110] Sharma, S., Parmar, A., Kori, S.&Sandhir, R. Plga-based nanoparticles: A new paradigm in biomedical applications. TrAC Trends in Analytical Chemistry 2016, 80, 30-40.

[111] Khalili Fard, J., Jafari, S.&Eghbal, M. A. A review of molecular mechanisms involved in toxicity of nanoparticles. Advanced pharmaceutical bulletin 2015, 5, 447-454.

[112] Li, Y.&Ju, D., Chapter 12 - the application, neurotoxicity, and related mechanism of cationic polymers∗∗conflict of interests: All the figures and table in “the application, neurotoxicity, and related mechanism of cationic polymers” are original, unpublished materials designed and prepared by yubin li and dianwen ju. The authors declared that there’s no conflict of interests, in Neurotoxicity of nanomaterials and nanomedicine, X. Jiang and H. Gao, Editors. 2017, Academic Press. p. 285-329.

[113] Xiong, S., George, S., Yu, H., Damoiseaux, R., France, B., Ng, K. W.&Loo, J. S. Size influences the cytotoxicity of poly (lactic-co-glycolic acid) (plga) and titanium dioxide (tio(2)) nanoparticles. Archives of toxicology 2013, 87, 1075-1086.

[114] Rodrigues de Azevedo, C., von Stosch, M., Costa, M. S., Ramos, A. M., Cardoso, M. M., Danhier, F., Préat, V.&Oliveira, R. Modeling of the burst release from plga micro- and nanoparticles as function of physicochemical parameters and formulation characteristics. International Journal of Pharmaceutics 2017, 532, 229-240.

[115] Iqbal, M., Zafar, N., Fessi, H.&Elaissari, A. Double emulsion solvent evaporation techniques used for drug encapsulation. International Journal of Pharmaceutics 2015, 496, 173-190.

[116] Elgadir, M. A., Uddin, M. S., Ferdosh, S., Adam, A., Chowdhury, A. J. K.&Sarker, M. Z. I. Impact of chitosan composites and chitosan nanoparticle composites on various drug delivery systems: A review. Journal of Food and Drug Analysis 2015, 23, 619-629.

[117] Hussein-Al-Ali, S. H., Kura, A., Hussein, M. Z.&Fakurazi, S. Preparation of chitosan nanoparticles as a drug delivery system for perindopril erbumine. Polymer Composites 2016, n/a-n/a.

[118] Palazzo, C., Trapani, G., Ponchel, G., Trapani, A.&Vauthier, C. Mucoadhesive properties of low molecular weight chitosan- or glycol chitosan- and corresponding thiomer-coated poly (isobutylcyanoacrylate) core-shell nanoparticles. Eur J Pharm Biopharm 2017, 117, 315-323.

[119] Ahmed, T. A.&Aljaeid, B. M. Preparation, characterization, and potential application of chitosan, chitosan derivatives, and chitosan metal nanoparticles in pharmaceutical drug delivery. Drug Des Devel Ther 2016, 10, 483-507.

[120] Loureiro, J. A., Gomes, B., Fricker, G., Coelho, M. A. N., Rocha, S.&Pereira, M. C. Cellular uptake of plga nanoparticles targeted with anti-amyloid and anti-transferrin receptor

antibodies for alzheimer's disease treatment. Colloids and surfaces. B, Biointerfaces 2016, 145, 8-13.

[121] Saeedi, M., Eslamifar, M., Khezri, K.&Dizaj, S. M. Applications of nanotechnology in drug delivery to the central nervous system. Biomedicine & Pharmacotherapy 2019, 111, 666-675.

[122] Lajoie, J. M.&Shusta, E. V. Targeting receptor-mediated transport for delivery of biologics across the blood-brain barrier. Annu Rev Pharmacol 2015, 55, 613-631.

[123] Pulgar, V. M. Transcytosis to cross the blood brain barrier, new advancements and challenges. Frontiers in Neuroscience 2019, 12,

[124] Brenza, T. M., Schlichtmann, B. W., Bhargavan, B., Vela Ramirez, J. E., Nelson, R. D., Panthani, M. G., McMillan, J. M., Kalyanaraman, B., Gendelman, H. E., Anantharam, V., Kanthasamy, A. G., Mallapragada, S. K., Narasimhan, B.&Kanmogne, G. D. Biodegradable polyanhydride-based nanomedicines for blood to brain drug delivery. Journal of Biomedical Materials Research Part A 2018, 106, 2881-2890.

[125] Johnsen, K. B., Burkhart, A., Thomsen, L. B., Andresen, T. L.&Moos, T. Targeting the transferrin receptor for brain drug delivery. Progress in Neurobiology 2019, 181, 101665.

[126] Voth, B., Nagasawa, D. T., Pelargos, P. E., Chung, L. K., Ung, N., Gopen, Q., Tenn, S., Kamei, D. T.&Yang, I. Transferrin receptors and glioblastoma multiforme: Current findings and potential for treatment. Journal of Clinical Neuroscience 2015, 22, 1071-1076.

[127] Cheng, Z., Zaki, A. A., Hui, J. Z., Muzykantov, V. R.&Tsourkas, A. Multifunctional nanoparticles: Cost versus benefit of adding targeting and imaging capabilities. Science 2012, 338, 903-910.

[128] Lee, H. J., Engelhardt, B., Lesley, J., Bickel, U.&Pardridge, W. M. Targeting rat anti-mouse transferrin receptor monoclonal antibodies through blood-brain barrier in mouse. Journal of Pharmacology and Experimental Therapeutics 2000, 292, 1048-1052.

[129] Ramalho, M. J., Loureiro, J. A., Coelho, M. A.&Pereira, M. C. Transferrin receptor-targeted nanocarriers: Overcoming barriers to treat glioblastoma. Pharmaceutics 2022, 14, 279.

[130] Loureiro, J. A., Andrade, S., Duarte, A., Neves, A. R., Queiroz, J. F., Nunes, C., Sevin, E., Fenart, L., Gosselet, F., Coelho, M. A. N.&Pereira, M. C. Resveratrol and grape extract-loaded solid lipid nanoparticles for the treatment of alzheimer’s disease. Molecules 2017, 22, 1-16.

[131] Lange, A., Prenzler, A., Frank, M., Kirstein, M., Vogel, A.&Von Der Schulenburg, J. A systematic review of cost-effectiveness of monoclonal antibodies for metastatic colorectal cancer. European journal of cancer 2014, 50, 40-49.

[132] Liu, M., Wu, L., Shan, W., Cui, Y.&Huang, Y. Iron-mimic peptide converts transferrin from foe to friend for orally targeting insulin delivery. Journal of Materials Chemistry B 2018, 6, 593-601.

[133] Lee, J. H., Engler, J. A., Collawn, J. F.&Moore, B. A. Receptor mediated uptake of peptides that bind the human transferrin receptor. European journal of biochemistry 2001, 268, 2004-2012.

[134] Song, K.-M., Lee, S.&Ban, C. Aptamers and their biological applications. Sensors 2012, 12, 612-631.

[135] Mourtas, S., Lazar, A. N., Markoutsa, E., Duyckaerts, C.&Antimisiaris, S. G. Multifunctional nanoliposomes with curcumin–lipid derivative and brain targeting functionality with potential applications for alzheimer disease. European Journal of Medicinal Chemistry 2014, 80, 175-183.

[136] Liu, X., Liu, Z., Wang, X.&Zhao, Y. Therapeutic effect of multifunctional nano-liposomes on alzheimer's disease. Materials Express 2021, 11, 1331-1338.

[137] Meng, F., Asghar, S., Gao, S., Su, Z., Song, J., Huo, M., Meng, W., Ping, Q.&Xiao, Y. A novel ldl-mimic nanocarrier for the targeted delivery of curcumin into the brain to treat alzheimer's disease. Colloids and Surfaces B: Biointerfaces 2015, 134, 88-97.

[138] Mathew, A., Fukuda, T., Nagaoka, Y., Hasumura, T., Morimoto, H., Yoshida, Y., Maekawa, T., Venugopal, K.&Sakthi Kumar, D. Curcumin loaded-plga nanoparticles conjugated with tet-1 peptide for potential use in alzheimer's disease. PLoS ONE 2012, 7, 1-10.

[139] Fan, S., Zheng, Y., Liu, X., Fang, W., Chen, X., Liao, W., Jing, X., Lei, M., Tao, E., Ma, Q., Zhang, X., Guo, R.&Liu, J. Curcumin-loaded plga-peg nanoparticles conjugated with b6 peptide for potential use in alzheimer's disease. Drug Delivery 2018, 25, 1091-1102.

[140] Mulik, R. S., Mönkkönen, J., Juvonen, R. O., Mahadik, K. R.&Paradkar, A. R. Apoe3 mediated poly(butyl) cyanoacrylate nanoparticles containing curcumin: Study of enhanced activity of curcumin against beta amyloid induced cytotoxicity using in vitro cell culture model. Molecular Pharmaceutics 2010, 7, 815-825.

[141] Jia, T., Sun, Z., Lu, Y., Gao, J., Zou, H., Xie, F., Zhang, G., Xu, H., Sun, D., Yu, Y.&Zhong, Y. A dual brain-targeting curcumin-loaded polymersomes ameliorated cognitive dysfunction in intrahippocampal amyloid-beta1-42-injected mice. Int J Nanomedicine 2016, 11, 3765-3775.

[142] Huang, N., Lu, S., Liu, X.-G., Zhu, J., Wang, Y.-J.&Liu, R.-T. Plga nanoparticles modified with a bbb-penetrating peptide co-delivering aβ generation inhibitor and curcumin attenuate memory deficits and neuropathology in alzheimer's disease mice. Oncotarget 2017, 8, 81001.

[143] Kuo, Y.-c.&Lin, C.-C. Rescuing apoptotic neurons in alzheimer's disease using wheat germ agglutinin-conjugated and cardiolipin-conjugated liposomes with encapsulated nerve growth factor and curcumin. International journal of nanomedicine 2015, 10, 2653.

[144] Kuo, Y.-C., Lou, Y.-I., Rajesh, R.&Chen, C.-L. Multiple-component dual-phase solid lipid nanoparticles with conjugated transferrin for formulating antioxidants and nerve growth factor against neuronal apoptosis. Journal of the Taiwan Institute of Chemical Engineers 2020, 110, 140-152.

[145] Pinheiro, R., Granja, A., Loureiro, J. A., Pereira, M. C., Pinheiro, M., Neves, A. R.&Reis, S. Quercetin lipid nanoparticles functionalized with transferrin for alzheimer's disease. European Journal of Pharmaceutical Sciences 2020, 148, 105314.

[146] Kuo, Y.-C.&Tsao, C.-W. Neuroprotection against apoptosis of sk-n-mc cells using rmp-7- and lactoferrin-grafted liposomes carrying quercetin. International Journal of Nanomedicine 2017, 12, 2857-2869.

[147] Mufamadi, M. S., Choonara, Y. E., Kumar, P., Modi, G., Naidoo, D., van Vuuren, S., Ndesendo, V. M. K., Toit, L. C. d., Iyuke, S. E.&Pillay, V. Ligand-functionalized nanoliposomes for targeted delivery of galantamine. International Journal of Pharmaceutics 2013, 448, 267-281.

[148] Kong, L., Li, X.-t., Ni, Y.-n., Xiao, H.-h., Yao, Y.-j., Wang, Y.-y., Ju, R.-j., Li, H.-y., Liu, J.-j.&Fu, M. Transferrin-modified osthole pegylated liposomes travel the blood-brain barrier and mitigate alzheimer's disease-related pathology in app/ps-1 mice. International journal of nanomedicine 2020, 15, 2841.

[149] Zhang, J., Zhou, X., Yu, Q., Yang, L., Sun, D., Zhou, Y.&Liu, J. Epigallocatechin-3-gallate (egcg)-stabilized selenium nanoparticles coated with tet-1 peptide to reduce amyloid-β aggregation and cytotoxicity. ACS Applied Materials & Interfaces 2014, 6, 8475-8487.

[150] Loureiro, J., Andrade, S., Duarte, A., Neves, A., Queiroz, J., Nunes, C., Sevin, E., Fenart, L., Gosselet, F., Coelho, M.&Pereira, M. Resveratrol and grape extract-loaded solid lipid nanoparticles for the treatment of alzheimer's disease. Molecules 2017, 22, 277.

[151] Meng, Q., Wang, A., Hua, H., Jiang, Y., Wang, Y., Mu, H., Wu, Z.&Sun, K. Intranasal delivery of huperzine a to the brain using lactoferrin-conjugated n-trimethylated chitosan surface-modified plga nanoparticles for treatment of alzheimer's disease. International Journal of Nanomedicine 2018, 13, 705-718.

[152] Mathew, A., Aravind, A., Fukuda, T., Hasumura, T., Nagaoka, Y., Yoshida, Y., Maekawa, T., Venugopal, K.&Kumar, D. S., presented at 2011 11th IEEE International Conference on Nanotechnology. Curcumin nanoparticles- a gateway for multifaceted approach to tackle alzheimer's disease, 2011.

[153] Yang, S.-g., Wang, S.-w., Zhao, M., Zhang, R., Zhou, W.-w., Li, Y.-n., Su, Y.-j., Zhang, H., Yu, X.-l.&Liu, R.-t. A peptide binding to the β-site of app improves spatial memory and attenuates aβ burden in alzheimer's disease transgenic mice. PloS one 2012, 7, e48540.

[154] Hwang, S. R.&Kim, K. Nano-enabled delivery systems across the blood–brain barrier. Archives of Pharmacal Research 2014, 37, 24-30.

[155] Crowe, T. P., Greenlee, M. H. W., Kanthasamy, A. G.&Hsu, W. H. Mechanism of intranasal drug delivery directly to the brain. Life Sciences 2018, 195, 44-52.

Chapter 3

Anti-Amyloidogenic Activity of Natural Compounds in the Presence of a Neuronal Membrane Model

3.1. Introduction

The aggregation of Aβ monomers into toxic fibrils has been linked to the pathogenesis of AD [1]. According to scientific evidence, the Aβ peptide undergoes an α-helix to β-sheet conformational transition during the fibril formation [2]. Amyloid aggregation is a complex and heterogeneous process that highly depends on the surrounding environment [3]. Especially, biological membranes are suggested to be key players in the Aβ misfolding process by enhancing the aggregation rates and stabilizing specific protein arrangements [4].

Several researchers are making encouraging advances regarding the prevention and treatment of AD. It is believed that decreasing the levels of toxic Aβ in the brain, either by inhibiting the aggregation process or disaggregating mature fibrils into nontoxic species, is one of the promising approaches for AD therapy [5]. There is a growing consensus in the literature that naturally occurring compounds could be promising as therapeutics or as part of a prevention strategy for AD due to their anti-amyloidogenic properties [6].

Thus, the first goal of this chapter was to evaluate the ability of eight natural compounds – ferulic acid (FA), nicotine (NIC), caffeine (CAF), caffeic acid (CA), ascorbic acid (AA), vanillic acid (VA), gallic acid (GA) and vitamin B12 (VB12) - to inhibit the $A\beta_{1-42}$ aggregation as well as to disrupt mature fibrils in an aqueous medium. To this end, a thioflavin T (ThT) fluorescence assay was used to detect the content of amyloid fibrils.

Given the rate of failures in AD drug development, there is a serious need to identify strategies that increase the number of compounds entering the pipeline and progress successfully towards a new therapy for AD [7]. Better replicating of *in vivo* conditions in *in vitro* studies will enable stopping earlier the study of molecules without success *in vivo*, thus preserving resources that can be assigned to testing drugs with a greater chance of success [7]. In this context, *in vitro* lipid membrane models emerged to offer a helpful tool to mimic *in vivo* conditions. These engineered synthetic membranes create a well-defined environment with comparable composition and structural features to cell membranes [8].

As the *in vivo* environment may affect the drugs' efficacy in inhibiting the amyloid aggregation or disrupting mature fibrils, it becomes crucial to study their anti-amyloidogenic activity in the presence of specific cellular components [3, 9]. Thus, the second goal of this chapter was to evaluate the ability of the natural compounds with anti-amyloidogenic activity in the aqueous medium to prevent the Aβ aggregation and disrupt mature fibrils in a cellular membrane-like environment. To this end, an *in vitro* model of neuronal membranes was designed to predict the molecules' therapeutic activity before testing them *in vivo.* The detailed reproduction of *in vivo* conditions in *in vitro* studies is of utmost importance to reduce the number of compounds failing to enter the pipeline, thus preserving resources that can be devoted to discovering and developing effective drugs. Thus, liposomes made of 1,2-dimyristoyl-sn-glycero-3-phosphocholine (DMPC), CHOL, SM, and L-α-phosphatidylserine (PS) - the major lipid components of neurons - were used as neuronal membrane models [10]. ThT fluorescence assay and transmission electron microscopy (TEM) were employed to quantify the amyloid fibrils content and observe the structural morphology of $A\beta_{1-42}$, respectively. Attenuated total reflectance - Fourier transform infrared spectroscopy (ATR-FTIR) and circular dichroism (CD) were used to evaluate the secondary structure of $A\beta_{1-42}$. The anti-amyloidogenic activity of the natural compounds in the cell membrane-like environment was compared to the bulk solution and discussed based on the compound's lipophilicity.

3.2. Materials and Methods

3.2.1. Materials

Human amyloid-β peptide ($_{1-42}$) ($A\beta_{1-42}$, purity>95%, MW 4514) was acquired from GenScript Biotech (Piscataway, NJ, EUA). Sigma-Aldrich (St. Louis, MO, USA) provided FA (purity>99%, MW 194), NIC (purity≥99%, MW 162), CAF (purity>99%, MW 194), GA (purity≥99%, MW 170), AA (purity>99%, MW 176), VA (purity>97%, MW 168), CA (purity>99%, MW 180) and VB12 (purity≥98%, MW 1355), 1,1,1,3,3,3-hexafluoro-2-propanol (HFIP, purity≥99%, MW 168), chloroform (purity≥99%, MW 119) and ThT (MW 319). The lipids DMPC (purity>99%, MW 678), CHOL (ovine wool, purity>98%, MW 387), SM (chicken egg yolk, purity≥95%, MW 711) and PS (porcine brain, purity>99%, MW 825) were acquired from Avanti Polar Lipids Inc. (Alabaster, AL, USA). Uranyl acetate dihydrate (purity>99%, MW 424) was obtained from Electron Microscopy Sciences (Hatfield, PA, USA). Phosphate buffer saline (PBS tablets, pH 7.4 ± 0.1, 137 mM sodium chloride, 2.7 mM potassium chloride and 10 mM phosphate buffer) was purchased from VWR International (Radnor, PA, EUA) and prepared using ultrapure water (Milli-Q Academic, Millipore, France).

3.2.2. Preparation of Liposomes

Based on the lipid composition of neuronal membranes, lipid vesicles comprised of DMPC:CHOL:SM:PS (65:15:10:10 molar ratio) were used as lipid membrane mimics [11]. Liposomes were produced by the thin-film hydration method followed by extrusion, according to a previous report [12]. In the first stage, lipids were dissolved and mixed in chloroform to ensure the mixture's homogeneity. Dichloromethane, ethanol, or a combination of chloroform and methanol are also commonly used as organic solvents. Then, the organic solvent was removed by evaporation under a nitrogen stream to obtain a thin lipid film. For significant volumes of organic solvents, rotary evaporation using a round bottom flask is often preferred. The lipid film was then rehydrated with PBS at a final concentration of 5 mM, and the lipid mixture was vigorously vortexed for 10 minutes. When hydrated, phospholipids spontaneously assemble into liposomes due to their amphiphilic nature. They tend to assemble in vesicles to decrease the system’s free energy by reducing

the contact of phospholipids' hydrophobic tails with water [13]. The phospholipids dispersed in an aqueous buffer yield a heterogeneous population of MLVs, both in size and shape. Therefore, LUVs were produced by extruding the suspension eleven times through a Nuclepore™ track-etched polycarbonate membrane (Maidstone, UK) with pores of 400 nm, 200 nm, and finally 100 nm at 37 °C. The extrusion must be performed at temperatures above the phase transition temperature of the lipids. At lower temperatures, the liposomes' lipid membrane is rigid and inflexible, which hinders their passage through the pores. Figure 3.1 shows the step-by-step of the methodology used.

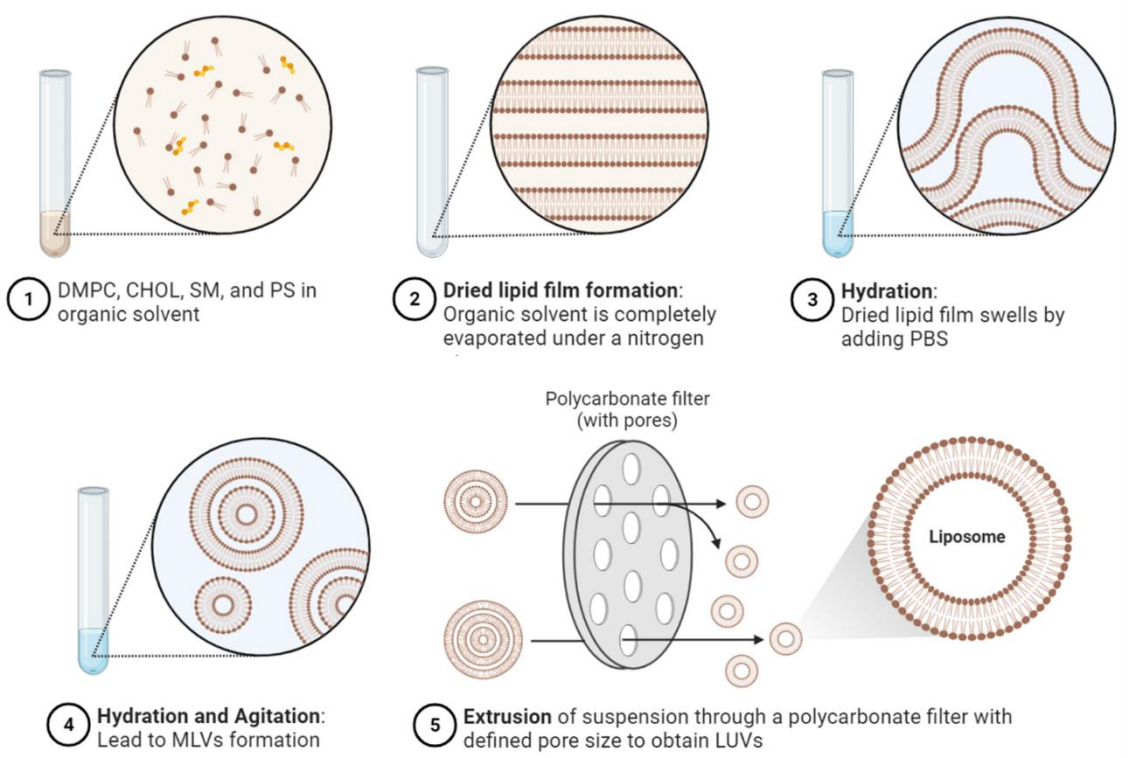

Figure 3.1. Step-by-step of the thin-film hydration technique for liposome production.

3.2.2. Physicochemical Characterization of Liposomes

The produced liposomes were characterized by their physicochemical properties, including hydrodynamic diameter, polydispersity index (PdI), and zeta potential. The mean diameter and PdI of the lipid vesicles were determined by dynamic light scattering (DLS), while zeta potential of the liposomes was assessed by electrophoretic light scattering (ELS), both using a Zetasizer Nano ZS (Malvern Instruments, Worcestershire, UK). Size measurements were achieved with a backscatter angle of 173°. The obtained values were determined from three measurements of eleven runs each. Zeta potential values resulted

from three measurements of twenty runs each, determined by the Smoluchowski mathematical model.

3.2.2.1. Dynamic Light Scattering

DLS technique allows determining the average dimensions and size distribution of NPs by detecting fluctuations in scattered light intensity as a function of time. When light irradiates an NPs suspension, NPs scatter some of the incident light. The amount of scattered light is constant if the NP is not moving. However, in colloidal suspensions, Brownian movements cause the NPs to move continually, causing changes in the intensity of scattered light.

The rate of variation of the scattered light is directly proportional to the movement of the NPs, which can be related to their diffusion coefficient. Because NPs diffusion is affected by temperature (the higher the temperature, the faster the movement), viscosity (the higher the viscosity, the slower the movement), and NPs size (the bigger the NPs, the slower the movement), and because the solvent and temperature are known and constant, the Stokes-Einstein equation (Equation 3.1) can be used to determine the NPs size [14]:

$$R_H = \frac{kT}{6\pi\eta D} \qquad \text{Equation 3.1}$$

where R_H is the hydrodynamic radius, k is the Boltzmann constant, T is the absolute temperature, η is the viscosity of the medium, and D is the diffusion coefficient.

DLS can also be used to determine the PdI, which is a measure of the size heterogeneity of NPs in a suspension. A suspension is considered monodisperse, i.e., NPs with approximately the same size, when PdI values are lower than 0.1. On the other hand, if NPs have varying sizes, the sample is classified as polydisperse. The presence of aggregates can skew the results since the equipment analyze them as a single larger particle, resulting in higher PdI [14].

3.2.2.2. Electrophoretic Light Scattering

ELS, also known as laser doppler electrophoresis, is used to estimate the zeta potential of NPs. Zeta potential refers to the overall charge that a particle acquires in a particular medium. Measurements of zeta potential are commonly used to study the

stability of colloidal systems. If particles in suspension have a high zeta potential (negative or positive), they will tend to repel each other, thus preventing their aggregation. However, if the zeta potential of the particles is low, there will be no force to keep them from aggregating. Particles with zeta potential values larger than |30| mV are usually considered stable [15].

The sample is placed in a capillary cell with two electrodes at the capillary's ends for measurements. When an electric field is applied, electrophoresis occurs since charged particles of the sample are attracted to the electrode of opposite charge. While the sample undergoes electrophoresis, an emitting beam hits the particles. The light is scattered by the particles, which is detected by a photodetector. The light frequency shift is proportional to the velocity of the particles, allowing the determination of the electrophoretic mobility, μ, using the following equation (Equation 3.2):

$$\mu = \frac{\nu}{E} \qquad \text{Equation 3.2}$$

where ν is the velocity and E the applied electric field.

The zeta potential is then determined using the Smoluchowski equation (Equation 3.3):

$$\zeta = \frac{\eta \mu_E}{\varepsilon} \qquad \text{Equation 3.3}$$

where ζ is the zeta potential, η is the viscosity coefficient, and ε is the dielectric constant [15].

3.2.3. $A\beta_{1\text{-}42}$ preparation

Stock solutions of monomeric $A\beta_{1\text{-}42}$ were prepared as described previously [16]. In brief, lyophilized Aβ was dissolved in HFIP at 0.25 mg/mL. The solution was stirred at 250 rpm for 3 days at room temperature to ensure the disaggregation of preformed aggregates. The organic solvent was then evaporated under a nitrogen stream. The attained film was dissolved in PBS at a concentration of 20 μM, and the solution vortexed for 2 min followed by 2 min of sonication in a cold-water bath sonicator (ultrasonic cleaner, VWR, USA).

For fibril destabilization assays, $A\beta_{1\text{-}42}$ fibrils (10 μM) were prepared by incubating $A\beta_{1\text{-}42}$ monomers solution in presence or absence of *in vitro* neuronal membrane models (500 μM) at 37 °C and 300 rpm for 2 h.

Stock solutions of $A\beta_{1-42}$ monomers and fibrils were immediately used on aggregation and disaggregation assays, respectively.

3.2.4. Thioflavin T Fluorescence Assay

ThT is a cationic benzothiazole, a classic amyloid dye often employed to investigate the Aβ fibril formation because of its strong fluorescence emission upon binding to amyloid fibrils. It is presumed that the quantity the amyloid fibrils is proportional to the intensity of fluorescence.

The ability of eight natural compounds - FA, NIC, CAF, CA, AA, VA, GA, and VB12 - to inhibit the $A\beta_{1-42}$ fibrillation and disrupt preformed fibrils was monitored through a ThT binding assay as previously described [17]. Briefly, each natural compound in PBS (800 μM) was mixed with $A\beta_{1-42}$ monomers of fibrils (8 μM) in a 96-well plate (non-treated, flat bottom, UV-Star®). Respective controls in absence of natural compound were also prepared. A 50 μM ThT solution previously filtered (0.2 μm) was immediately mixed to the samples. The plate was then sealed to prevent evaporation, and incubated at 37 °C for 4 h, with continuous medium agitation to ensure the homogeneity of the samples. The fluorescence intensity was recorded with 2 min intervals using a Synergy™ 2 Multi-Mode Microplate Reader (BioTek Instruments, Winooski, VT, USA) with excitation and emission filters of 420/50 nm and 485/20 nm, respectively.

The influence of *in vitro* neuronal membrane models on the anti-amyloidogenic activity of the natural compounds – CA, GA, and VB12 – was also studied. For aggregation assays in a neuronal membrane-like environment, DMPC:CHOL:SM:PS liposomes (400 μM) were mixed with a CA, GA, or VB12 solution in PBS (800 μM) in a 96-well plate. The plate was sealed and incubated at 37 °C for 30 min with medium agitation, to ensure that the natural compounds' partition equilibrium between the aqueous and lipid phases is attained. $A\beta_{1-42}$ monomers (8 μM) were added to the liposomes/natural compound mixture at lipid-to-peptide molar ratio ([L]/[P]) of 50:1 and a compound-to-peptide molar ratio ([C]/[P]) of 100:1. Respective controls without natural compound were also prepared. A ThT solution in PBS (50 μM) was added to the samples. The plate was sealed and incubated at 37 °C for 4 h, with constant medium agitation to ensure the homogeneity of the samples. ThT fluorescence intensities were obtained as explained above.

For fibril disaggregation experiments in a neuronal membrane-like environment, $A\beta_{1-42}$ fibrils (8 μM) formed in presence of liposomes (400 μM) were mixed with a solution of GA, CA, or VB12 in PBS (800 μM) in a 96-well plate. Respective controls without natural compounds were prepared. The ThT solution (50 μM) was added to the samples, the plate was sealed, and then incubated at 37 °C for 2 h with continuous medium agitation. ThT fluorescence intensities were recorded as described above.

3.2.5. Kinetic Model of $A\beta_{1-42}$ Fibrillation

Following ThT fluorescence data acquisition, controls were subtracted to the corresponding samples. ThT fluorescence intensities (F) were normalized according to the data of control (Aβ) and fitted as function of time (t) (hours) according to Equation 3.4 [18]:

$$F(t) = F_0 + \frac{F_{max}}{1+e^{[-k(t-t_{1/2})]}} \quad \text{Equation 3.4}$$

where F_0 is the ThT fluorescence intensity at the beginning of the kinetics (t=0 h) and F_{max} is the maximum ThT fluorescence intensity. $t_{1/2}$ and k indicate the time taken to reach half of the F_{max} and the elongation rate constant of the fibrillation kinetics, respectively. The lag time of the fibril growth (t_{lag}) was calculated based on these two parameters, according to the following equation (Equation 3.5):

$$t_{lag} = t_{1/2} - \frac{2}{k} \quad \text{Equation 3.5}$$

3.2.6. Transmission Electron Microscopy

TEM is one of the most efficient and versatile tools for the characterization of nanomaterials morphology. This microscopic technique is characterized by a higher resolution compared to conventional light microscopes. TEM is based on the principle of electron wave-particle duality. Since an electron is a charged particle, it can be accelerated in an electric field, and electric and magnetic fields can deflect its trajectory. As this accelerated electron also behaves like a wave, it is possible to control its wavelength by potential differences. The wavelength depends on the velocity, according to the following equation (Equation 3.6):

$$\lambda = \frac{h}{m\,v} \quad \text{(Equation 3.6)}$$

where λ is the electron wavelength, h is Planck's constant, m is the electron mass, and ν is the electron velocity. Therefore, depending on the accelerating voltage used, it is possible to choose the wavelength of the electron beam. The higher the accelerating voltage, the shorter the wavelength.

Figure 3.2 illustrates a simplified diagram of TEM operation. Initially, a beam of electrons is applied and accelerated by an electric field formed by a voltage difference. The set of condenser lenses focus the electron beam on strong magnetic fields to a spot on the sample to be investigated. Then, the beam hits the sample, and the electrons interact with the matter. Depending on the sample density, some electrons are scattered, and some are transmitted through the sample. The electrons are then magnified and focused on an objective lens, leading to the image's appearance on the screen.

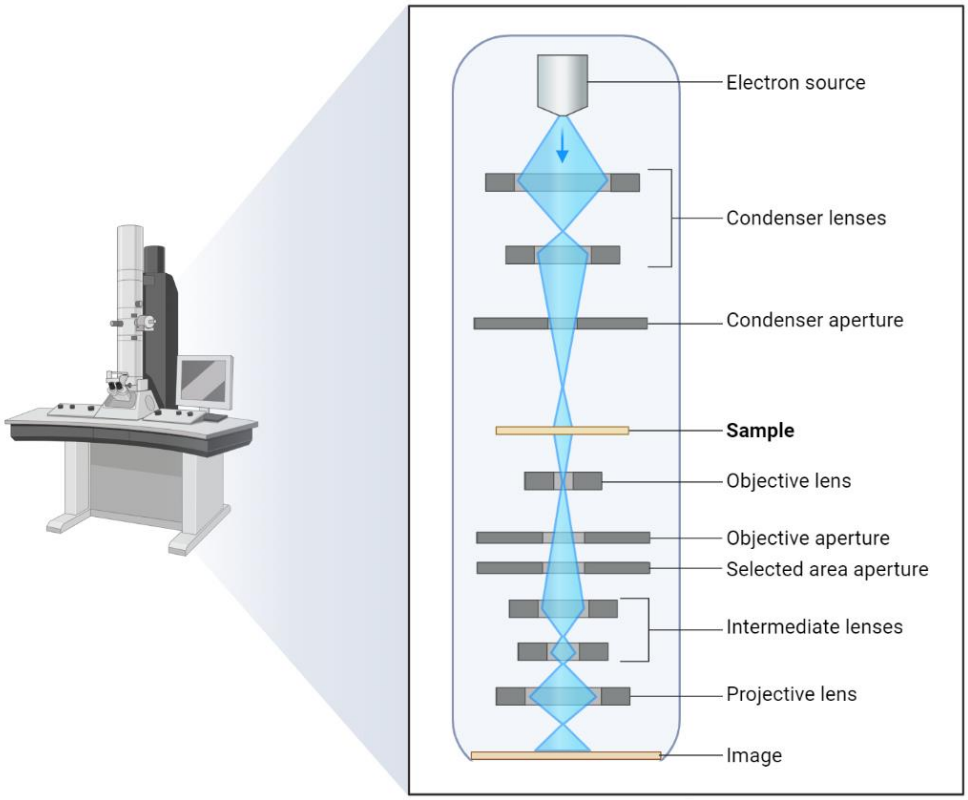

Figure 3.2. Simplified diagram of TEM operation.

The objective diaphragm ensures the exclusion of inelastically scattered electrons to enhance the image's contrast. The beam that reaches the phosphor screen has different amounts of electrons that pass through particular regions of the sample. This difference is responsible for the image contrast. Darker areas of the image represent the regions of the

sample through which fewer electrons were transmitted due to the greater thickness or density. Contrariwise, brighter areas result from the increased electronic transmission, representing thin regions of the sample.

TEM was used to monitor the structural morphology of $A\beta_{1-42}$ peptide upon 4 h of incubation with CA, GA, or VB12, in the presence or absence of the *in vitro* neuronal membrane model, according to previous reports [19]. Briefly, 5 µL aliquots directly drawn from ThT assays solutions were placed on a carbon-formvar coated 400 mesh spacing grid for 5 min at room temperature and removed with filter paper. Negative staining was performed with a 2% (w/v) uranyl acetate solution for 45 s. The staining solution was then blotted, and the grid was rinsed with the uranyl acetate solution. TEM images were acquired using a JEM 1400 electron microscope (JEOL, Tokyo, Japan) with an acceleration voltage of 80 kV.

3.2.7. Attenuated Total Reflection-Fourier Transform Infrared

FTIR spectroscopy allows for studying the interaction of infrared radiation with matter, including organic or inorganic, solid, liquid, or gaseous. Because each distinct chemical bond absorbs incident light at a particular wavelength, this approach can identify chemical bonds in molecules. When a given bond absorbs radiation, it will become excited, and consequently, the frequency of its molecular vibration will increase. A molecule's infrared vibrational spectrum comprises several bands resulting from the transition between pairs of vibrational levels related to the ground electronic state.

ATR accessories are particularly helpful for collecting infrared spectra of samples that are difficult to investigate using the standard transmission approach. They are appropriate for examining dense or highly absorbing solid and liquid materials, such as aqueous samples, threads, coatings, powders, and adhesives.

ATR-FTIR spectra of $A\beta_{1-42}$ peptide upon 4 h of incubation with CA, GA, or VB12, in the presence or absence of the *in vitro* neuronal membrane model, were gathered as reported in a previous study [19]. Briefly, 5 µL of the end-point products from ThT assays were placed on the surface of the FTIR crystal, followed by solvent evaporation under a nitrogen flow. Spectra were collected in the amide I region of Aβ (1600 to 1700 cm^{-1}), as this region is considered the most sensitive to proteins/peptides secondary structures. Spectra of the background and control samples were also obtained and subtracted from the

corresponding spectrum. ATR-FTIR measurements resulted from 64 scans and were obtained using an ALPHA-P spectrophotometer (Bruker Corporation, Billerica, MA, EUA).

Following ATR-FTIR spectroscopy acquisition, spectra were processed according to previous work [17]. Fourier self-deconvolution algorithm with a smoothing factor of 0.4 was applied to the spectra to enhance their resolution, followed by the baseline correction. The resulting spectra were deconvoluted using the Gaussian-Lorentzian function, and successive iterations were completed until convergence was reached. Antiparallel β-sheet structures have two typical bands at 1615-1627 cm^{-1} and 1674-1695 cm^{-1}. β-turn structures display a single band at 1662-1686 cm^{-1}, while parallel β-sheets are characterized by a band at 1623-1641 cm^{-1}. α-helix structures exhibit a single band around 1648-1657 cm^{-1} [20]. ATR-FTIR data analysis was completed using Origin 2021 software (OriginLab Corp., MA, USA).

3.2.8. Circular Dichroism

CD spectroscopy is a widely-used technique to investigate the secondary structure, folding, and interactions of proteins in solution. This method depends on the differential absorption of left and right circularly polarized radiation by chromophores which either have intrinsic chirality or are placed in chiral environments. Proteins have some chromophores that originate CD signals. The CD spectra can be examined to determine the content of regular secondary structural characteristics like α-helix and β-sheet in the far UV region (240-180 nm), which corresponds to peptide bond absorption [21].

CD spectra were recorded on a JASCO J-815 spectropolarimeter (JASCO Corporation, Tokyo, Japan), according to the previous work [22]. Briefly, 120 μL aliquots of the end-point products from ThT assays were placed on a 1 mm path length quartz cell. CD spectra were recorded between 200 and 260 nm with a scan rate of 50 nm/min at 37 °C. Spectra of the background and blank samples were also collected and subtracted from the corresponding protein spectrum. Each spectrum results from the mean of 16 scans. Fourier self-deconvolution algorithm with a smoothing factor of 0.2 was applied to enhance the spectra resolution.

3.2.9. UV-Vis Derivative Spectrophotometry

UV/Vis spectrophotometry is a widely used technique in analytical chemistry for quickly, easily, and accurately estimating the concentration of compounds in solution [23]. Spectrophotometers are composed of a radiation source and a detector. The radiation source emits a monochromatic light beam, which hits the substances in a given solution. While part of the radiation is absorbed, another is transmitted through the sample, reaching the detector. The amount of absorbed radiation is then determined by the difference between the incident light and the light that reached the detector. This relationship is translated by the following equation (Equation 3.7) [24]:

$$A = -\log_{10}\left(\frac{I}{I_0}\right) \qquad \text{(Equation 3.7)}$$

where A is the absorbance, I is the light that reached the detector, and I0 is the incident light.

Quantifying substances by spectrophotometry is based on the Lambert-Beer law (Equation 3.8).

$$A = \varepsilon . c . l \qquad \text{(Equation 3.8)}$$

where A is the absorbance, ε is the molar absorptivity, c is the sample concentration, and l is the path length [25].

In this experiment, derivative UV-Vis spectrophotometry was used to assess the partition coefficient (KP) values of CA, GA, and VB12. Conventionally, KP is calculated in a biphasic octanol/water system. However, liposome/water systems simulate the membrane characteristic of biological membranes ensuring the presence of electrostatic interactions between drugs and the polar groups of the phospholipids that are not simulated in the octanol/water system [26]. Besides that, the combination of derivative spectroscopic methods with liposome/water systems ensures the study of drug distribution between the lipid and aqueous media without calculating the drug amount in each phase. Furthermore, the derivative spectrophotometry eliminates the background signals caused by the liposome light scattering, providing an improved resolution of overlapped bands [26].

The KP of CA, GA, and VB12 between the lipid vesicles and the aqueous media was determined by derivative spectrophotometry [27]. Briefly, CA, GA, or VB12 (100 μM) was added to increasing concentrations of LUVs (from 0 to 4000 μM). Controls in the absence of natural compounds were also completed. Absorbance spectra were obtained at 37 °C, in a

range of 200 to 500 nm, using a Synergy™ 2 Multi-Mode Microplate Reader (BioTek Instruments, Winooski, VT, USA).

To assess natural compounds' KP values in the presence of $A\beta_{1-42}$ fibrils, preformed fibrils in PBS were added to increasing concentrations of LUVs (from 0 to 4000 μM). The plate was sealed and incubated at 37 °C for 30 min with medium agitation to allow the peptide-biomembrane interactions to be established. Natural compounds were added, and KP values were calculated as described above. The [C]/[P] of 100:1 was kept constant throughout the experiment.

A previously designed routine known as KP Calculator was used to analyze the data [38]. The analysis is based on three stages: (i) the blank spectrum was subtracted to the correspondent absorption spectrum of liposomes to correct the absorption spectrum; (ii) to enhance the band resolution and facilitate the detection of spectral details, the second-derivative spectra were assessed to remove the light scattering induced by liposomes; (iii) KP values were determined based on the wavelength of second derivative spectra where the scattered light was removed, by plotting the Equation 3.9 to the experimental data (D_T *versus [L]*) through the use of a nonlinear least-squares regression where the KP is the variable parameter [28]:

$$D_T = D_W + \frac{(D_m - D_W)\, K_P\, [L]\, V_m}{1 + K_P\, [L]\, V_m} \qquad \text{(Equation 3.9)}$$

where D represents the second derivative ($D = dn\ Abs/d\lambda n$) calculated from the absorbance values of the total amount of natural compound (D_T), the amount present in the lipid membrane (D_m), and aqueous phases (D_W). [L] defines the lipid concentration (in M) and V_m is the lipid molar volume, which corresponds to 0.5977 L/mol for DMPC:CHOL:SM:PS LUVs [65:15:10:10].

The dimensionless partition coefficient of CA, GA, and VB12 (log D) was calculated according to the following equation (Equation 3.10):

$$\log D = \log (KP/V_m) \qquad \text{(Equation 3.10)}$$

The theoretical octanol/buffer partition coefficients (log P) of CA, GA, and VB12 were determined by the Marvin Sketch Calculator (v.5.11.0) from Chemaxon™.

3.2.10. Statistical Analysis

Data are expressed as the mean ± standard deviation (SD) of at least three independent assays. Student's t-tests with a confidence interval of 95% were performed using GraphPad Prism 8 software to assess significant differences between data.

3.3. Results and Discussion

3.3.1. Screening of Natural Compounds for Anti-Amyloidogenic Properties

The ability of FA, NIC, CAF, CA, AA, VA, GA, and VB12 to inhibit the $A\beta_{1-42}$ aggregation and disrupt mature fibrils in an aqueous medium was investigated by a ThT fluorescence assay. Figure 3.3 shows the chemical structure of the eight natural compounds used in this study. To this end, $A\beta_{1-42}$ monomers or fibrils were mixed with the natural compounds at a [C]/[P] of 100:1. Control samples in the absence of natural compounds were also prepared.

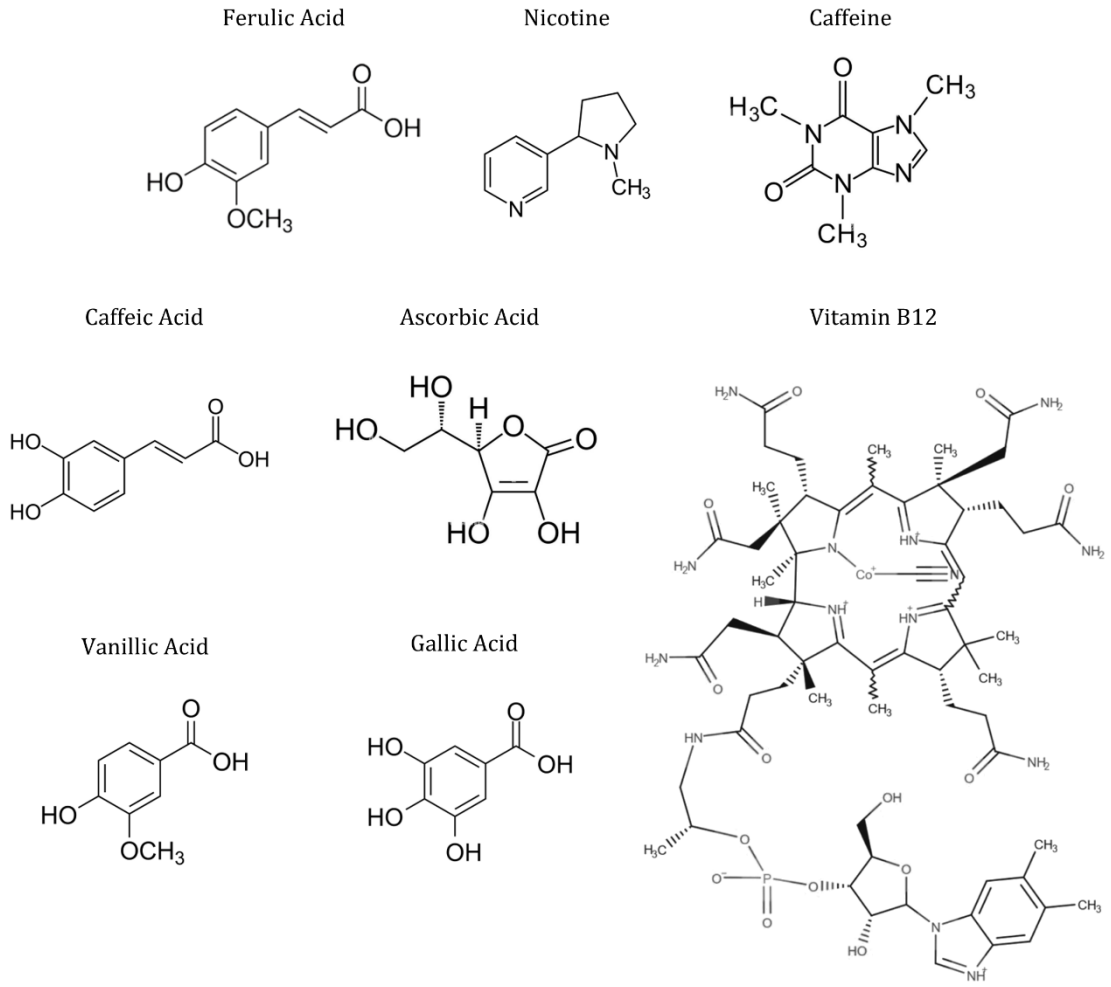

Figure 3.3. Chemical structure of the studied natural compounds.

Figure 3.4 shows the complete sets of normalized ThT fluorescence kinetic curves after incubating Aβ monomers with the eight natural compounds in PBS. The kinetic parameters of the ThT traces were determined by combining the data with a nonlinear mathematic model (Equation 3.4). The estimated parameters include the lag phase time (t_{lag}, h), the time needed to reach half of the maximum fluorescence signal ($t_{1/2}$, h), the fibril elongation rate (k, h^{-1}), the maximum normalized fluorescence intensity (F_{max}), and are summarized in Table 3.1.

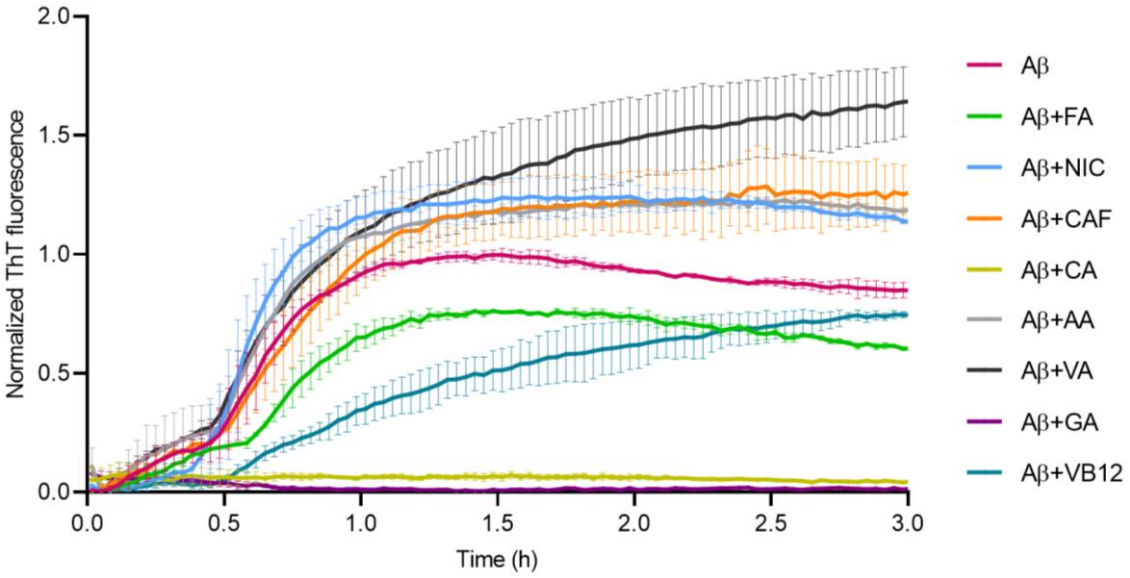

Figure 3.4. Normalized Thioflavin T (ThT) fluorescence of $A\beta_{1-42}$ (8 μM) as a function of time (h) upon incubation of monomers with the natural compounds (800 μM) in PBS.

Table 3.1. Kinetic parameters calculated by fitting Equation 3.4 to the ThT curves of Figure 3.4. *p<0.05, **p< 0.01 and ***p<0.001 indicate statistically differences between $A\beta_{1-42}$ in the absence and presence of the natural compounds.

	t_{lag} (h)	$t_{1/2}$ (h)	k (h^{-1})	Max. fluorescence
Aβ	0.40 ± 0.08	0.61 ± 0.06	7.5 ± 1.6	0.98 ± 0.04
Aβ+FA	0.39 ± 0.08	0.72 ± 0.02	6.5 ± 1.9	0.74 ± 0.05 **
Aβ+NIC	0.39 ± 0.06	0.60 ± 0.05	9.7 ± 0.3	1.24 ± 0.07 **
Aβ+CAF	0.31 ± 0.02	0.73 ± 0.03	4.8 ± 0.2	1.26 ± 0.14 *
Aβ+CA	n.d.	n.d.	n.d.	n.d.
Aβ+AA	0.30 ± 0.06	0.62 ± 0.04	6.3 ± 0.5	1.17 ± 0.03 **
Aβ+VA	0.14 ± 0.02 *	0.76 ± 0.14	2.9 ± 0.3 *	1.73 ± 0.36 *
Aβ+GA	n.d.	n.d.	n.d.	n.d.
Aβ+VB12	0.34 ± 0.02	1.19 ± 0.21 *	2.5 ± 0.6 *	0.78 ± 0.01 **

n.d. not determined

From Figure 3.4, it can be seen that the ThT fluorescence kinetic curve of Aβ exhibits a typical sigmodal tendency. A low ThT intensity is detected in the beginning, indicating the residual presence of β-sheet structures. In this phase, known as the lag phase, monomeric Aβ aggregates into small oligomers. The ThT signal then increases due to the rapid fibrils

growth (elongation phase), which reaches a plateau when most peptide has aggregated into fibrils (stationary phase) [29].

Figure 3.4 and Table 3.1 reveal that all the natural compounds affected the time course of $A\beta_{1-42}$ fibrillation kinetic. FA, CA, GA, and VB12 prevented the Aβ fibrillation, however, NIC, CAF, AA, and VA demonstrated to promote the fibril formation. CA and GA are the natural compounds with the best anti-fibrillation properties. As shown in Figure 3.4, the ThT fluorescence signal of Aβ in the presence of CA and GA did not increase during the incubation period, implying that these compounds entirely prevented the formation of Aβ fibrils. VB12, in turn, significantly affected the elongation rate by reducing it by 3 times ($p<0.05$). As a result, the time required for 50% of the maximum fluorescence intensity to be achieved has doubled ($p<0.05$), thus suggesting that VB12 slows the transition from Aβ oligomers to mature fibrils. Moreover, VB12 also reduced the maximum fluorescence intensity to around 22% ($p<0.01$). As the ThT fluorescence is directly proportional to the fibril content, this data indicates that VB12 can also reduce the amount of Aβ fibrils formed. FA also reduced the fibril content by approximately 26% ($p<0.01$) without modifying the remaining kinetic parameters.

Nevertheless, NIC, CAF, AA, and VA negatively impacted the $A\beta_{1-42}$ fibrillation kinetic by increasing the fibril content is about 24, 26, 17, and 73%, respectively. The remaining kinetic parameters remained unchanged ($p>0.05$), except for VA, which significantly decreased the t_{lag} compared to the control ($p<0.05$), indicating that VA accelerates the transition of Aβ monomers to oligomers, and significantly reduced the elongation rate by 2.6 times ($p<0.05$).

Figure 3.5 displays the complete sets of normalized ThT fluorescence kinetic curves after incubating Aβ fibrils with the eight natural compounds in PBS. Again, CA, GA, and VB12 are the natural compounds with the best fibril disaggregating properties. The presence of these natural compounds significantly suppressed the ThT fluorescence intensity, suggesting the disaggregation of Aβ fibril. CA and VB12 prompted an abrupt reduction of the ThT signal ($p<0.001$) immediately upon their addition to Aβ fibrils, reducing the content of fibrils by approximately 80%. In turn, the GA's disaggregating activity seems to be time-dependent. Over time, a decrease of the ThT signal is observed, implying a gradual reduction in the fibril content. Immediately upon adding GA to Aβ fibrils, a decline of about 41% in the ThT signal is detected until GA totally inhibits the ThT fluorescence after 1.5 h of incubation ($p<0.001$), suggesting the complete fibril disruption. However, an opposite behavior was

observed after incubating CAF, AA, and VA with Aβ fibrils. These natural compounds significantly increased the ThT fluorescence signal compared to the control ($p<0.05$) by approximately 17, 36, and 12%, respectively, indicating an increase in the number of fibrils. NIC and FA did not affect the ThT intensity ($p>0.05$).

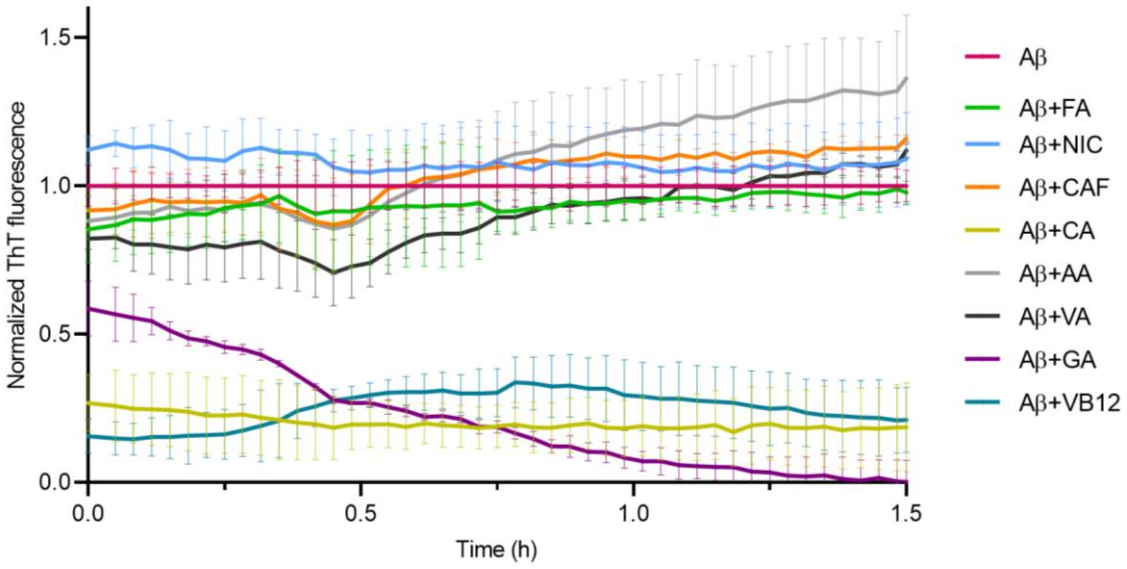

Figure 3.5. Normalized ThT fluorescence of $A\beta_{1-42}$ (8 μM) as a function of time (h) upon incubation of fibrils with the natural compounds (800 μM) in PBS.

Based on the presented results, the natural compounds with the best anti-amyloidogenic properties for both inhibiting the fibril formation and disaggregating mature fibrils – CA, GA, and B12 – were selected for additional assays. The influence of *in vitro* neuronal membrane on the anti-amyloidogenic properties of these natural compounds was investigated.

3.3.2. Influence of *in vitro* Neuronal Membranes on the Anti-Amyloidogenic Activity of Caffeic Acid

The content of this section is published in: *Andrade, S., Loureiro, J.A. & Pereira, M.C. (2021). Caffeic acid for the prevention and treatment of Alzheimer's disease: The effect of lipid membranes on the inhibition of aggregation and disruption of Aβ fibrils. International Journal of Biological Macromolecules, 190, 853-861.*

3.3.2.1. Aβ Fibrillation Study

The effect of CA on the $A\beta_{1-42}$ fibrillation kinetics in both PBS and membrane environment was examined by combining ThT binding experiments with mathematical modeling. ThT fluorescence is a methodology widely employed to detect and quantify amyloid fibrils *in vitro* since ThT molecules emit fluorescence after binding to β-sheet structures [30]. To this end, $A\beta_{1-42}$ monomers and CA were incubated in the absence or presence of DMPC:CHOL:SM:PS liposomes at 37 °C, and the ThT fluorescence was monitored for 4 h. The characterization of the produced liposomes is shown in Table S3.1 (Supplementary Material). The kinetics of $A\beta_{1-42}$ aggregation in the absence of CA in both aqueous and membrane environments were also monitored. The full sets of ThT fluorescence data are displayed in Figure 3.6. The kinetics parameters of aggregation were determined by fitting Equation 3.4 to the ThT traces and are shown in Table 3.2.

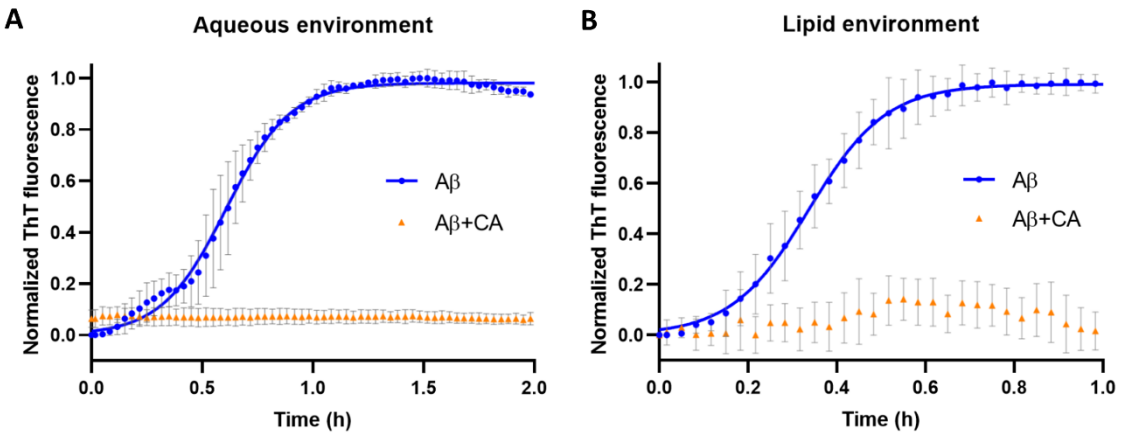

Figure 3.6. Normalized ThT fluorescence of $A\beta_{1-42}$ (8 μM, blue circle) as a function of time (h) upon incubation with caffeic acid (CA) (800 μM, orange triangle) in A) PBS and B) in the presence of liposomes (400 μM).

Table 3.2. Kinetic parameters of $A\beta_{1-42}$ aggregation in the presence and absence of CA, both in aqueous and membrane-like environments, are determined by fitting Equation 3.4 to the ThT data. *p<0.05 suggests a statistical difference between $A\beta_{1-42}$ in aqueous and lipid media.

	Aqueous environment		**Lipid environment**	
	$A\beta_{1-42}$	**$A\beta_{1-42}$ + CA**	**$A\beta_{1-42}$**	**$A\beta_{1-42}$ + CA**
t_{lag} (h)	0.39 ± 0.09	n.d.	0.17 ± 0.03 *	n.d.

$t_{1/2}$ (h)	0.58 ± 0.09	n.d.	0.30 ± 0.04 *	n.d.
k (h^{-1})	7.4 ± 1.4	n.d.	12.1 ± 2.5 *	n.d.
Max. fluorescence	1.00 ± 0.02	n.d.	1.00 ± 0.01	n.d.

n.d. not determined

In agreement with previous studies [31, 32], ThT data of $A\beta_{1-42}$, both in the presence and absence of liposomes, display a typical sigmoidal curve (Figure 3.6). The beginning of each kinetic is characterized by low values of ThT fluorescence, suggesting the absence of β-sheet structures. In this stage, known as the lag phase, Aβ monomers are converted into oligomers. Then, ThT intensities increase due to the fibrils' growth, known as the elongation phase, until reaching a plateau when protofibrils are assembled into mature amyloid fibrils (stationary phase) [32].

In the aqueous medium, the $A\beta_{1-42}$ aggregation process exhibit a t_{lag} of 0.39 ± 0.09 h (around 23 min) (Table 3.2). However, lipid vesicles induced a significant reduction of this parameter to 0.17 ± 0.03 h (approximately 10 min) ($p<0.05$), inferring that $A\beta_{1-42}$ starts to aggregate faster in the lipid environment. The presence of the artificial lipid membranes has also affected the growing phase by enhancing the fibril elongation rate (k) by a factor of approximately 2 when compared with the aqueous environment ($p<0.05$). As a result, the time needed to reach half of the maximum fluorescence ($t_{1/2}$) has halved ($p<0.05$). Lindberg et al. (2017) draw comparable conclusions using liposomes made of 1,2-dioleoyl-sn-glycero-3-phospho-L-serine as synthetic membranes [24]. Moreover, despite the electrostatic repulsions between Aβ (net charge of −2.8 at pH 7.4) and PS (net charge of -1 at pH 7.4), the interaction of $A\beta_{1-42}$ with anionic lipid membranes was already discussed in previous works [33, 34]. It seems that other highly favorable interactions between the hydrophobic tail of the peptide and the core of the phospholipid bilayer overcome the electrostatic repulsions. Collectively, these results suggest that lipid membranes play a catalytic role in the $A\beta_{1-42}$ fibrillation process by accelerating the elongation phase, as previously described [35]. Substantial evidence indicate that lipid membranes play a key role in the aggregation of $A\beta_{1-42}$ by influencing the Aβ folding and enhancing the aggregation rates [24, 36]. Particularly, the composition of membranes is the main factor modulating the peptide-membrane interactions by affecting the Aβ structural transitions and consequent aggregation [37]. Negatively charged phospholipids and CHOL were identified as the main membranes' components involved in the Aβ-biomembranes interactions [38].

The incubation of the peptide with CA prompted modifications in the time course of the $A\beta_{1-42}$ aggregation kinetics in PBS (Figure 3.6). No significant difference in the ThT signal at the beginning and end of the experiments was detected ($p>0.05$), suggesting that CA fully prevents the fibrillation process in the aqueous environment. In addition, Figure 3.6 suggests that the overall CA's ability to prevent the fibril formation was not disturbed by the lipid membranes since no difference between the endpoint of ThT emission intensities of the two tested conditions was noticed ($p>0.05$). A plausible scenario for the similar anti-fibrillation activity of CA in both the membrane and non-membrane environments is that the natural product interacts preferentially with $A\beta_{1-42}$ peptides than with the lipid membranes.

Therefore, the CA-lipid membrane interactions were investigated in terms of CA's lipophilicity. The CA's KP between the aqueous and membrane phase was assessed by derivative UV–Vis spectrophotometry. Due to the amphiphilic nature of the phospholipids, this methodology provides a promising alternative to the conventional techniques by simulating interactions other than the hydrophobic interactions between ionized drugs and phospholipids' heads, unlike the octanol/water system. Moreover, using the derivative allows removing the noise caused by vesicles' light scattering, which improves the band resolution [39]. An example of the data processing performed to determine CA's KP is illustrated in Figure S3.1 (Supplementary Material). The KP and log D of CA as well as its theoretical octanol/water partition coefficient (log P) at pH 7.4 are presented in Table 3.3. The CA's log P was estimated using the log P calculator from ChemAxon (Hungary).

Table 3.3. Partition coefficient (KP) and distribution coefficient (log D) of CA (100 μM) between the aqueous and lipid membrane phases (pH 7.4, 37 °C). ¥ Predicted using the MarvinSketch calculator (ChemAxon).

KP	log D	log P ¥
1191 ± 195	3.3 ± 0.1	1.83

As shown in Table 3.3, the CA's KP value of 1191 ± 195 suggests that CA has a moderate affinity for the lipid membrane, with some molecules partitioning from the PBS to the membrane media. It is thus conceivable that the molecules of CA remaining in the aqueous phase are enough to completely inhibit the formation of Aβ fibrils in solution. In

addition, it is possible to notice from Table 3.3 that the CA's log D (3.3 ± 0.1) is significantly higher than its log P (1.83). This difference occurs due to the amphiphilic nature of the phospholipids that allows contemplating electrostatic, ion-dipole, and dipole-dipole forces between the phospholipids and ionized molecules, that the classic two-phase octanol/water system fails in considering [40]. Predictions from Marvin Sketch Calculator software reveal that the totality of CA molecules is negatively charged at pH 7.4. Therefore, it is expected that, in addition to the hydrophobic forces, CA interacts with the phospholipid bilayer through ion-dipole forces with the negative charge of the DMPC polar head.

The morphology of the ThT end-point products after 4 h of incubation was examined by TEM (Figure 3.7). Without CA, $A\beta_{1-42}$ samples formed thin and long fibrils in the aqueous (Figure 3.7 A) and lipid environments (Figure 3.7 C). Some aggregates corresponding to protofibrils were also noticed. In contrast, when $A\beta_{1-42}$ was incubated with the natural compound, no fibrils were detected, and only small structures and short filaments appeared, both in the presence (Figure 3.7 D) and absence of artificial lipid membranes (Figure 3.7 B).

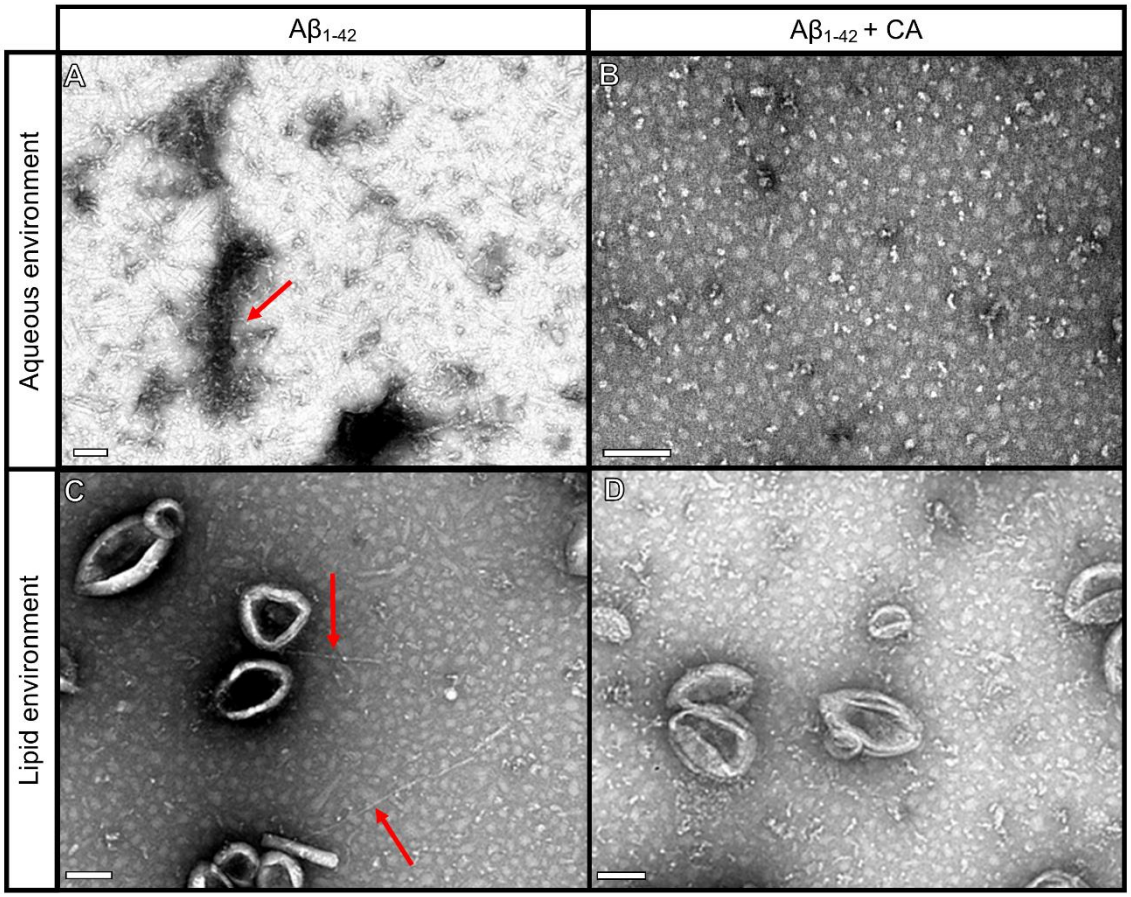

Figure 3.7. TEM images of $A\beta_{1-42}$ (8 μM) incubated in the A) absence and B) presence of CA (800 μM) in PBS. $A\beta_{1-42}$ incubated with liposomes (400 μM) in the C) absence and D) presence of CA. Red arrows demonstrate $A\beta_{1-42}$ fibrils. Scale bars indicate 100 nm.

CD measurements were performed to investigate the conformational changes of $A\beta_{1-42}$ upon its incubation with CA for 4 h, either in the presence or absence of lipid vesicles. This is the most used technique to characterize the secondary structure of peptides [41]. Multiple evidence recognize that Aβ peptide undergoes a conformational change from α-helix to β-sheet structures during fibrillation [42]. Thus, monitoring the Aβ secondary structures upon adding CA allows for validating its anti-amyloidogenic activity.

Figure 3.8 illustrates the CD spectra of $A\beta_{1-42}$ in the absence and presence of CA, both in the aqueous (Figure 3.8 A) and lipid (Figure 3.8 B) environments. As expected, CD spectra of $A\beta_{1-42}$ following 4 h of incubation in the absence and presence of DMPC:CHOL:SM:PS liposomes exhibit a canonical peak at around 218 nm, which is representative of β-sheet-rich structures [43]. In the presence of CA in the aqueous medium, the CD spectrum of $A\beta_{1-42}$ exhibits two negative bands at 215 and 225 nm, which is the specific fingerprint characteristic of α-helix structures [44]. These results are in accordance with ThT data and TEM images, reinforcing the CA's ability to prevent fibril formation in PBS. In turn, when $A\beta_{1-42}$ was co-incubated with CA in the lipid environment for 4 h, the peptide displayed a similar profile to what was observed previously in the absence of the natural compound, with an absorption minimum at 218 nm. However, the band intensity was lower as compared to the control sample, which highlights the capacity of CA to prevent the $A\beta_{1-42}$ fibrillation by reducing the content of β-sheet-rich structures formed. These findings agree with the previous reports that depicted the ability of other natural compounds, such as AA and VB12, to prevent the structural transition of amyloid peptides toward forming β-sheet-rich structures [45, 46].

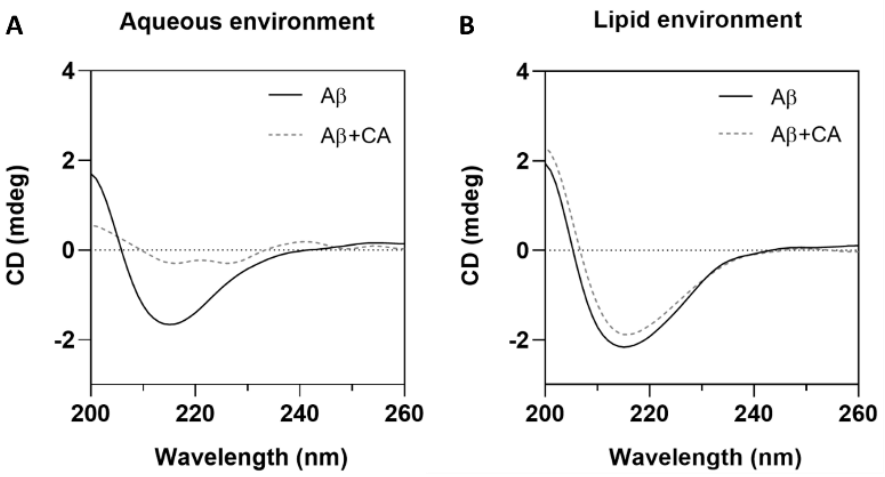

Figure 3.8. Circular dichroism (CD) spectra of $A\beta_{1-42}$ (8 μM, solid black line) upon incubation with CA (800 μM, dashed gray line) in A) PBS and B) in the presence of liposomes (400 μM).

ATR-FTIR measurements combined with deconvolution analysis using a Gaussian-Lorentzian function were conducted to get further insights into the secondary structure of $A\beta_{1-42}$, namely, into the content of each secondary structures. Figure 3.9 exemplifies the self-deconvoluted spectra (black line) of the amide I region of $A\beta_{1-42}$ (1600-1700 cm^{-1}) following 4 h of incubation in the absence and presence of CA in the aqueous and lipid environments. The quantitative estimation of the secondary structures of $A\beta_{1-42}$ upon its incubation with CA in the presence and absence of DMPC:CHOL:SM:PS liposomes is shown in Table 3.4.

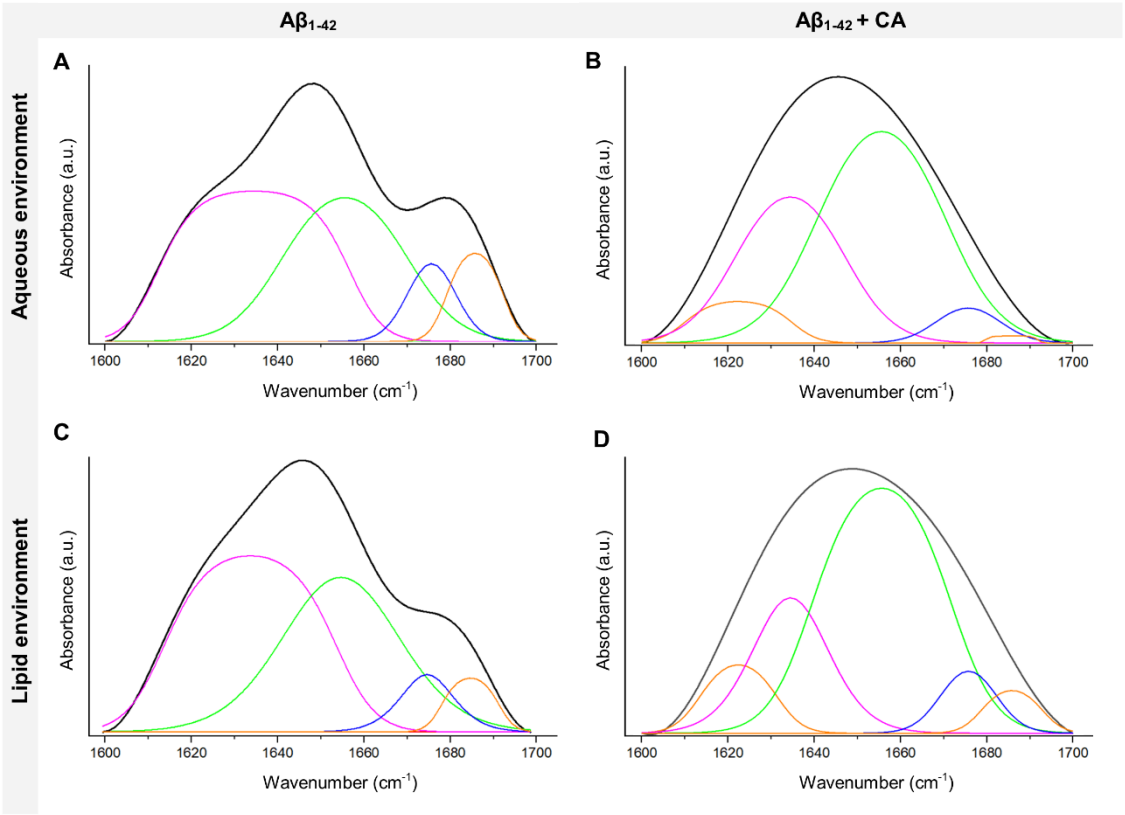

Figure 3.9. Attenuated total reflection-Fourier transform infrared (ATR-FTIR) spectra of $A\beta_{1-42}$ (8μM) in PBS in the A) absence or B) presence of CA (800 μM). C) and D) show the ATR-FTIR spectra of $A\beta_{1-42}$ in the presence of liposomes (400 μM), without and with CA, respectively. Antiparallel β-sheet, parallel β-sheet, α-helix, and β-turn structures are represented by orange, pink, green, and blue lines, respectively.

Table 3.4. Content of secondary structures of $A\beta_{1-42}$ upon 4 h of incubation at 37 °C with and without CA, both in aqueous and lipid environment, estimated from the Fourier self-deconvolution of ATR-FTIR spectra, followed by the curve fitting of amide I band. *p<0.05 and ****p<0.0001 denote statistical differences between $A\beta_{1-42}$ in the absence and presence of CA.

	Aqueous environment		**Lipid environment**	
	$A\beta_{1-42}$	**$A\beta_{1-42}$ + CA**	**$A\beta_{1-42}$**	**$A\beta_{1-42}$ + CA**
Antiparallel β-sheet 1615-1627 cm^{-1}/1674-1695 cm^{-1}	7 ± 1	8 ± 4	7 ± 4	6 ± 3
Parallel β-sheet 1623-1641 cm^{-1}	47 ± 1	33 ± 1 ****	48 ± 8	33 ± 9 *
α-helix 1648-1657 cm^{-1}	37 ± 2	53 ± 1 ****	32 ± 6	50 ± 5 *

β-turn 1662-1686 cm^{-1}	10 ± 2	6 ± 1	13 ± 7	11 ± 5

When incubated in PBS for 4 h at 37 °C, $A\beta_{1-42}$ peptide exhibits predominantly a parallel β-sheet conformation, accounting for approximately 47% of the total content (Table 3.4). This is the primary structural characteristic of amyloid fibrils [47]. In addition, a smaller content (37%) of α-helix structures was noticed, suggesting the presence of some Aβ monomers [48]. A low percentage of antiparallel β-sheet and β-turn structures was also detected, indicating the presence of few oligomers in the tested samples [49]. The content of secondary structures at the end of the $A\beta_{1-42}$ fibrillation process is consistent with previous works [50]. The aggregation process of $A\beta_{1-42}$ in the presence of artificial lipid membranes induced similar secondary structure content to the fibrillation process in bulk solution ($p>0.05$), as previously depicted [51].

As shown in Table 3.4, adding CA to the monomeric solution modified the overall secondary structure content of $A\beta_{1-42}$ regardless of the tested environment. In the aqueous medium, CA significantly reduced the content of parallel β-sheet structures from 47% to 33% ($p<0.0001$) while increasing the α-helix conformation from 37% to 53% ($p<0.0001$). In turn, the amount of antiparallel β-sheet and β-turn structures remained unchanged ($p>0.05$). The CA-induced $A\beta_{1-42}$ conformational changes in the aqueous and lipid environments were comparable ($p>0.05$). These findings indicate that CA is effective in preventing $A\beta_{1-42}$ from undergoing α-helix to β-sheet transition, which is strongly associated with the amyloid fibrils formation [52]. Thus, in agreement with ThT fluorescence, TEM images, and CD results, ATR-FTIR data imply that CA prevents the $A\beta_{1-42}$ aggregation process, both in the aqueous and lipid membrane-like environments.

Beyond Aβ, CA demonstrated to have anti-aggregating properties on other amyloid proteins such as α-synuclein [53], lysozyme [49], and bovine serum albumin [54]. However, the detailed mechanism behind such activity is still unclear. According to Alam et al. (2017) [55], the CA-Aβ interactions occur through hydrogen bonding between the catechol moiety of CA and the peptide. Li and colleagues (2010) [56] revealed that the hydrogen bond forces might also occur between the phenolic hydroxyl groups of CA and the polar groups of amyloid proteins. Furthermore, molecular modeling analysis performed by other groups demonstrated that hydrophobic forces between the aromatic ring of CA and the hydrophobic amino acid residues of amyloid proteins, such as Aβ and α-synuclein, are also involved in the CA-protein interactions [47, 54, 56].

3.3.2.2. Aβ Fibril Disaggregation Study

The efficiency of CA in disrupting preformed $A\beta_{1-42}$ fibrils both in the presence and absence of DMPC:CHOL:SM:PS liposomes was investigated by ThT fluorescence measurements. Figure 3.10 displays the full sets of normalized ThT fluorescence kinetic traces. The percentages of CA-induced fibril disruption through the assay, both in the aqueous and lipid environment, are resumed in Table 3.5.

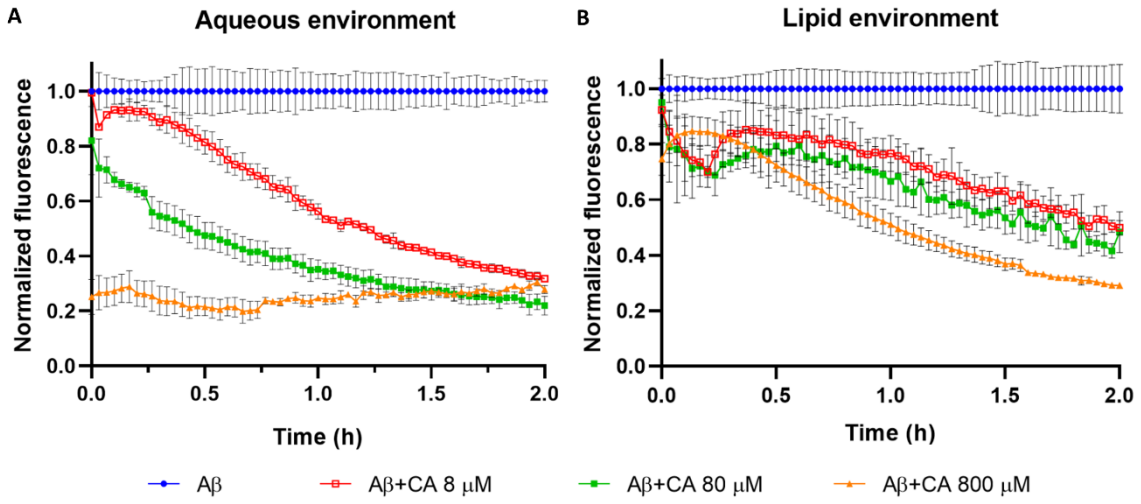

Figure 3.10. Normalized ThT fluorescence intensities of mature $A\beta_{1-42}$ fibrils (8 μM, blue circles) as a function of time (h) in the absence and presence of CA (8 μM, red squares; 80 μM, green square; 800 μM, orange triangles) in A) PBS and B) in the presence of liposomes (400 μM).

Table 3.5. Percentage of CA-induced $A\beta_{1-42}$ fibril disruption over time, determined from ThT data. ** p<0.01, ***p<0.001, and **** p<0.0001 indicate a statistical difference between the aqueous and lipid environments.

	$A\beta_{1-42}$ fibril disruption (%)					
Time (h)	**Aqueous environment**			**Lipid environment**		
	8 μM	**80 μM**	**800 μM**	**8 μM**	**80 μM**	**800 μM**
0	1 ± 1	18 ± 12	75 ± 6	8 ± 5	5 ± 9	25 ± 6 ****
1	42 ± 3	65 ± 4	75 ± 1	21 ± 7 **	31 ± 7 ****	48 ± 4 ****
2	67 ± 1	77 ± 3	72 ± 1	48 ± 8 **	58 ± 6 ***	71 ± 1

As revealed in Figure 3.10 A, the presence of CA dramatically suppressed the ThT fluorescence intensity in the aqueous medium in a concentration-dependent manner, suggesting the $A\beta_{1-42}$ fibril disaggregation. No significant variation ($p>0.05$) was observed in the ThT signal immediately upon the addition of CA at 8 μM ([C]/[P] of 1:1). However, as the incubation time increases, a significant decline in the ThT intensity is observed ($p<0.05$). As shown in Table 3.5, at the lowest concentration, the natural compound disrupted approximately 42% and 67% of the fibrils after 1 h and 2 h of incubation at 37 °C in the aqueous medium, respectively. A further increase in CA concentration to ten times ([C]/[P] of 10:1) yielded an additional decrease in the ThT signal ($p<0.05$). As displayed in Table 3.5, CA at 80 μM immediately reduced the fibrils' content by 18% after its addition. This CA's disaggregating activity increased over time ($p<0.05$), disrupting approximately 65% of the fibrils after 1 h of incubation at 37 °C and 77% after 2 h of incubation in the aqueous medium. Furthermore, the highest CA concentration (800 μM) prompted an abrupt reduction of the ThT signal ($p<0.001$) immediately upon its addition to $A\beta_{1-42}$ fibrils formed in the aqueous medium. As Table 3.5 reveals, CA reduced the content of fibrils by approximately 75% at the beginning of the assay. This activity remained constant over the experiment ($p>0.05$), disrupting about 75% and 72% of the fibrils after 1 h and 2 h of incubation at 37 °C, respectively. These results suggest that the CA's disaggregating activity at 800 μM is instantaneous and sustained. Overall, this finding reveals the ability of CA to disrupt mature fibrils in PBS in a concentration-dependent manner. As the concentration of CA increases, the faster the mature $A\beta_{1-42}$ fibrils disrupt. Epigallocatechin gallate, amentoflavone, and safranal are examples of other natural products that exhibit a dose-dependent disaggregating activity against amyloid fibrils in buffer solutions [47, 57, 58].

From Figure 3.10, it is also possible to observe that the capacity of CA to disaggregate mature fibrils was affected by the presence of the lipid membrane model. Following 2 h of incubation at 37 °C, the fibril disruption activity of CA at 8 and 80 μM was significantly lower in the lipid environment than in the aqueous one (Table 3.5). While CA at 8 μM lost approximately 30% ($p<0.01$) of its anti-amyloidogenic activity in the presence of membranes, the CA's fibril disaggregating activity at 80 μM decreased by around 25% ($p<0.001$). In turn, instead of being immediate, as observed in the aqueous medium (Figure 3.10 A), the CA's disaggregating activity at 800 μM in the membrane-like environment increased over time (Figure 3.10 B). While at the beginning of the assay, CA reduced approximately 25% of the amount of fibrils (Table 3.5), this value significantly increased to 48% after 1 h of incubation at 37 °C ($p<0.05$) and to 71% after 2 h of incubation ($p<0.05$).

At the end-point of the ThT binding assay (2 h), no significant difference was detected in the percentage of CA-induced fibril disruption between the two environments ($p>0.05$). Overall, the results imply that the CA-induced disaggregation of fibrils is modulated by the environment mimicked. Since CA has a moderate affinity for the lipid vesicles (Table 3.3), it is expected that as soon as CA is added to the fibrils in the presence of liposomes, there is a competitive interaction of this natural compound with the fibrils and the lipid vesicles. Therefore, as a result of CA-lipid membrane interactions, fewer molecules of CA are available in the aqueous phase to interact with the Aβ fibrils and induce their disruption, compared to the non-membrane-like environment. Similar conclusions were drawn by other groups. Vu et al. (2013) [59] revealed that the efficiency of dopamine in disrupting $A\beta_{1-40}$ and $A\beta_{1-42}$ fibrils depends on the environmental conditions, with the lipid composition of liposomes affecting directly the dopamine-induced disaggregation rate. Andrade et al. (2021) [60] also demonstrated that synthetic neuronal membranes compromise the VB12's ability to maintain the disaggregation rates of $A\beta_{1-42}$ fibrils over time.

To confirm the ability of CA in disaggregating $A\beta_{1-42}$ fibrils in the aqueous and lipid environments, the morphologies of $A\beta_{1-42}$ aggregates were examined by TEM in the presence or absence of the natural compound. When mature fibrils were incubated alone for 2 h, either in PBS or in the presence of DMPC:CHOL:SM:PS liposomes, fibrils revealed to be thin and long (Figure 3.11), with lengths ranging between 100 and 300 nm. Moreover, it is possible to observe that the finest fibrils are composed of rounded ring oligomers. These ring-like oligomers interact with each other either directly ring-to-ring or, more frequently, ring-on-ring with some shift. In this last event, oligomers overlap slightly, decreasing the fibril diameter [61]. A similar fibrils morphology was reported earlier by Selivanova et al. (2016) [62]. When $A\beta_{1-42}$ fibrils were incubated with CA for 2 h, numerous short, disintegrated fragments were detected, but no fibrils were observed, regardless of the simulated environment (Figure 3.11 B and D). This outcome is in concordance with ThT fluorescence results and validates the CA's ability to disrupt $A\beta_{1-42}$ fibrils in both environments.

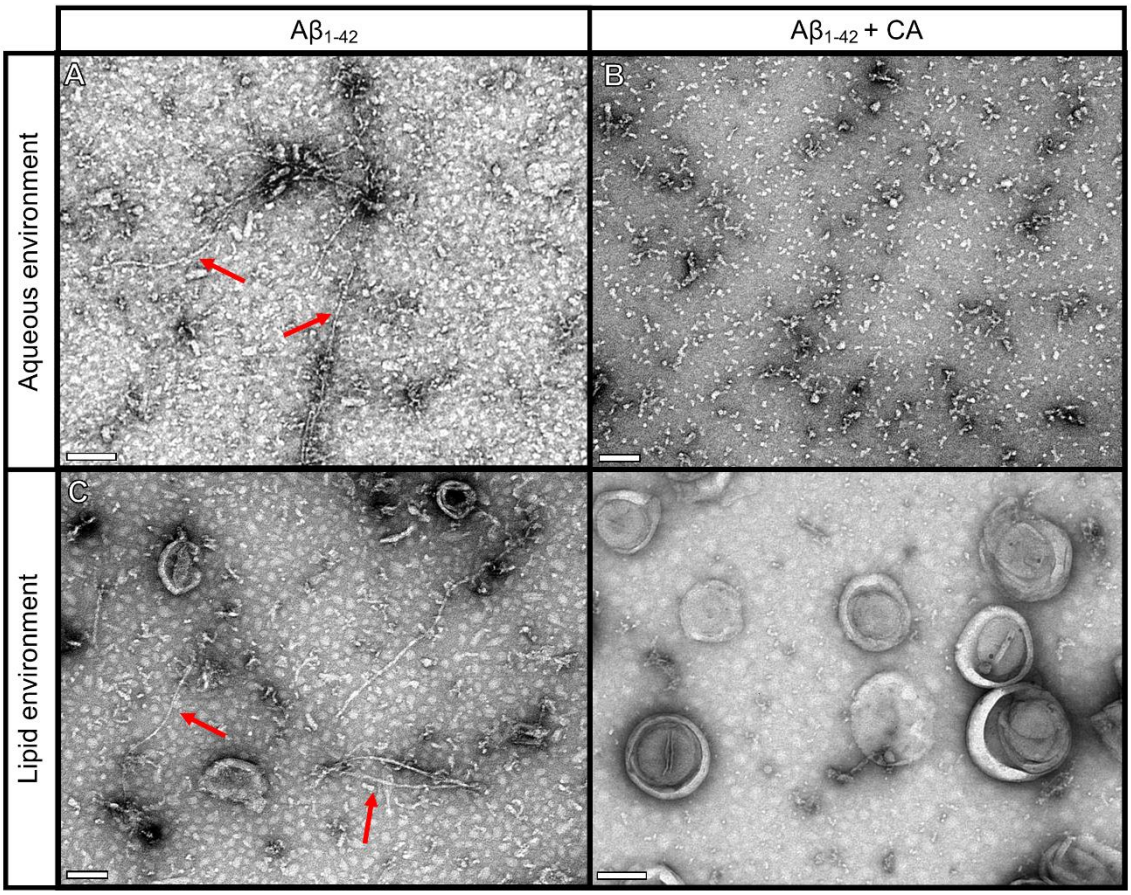

Figure 3.11. TEM images of $A\beta_{1-42}$ fibrils (8 μM) formed in the A) absence and presence of C) liposomes (400 μM). B) and D) represent the resulting morphologies of $A\beta_{1-42}$ after 2 h of incubation with CA (800 μM) at 37 °C, in the absence or presence of liposomes, respectively. Red arrows show $A\beta_{1-42}$ fibrils. Scale bars are 100 nm.

CD measurements were conducted to investigate the conformational changes of $A\beta_{1-42}$ fibrils upon incubation with CA for 2 h, both in the presence or absence of lipid vesicles. As shown in Figure 3.12, $A\beta_{1-42}$ fibrils formed in bulk solution and the presence of artificial lipid membranes formed β-sheet rich structures, as judged from the minimum at 218 nm. Aβ fibrils co-incubated with CA for 2 h in both media also displayed an absorption minimum at 218 nm, but this value was less than the control samples. Since the CD signal intensity is directly correlated with the β-sheet content [63], these results depict that CA reduces the number of β-sheet-rich structures present in the solution. These findings are in accordance with the ThT data and TEM images, thus corroborating the CA's ability to disrupt preformed $A\beta_{1-42}$ fibrils.

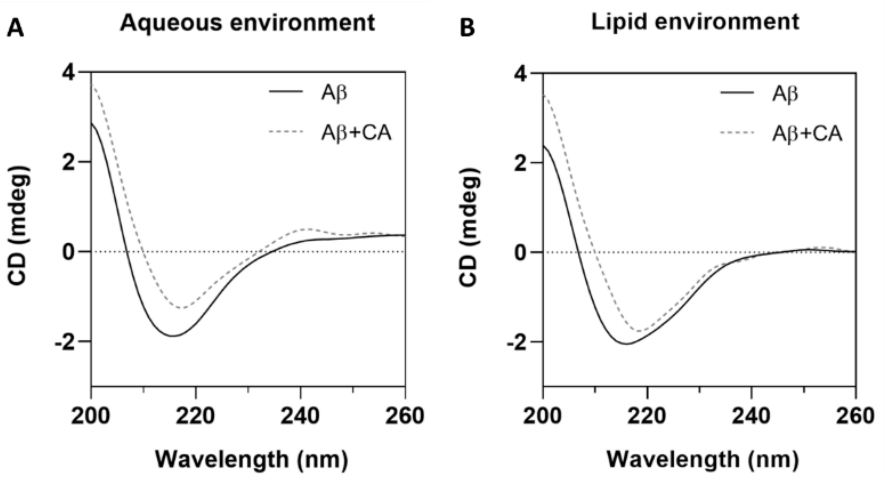

Figure 3.12. CD spectra of $A\beta_{1-42}$ fibrils (8 μM, solid black line) upon incubation with CA (800 μM, dashed gray line) in A) PBS and B) in the presence of liposomes (400 μM).

ATR-FTIR measurements were performed to quantify the secondary structural components of $A\beta_{1-42}$ fibrils upon incubation with CA for 2 h at 37 °C, both in the aqueous and lipid environment, and thus, validate the CA's ability to disaggregate mature fibrils. Figure 3.13 shows examples of ATR-FTIR spectra of $A\beta_{1-42}$ in the amide I region (1600-1700 cm^{-1}) incubated with or without CA, in PBS, or the presence or DMPC:CHOL:SM:PS LUVs. The content of the different protein secondary structures under each incubation condition was estimated by Fourier self-deconvolution followed by curve fitting. The quantitative analysis of the secondary structural components of $A\beta_{1-42}$ is summarized in Table 3.6.

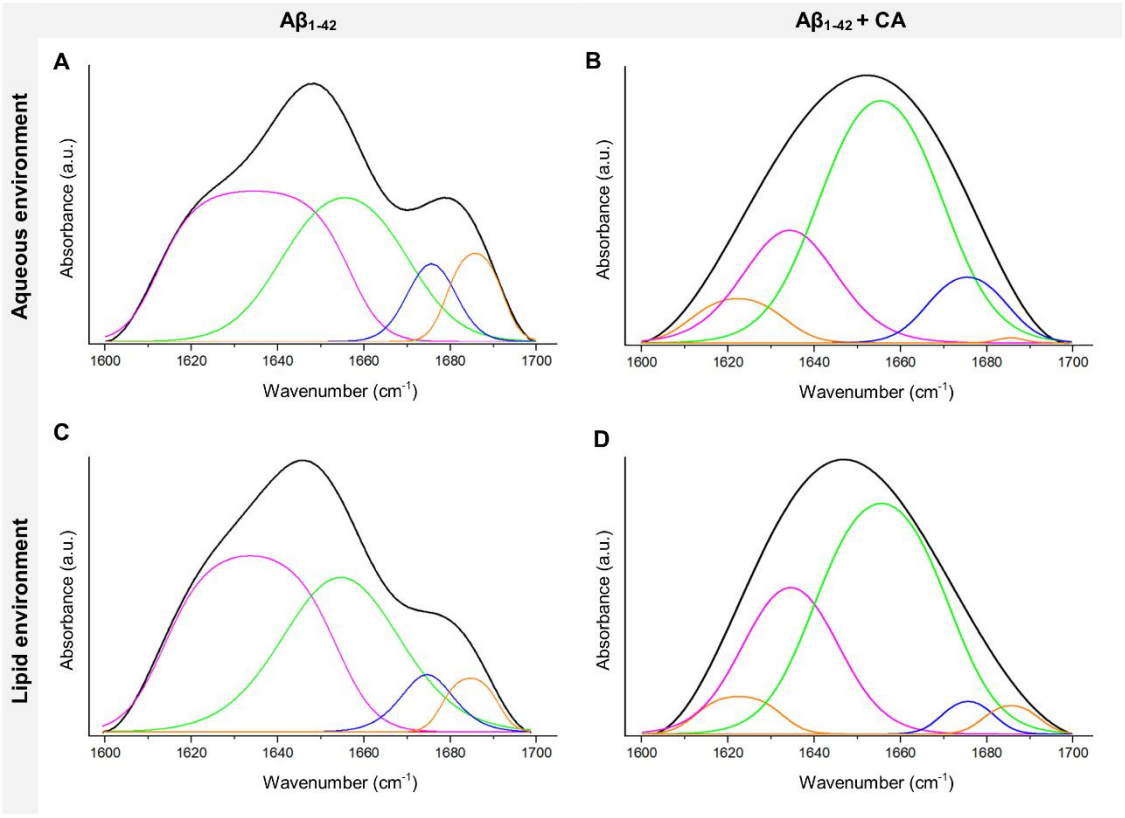

Figure 3.13. ATR-FTIR spectra of $A\beta_{1-42}$ fibrils (8μM) formed in A) PBS and C) in the presence of liposomes (400 μM). B) and D) indicate the ATR-FTIR spectra of $A\beta_{1-42}$ upon CA (800 μM) incubation with fibrils formed in aqueous and lipid environments, respectively. Antiparallel β-sheet, parallel β-sheet, α-helix, and β-turn structures are represented by orange, pink, green, and blue lines, respectively.

Table 3.6. Content of the secondary structures of $A\beta_{1-42}$ fibrils upon 2 h of incubation at 37 °C with and without CA, both in the aqueous and lipid environments, estimated from the Fourier self-deconvolution of ATR-FTIR spectra, followed by the curve fitting of amide I band. **p<0.01 and ****p<0.0001 indicate statistical differences between $A\beta_{1-42}$ in the absence and presence of CA.

	Aqueous environment		**Lipid environment**	
	$A\beta_{1-42}$	**$A\beta_{1-42}$ + CA**	**$A\beta_{1-42}$**	**$A\beta_{1-42}$ + CA**
Antiparallel β-sheet 1615-1627 cm^{-1}/1674-1695 cm^{-1}	5 ± 8	7 ± 1	3 ± 6	8 ± 3
Parallel β-sheet 1623-1641 cm^{-1}	41 ± 12	24 ± 2 **	58 ± 18	35 ± 5
α-helix 1648-1657 cm^{-1}	35 ± 3	60 ± 1 ****	26 ± 7	52 ± 7 **

β-turn 1662-1686 cm^{-1}	20 ± 11	9 ± 2	13 ± 9	4 ± 1

As shown in Table 3.6, $A\beta_{1-42}$ fibrils formed in bulk solution and the presence of artificial lipid membranes are mainly characterized by the parallel β-sheet conformation, the primary structural characteristic of amyloid fibrils [64]. Smaller percentages of α-helix, antiparallel β-sheet, and β-turn structures are also detected, suggesting the presence of some monomers and oligomers [65, 66]. The incubation of CA with mature fibrils formed both in the presence and absence of *in vitro* membranes modified the overall content of Aβ's secondary structures. In the aqueous medium, CA significantly increased the content of α-helix structures ($p<0.0001$) while decreasing the parallel β-sheet structures ($p<0.01$). Furthermore, the amount of antiparallel β-sheet and β-turn structures remained unchanged regardless of the environment ($p>0.05$). Comparable effects were observed in the lipid environment ($p>0.05$). These findings imply that CA promotes the conversion of parallel β-sheet, characteristic of amyloid fibrils, into α-helix structures, the main secondary conformation of Aβ monomers. Thus, in agreement with ThT fluorescence results, TEM images, and CD data, FTIR results suggest that CA disaggregates mature $A\beta_{1-42}$ fibrils in the aqueous as well as lipid media.

3.3.3. Influence of *in vitro* Neuronal Membranes on the Anti-Amyloidogenic Activity of Gallic Acid

The content of this section is published in: *Andrade, S., Loureiro, J.A. & Pereira, M.C. (2021). Influence of in vitro neuronal membranes on the anti-amyloidogenic activity of gallic acid: Implication for the therapy of Alzheimer's disease. Archives of Biochemistry and Biophysics, 711, 109022.*

3.3.3.1. Aβ Fibrillation Study

The effect of *in vitro* neuronal membranes on the inhibition of $A\beta_{1-42}$ fibrils formation by GA was investigated by a ThT fluorescence assay. ThT is a dye widely employed to detect and quantify amyloid fibrils *in vitro* since ThT exhibits enhanced fluorescence intensity upon binding to amyloid fibrils [50]. To this end, GA and the negatively charged liposomes comprised of DMPC:CHOL:SM:PS [65:15:10:10] (physicochemical characterization in Table

S3.2 of the Supplementary Material) were mixed and incubated at 37 °C for 30 min, with constant medium agitation. This critical stage allows GA to reach the partition equilibrium between the aqueous media and the lipid bilayer [51]. Then, $A\beta_{1-42}$ monomers were added to the GA-liposomes mixture at a [L]/[P] of 50:1 and a [C]/[P] of 100:1. Both the liposomes' composition and the [L]/[P] were carefully selected to simulate the characteristics of neuronal membranes [67, 68]. For comparison purposes, the GA's ability to prevent the $A\beta_{1-42}$ fibrillation was also assessed in a bulk solution by replacing the liposomes with PBS. Control samples in the absence of GA were also prepared.

Figure 3.14 illustrates the complete sets of normalized ThT fluorescence kinetic curves. The kinetic parameters of the ThT traces were estimated by combining the data with a nonlinear mathematic model (Equation 3.4). The estimated parameters were the lag phase time (t_{lag}, h), the time required to reach half of the maximum fluorescence signal ($t_{1/2}$, h), the fibril elongation rate (k, h^{-1}) and the maximum normalized fluorescence intensity (F_{max}). The results are shown in Table 3.7.

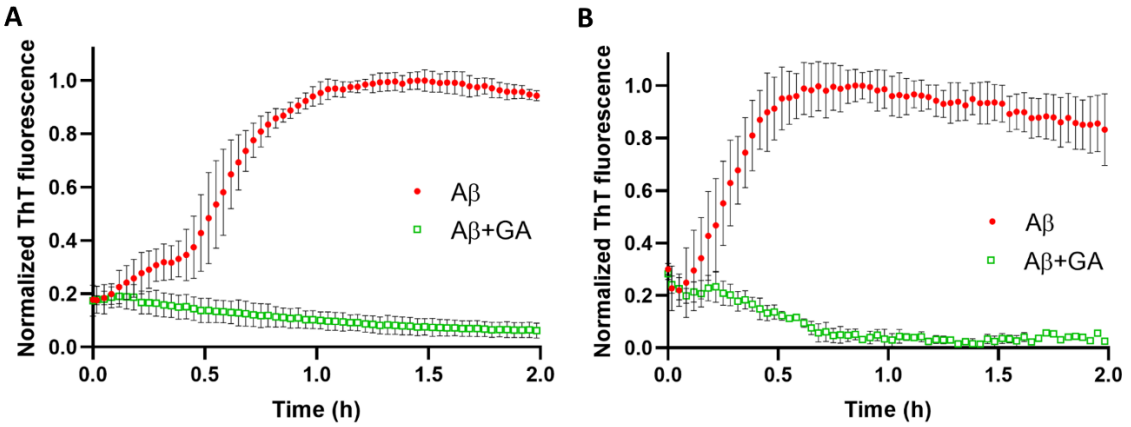

Figure 3.14. Normalized ThT fluorescence intensities of $A\beta_{1-42}$ (8 μM, red circles) as a function of time (h) upon incubation with gallic acid (GA) (800 μM, green squares) in A) PBS and in the B) presence of liposomes (400 μM) at 37 °C.

Table 3.7. Kinetic parameters of $A\beta_{1-42}$ aggregation in the presence and absence of liposomes, with and without GA, estimated by fitting Equation 3.4 to the ThT data. *p<0.05 indicates a statistical difference between $A\beta_{1-42}$ in buffered medium (PBS) and the presence of liposomes (cell membrane-like environment).

	Buffered medium		**Cell membrane-like environment**	
	$A\beta_{1-42}$	**$A\beta_{1-42}$ + GA**	**$A\beta_{1-42}$**	**$A\beta_{1-42}$ + GA**

t_{lag} (h)	0.39 ± 0.09	n.d.	0.17 ± 0.04 *	n.d.
$t_{1/2}$ (h)	0.58 ± 0.09	n.d.	0.33 ± 0.04 *	n.d.
k (h^{-1})	7.4 ± 1.4	n.d.	12.8 ± 2.1 *	n.d.
F_{max}	1.00 ± 0.02	n.d.	1.00 ± 0.06	n.d.

n.d. not determined

When $A\beta_{1-42}$ monomers were incubated in the absence of GA, both in the buffered medium and in the lipid membrane-like environment, the ThT data exhibited a well-defined sigmoidal trend, as observed previously [37]. The beginning of these kinetics is characterized by a low ThT fluorescence signal, suggesting the presence of few β-sheet structures (Figure 3.14). In this stage, known as lag phase, Aβ monomers self-assemble into oligomers. Aβ oligomers aggregate into fibril (elongation phase), which translates into an increase of the ThT intensity. ThT fluorescence signal reaches a plateau when most of Aβ has aggregated into fibrils, known as the stationary phase [69].

In the buffered medium, the kinetic of $A\beta_{1-42}$ aggregation in the absence of GA exhibits a t_{lag} of 0.39 ± 0.09 h (about 24 min) (Table 3.7). Nevertheless, in the presence of liposomes, $A\beta_{1-42}$ peptide starts to aggregate faster, as revealed by the significant reduction of the t_{lag} to 0.17 ± 0.04 h (about 10 min) ($p<0.05$). The *in vitro* neuronal membrane model also significantly reduced the $t_{1/2}$ to about half ($p<0.05$), resulting in a significant increase of the fibril elongation rate by a factor of approximately 1.7 ($p<0.05$). Comparable observations were found by Lindberg et al. (2017) using liposomes composed of 1,2-dioleoyl-sn-glycero-3-phospho-L-serine as a biomembrane model [48]. Collectively, these findings reinforce the catalytic role of biological membranes in the Aβ fibrillation process, in concordance with previous evidence [31, 70]. Despite the electrostatic repulsions between Aβ and the liposomes (zeta potential of -12 mV), both negatively charged at physiological pH [71], the affinity of the peptide to anionic phospholipids was also shown in previous studies [72, 73]. The electrostatic repulsions are apparently overcome by other highly favorable forces between the Aβ's hydrophobic tail and the lipid bilayer.

The addition of GA to the $A\beta_{1-42}$ monomers in the buffered medium significantly affected the time course of the Aβ fibrillation kinetic. As shown in Figure 3.14 A, the ThT fluorescence signal did not increase during the incubation period ($p>0.05$), implying that GA fully prevented the formation of $A\beta_{1-42}$ fibrils. Instead, GA induced a slight decrease of the ThT signal after 2 h of incubation in PBS ($p<0.0001$). This could be related to the GA's

capacity to disaggregate preexistent β-sheet structures in the tested samples. Previous evidence revealed that GA also inhibits the formation of amyloid fibrils by α-synuclein [35], insulin [72], lysozyme [74], and k-casein [75] in buffered media. Thus, it seems that GA displays a generic fibrillation inhibitory activity in bulk solutions of a vast array of amyloidogenic proteins.

Additionally, Figure 3.14 reveals that the presence of the neuronal membrane model did not affect the GA's ability to inhibit the $A\beta_{1-42}$ fibrillation. Similar to the buffered medium, GA also fully prevented the formation of fibrils in a cell membrane-like environment, as no increase in the ThT signal was observed ($p>0.05$). A plausible scenario for the comparable kinetic traces between the two tested environments is that GA interacts preferentially with $A\beta_{1-42}$ peptides than with the liposomes, allowing GA to exercise its anti-fibrillation activity. To validate this hypothesis, the interaction between GA and the lipid membranes was analyzed in terms of lipophilicity. This is an important property that defines the affinity of a drug for a lipid environment [76]. Thus, the GA's KP between the aqueous and lipid membrane phases was determined by derivative UV–Vis spectrophotometry. This is an alternative to the conventional techniques that use the water/octanol biphasic system. Beyond hydrophobic interactions, this methodology contemplates other forces, such as electrostatic, ion-dipole, and dipole-dipole forces, between ionized drugs and the phospholipids' heads [77]. In addition, applying the derivative reduces the liposomes' contribution, thus improving the band resolution [78]. Figure S3.2 in Supplementary Material exemplifies the main steps of the data processing to determine GA's KP. The KP and log D of GA are summarized in Table 3.8. The octanol/water partition coefficient (log P) of GA at pH 7.4 was predicted using the log P calculator from ChemAxon (Hungary) and is also shown in Table 3.8.

Table 3.8. KP and log D values of GA between the aqueous phase and the DMPC:CHOL:SM:PS liposomes at 37 °C. ¥ Prediction from log P calculator (ChemAxon) at pH 7.4.

KP	log D	log P ¥
401 ± 64	2.8 ± 0.1	0.71

As shown in Table 3.8, GA exhibits a KP value of 401 ± 64, which indicates a moderate affinity of the compound for the lipid membrane. These results imply that although some

molecules permeabilize the membrane, others remain in the aqueous phase. It is plausible that the GA's remaining molecules in the solution are enough to fully prevent the aggregation of $A\beta_{1-42}$.

Besides, as revealed in Table 3.8, the GA's log D (2.8 ± 0.1) is significantly higher than its log P (0.71). While log P reflects the lipophilicity for neutral molecules, log D describes the lipophilicity of ionizable drugs [79]. All GA molecules are negatively charged at physiological pH due to the deprotonation of the carboxyl group [80]. Hence, the discrepancy in the log values suggests that in addition to the hydrophobic forces, the negative charge of GA interacts with the lipid membrane through ion-dipole forces with the positively charged choline of the DMPC polar head. These results highlight the significance of using log D instead of log P in drug discovery and development, especially when working with ionizable molecules.

The effect of *in vitro* neuronal membranes on the inhibition of $A\beta_{1-42}$ fibrillation by GA was verified by TEM. This high-resolution imaging technique provides qualitative information about the morphology of amyloid fibrils and prefibrillar species [81]. Figure 3.15 shows the TEM pictures of $A\beta_{1-42}$ incubated in the absence and presence of GA for 4 h at 37 °C, both in the buffered medium and membrane-mimicking environment. The images confirmed the formation of long and thin fibrils when $A\beta_{1-42}$ was incubated without GA, regardless of the tested environment (Figure 3.15 A and B). However, when incubated with GA in the absence and presence of liposomes, $A\beta_{1-42}$ did not form fibrils, which agrees with the ThT assay. Instead, just short fragments are observed (Figure 3.15 C and D). In addition, there were no significant changes in the detected structures in the absence (Figure 3.15 C) and the presence of liposomes (Figure 3.15 D).

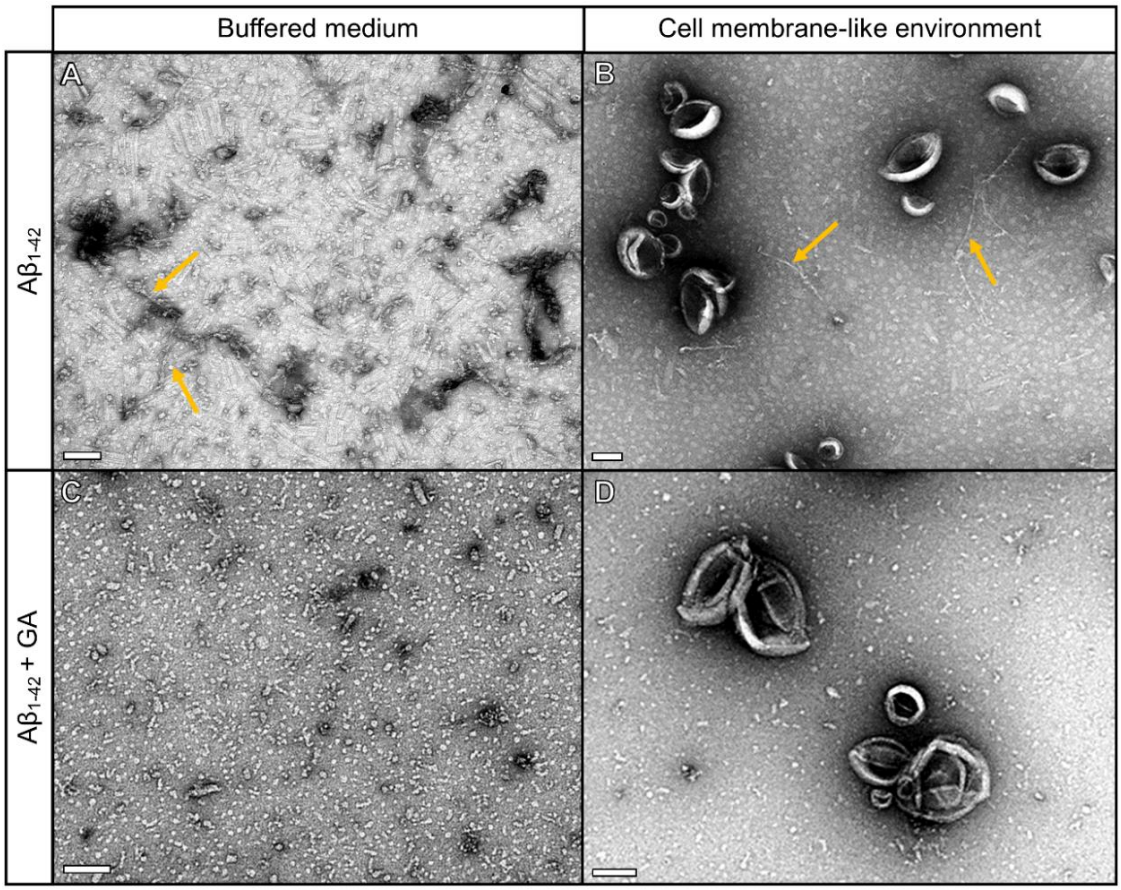

Figure 3.15. TEM images of $A\beta_{1-42}$ (8 μM) in A) PBS and B) in the presence of liposomes (400 μM). C) and D) correspond to $A\beta_{1-42}$ incubated with GA (800 μM) in the C) absence and D) presence of liposomes. Orange arrows signalize $A\beta_{1-42}$ fibrils. Scale bars correspond to 100 nm.

ATR-FTIR was employed to investigate the secondary structural changes of $A\beta_{1-42}$ upon the incubation with GA for 4 h, both in buffered media and in the cell membrane-like environment. This is one of the most frequently used techniques to assess the conformational changes of peptides and proteins [68]. Despite the recent studies pointing to GA as an Aβ aggregation inhibitor in bulk solutions, its effect on the secondary structure of Aβ is still unknown. Figure 3.16 shows the self-deconvoluted FTIR spectra of $A\beta_{1-42}$ in the amide I region (black line) - which is the more sensitive to conformational changes of Aβ - in the absence and presence of GA, both in aqueous and membrane-mimicking environments, after 4 h of incubation at 37 °C. The fitting subspectra represented by the orange, pink, green, and blue lines correspond to antiparallel β-sheet, parallel β-sheet, α-

helix, and β-turn structures, respectively. The secondary structure contents of $A\beta_{1-42}$ in the distinct tested conditions are given in Table 3.9.

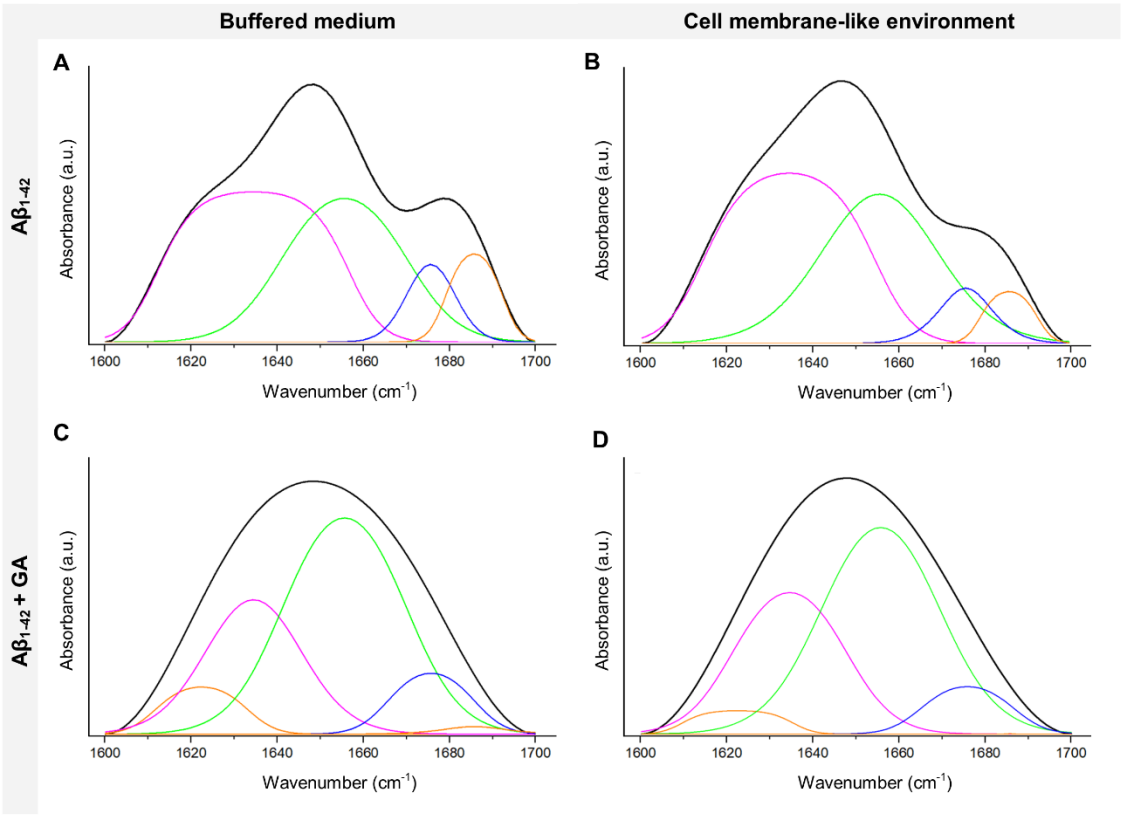

Figure 3.16. Self-deconvoluted ATR-FTIR spectra (black line) of $A\beta_{1-42}$ (8μM) incubated in A) PBS and B) in the presence of liposomes (400 μM) at 37 °C for 4 h. C) and D) indicate the ATR-FTIR spectra of $A\beta_{1-42}$ incubated with GA (800 μM) in the C) absence and D) presence of liposomes, respectively. Antiparallel β-sheet, parallel β-sheet, α-helix, and β-turn structures are represented by the orange, pink, green, and blue lines, respectively.

Table 3.9. Percentage of the secondary structure content of $A\beta_{1-42}$ (8 μM) in the absence and presence of GA (800 μM), with and without liposomes (400 μM), after 4 h of incubation at 37 °C. Results were obtained after Fourier self-deconvolution followed by curve fitting of the amide I region. *p<0.05 and **p<0.01 indicate statistical differences between $A\beta_{1-42}$ in the absence and presence of GA.

	Buffered medium		**Cell membrane-like environment**	
	$A\beta_{1-42}$	**$A\beta_{1-42}$ + GA**	**$A\beta_{1-42}$**	**$A\beta_{1-42}$ + GA**
Antiparallel β-sheet 1615-1627 cm^{-1}/1674-1695 cm^{-1}	7 ± 2	12 ± 3	7 ± 2	9 ± 6

Parallel β-sheet 1623-1641 cm^{-1}	47 ± 1	25 ± 3 **	48 ± 8	25 ± 9 *
α-helix 1648-1657 cm^{-1}	37 ± 2	54 ± 3 **	32 ± 6	55 ± 11 *
β-turn 1662-1686 cm^{-1}	10 ± 2	9 ± 2	13 ± 7	11 ± 3

After incubated in PBS for 4 h at 37 °C, $A\beta_{1-42}$ peptide is mainly characterized by a parallel β-sheet conformation (47%). As the conversion of secondary structures from α-helix to parallel β-sheet is related to the formation of amyloid fibrils [82], this result confirms the formation of $A\beta_{1-42}$ fibrils during the incubation period which is consistent with ThT and TEM data. Table 3.9 also reveals a smaller number of α-helix structures (37%), which indicates the presence of some $A\beta_{1-42}$ molecules in the native state. Moreover, the residual content of antiparallel β-sheet (7%) and β-turn structures (10%) points to the presence of few oligomers on the examined samples [83]. From Table 3.9, it is also found that the liposomes did not affect the secondary structures of $A\beta_{1-42}$ ($p>0.05$). The quantitative estimation of the Aβ secondary structures in the presence of lipid vesicles is in concordance with Dai et al. (2020) [84]. According to the authors, following 72 h of incubation in the presence of SM:CHOL, $A\beta_{1-42}$ peptide was also mostly characterized by a β-sheet conformation. In addition, about a third of the total content corresponds to α-helix structures, and a minor amount was identified as β-turn structures (10%) [85].

The presence of GA substantially modified the ATR-FTIR spectra of $A\beta_{1-42}$, regardless of the environment (Figure 3.16). In PBS, GA significantly decreased the amount of parallel β-sheet structures (from 47 to 25%) ($p<0.01$), while increasing the content of α-helix (from 37 to 54%) ($p<0.01$). These findings imply that GA prevented the α-helix → parallel β-sheet transition, thus validating the GA's ability to inhibit the Aβ fibrillation. In addition, Table 3.9 reveals that the number of oligomers remained unaffected, as no significant variations were detected in the content of antiparallel β-sheet and β-turn structures ($p>0.05$). The $A\beta_{1-42}$ ATR-FTIR spectrum upon incubation of GA in the cell membrane-like environment (Figure 3.16 D) showed similar features to that in bulk solution (Figure 3.16 C). Hence, a similar secondary structure content was noticed ($p>0.05$). These outcomes are in accordance with ThT measurements and TEM images, suggesting that the presence of lipid membranes does not affect the GA's ability to inhibit the formation of $A\beta_{1-42}$ fibrils.

3.3.3.2. Aβ Fibril Disaggregation Study

The effect of *in vitro* neuronal membranes on the disaggregation of mature $A\beta_{1-42}$ fibrils induced by GA was investigated by a ThT fluorescence assay. DMPC:CHOL:SM:PS liposomes were incubated with $A\beta_{1-42}$ monomers ([L]/[P] of 50:1) at 37 °C for 2 h, to allow the formation of fibrils. GA (800 μM) was then added to the fibrils (8 μM) in the cell membrane-like environment and incubated at 37 °C for 2 h, with constant medium agitation. For comparison purposes, the GA's ability to disrupt $A\beta_{1-42}$ fibrils was also evaluated in a bulk solution by replacing the liposomes with PBS. Control samples in the absence of GA were also prepared. The ThT fluorescence intensity of the samples was recorded each 2 min for 2 h. Figure 3.17 shows the full sets of normalized ThT fluorescence signals. The percentages of GA-induced $A\beta_{1-42}$ fibrils disaggregation as a function of time, both in the presence and absence of liposomes, are summarized in Table 3.10.

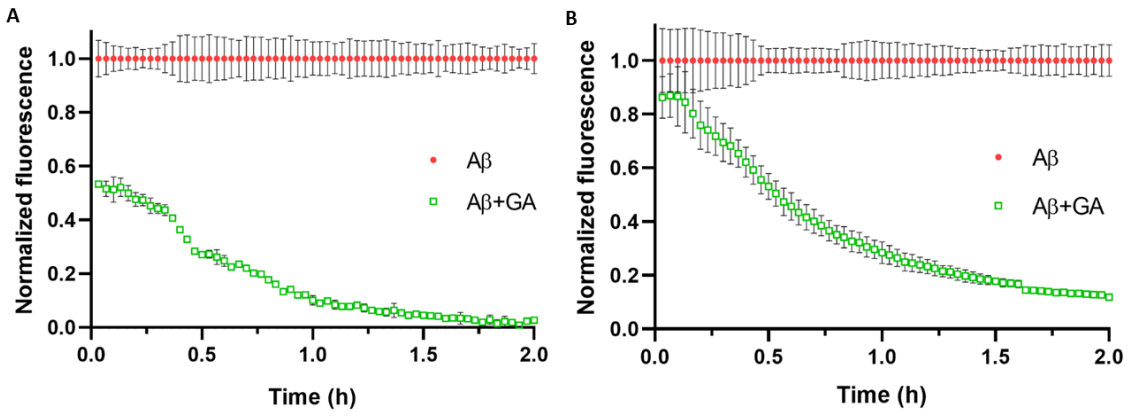

Figure 3.17. Normalized ThT fluorescence signal of mature $A\beta_{1-42}$ fibrils (8 μM, red circles) as a function of time (h) in A) PBS and B) in the presence of liposomes (400 μM). Green squares indicate the normalized ThT intensity of $A\beta_{1-42}$ fibrils upon 2 h of incubation with GA (800 μM) in A) PBS and B) in the presence of liposomes.

Table 3.10. Percentage of $A\beta_{1-42}$ fibrils disaggregation (8 μM) induced by GA (800 μM) as a function of time (h), in the presence and absence of liposomes (400 μM). *p<0.05, ***p<0.001 and ****p<0.0001 indicate statistically differences comparing with mature fibrils. #p< 0.05 and ##p<0.01 indicate a statistical difference between the buffered medium and the cell membrane-like environment.

Time (h)	Buffered medium	Cell membrane-like environment
0	47 ± 1 ***	14 ± 8 *, #

1	90 ± 1 ****	72 ± 4 ****, ##
2	97 ± 1 ****	88 ± 1 ***, #

Following the addition of GA to the preformed $A\beta_{1-42}$ fibrils in PBS, the ThT signal dropped in a time-dependent manner (Figure 3.17 A), suggesting the reduction in the number of fibrils over the incubation period. Immediately upon its addition to $A\beta_{1-42}$ fibrils, GA led to an immediate decrease of about 53% in the ThT fluorescence signal, implying the disruption of 47% of mature fibrils ($p<0.001$) (Table 3.10). After 1 h and 2 h of incubation at 37 °C, the GA's disaggregation rates in PBS increased to 90% ($p<0.0001$) and 97% ($p<0.0001$), respectively (Table 3.10). These results validate the GA's ability to fully disrupt mature $A\beta_{1-42}$ fibrils in a bulk solution. Ferulic acid, tannic acid, retinol, and retinoic acid are some examples of other naturally occurring products with similar destabilization kinetic profiles in buffered media [86, 87].

As revealed by Figure 3.17 B, adding GA to mature $A\beta_{1-42}$ fibrils in the presence of liposomes also significantly decreased the ThT fluorescence signal over time, implying that GA also acts as a potent disruptor of $A\beta_{1-42}$ fibrils in a cell membrane-mimicking environment. However, the presence of lipid membranes affected the rates of GA-induced fibrils disaggregation (Table 3.10). In fact, GA prompted the immediate disruption of 14% upon its addition to Aβ fibrils ($p<0.05$), which is significantly lower than the rate in buffered medium (47%) ($p<0.05$). Likewise, GA induced the disaggregation of 72% of $A\beta_{1-42}$ fibrils after 1 h of incubation ($p<0.0001$), which was around 18% lower than the rate observed in PBS ($p<0.01$). After 2 h of incubation, the number of disrupted fibrils increased to 88% ($p<0.001$), which is still 9% below the rate of GA-induced fibrils disaggregation in bulk solution ($p<0.05$). GA achieved a disaggregation rate similar to that obtained in PBS after 2h of incubation (99%) ($p>0.05$), after 4 h of incubation with $A\beta_{1-42}$ fibrils in the presence of lipid membranes (data not shown). Overall, these results indicate that lipid membranes modulate the GA-induced fibrils disruption. Comparable conclusions were proposed by Vu et al. (2013) by revealing that the dopamine's ability to disrupt $A\beta_{1-40}$ and $A\beta_{1-42}$ fibrils depends on the environment mimicked, with the lipid composition of liposomes modulating the dopamine's disaggregation rates [88].

A plausible explanation for the differences observed in the profiles of fibrils disaggregation kinetics induced by GA in the absence and presence of liposomes could be related to the interaction of the natural compound with the lipid bilayers. To validate this

theory, the GA's KP in the presence of mature $A\beta_{1-42}$ fibrils was evaluated by derivative UV–Vis spectrophotometry. To this end, liposomes and $A\beta_{1-42}$ fibrils were incubated for 30 min at 37 °C to allow the membrane-peptide interactions to be established. GA was then added to the previous solution, and its KP was determined. This is an important step that simulates a condition of AD treatment, where $A\beta_{1-42}$ fibrils are already formed when GA is administered. GA displays a KP value of 222 ± 61 in the presence of Aβ fibrils at 37 °C (log D = 2.6 ± 0.1), which indicates a moderate affinity of the compound for the lipid bilayer. These results suggest that some GA molecules permeabilize the membrane while others remain in the solution. It is thus conceivable that the lower rates of GA-induced fibrils disruption in a cell membrane-like environment are related to the partition of the compound to the membrane. Hence, fewer GA molecules are available in the aqueous phase to interact with the fibrils and induce their disaggregation. Furthermore, it is possible to notice a significant difference ($p<0.05$) between the GA's KP in the absence (401 ± 64) and in the presence of $A\beta_{1-42}$ fibrils (222 ± 61), thus suggesting that the fibrils affect the partition of GA into the membrane. As soon as GA is added to the fibrils in the presence of liposomes, it is expected that there is competitive interaction of the compound with the fibrils and the lipid vesicles. Thus, as a result of the GA-Aβ interactions, fewer molecules of GA are available from partitioning into the lipid membrane, which translates to lower KP values.

The fibrils disaggregation efficiency of GA in the absence and presence of liposomes was validated by TEM (Figure 3.18). This is the first visual observation of the GA's ability to disrupt mature Aβ fibrils. When $A\beta_{1-42}$ fibrils preformed in the buffered medium or lipid membrane-mimicking environment were incubated in the absence of GA for 2 h, thin and long fibrils as well as smaller aggregates were noticed (Figure 3.18 A and B). However, when GA was added to $A\beta_{1-42}$ fibrils in both environments and incubated for 2 h at 37 °C, no fibrils were observed (Figure 3.18 C and D). Instead, numerous short and fragmented structures were detected. These results reveal the GA's ability to disrupt mature Aβ fibrils, both in the presence and absence of lipid membranes, which agree with ThT fluorescence measurements.

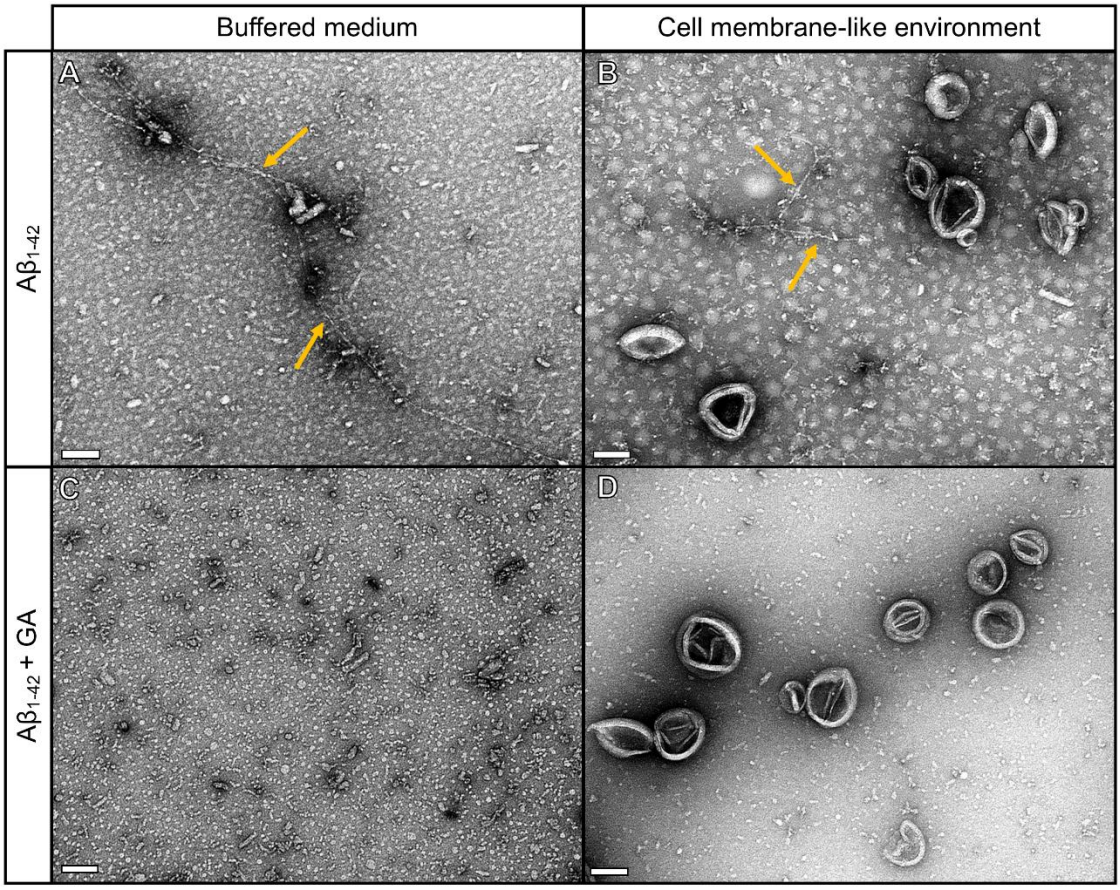

Figure 3.18. TEM images of mature $A\beta_{1-42}$ fibrils (8 μM) in A) PBS and B) in the presence of liposomes (400 μM). C) and D) correspond to Aβ fibrils incubated with GA (800 μM) in the C) absence and D) presence of liposomes. Orange arrows show Aβ fibrils. Scale bars correspond to 100 nm.

ATR-FTIR analysis was employed to identify possible variations on the secondary structure content of $A\beta_{1-42}$ fibrils upon 2 h of incubation with GA, both in buffered media and cell membrane-like environments. This is the first report investigating eventual secondary structural changes of mature $A\beta_{1-42}$ fibrils induced by GA. The self-deconvoluted FTIR spectra of $A\beta_{1-42}$ fibrils in the amide I region (black lines) in the absence and presence of GA, both in the aqueous and membrane-mimicking environments, after 2 h of incubation at 37 °C, are presented in Figure 3.19. The orange, pink, green, and blue subspectra denote antiparallel β-sheet, parallel β-sheet, α-helix, and β-turn structures, respectively. The secondary structure content of $A\beta_{1-42}$ in each simulated condition is provided in Table 3.11.

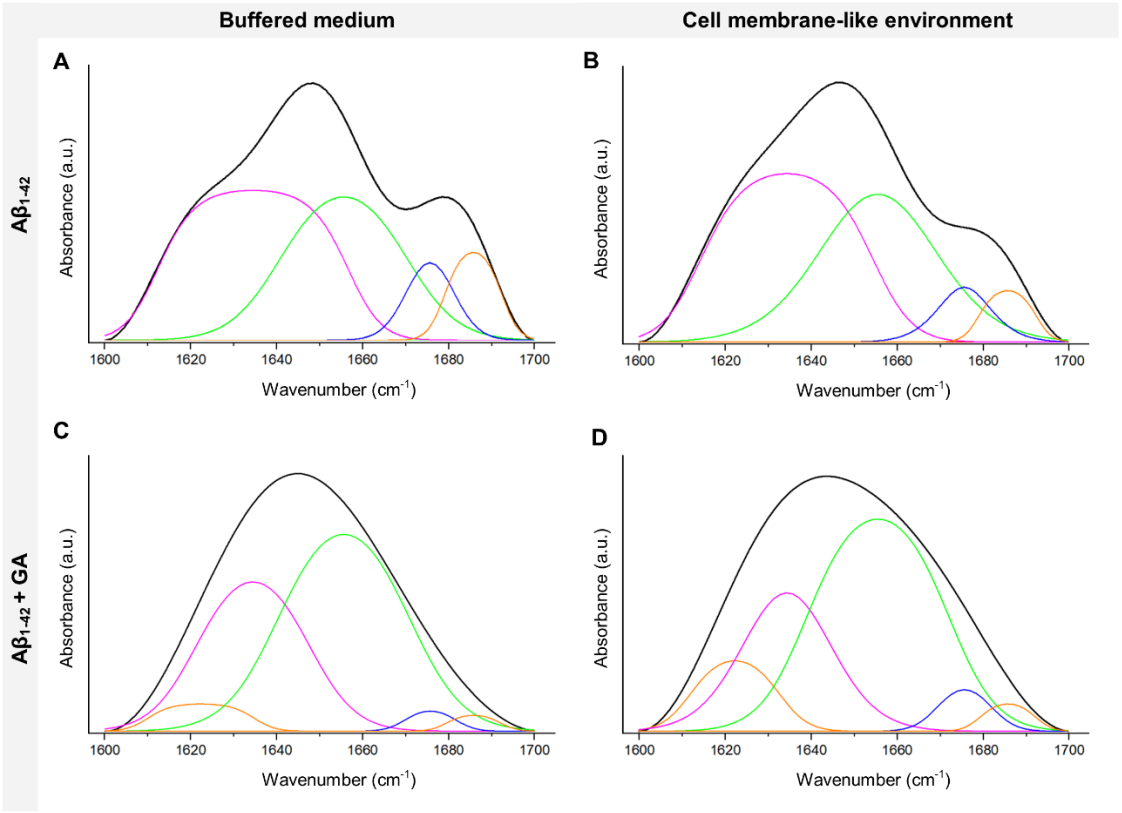

Figure 3.19. Fourier self-deconvoluted ATR-FTIR spectra of mature $A\beta_{1-42}$ fibrils (8μM) (black line) incubated in A) PBS and B) in the presence of liposomes (400 μM) at 37 °C for 2 h. C) and D) indicate the ATR-FTIR spectra of mature $A\beta_{1-42}$ fibrils incubated with GA (800 μM) in the C) absence and D) presence of liposomes, respectively. Orange, pink, green, and blue subspectra correspond to antiparallel β-sheet, parallel β-sheet, α-helix, and β-turn structures.

Table 3.11. Percentage of the secondary structure content of mature $A\beta_{1-42}$ fibrils (8 μM) in the absence and presence of GA (800 μM), with and without liposomes (400 μM), after 2 h of incubation at 37 °C. Results were obtained after Fourier self-deconvolution followed by curve fitting of the amide I region. *p<0.05, **p<0.01 and ***p<0.001 indicate statistical differences between $A\beta_{1-42}$ in the absence and presence of GA. # p<0.05 reveals statistical differences between $A\beta_{1-42}$ in the presence of GA in aqueous and cell membrane-like environments.

	Buffered medium		**Cell membrane-like environment**	
	$A\beta_{1-42}$	**$A\beta_{1-42}$ + GA**	**$A\beta_{1-42}$**	**$A\beta_{1-42}$ + GA**
Antiparallel β-sheet	5 ± 8	4 ± 3	3 ± 4	12 ± 2 *, #

1615-1627 cm^{-1}/1674-1695 cm^{-1}				
Parallel β-sheet 1623-1641 cm^{-1}	41 ± 12	35 ± 3 ***	58 ± 18	24 ± 4 *, #
α-helix 1648-1657 cm^{-1}	35 ± 3	59 ± 8 *	26 ± 7	57 ± 5 **
β-turn 1662-1686 cm^{-1}	20 ± 11	2 ± 2 *	13 ± 9	8 ± 3

As revealed in Table 3.11, when $A\beta_{1-42}$ was incubated without GA at 37 °C for 2 h, regardless of the mimicked environment, the major secondary conformation was found to be the parallel β-sheet, which confirms the formation of Aβ fibrils [89]. A smaller amount of antiparallel β-sheet, β-turn, and α-helix structures was also identified, implying the existence of some monomers and oligomers on the tested samples [90, 91], which is in accordance with TEM images.

From Figure 3.19, it is noticed that the 2 h incubation of GA with $A\beta_{1-42}$ fibrils significantly modified the self-deconvoluted ATR-FTIR spectra of the peptide as well as the fitting subspectra. As a result, significant variations in the secondary structure content of Aβ were observed (Table 3.11). In PBS, GA significantly decreased the content of parallel β-sheet from 41% to 35% ($p<0.001$) and β-turn structures from 20% to 2% ($p<0.05$) while increasing the content of α-helix structures from 35% to 59% ($p<0.05$). The amount of antiparallel β-sheet structures was not affected by GA ($p>0.05$). This indicates that GA promotes the disaggregation of $A\beta_{1-42}$ fibrils and oligomeric species, which are characterized by parallel β-sheet and β-turn conformations, respectively, into α-helical monomers. These results are consistent with ThT fluorescence data and TEM images, which validate the effective disassembly of $A\beta_{1-42}$ fibrils by GA in the buffered medium.

In agreement with the ThT assay, ATR-FTIR analysis corroborates the fact that lipid membranes modulate the disaggregation activity of GA. In the presence of liposomes, GA significantly decreased the parallel β-sheet content from 58% to 24% ($p<0.05$), which is about 11% lower than that observed in bulk solution ($p<0.05$) (Table 3.11). This reduction was accompanied by an increase in the number of α-helix structures from 26% to 57% ($p<0.01$), which is similar to that detected in the absence of liposomes ($p>0.05$). Furthermore, GA increased the content of antiparallel β-sheet structures from 3% to 12% ($p<0.05$) but did not affect the number of β-turns ($p>0.05$). This denotes that GA induces the disruption of $A\beta_{1-42}$ fibrils (parallel β-sheet) into monomers (α-helix) and oligomers

(antiparallel β-sheet) in the cell membrane-like environment, which agrees with TEM imaging.

3.3.4. Influence of *in vitro* Neuronal Membranes on the Anti-Amyloidogenic Activity of Vitamin B12

The content of this section is published in: *Andrade, S., Loureiro, J.A. & Pereira, M.C. (2021). Vitamin B12 Inhibits Aβ Fibrillation and Disaggregates Preformed Fibrils in the Presence of Synthetic Neuronal Membranes. ACS Chemical Neuroscience, 12(13), 2491-2502.*

3.3.4.1. Aβ Fibrillation Study

A ThT fluorescence assay combined with a mathematical model for the formation of amyloid fibrils was employed to investigate the VB12's ability to affect the aggregation process of $A\beta_{1-42}$ in both buffer solution and lipid membrane environment. This assay is an analytical method commonly used to determine the β-sheet content of Aβ peptide, a feature of fibrils, as ThT molecules exhibit enhanced fluorescence intensity upon binding to β-sheet structures [92].

For this purpose, monomeric $A\beta_{1-42}$ – whose state was confirmed by TEM (Figure S3.3 of the Supplementary Material) – and VB12 were incubated in PBS at 37 °C for 4 h at a [C]/[P] of 100:1 to ensure that any absence of activity is not related with low amounts of VB12. The relevance of the lipid environment on the anti-amyloidogenic activity of VB12 was assessed by incubating the vitamin with negatively charged LUVs composed of DMPC:CHOL:SM:PS (characterization of liposomes in Table S3.3 of the Supplementary Material) at 37 °C for 30 min. This crucial step allows the VB12's partition equilibrium to be reached, mimicking a disease prevention condition with early vitamin intake. Then, monomeric $A\beta_{1-42}$ was incubated with the mixture of VB12-membranes at a [L]/[P] of 50:1. Self-assembly kinetics of $A\beta_{1-42}$ in the absence of the natural compound were also recorded. Both lipid membrane composition and [L]/[P] were carefully selected to closely mimic the characteristics of lipid rafts domains according to the scientific evidence available [67, 85].

Figure 3.20 shows the full sets of normalized ThT fluorescence kinetic curves. All ThT data exhibit a typical sigmoidal curve, as observed previously [93]. The kinetic parameters of all ThT curves were calculated by fitting a nonlinear mathematic model (Equation 3.4) to

the kinetic traces. The parameters determined include the lag phase time (t_{lag}, h), the time at which 50% of the maximum fluorescence value is reached ($t_{1/2}$, h), the fibril elongation rate (k, h^{-1}), and the maximum normalized fluorescence [69]. The results are provided in Table 3.12.

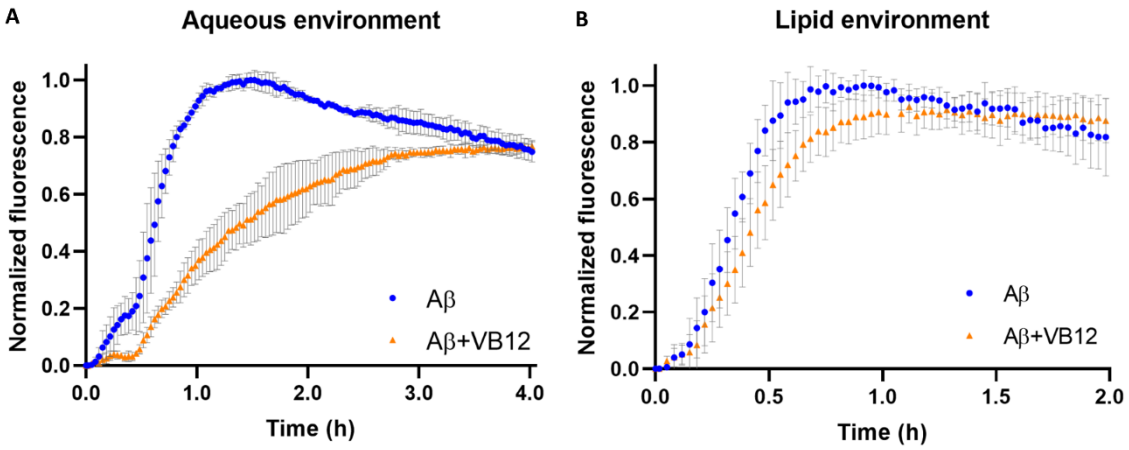

Figure 3.20. Normalized ThT fluorescence of $A\beta_{1-42}$ (8 µM, blue circle) as a function of time (h) upon incubation with vitamin B12 (VB12) (800 µM, orange triangle) in both A) PBS, and B) in the presence of liposomes (400 µM).

Table 3.12. Kinetic parameters were calculated by fitting Equation 3.4 to the ThT curves. *p<0.05, **p< 0.01 and ***p<0.001 indicate statistical differences between $A\beta_{1-42}$ in the absence and presence of VB12. #p<0.05 and ###p<0.001 indicate statistical differences between $A\beta_{1-42}$ in aqueous and lipid media.

	Aqueous environment		**Lipid environment**	
	$A\beta_{1-42}$	**$A\beta_{1-42}$ + VB12**	**$A\beta_{1-42}$**	**$A\beta_{1-42}$ + VB12**
t_{lag} (h)	0.40 ± 0.08	0.34 ± 0.02	0.17 ± 0.04 #	0.18 ± 0.06
$t_{1/2}$ (h)	0.61 ± 0.08	1.19 ± 0.21 *	0.33 ± 0.04 #	0.41 ± 0.06 **
k (h^{-1})	7.4 ± 1.9	2.5 ± 0.6 *	12.8 ± 2.1 #	7.2 ± 0.7 **
Max. fluorescence	1.00 ± 0.03	0.78 ± 0.01 ***	0.27 ± 0.02 ###	0.25 ± 0.02 *

At the beginning of each kinetic, a low ThT intensity is detected, indicating the residual presence of β-sheet structures in all studied conditions, which remained minimal in the first minutes (Figure 3.20). In this phase, known as lag phase, monomeric Aβ aggregates into small oligomers. The ThT signal then increases due to the rapid fibrils

growth (elongation phase), which reaches a plateau when most peptide has aggregated into fibrils (stationary phase) [67].

In PBS solution, $A\beta_{1-42}$ fibrillation kinetic has a t_{lag} of 0.40 ± 0.08 h (approximately 24 min) (Table 3.12). However, in the lipid environment, Aβ starts to self-assemble faster as suggested by the significant decrease of the t_{lag} to 0.17 ± 0.04 h (approximately 10 min) ($p<0.05$). The presence of synthetic neuronal membranes also prompted a significant reduction in the reaction halftimes ($t_{1/2}$) by a factor of approximately 2 ($p<0.05$), resulting in a significantly higher fibril elongation rate ($p<0.05$). Similar results were observed by Lindberg et al. (2017) using negatively charged 1,2-dioleoyl-sn-glycero-3-phospho-L-serine LUVs as membrane model [94]. In addition, the maximum ThT fluorescence intensity of $A\beta_{1-42}$ in the presence of LUVs was reduced by around 73% compared to aqueous fibrils ($p<0.001$). This is due to the competitive binding of ThT molecules (positively charged) with liposomes and Aβ, both negatively charged [31].

Together, these results imply that lipid membranes catalyze the $A\beta_{1-42}$ aggregation process by providing a distinct environment than an aqueous medium for the fibrils' growth, agreeing with previous experimental findings [95, 96]. Despite the electrostatic repulsions between Aβ (net charge of −2.8 at pH 7.4) and negatively charged liposomes (PS has a net charge of -1), the affinity of the peptide to anionic lipids was previously described [71]. Thus, it seems that the electrostatic repulsions are overcome by other highly favorable interactions between the hydrophobic tail of Aβ and the core of the bilayer.

The presence of VB12 significantly modified the time course of $A\beta_{1-42}$ fibrillation kinetics, both in the aqueous and lipid environments (Figure 3.20). When $A\beta_{1-42}$ was incubated with VB12 in the absence of lipid vesicles, no significant differences were identified in the t_{lag} compared to the respective control (Table 3.12) ($p>0.05$), indicating that the vitamin does not affect the transition of Aβ monomers to oligomers. However, VB12 significantly affected the elongation rate by reducing it by 3 times ($p<0.05$). As a result, the time required for 50% of the maximum fluorescence intensity to be achieved has doubled ($p<0.05$), thus suggesting that VB12 slows the transition from Aβ oligomers to mature fibrils. Moreover, the natural compound also reduced the maximum fluorescence intensity by around 22% ($p<0.001$). As the ThT fluorescence is directly proportional to the fibrils content [72], this data indicates that VB12 is also able to reduce the amount of Aβ fibrils formed. This observation is consistent with a previous study reported by Allam and colleagues (2017) [35] that showed the inhibitory effect of VB12 (50 μM) on $A\beta_{1-42}$

fibrillization (100 μM) in sodium phosphate buffer (37 °C, pH 7.4). However, it should be noted that other factors have been associated with the reduction of the ThT fluorescence intensity. Recent reports have shown that amyloid fibrils with distinct morphologies [97] and conformations [48, 98] may possess distinct binding modes, resulting in different ThT fluorescence intensities. Moreover, the presence of other compounds may modulate the ThT signal either by fluorescence quenching [99] or by binding to the fibrils' surface, which may affect the ability of ThT to bind to amyloid fibrils [100]. Therefore, ATR-FTIR experiments will be crucial to validate the VB12's ability to reduce the Aβ fibrils content.

VB12 in the presence of lipid vesicles showed a comparable t_{lag} value of 0.18 ± 0.06 h (approximately 11 min) to that observed in the absence of the natural compound 0.17 ± 0.04 h (approximately 10 min) (Table 3.12) ($p>0.05$). Thus, similarly to what was observed in the aqueous medium, also in the lipid environment, VB12 does not affect the transition time of Aβ monomers to oligomers. However, the incubation of VB12 with synthetic neuronal membranes significantly affected the remaining kinetic parameters. Although less pronounced compared to the aqueous environment, the vitamin also significantly reduced the elongation rate by half in the lipid environment ($p<0.01$). This suggests that the elongation phase was significantly delayed compared to the time course curve observed in the absence of VB12, as reveals the increase of the $t_{1/2}$ value (Table 3.12) ($p<0.01$). In addition, although to a lesser extent than the aqueous medium, VB12 decreased the intensity of the overall ThT signal to 92% of the control signal ($p<0.05$), indicating a reduction of the Aβ fibril content.

Taken together, our findings demonstrate that the overall ability of VB12 to inhibit $A\beta_{1-42}$ fibrillization was weakened in the presence of the lipid environment. Even so, the natural product was able to slow down the transition from Aβ oligomers to mature fibrils and reduce the extent of fibrils formed. A plausible scenario is that VB12 may not be fully available to inhibit the $A\beta_{1-42}$ aggregation efficiently. Hence, the interaction between VB12 and the lipid vesicles was evaluated in terms of the vitamin's lipophilicity. The KP of VB12 between the lipid and aqueous phases was determined by derivative UV–Vis spectrophotometry. Due to the amphiphilic structure of the phospholipids, the liposome/aqueous system mimics electrostatic interactions between charged molecules and the phospholipids polar head, which are not considered in the octanol/water system. Besides, this technique removes the background signal produced by the liposomes' light scattering, improving the band resolution. Figure S3.4 (Supplementary Material) illustrates,

as an example, the steps involved in data processing to obtain the VB12's KP. The results are summarized in Table 3.13 as KP and log D. The theoretical octanol/water partition coefficient (log P) of VB12 (37 °C, pH 7.4) was predicted by MarvinSketch calculator (ChemAxon, Hungary) and is also shown in Table 3.13.

Table 3.13. VB12's KP and respective log D between liposomes and the aqueous phase. Log P (octanol:water) prediction from MarvinSketch calculator (ChemAxon) is also presented.

KP	log D	log P
2169 ± 84	3.56 ± 0.02	-3.24

By presenting a KP value of 2169 ± 84 at 37 °C, Table 3.13 suggests that VB12 has a high affinity for the lipid membrane, partitioning from the aqueous to de lipid phase. Consequently, the amount of VB12 that would inhibit the Aβ fibrillation in solution is reduced, leaving the peptide free to aggregate. Similar conclusions were recently proposed by Beasley et al. (2019) [101]. The authors investigated the curcumin's ability to inhibit the fibrils formation of huntingtin (htt), a protein associated with the onset of Huntingtin's disease, in both aqueous and lipid environments. The presence of lipid membranes prevented curcumin from inhibiting htt fibrils formation also due to the imprisonment of the natural product into the lipid vesicles. In line, Matsuzaki et al. (2007) [102] examined the mechanism of the Aβ fibrillization inhibitory activity of four compounds - nordihydroguaiaretic acid (NDGA), rifampicin (RIF), tannic acid (TA) and quercetin (QUE) - in the presence of GM1-containing raft-like liposomes. To this end, the authors investigated the binding of Aβ1−40 to GM1 liposomes in the presence of the inhibitors and revealed that NDGA and RIF bound to lipid membranes, which partially prevented the binding of Aβ to the liposomes. Regarding QUE and TA, the group related their fibrillization inhibitory activity to their ability to interact with the peptide in solution since the compounds did not affect the binding of Aβ to the membranes.

Moreover, the detailed examination of Table 3.13 reveals a significant difference between the theoretical (log P) and experimental (log D) VB12's partition coefficients. This discrepancy can be due to the different interactions evaluated by the octanol:water and lipid:aqueous systems. While the first system only considers neutral molecules, simulating only hydrophobic interactions, the lipid:aqueous model evaluates the partition of neutral

and ionized molecules, contemplating both hydrophobic and electrostatic interactions. Thus, the higher experimental log D value reveals the existence of other forces beyond the hydrophobic ones, such as ion-dipole and electrostatic interactions, between the vitamin and the lipid vesicles. Since 99% of VB12's molecules are positively charged at pH 7.4 [3], the cationic species are expected to interact with the negatively charged phospholipid – PS – and with the negative charge of the DMPC polar head.

TEM imaging was performed to confirm the formation of $A\beta_{1-42}$ fibrils and compare the resulting morphological features in the absence and presence of VB12 in both aqueous and lipid environments (Figure 3.21). TEM images confirmed the formation of $A\beta_{1-42}$ fibrils in the presence and absence of VB12, both in the presence and absence of DMPC:CHOL:SM:PS lipid vesicles. After the incubation time of 4 h, no significant differences in the fibrils' length and thickness were observed between the samples, revealing thin fibrils with lengths ranging between approximately 100 to 200 nm.

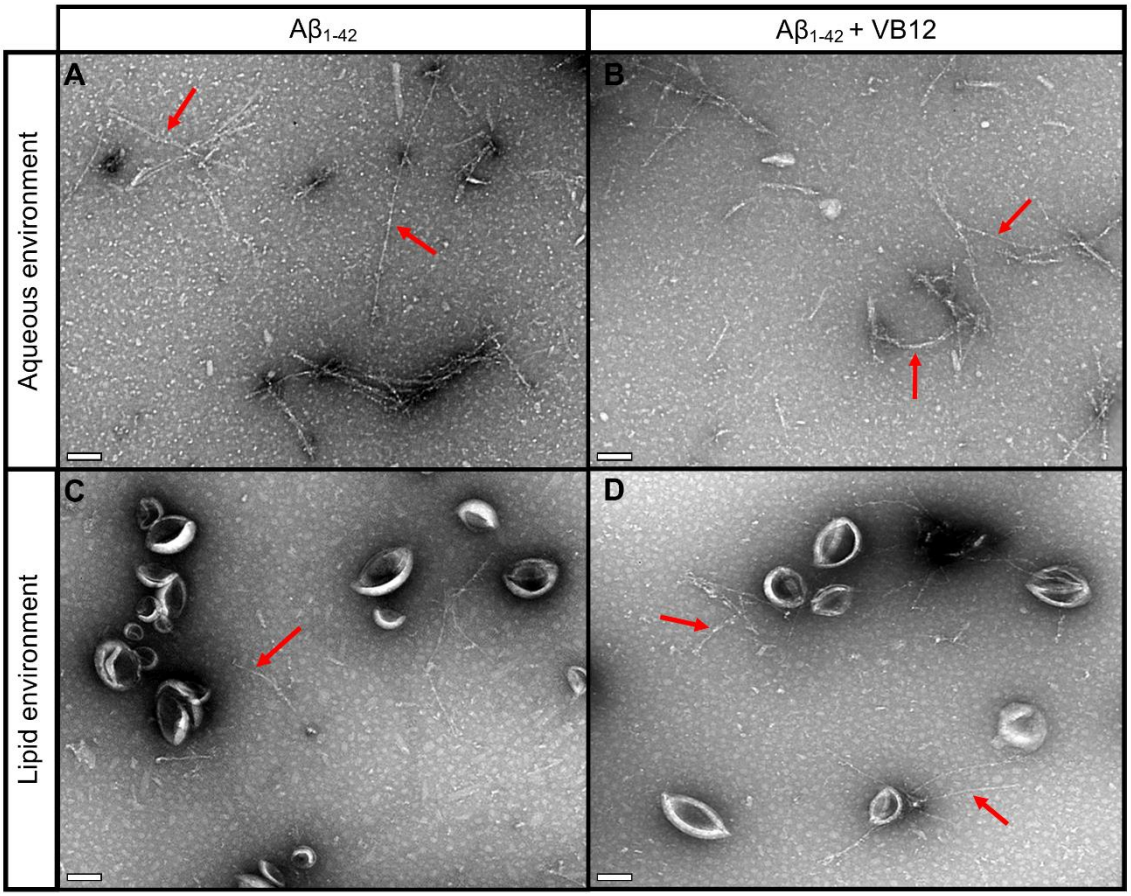

Figure 3.21. Negatively stained TEM images of A) $A\beta_{1-42}$ (8 μM) and B) $A\beta_{1-42}$ after incubation with VB12 (800 μM) in PBS. $A\beta_{1-42}$ incubated with liposomes (400 μM) in C)

absence and D) presence of VB12. Red arrows indicate $A\beta_{1-42}$ fibrils. Scale bars indicate 100 nm.

The secondary structure of $A\beta_{1-42}$ upon incubation with VB12, both in the presence and absence of lipid vesicles, was monitored by ATR-FTIR. In peptides and proteins, the amide I region (1600-1700 cm^{-1}) is assigned to the C=O stretching vibrations of the bounds. It is the most sensitive spectral region to protein secondary structures, distinguishing between the various conformations [103]. Figure 3.22 shows examples of self-deconvoluted spectra (black line) and fitting subspectra of the amide I band of $A\beta_{1-42}$ incubated with VB12, both in aqueous and lipid environments. The orange, pink, green, and blue lines represent antiparallel β-sheet, parallel β-sheet α-helix, and β-turn structures, respectively. The distribution of the different secondary structural components of $A\beta_{1-42}$ under each incubation condition is summarized in Table 3.14.

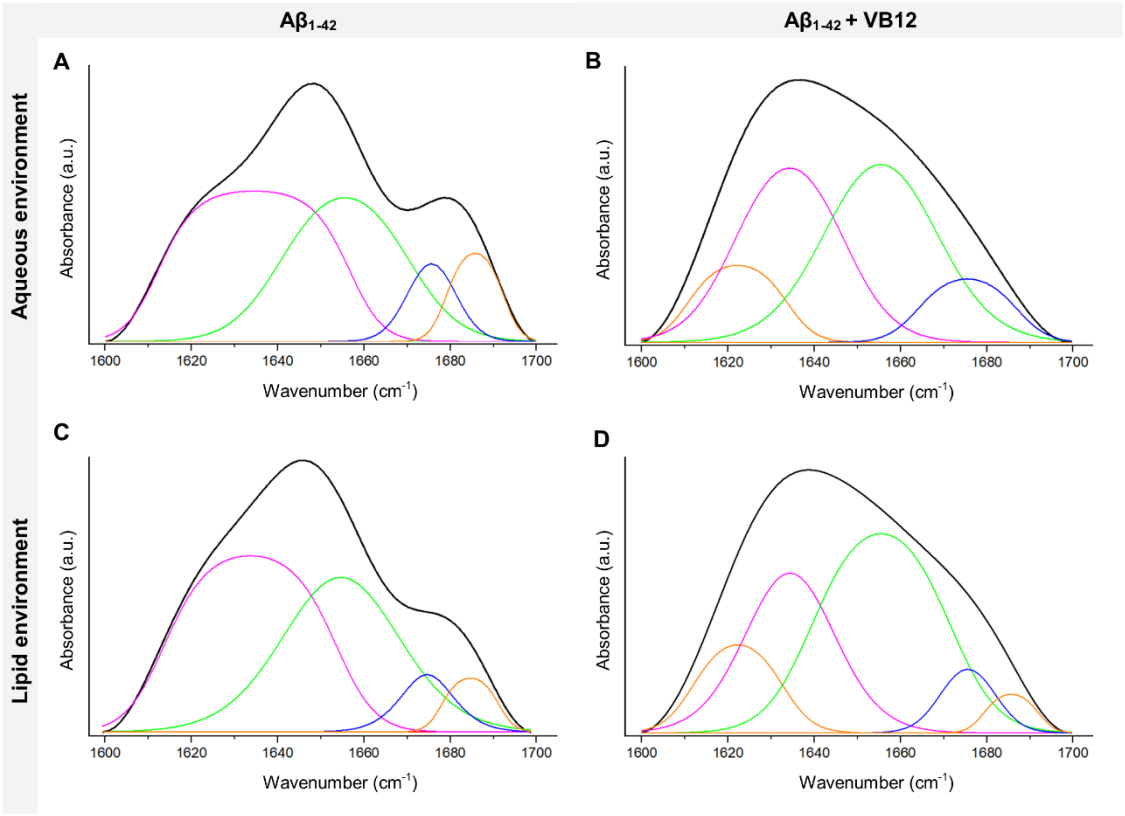

Figure 3.22. ATR-FTIR spectra of $A\beta_{1-42}$ (8 μM) incubated in the A) absence or B) presence of VB12 (800 μM) in PBS for 4h. C) and D) indicate ATR-FTIR spectra of $A\beta_{1-42}$ incubated with liposomes (400 μM) in the absence and presence of VB12 for 4 h, respectively. Black

lines represent the obtained spectra. Orange, pink, green, and blue lines represent antiparallel β-sheet, parallel β-sheet, α-helix, and β-turn structures, respectively.

Table 3.14. Quantitative estimation of the secondary structures of $A\beta_{1-42}$ upon incubation with VB12 in both aqueous and lipid media, obtained after Fourier self-deconvolution and curve fitting of amide I band. *p<0.05 indicates a statistical difference between $A\beta_{1-42}$ in the absence and presence of VB12.

	Aqueous environment		**Lipid environment**	
	$A\beta_{1-42}$	**$A\beta_{1-42}$ + VB12**	**$A\beta_{1-42}$**	**$A\beta_{1-42}$ + VB12**
Antiparallel β-sheet 1615-1627 cm^{-1}/1674-1695 cm^{-1}	7 ± 1	14 ± 2 *	7 ± 4	18 ± 2 *
Parallel β-sheet 1623-1641 cm^{-1}	47 ± 1	25 ± 14 *	48 ± 8	22 ± 10 **
α-helix 1648-1657 cm^{-1}	37 ± 2	41 ± 1 *	32 ± 6	45 ± 4 *
β-turn 1662-1686 cm^{-1}	10 ± 2	19 ± 12	13 ± 7	16 ± 8

As shown in Table 3.14, $A\beta_{1-42}$ molecules incubated for 4 h at 37 °C in PBS were mainly characterized by a parallel β-sheet conformation (47%), the primary structural characteristic of amyloid fibrils [104]. A smaller number of α-helix structures (37%) was detected, which are indicators of monomeric peptide forms [105]. Besides, the low content of antiparallel β-sheet (7%) and β-turn structures (10%) suggests the presence of few oligomers in the tested samples [84]. This finding is in good agreement with Dai's work (2020) [92]. The fibrillation process of $A\beta_{1-42}$ in the presence of DMPC:CHOL:SM:PS LUVs did not induce significant differences in the secondary structures compared to the fibrils formed in solution ($p>0.05$), which agrees with previous reports [85].

The incubation of $A\beta_{1-42}$ monomers with VB12 affected the secondary structure content of $A\beta_{1-42}$, both in the aqueous and lipid environments. As suggested in Table 3.14, adding VB12 significantly reduced the content of parallel β-sheets from 47% to 25% and from 48% to 22% in aqueous and lipid media, respectively ($p<0.05$), suggesting the presence of fewer fibrils in the samples. CD measurements performed by Alam and colleagues (2017) also showed that aggregates formed in the presence of VB12 contain fewer β-sheet structures [106]. In turn, the content of α-helix structures significantly increased from 37% to 41% in the aqueous medium and from 32% to 45% in the lipid one

(p<0.05), implying the presence of more Aβ monomers upon the addition of VB12. The amount of antiparallel β-sheet structures also significantly increased in both environments, from 7% to 14% in the aqueous medium and from 7% to 18% in the lipid environment (p<0.05). This finding implies that VB12 also increases the content of oligomers. Overall, these outcomes denote that VB12 prevents fibrils formation, which is consistent with ThT fluorescence experiments.

3.3.4.2. Aβ Fibril Disaggregation Study

The VB12's ability to disaggregate mature $A\beta_{1-42}$ fibrils in both PBS solution and lipid medium was evaluated by a ThT fluorescence assay. For this purpose, $A\beta_{1-42}$ monomers (10 μM) were incubated in the presence and absence of DMPC:CHOL:SM:PS LUVs (500 μM) ([L]/[P] of 50:1) at 37 °C for 2 h to produce mature fibrils. VB12 (800 μM) was then incubated with $A\beta_{1-42}$ fibrils (8 μM) ([C]/[P] of 100:1) at 37 °C for 2 h. ThT fluorescence intensities of these samples were recorded each 2 min. Controls were also prepared and subtracted. Figure 3.23 displays the full set of normalized ThT fluorescence kinetic traces.

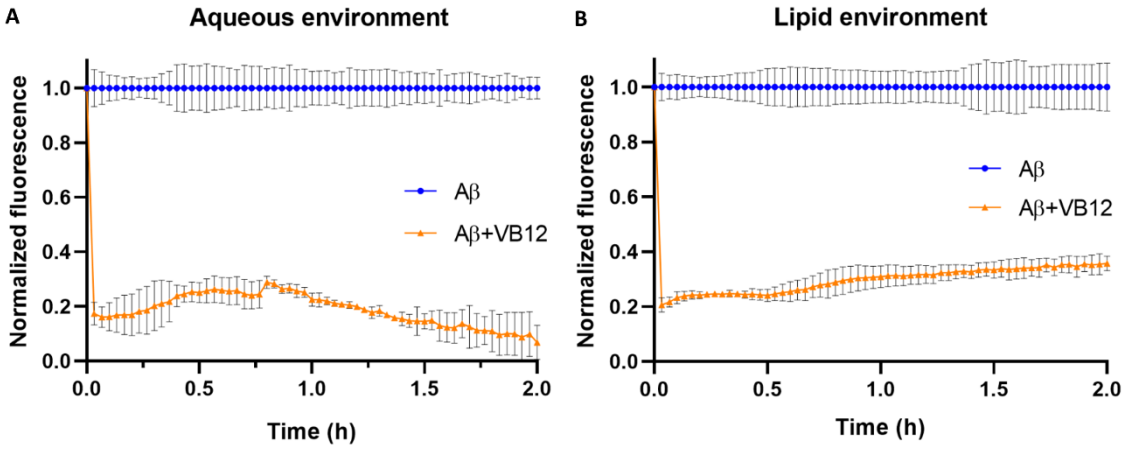

Figure 3.23. Normalized ThT fluorescence of preformed $A\beta_{1-42}$ fibrils (8 μM, blue circles) as a function of time (h) upon incubation with VB12 (800 μM, orange triangles) in both A) PBS and B) in the presence of liposomes (400 μM).

As shown in Figure 3.23, the addition of VB12 at the completion of the fibrillation reaction led to an immediate decrease in the ThT fluorescence signal compared with the control (P<0.05), both in aqueous and lipid environments. This reveals the ability of VB12 to disaggregate preformed $A\beta_{1-42}$ fibrils immediately. Safranal, amentoflavone, and EGCG

are examples of other natural compounds with the capacity to instantaneously disrupt existing fibrils in solution [48, 107, 108]. The percentages of Aβ fibrils disaggregation by B12 over time, both in aqueous and lipid media, are summarized in Table 3.15.

Table 3.15. Percentage of $A\beta_{1-42}$ fibrils disaggregation upon incubation with VB12 for 2h at 37 °C, determined from ThT data. ** p< 0.01 and *** p<0.001 indicate statistical differences compared with the beginning of the experiment. #p< 0.05 and ##p<0.01 indicate statistical differences between the aqueous and lipid media.

	Fibrils disaggregation (%)	
Time (h)	**Aqueous environment**	**Lipid environment**
0	83 ± 4	79 ± 3
1	78 ± 3	69 ± 4 **, #
2	92 ± 8	64 ± 3 ***, ##

As shown in Table 3.15, VB12 immediately disrupted Aβ fibrils in the non-membrane environment by reducing by approximately 83% the content of fibrils. This ability remained constant throughout the experiment (p>0.05), disaggregating about 92% of the fibrils after 2 h of incubation at 37 °C. VB12 induced a similar effect in the presence of lipid vesicles compared to the aqueous environment (p>0.05) by promptly reducing the fibril content by 79%. However, synthetic neuronal membranes seem to compromise the VB12's ability to maintain the disaggregation rates over time since a slight increase in the ThT fluorescence intensities is observed throughout the assay (Figure 3.23). After 1 h and 2 h of incubation at 37 °C, the disaggregation rates of VB12 in the lipid medium decreased from 79% to 69% (p<0.01) and 64% (p<0.001), respectively. After this time, the percentage of disaggregated fibrils by VB12 remained constant (p>0.05) (data not shown). Hence, VB12 lost about 30% of its disaggregating activity in the lipid environment compared to the aqueous environment after 2 h of incubation (p<0.01). Vu et al. (2013) [109] also demonstrated that the ability of dopamine to disaggregate $A\beta_{1-40}$ and $A\beta_{1-42}$ fibrils depends on the environment, with liposomes' composition playing a key role in modulating dopamine's disaggregation rates.

To assess whether VB12-lipid membrane interactions could be implicated in the loss of the vitamin's disaggregating activity over time, the KP of VB12 in the presence of mature

$A\beta_{1-42}$ fibrils was estimated at time 0 and after 2 h of incubation at 37 °C by derivative UV–Vis spectrophotometry. The results of the lipophilicity assays are presented in Table 3.16 and are expressed as KP and log D.

Table 3.16. VB12's KP and respective log D between the liposomes and the aqueous phase (PBS) in the presence of preformed $A\beta_{1-42}$ fibrils. * $p < 0.05$ indicates a statistically.

Time (h)	KP	log D
0	573 ± 66	2.98 ± 0.05
2	1068 ± 209 *	3.25 ± 0.09 *

The obtained results (Table 3.16) reveal a significant variation ($p<0.05$) of the VB12's KP value in the presence of mature fibrils over time. At 0 h, the vitamin has a low affinity for the synthetic membranes, which is translated by a K_P value of 573 ± 66. This emphasizes that as soon as VB12 is added, the compound immediately interacts with the fibrils present in the solution, the reason why no significant difference in the VB12's disaggregating ability between the aqueous and lipid media was detected at the beginning of the ThT assay. However, after 2 h of incubation, VB12 exhibits a significantly larger KP value (1068 ± 209), indicating that more molecules are partitioning from the aqueous to the lipid phase after 2 h of incubation compared to time 0. As a result, the number of molecules available in the aqueous phase decreases, preventing them from interacting with the fibrils and inducing their disruption.

TEM analysis was performed to validate the VB12's ability to disassemble mature $A\beta_{1-42}$ fibrils in the absence and presence of synthetic neuronal membranes (Figure 3.24). Figure 3.24 A and C show the images of $A\beta_{1-42}$ fibrils after 2 h of incubation in PBS and with DMPC:CHOL:SM:PS LUVs, respectively. As noted above, there were no apparent differences in the fibrils' morphology formed in aqueous (Figure 3.24 A) and lipid medium (Figure 3.24 C).

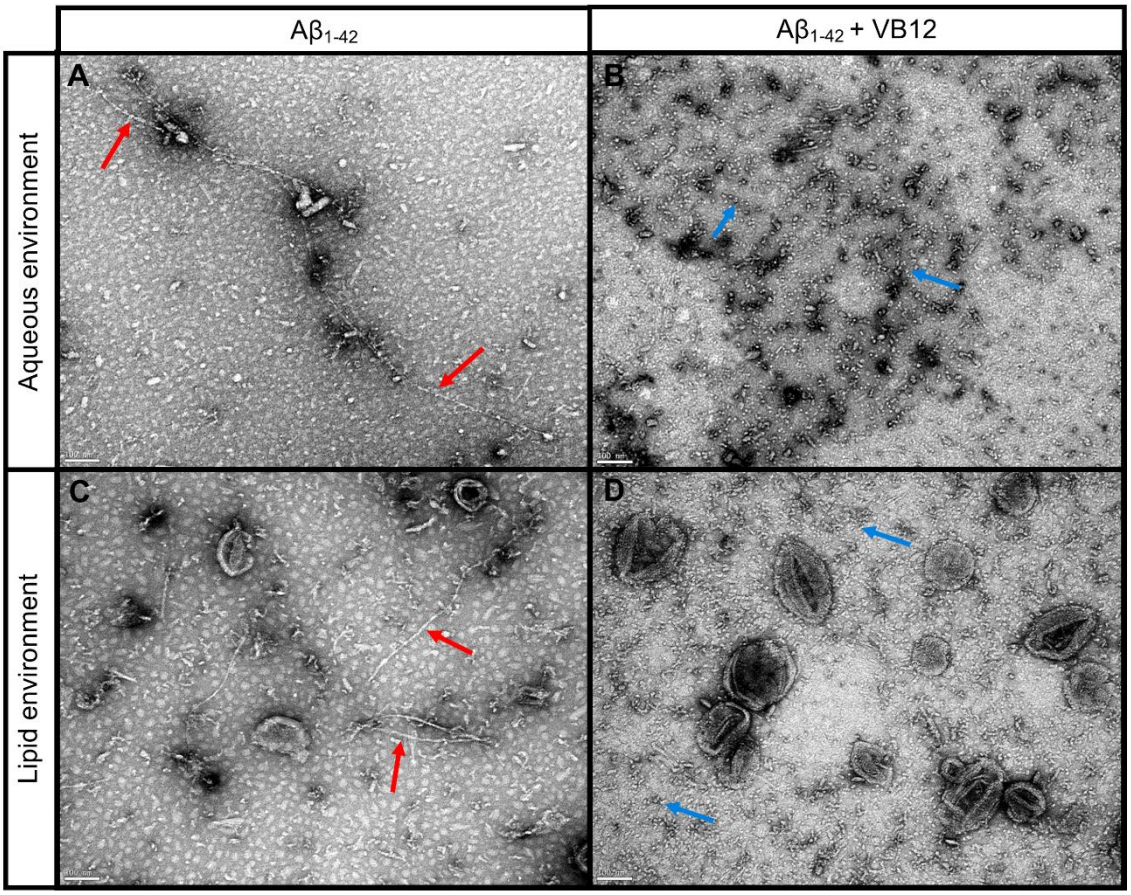

Figure 3.24. Negatively stained TEM images of A) preformed $A\beta_{1-42}$ fibrils in PBS (8 μM) and B) after their incubation with VB12 (800 μM). $A\beta_{1-42}$ fibrils preformed in the presence of liposomes (400 μM) in C) absence and D) presence of VB12. Red arrows indicate $A\beta_{1-42}$ fibrils, while blue arrows represent disintegrated fragments. Scale bars indicate 100 nm.

As expected by the ThT assays analysis, VB12 caused the fibrils disaggregation in both environments. While essentially long and thin fibrils and some protofibrils are present in the absence of VB12, both in aqueous and lipid medium, they are absent in the presence of the vitamin. Instead, short and disintegrated fragments are found (Figure 3.24 B and C), indicating the disaggregation of $A\beta_{1-42}$ fibrils upon incubation with VB12 for 2 h.

ATR-FTIR spectroscopy was employed to estimate the secondary structure of $A\beta_{1-42}$ and confirm the ability of VB12 to disaggregate preformed fibrils, both in aqueous and lipid environments. The spectral regions corresponding to the amide I band of $A\beta_{1-42}$ incubated with or without VB12 in the presence or absence of lipid vesicles are shown in Figure 3.25. Orange, pink, green, and blue lines represent antiparallel β-sheet, parallel β-sheet, α-helix,

and β-turn structures, respectively. The quantitative analyzes of the amide I region by Fourier self-deconvolution followed by curve fitting are detailed in Table 3.17.

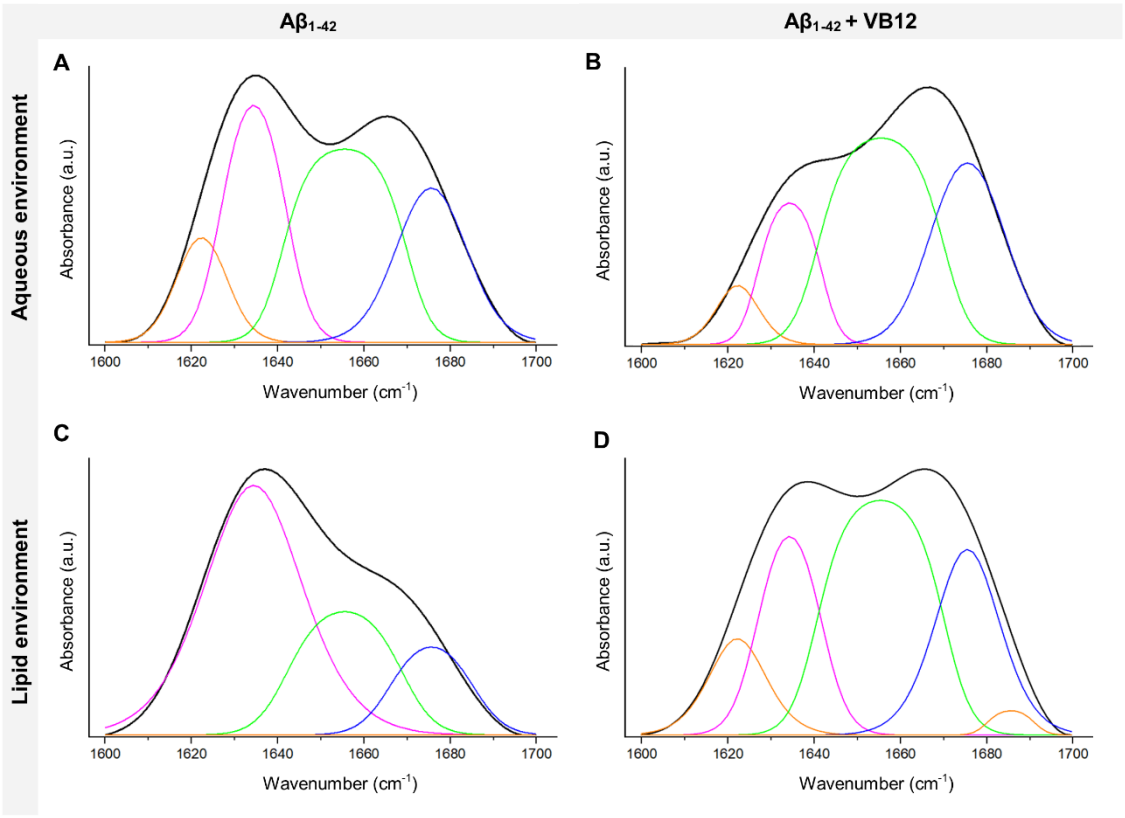

Figure 3.25. ATR-FTIR spectra of preformed $A\beta_{1-42}$ fibrils (8 μM) incubated in the A) absence or B) presence of VB12 (800 μM) in PBS. C) and D) indicate ATR-FTIR spectra of $A\beta_{1-42}$ fibrils formed in the presence of liposomes (400 μM), with and without VB12, respectively. Black lines represent the obtained spectra. Orange, pink, green, and blue lines represent antiparallel β-sheet, parallel β-sheet, α-helix, and β-turn structures, respectively.

Table 3.17. Quantitative estimation of the secondary structures of preformed $A\beta_{1-42}$ fibrils upon incubation with VB12 in both aqueous and lipid media, obtained after Fourier self-deconvolution and curve fitting of amide I band. *p<0.05 indicates a statistical difference between $A\beta_{1-42}$ in the absence and presence of VB12.

	Aqueous environment		**Lipid environment**	
	$A\beta_{1-42}$	**$A\beta_{1-42}$ + VB12**	**$A\beta_{1-42}$**	**$A\beta_{1-42}$ + VB12**
Antiparallel β-sheet 1615-1627 cm^{-1}/1674-1695 cm^{-1}	5 ± 8	11 ± 5	3 ± 6	16 ± 2 *
Parallel β-sheet 1623-1641 cm^{-1}	41 ± 12	14 ± 5 *	58 ± 18	13 ± 6 *

α-helix 1648-1657 cm^{-1}	35 ± 3	45 ± 2 *	26 ± 7	44 ± 3 *
β-turn 1662-1686 cm^{-1}	20 ± 11	30 ± 5	13 ± 9	27 ± 4

As presented in Table 3.17, parallel β-sheets are the most abundant secondary conformation of $A\beta_{1-42}$ upon incubation at 37 °C for 2 h, both in solution and in the presence of lipid vesicles, which is consistent with fibrils formation [110]. However, the incubation of preformed fibrils with VB12 significantly affected the secondary structures of Aβ. Both in aqueous and lipid environments, VB12 significantly decreased the content of parallel β-sheet structures from 41% to 14% and from 48% to 13%, respectively ($p<0.05$). Simultaneously, the number of α-helix structures significantly increased from 35% to 45% in the aqueous medium and from 26% to 44% in the lipid membrane environment ($p<0.05$). The content of antiparallel β-sheet structures remained unchanged ($p>0.05$) in PBS, but it increased from 3% to 16% in the presence of *in vitro* membranes ($p<0.05$). Furthermore, VB12 did not affect the amount of β-turns in both conditions ($p>0.05$). These alterations in the secondary structure of Aβ are consistent with that induced by other agents with amyloid fibrils disaggregating activity [90, 91, 111]. Tryptophan-galactosylamine hybrid molecules [112] or polyphenols (curcumin, resveratrol, baicalein, and EGCG) in combination with β-cyclodextrin [109] are examples of compounds that also reversed the β-sheet conformation of mature amyloid fibrils into soluble α-helix structures.

In short, these results suggest that the nature of the inhibited aggregates depends on the surrounding environment. In the aqueous solution, VB12 induced the disaggregation of mature fibrils (parallel β-sheet) into $A\beta_{1-42}$ monomers (α-helix). In the presence of lipid membranes, the fragmented structures correspond to monomers and oligomers (antiparallel β-sheet). This phenomenon is consistent with ThT fluorescence data and TEM imaging, revealing an effective disassembly of $A\beta_{1-42}$ fibrils by VB12. However, the disaggregation of amyloid fibrils only has a tangible significance if the disaggregates are not toxic. Numerous findings revealed that the toxicity of Aβ depends on its aggregation status. [111]. It appears that Aβ-induced toxicity requires the conversion of the soluble monomeric form to aggregated species-rich in β-sheets. While the monomeric form was revealed to be non-toxic, oligomers have been indicated as the most toxic species of Aβ. Fibrils also induce toxicity, although to a lesser extent. [112] Regardless of the environment, monomers are the main structure of the inhibited aggregates, which brings some hope to the AD treatment. However, the slight increase in the antiparallel β-sheet content in the lipid medium should

be examined with caution. Although oligomeric species are known to be toxic, some authors reported the stabilization of nontoxic Aβ oligomers [113-115]. Therefore, future studies are needed to evaluate the toxicity of the fragmented fibrils.

3.4. Conclusion

The anti-amyloidogenic properties of FA, NIC, CAF, CA, AA, VA, GA, and VB12 were investigated in PBS. CA, GA, and VB12 were revealed to be the most promising molecules for AD therapy by preventing the $A\beta_{1-42}$ aggregation and disrupting preformed fibrils.

The influence of an *in vitro* model of neuronal membranes on the CA, GA, and VB12's ability to inhibit $A\beta_{1-42}$ fibrillation and disaggregate mature fibrils was then examined. The combination of experimental techniques revealed that the presence of lipid membranes did not affect CA and GA's ability to inhibit $A\beta_{1-42}$ fibrillation. However, the VB12's anti-aggregation property was lower in the presence of the neuronal membrane model than in PBS. Furthermore, the lipid membrane model reduced the ability of the three natural compounds to disrupt mature fibrils. This is due to the partition of the natural compounds' molecules to the lipid membrane, which prevents them from interacting with Aβ. Even so, CA, GA, and VB12 showed strong *anti*-amyloidogenic properties in the cell membrane-like environment, supporting the view that these compounds could be a promising approach for preventing and curing AD. GA appears to be the most advantageous molecule because it entirely prevents the Aβ aggregation and disaggregates mature fibrils in the neuronal cell-like environment, followed by CA and VB12.

Additionally, these works highlight the importance of the study's design before testing drug candidates. The detailed reproduction of *in vivo* conditions in *in vitro* studies is of utmost importance to reduce the number of compounds failing to enter the pipeline, thus preserving resources that can be devoted to discovering and developing effective drugs. In this context, mimicking cell membranes through *in vitro* lipid membrane models provides a more realistic prediction of the drugs' activity *in vivo*, which helps the discovery and development of effective drugs.

References

[1] Magalingam, K. B., Radhakrishnan, A., Ping, N. S.&Haleagrahara, N. Current concepts of neurodegenerative mechanisms in alzheimer's disease. BioMed Research International 2018, 2018, 3740461.

[2] Okada, Y., Okubo, K., Ikeda, K., Yano, Y., Hoshino, M., Hayashi, Y., Kiso, Y., Itoh-Watanabe, H., Naito, A.&Matsuzaki, K. Toxic amyloid tape: A novel mixed antiparallel/parallel β-sheet structure formed by amyloid β-protein on gm1 clusters. ACS chemical neuroscience 2018, 10, 563-572.

[3] Beasley, M., Stonebraker, A. R., Hasan, I., Kapp, K. L., Liang, B. J., Agarwal, G., Groover, S., Sedighi, F.&Legleiter, J. Lipid membranes influence the ability of small molecules to inhibit huntingtin fibrillization. Biochemistry 2019, 58, 4361-4373.

[4] Niu, Z., Zhang, Z., Zhao, W.&Yang, J. Interactions between amyloid β peptide and lipid membranes. Biochimica et Biophysica Acta (BBA)-Biomembranes 2018, 1860, 1663-1669.

[5] Sharma, P., Srivastava, P., Seth, A., Tripathi, P. N., Banerjee, A. G.&Shrivastava, S. K. Comprehensive review of mechanisms of pathogenesis involved in alzheimer's disease and potential therapeutic strategies. Progress in Neurobiology 2019, 174, 53-89.

[6] Andrade, S., Ramalho, M. J., Loureiro, J. A.&Pereira, M. C. Natural compounds for alzheimer's disease therapy: A systematic review of preclinical and clinical studies. Int. J. Mol. Sci. 2019, 20, 1-41.

[7] Cummings, J., Feldman, H. H.&Scheltens, P. The "rights" of precision drug development for alzheimer's disease. Alzheimer's Res. Ther. 2019, 11, 1-14.

[8] Andrade, S., Ramalho, M. J., Loureiro, J. A.&Pereira, M. C. Liposomes as biomembrane models: Biophysical techniques for drug-membrane interaction studies. J. Mol. Liq. 2021, 334, 1-16.

[9] Zhang, J., Tan, J., Pei, R.&Ye, S. Acidic environment significantly alters aggregation pathway of human islet amyloid polypeptide at negative lipid membrane. Langmuir 2020, 36, 1530-1537.

[10] Siontorou, C. G., Nikoleli, G.-P., Nikolelis, D. P.&Karapetis, S. K. Artificial lipid membranes: Past, present, and future. Membranes 2017, 7, 1-24.

[11] Lim, L.&Wenk, M. R., Neuronal membrane lipids – their role in the synaptic vesicle cycle, in Handbook of neurochemistry and molecular neurobiology: Neural lipids, A. Lajtha, G. Tettamanti, and G. Goracci, Editors. 2009, Springer US: Boston. p. 223-238.

[12] Andrade, S., Ramalho, M. J., Loureiro, J. A.&Pereira, M. C. The biophysical interaction of ferulic acid with liposomes as biological membrane model: The effect of the lipid bilayer composition. J. Mol. Liq. 2020, 1-10.

[13] Dua, J. S., Rana, A. C. C.&Bhandari, A. K. Liposome: Methods of preparation and applications. International Journal of Pharmaceutical Studies and Research 2012, 3, 14-20.

[14] Jiang, J., Oberdörster, G.&Biswas, P. Characterization of size, surface charge, and agglomeration state of nanoparticle dispersions for toxicological studies. Journal of Nanoparticle Research 2009, 11, 77-89.

[15] Laouini, A., Jaafar-Maalej, C., Limayem-Blouza, I., Sfar, S., Charcosset, C.&Fessi, H. Preparation, characterization and applications of liposomes: State of the art. Journal of Colloid Science and Biotechnology 2012, 1, 147-168.

[16] Andrade, S., Loureiro, J. A., Coelho, M. A.&do Carmo Pereira, M., presented at 2015 IEEE 4th Portuguese Meeting on Bioengineering (ENBENG). Interaction studies of amyloid β-peptide with the natural compound resveratrol, 2015.

[17] Loureiro, J. A., Andrade, S., Duarte, A., Neves, A. R., Queiroz, J. F., Nunes, C., Sevin, E., Fenart, L., Gosselet, F., Coelho, M. A. N.&Pereira, M. C. Resveratrol and grape extract-loaded solid lipid nanoparticles for the treatment of alzheimer's disease. Molecules 2017, 22, 1-16.

[18] Loureiro, J. A., Rocha, S.&Pereira, M. C. Charged surfactants induce a non-fibrillar aggregation pathway of amyloid-beta peptide. Journal of Peptide Science 2013, 19, 581-587.

[19]

[20] Qin, Z., Hu, D., Han, S., Reaney, S. H., Di Monte, D. A.&Fink, A. L. Effect of 4-hydroxy-2-nonenal modification on α-synuclein aggregation. J. Biol. Chem. 2007, 282, 5862-5870.

[21] Chakraborty, R., Dey, S., Paul, S. S., Sil, P., Sengupta, J.&Chattopadhyay, K. Heme minimizes parkinson's disease-associated toxicity by inducing a conformational distortion in the oligomers of alpha-synuclein. bioRxiv 2019, 1-38.

[22] Srour, B., Bruechert, S., Andrade, S. L.&Hellwig, P., Secondary structure determination by means of atr-ftir spectroscopy, in Membrane protein structure and function characterization. 2017, Springer. p. 195-203.

[23] Wallace, B. A. The role of circular dichroism spectroscopy in the era of integrative structural biology. Current Opinion in Structural Biology 2019, 58, 191-196.

[24] Bera, S., Gayen, N., Mohid, S. A., Bhattacharyya, D., Krishnamoorthy, J., Sarkar, D., Choi, J., Sahoo, N., Mandal, A. K., Lee, D.&Bhunia, A. Comparison of synthetic neuronal model membrane mimics in amyloid aggregation at atomic resolution. ACS Chemical Neuroscience 2020, 11, 1965-1977.

[25] Rocha, F. R. P.&Teixeira, L. S. G. Estratégias para aumento de sensibilidade em espectrofotometria uv-vis. Química Nova 2004, 27, 807-812.

[26] El-Kabbany, F., Taha, S.&Hafez, M. A study of the phase transition of reheated diphenyl carbazide (dpc) by using uv spectroscopy. Spectrochimica Acta Part A: Molecular and Biomolecular Spectroscopy 2014, 128, 481-488.

[27] Lúcio, M., Nunes, C., Gaspar, D., Gołębska, K., Wisniewski, M., Lima, J. L. F. C., Brezesinski, G.&Reis, S. Effect of anti-inflammatory drugs in phosphatidylcholine membranes: A fluorescence and calorimetric study. Chemical Physics Letters 2009, 471, 300-309.

[28] Magalhães, L. M., Nunes, C., Lúcio, M., Segundo, M. A., Reis, S.&Lima, J. L. F. C. High-throughput microplate assay for the determination of drug partition coefficients. Nature Protocols 2010, 5, 1823.

[29] Magalhaes, L. M., Nunes, C., Lucio, M., Segundo, M. A., Reis, S.&Lima, J. L. High-throughput microplate assay for the determination of drug partition coefficients. Nature protocols 2010, 5, 1823-1830.

[30] Andrade, S., Loureiro, J. A.&Pereira, M. C. Green tea extract-biomembrane interaction study: The role of its two major components, (−)-epigallocatechin gallate and (−)-epigallocatechin. BBA – Biomembranes 2021, 1863, 1-10.

[31] L Almeida, Z.&MM Brito, R. Structure and aggregation mechanisms in amyloids. Molecules 2020, 25, 1-30.

[32] Xue, C., Lin, T. Y., Chang, D.&Guo, Z. Thioflavin t as an amyloid dye: Fibril quantification, optimal concentration and effect on aggregation. Royal Society open science 2017, 4, 160696.

[33] L Almeida, Z.&MM Brito, R. Structure and aggregation mechanisms in amyloids. Molecules 2020, 25, 1195.

[34] Lindberg, D. J., Wesén, E., Björkeroth, J., Rocha, S.&Esbjörner, E. K. Lipid membranes catalyse the fibril formation of the amyloid-β (1–42) peptide through lipid-fibril interactions that reinforce secondary pathways. Biochimica et Biophysica Acta (BBA) - Biomembranes 2017, 1859, 1921-1929.

[35] Sabaté, R., Espargaró, A., Barbosa-Barros, L., Ventura, S.&Estelrich, J. Effect of the surface charge of artificial model membranes on the aggregation of amyloid β-peptide. Biochimie 2012, 94, 1730-1738.

[36] Dorsey, M. P., Nguelifack, B. M.&Yates, E. A. Colorimetric detection of mutant β-amyloid(1–40) membrane-active aggregation with biosensing vesicles. ACS Applied Bio Materials 2019, 2, 4966-4977.

[37] Niu, Z., Zhang, Z., Zhao, W.&Yang, J. Interactions between amyloid β peptide and lipid membranes. Biochim. Biophys. Acta, Biomembr. 2018, 1860, 1663-1669.

[38] Rangachari, V., Dean, D. N., Rana, P., Vaidya, A.&Ghosh, P. Cause and consequence of aβ – lipid interactions in alzheimer disease pathogenesis. Biochimica et Biophysica Acta (BBA) - Biomembranes 2018, 1860, 1652-1662.

[39] Andrade, S., Loureiro, J. A.&Pereira, M. C. The role of amyloid β-biomembrane interactions in the pathogenesis of alzheimer's disease: Insights from liposomes as membrane models. ChemPhysChem n/a,

[40] Matsuzaki, K. Physicochemical interactions of amyloid β-peptide with lipid bilayers. Biochimica et Biophysica Acta (BBA) - Biomembranes 2007, 1768, 1935-1942.

[41] Ramalho, M. J., Andrade, S., Coelho, M. A., Loureiro, J. A.&Pereira, M. C. Molecular interactions between vitamin b12 and membrane models: A biophysical study for new insights into the bioavailability of vitamin. Colloids and Surfaces B: Biointerfaces 2020, 111187.

[42] Andrade, S., Loureiro, J. A.&Pereira, M. C. Green tea extract-biomembrane interaction study: The role of its two major components, (−)-epigallocatechin gallate and (−)-epigallocatechin. Biochimica et Biophysica Acta (BBA) - Biomembranes 2021, 1863, 183476.

[43] Greenfield, N. J. Using circular dichroism spectra to estimate protein secondary structure. Nat Protoc 2006, 1, 2876-2890.

[44] Ding, F., LaRocque, J. J.&Dokholyan, N. V. Direct observation of protein folding, aggregation, and a prion-like conformational conversion. Journal of Biological Chemistry 2005, 280, 40235-40240.

[45] Swiontek, M., Wasko, J., Fraczyk, J., Galecki, K., Kaminski, Z. J.&Kolesinska, B. Insulin hot-spot analogs formed with n-methylated amino acid residues inhibit aggregation of native hormone. Molecules 2019, 24, 3706.

[46] Wei, Y., Thyparambil, A. A.&Latour, R. A. Protein helical structure determination using cd spectroscopy for solutions with strong background absorbance from 190 to 230 nm. Biochimica et Biophysica Acta (BBA)-Proteins and Proteomics 2014, 1844, 2331-2337.

[47] Alam, P., Beg, A. Z., Siddiqi, M. K., Chaturvedi, S. K., Rajpoot, R. K., Ajmal, M. R., Zaman, M., Abdelhameed, A. S.&Khan, R. H. Ascorbic acid inhibits human insulin aggregation and protects against amyloid induced cytotoxicity. Archives of Biochemistry and Biophysics 2017, 621, 54-62.

[48] Alam, P., Siddiqi, M. K., Chaturvedi, S. K., Zaman, M.&Khan, R. H. Vitamin b12 offers neuronal cell protection by inhibiting aβ-42 amyloid fibrillation. Int. J. Biol. Macromol. 2017, 99, 477-482.

[49] Zaman, M., Zakariya, S. M., Nusrat, S., Chandel, T. I., Meeran, S. M., Ajmal, M. R., Alam, P.&Khan, R. H. Cysteine as a potential anti-amyloidogenic agent with protective ability against amyloid induced cytotoxicity. International journal of biological macromolecules 2017, 105, 556-565.

[50] Mudedla, S. K., Murugan, N. A.&Ågren, H. Effect of familial mutations on the interconversion of α-helix to β-sheet structures in an amyloid-forming peptide: Insight from umbrella sampling simulations. ACS Chemical Neuroscience 2019, 10, 1347-1354.

[51] Chandra, B., Bhowmik, D., Maity, B. K., Mote, K. R., Dhara, D., Bera, K., Das, A., Venkatramani, R., Maiti, S.&Madhu, P. K. Secondary structure flipping connected to salt-bridge formation converts toxic amyloid-β40 oligomers to fibrils. Biophysical Journal 2017, 112, 362a-363a.

[52] Dai, Y., Zhang, M., Shi, X., Wang, K., Gao, G., Shen, L.&Sun, T. Kinetic study of aβ (1-42) amyloidosis in the presence of ganglioside-containing vesicles. Colloids and Surfaces B: Biointerfaces 2020, 185, 110615.

[53] Kinoshita, M., Kakimoto, E., Terakawa, M. S., Lin, Y., Ikenoue, T., So, M., Sugiki, T., Ramamoorthy, A., Goto, Y.&Lee, Y.-H. Model membrane size-dependent amyloidogenesis of alzheimer's amyloid-β peptides. Physical Chemistry Chemical Physics 2017, 19, 16257-16266.

[54] Fazili, N. A.&Naeem, A. Anti-fibrillation potency of caffeic acid against an antidepressant induced fibrillogenesis of human α-synuclein: Implications for parkinson's disease. Biochimie 2015, 108, 178-185.

[55] Chen, S., Gong, X., Tan, H., Liu, Y., He, L.&Ouyang, J. Study of the noncovalent interactions between phenolic acid and lysozyme by cold spray ionization mass spectrometry (csi-ms), multi-spectroscopic and molecular docking approaches. Talanta 2020, 211, 120762.

[56] Li, S., Huang, K., Zhong, M., Guo, J., Wang, W.-z.&Zhu, R. Comparative studies on the interaction of caffeic acid, chlorogenic acid and ferulic acid with bovine serum albumin. Spectrochimica Acta Part A: Molecular and Biomolecular Spectroscopy 2010, 77, 680-686.

[57] Precupas, A., Sandu, R., Leonties, A. R., Anghel, D.-F.&Popa, V. T. Complex interaction of caffeic acid with bovine serum albumin: Calorimetric, spectroscopic and molecular docking evidence. New Journal of Chemistry 2017, 41, 15003-15015.

[58] Save, S. S., Rachineni, K., Hosur, R. V.&Choudhary, S. Natural compound safranal driven inhibition and dis-aggregation of α-synuclein fibrils. International Journal of Biological Macromolecules 2019, 141, 585-595.

[59] Choi, E. Y., Kang, S. S., Lee, S. K.&Han, B. H. Polyphenolic biflavonoids inhibit amyloid-beta fibrillation and disaggregate preformed amyloid-beta fibrils. Biomolecules & therapeutics 2020, 28, 145.

[60] Zhao, J., Liang, Q., Sun, Q., Chen, C., Xu, L., Ding, Y.&Zhou, P. (−)-epigallocatechin-3-gallate (egcg) inhibits fibrillation, disaggregates amyloid fibrils of α-synuclein, and protects pc12 cells against α-synuclein-induced toxicity. Rsc Advances 2017, 7, 32508-32517.

[61] Vu, H. T., Shimanouchi, T., Ishikawa, D., Matsumoto, T., Yagi, H., Goto, Y., Umakoshi, H.&Kuboi, R. Effect of liposome membranes on disaggregation of amyloid β fibrils by dopamine. Biochemical Engineering Journal 2013, 71, 118-126.

[62] Andrade, S., Loureiro, J. A.&Pereira, M. C. Vitamin b12 inhibits aβ fibrillation and disaggregates preformed fibrils in the presence of synthetic neuronal membranes. ACS Chemical Neuroscience 2021, 12, 2491-2502.

[63] Galzitskaya, O. V.&Selivanova, O. M. Rosetta stone for amyloid fibrils: The key role of ring-like oligomers in amyloidogenesis. Journal of Alzheimer's Disease 2017, 59, 785-795.

[64] Selivanova, O. M., Surin, A. K., Marchenkov, V. V., Dzhus, U. F., Grigorashvili, E. I., Suvorina, M. Y., Glyakina, A. V., Dovidchenko, N. V.&Galzitskaya, O. V. The mechanism underlying amyloid polymorphism is opened for alzheimer's disease amyloid-β peptide. Journal of Alzheimer's Disease 2016, 54, 821-830.

[65] Rajasekhar, K., Suresh, S., Manjithaya, R.&Govindaraju, T. Rationally designed peptidomimetic modulators of aβ toxicity in alzheimer's disease. Scientific reports 2015, 5, 1-9.

[66] Sarroukh, R., Cerf, E., Derclaye, S., Dufrêne, Y. F., Goormaghtigh, E., Ruysschaert, J.-M.&Raussens, V. Transformation of amyloid β (1–40) oligomers into fibrils is characterized by a major change in secondary structure. Cellular and molecular life sciences 2011, 68, 1429-1438.

[67] Xue, C., Lin, T. Y., Chang, D.&Guo, Z. Thioflavin t as an amyloid dye: Fibril quantification, optimal concentration and effect on aggregation. R. Soc. Open Sci. 2017, 4, 1-12.

[68] Andrade, S., Ramalho, M. J., Loureiro, J. A.&Pereira, M. C. Interaction of natural compounds with biomembrane models: A biophysical approach for the alzheimer's disease therapy. Colloids Surf., B 2019, 180, 83-92.

[69] Delgado, D. A., Doherty, K., Cheng, Q., Kim, H., Xu, D., Dong, H., Grewer, C.&Qiang, W. Distinct membrane disruption pathways are induced by 40-residue β-amyloid peptides. J. Biol. Chem. 2016, 291, 12233-12244.

[70] Lindberg, D. J., Wesén, E., Björkeroth, J., Rocha, S.&Esbjörner, E. K. Lipid membranes catalyse the fibril formation of the amyloid-β (1–42) peptide through lipid-fibril interactions that reinforce secondary pathways. Biochim. Biophys. Acta, Biomembr. 2017, 1859, 1921-1929.

[71] Bera, S., Gayen, N., Mohid, S. A., Bhattacharyya, D., Krishnamoorthy, J., Sarkar, D., Choi, J., Sahoo, N., Mandal, A. K., Lee, D.&Bhunia, A. Comparison of synthetic neuronal model membrane mimics in amyloid aggregation at atomic resolution. ACS Chem. Neurosci. 2020, 11, 1965-1977.

[72] Lee, J., Kim, Y. H., T. Arce, F., Gillman, A. L., Jang, H., Kagan, B. L., Nussinov, R., Yang, J.&Lal, R. Amyloid β ion channels in a membrane comprising brain total lipid extracts. ACS Chem. Neurosci. 2017, 8, 1348-1357.

[73] Yang, X., Meisl, G., Frohm, B., Thulin, E., Knowles, T. P. J.&Linse, S. On the role of sidechain size and charge in the aggregation of aβ42 with familial mutations. Proc. Natl. Acad. Sci. 2018, 115, E5849-E5858.

[74] Liu, Y., Carver, J. A., Calabrese, A. N.&Pukala, T. L. Gallic acid interacts with α-synuclein to prevent the structural collapse necessary for its aggregation. Biochim. Biophys. Acta, Proteins Proteomics 2014, 1844, 1481-1485.

[75] Jayamani, J.&Shanmugam, G. Gallic acid, one of the components in many plant tissues, is a potential inhibitor for insulin amyloid fibril formation. Eur. J. Med. Chem. 2014, 85, 352-358.

[76] Konar, M., Bag, S., Roy, P.&Dasgupta, S. Gallic acid induced dose dependent inhibition of lysozyme fibrillation. Int. J. Biol. Macromol. 2017, 103, 1224-1231.

[77] Liu, Y., Pukala, T. L., Musgrave, I. F., Williams, D. M., Dehle, F. C.&Carver, J. A. Gallic acid is the major component of grape seed extract that inhibits amyloid fibril formation. Bioorg. Med. Chem. Lett. 2013, 23, 6336-6340.

[78] Chmiel, T., Mieszkowska, A., Kempińska-Kupczyk, D., Kot-Wasik, A., Namieśnik, J.&Mazerska, Z. The impact of lipophilicity on environmental processes, drug delivery and bioavailability of food components. Microchem. J. 2019, 146, 393-406.

[79] Andrade, S., Ramalho, M. J., Loureiro, J. A.&Pereira, M. C. The biophysical interaction of ferulic acid with liposomes as biological membrane model: The effect of the lipid bilayer composition. J. Mol. Liq. 2020, 324, 1-10.

[80] Ramalho, M. J., Andrade, S., Coelho, M. Á. N., Loureiro, J. A.&Pereira, M. C. Biophysical interaction of temozolomide and its active metabolite with biomembrane models: The relevance of drug-membrane interaction for glioblastoma multiforme therapy. European Journal of Pharmaceutics and Biopharmaceutics 2019, 136, 156-163.

[81] Kah, M.&Brown, C. D. Logd: Lipophilicity for ionisable compounds. Chemosphere 2008, 72, 1401-1408.

[82] Gras, S. L., Waddington, L. J.&Goldie, K. N., Transmission electron microscopy of amyloid fibrils, in Protein folding, misfolding, and disease: Methods and protocols, A.F. Hill, et al., Editors. 2011, Humana Press: Totowa, NJ. p. 197-214.

[83] Ruysschaert, J.-M.&Raussens, V., Atr-ftir analysis of amyloid proteins, in Peptide self-assembly: Methods and protocols, B.L. Nilsson and T.M. Doran, Editors. 2018, Springer New York: New York, NY. p. 69-81.

[84] Close, W., Neumann, M., Schmidt, A., Hora, M., Annamalai, K., Schmidt, M., Reif, B., Schmidt, V., Grigorieff, N.&Fändrich, M. Physical basis of amyloid fibril polymorphism. Nat. Commun. 2018, 9, 1-7.

[85] Chandra, B., Bhowmik, D., Maity, B. K., Mote, K. R., Dhara, D., Bera, K., Das, A., Venkatramani, R., Maiti, S.&Madhu, P. K. Secondary structure flipping connected to salt-bridge formation converts toxic amyloid-β40 oligomers to fibrils. Biophys. J. 2017, 112, 362a-363a.

[86] Dai, Y., Zhang, M., Shi, X., Wang, K., Gao, G., Shen, L.&Sun, T. Kinetic study of aβ (1-42) amyloidosis in the presence of ganglioside-containing vesicles. Colloids Surf., B 2020, 185, 1-6.

[87] Ono, K., Hirohata, M.&Yamada, M. Ferulic acid destabilizes preformed β-amyloid fibrils in vitro. Biochem. Biophys. Res. Commun. 2005, 336, 444-449.

[88] Ono, K., Hasegawa, K., Naiki, H.&Yamada, M. Anti-amyloidogenic activity of tannic acid and its activity to destabilize alzheimer's β-amyloid fibrils in vitro. Biochim. Biophys. Acta, Mol. Basis Dis. 2004, 1690, 193-202.

[89] Ono, K., Yoshiike, Y., Takashima, A., Hasegawa, K., Naiki, H.&Yamada, M. Vitamin a exhibits potent antiamyloidogenic and fibril-destabilizing effects in vitro. Exp. Neurol. 2004, 189, 380-392.

[90] Vu, H. T., Shimanouchi, T., Ishikawa, D., Matsumoto, T., Yagi, H., Goto, Y., Umakoshi, H.&Kuboi, R. Effect of liposome membranes on disaggregation of amyloid β fibrils by dopamine. Biochem. Eng. J. 2013, 71, 118-126.

[91] Sarroukh, R., Cerf, E., Derclaye, S., Dufrêne, Y. F., Goormaghtigh, E., Ruysschaert, J.-M.&Raussens, V. Transformation of amyloid β (1–40) oligomers into fibrils is characterized by a major change in secondary structure. Cell. Mol. Life Sci. 2011, 68, 1429-1438.

[92] Mudedla, S. K., Murugan, N. A.&Ågren, H. Effect of familial mutations on the interconversion of α-helix to β-sheet structures in an amyloid-forming peptide: Insight from umbrella sampling simulations. ACS Chem. Neurosci. 2019, 10, 1347-1354.

[93] Niu, Z., Zhang, Z., Zhao, W.&Yang, J. Interactions between amyloid β peptide and lipid membranes. BBA – Biomembranes 2018, 1860, 1663-1669.

[94] Loureiro, J. A., Crespo, R., Börner, H., Martins, P. M., Rocha, F. A., Coelho, M., Pereira, M. C.&Rocha, S. Fluorinated β-sheet breaker peptides. J. Mater. Chem. B 2014, 2, 2259-2264.

[95] Lindberg, D. J., Wesén, E., Björkeroth, J., Rocha, S.&Esbjörner, E. K. Lipid membranes catalyse the fibril formation of the amyloid-β (1–42) peptide through lipid-fibril interactions that reinforce secondary pathways. BBA - Biomembranes 2017, 1859, 1921-1929.

[96] Fukunaga, S., Ueno, H., Yamaguchi, T., Yano, Y., Hoshino, M.&Matsuzaki, K. Gm1 cluster mediates formation of toxic aβ fibrils by providing hydrophobic environments. Biochemistry 2012, 51, 8125-8131.

[97] Šmidlehner, T., Bonnet, H., Chierici, S.&Piantanida, I. Fluorescently-labelled amyloid paired helical filaments (phf) in monitoring its fibrillation kinetics. Bioorg. Chem. 2020, 104, 1-5.

[98] Sidhu, A., Vaneyck, J., Blum, C., Segers-Nolten, I.&Subramaniam, V. Polymorph-specific distribution of binding sites determines thioflavin-t fluorescence intensity in α-synuclein fibrils. Amyloid 2018, 25, 189-196.

[99] Ziaunys, M., Sakalauskas, A.&Smirnovas, V. Identifying insulin fibril conformational differences by thioflavin-t binding characteristics. Biomacromolecules 2020, 21, 4989-4997.

[100] Ziaunys, M., Sakalauskas, A., Mikalauskaite, K.&Smirnovas, V. Exploring the occurrence of thioflavin-t-positive insulin amyloid aggregation intermediates. PeerJ 2021, 9, 1-16.

[101] Mikalauskaite, K., Ziaunys, M., Sneideris, T.&Smirnovas, V. Effect of ionic strength on thioflavin-t affinity to amyloid fibrils and its fluorescence intensity. Int. J. Mol. Sci. 2020, 21, 1-13.

[102] Ziaunys, M., Mikalauskaite, K.&Smirnovas, V. Amyloidophilic molecule interactions on the surface of insulin fibrils: Cooperative binding and fluorescence quenching. Sci. Rep. 2019, 9, 1-10.

[103] Matsuzaki, K., Noguch, T., Wakabayashi, M., Ikeda, K., Okada, T., Ohashi, Y., Hoshino, M.&Naiki, H. Inhibitors of amyloid β-protein aggregation mediated by gm1-containing raft-like membranes. BBA-Biomembranes 2007, 1768, 122-130.

[104] Ramalho, M. J., Andrade, S., Coelho, M. A., Loureiro, J. A.&Pereira, M. C. Molecular interactions between vitamin b12 and membrane models: A biophysical study for new insights into the bioavailability of vitamin. Colloids Surf. B: Biointerfaces 2020, 1-8.

[105] Li, H., Lantz, R.&Du, D. Vibrational approach to the dynamics and structure of protein amyloids. Molecules 2019, 24, 1-21.

[106] Dai, Y., Zhang, M., Shi, X., Wang, K., Gao, G., Shen, L.&Sun, T. Kinetic study of aβ (1-42) amyloidosis in the presence of ganglioside-containing vesicles. Colloids Surf. B: Biointerfaces 2020, 185, 1-6.

[107] Kinoshita, M., Kakimoto, E., Terakawa, M. S., Lin, Y., Ikenoue, T., So, M., Sugiki, T., Ramamoorthy, A., Goto, Y.&Lee, Y.-H. Model membrane size-dependent amyloidogenesis of alzheimer's amyloid-β peptides. PCCP 2017, 19, 16257-16266.

[108] Save, S. S., Rachineni, K., Hosur, R. V.&Choudhary, S. Natural compound safranal driven inhibition and disaggregation of α-synuclein fibrils. Int. J. Biol. Macromol. 2019, 141, 585-595.

[109] Zhao, J., Liang, Q., Sun, Q., Chen, C., Xu, L., Ding, Y.&Zhou, P. (−)-epigallocatechin-3-gallate (egcg) inhibits fibrillation, disaggregates amyloid fibrils of α-synuclein, and protects pc12 cells against α-aynuclein-induced toxicity. RSC Adv. 2017, 7, 32508-32517.

[110] Choi, E. Y., Kang, S. S., Lee, S. K.&Han, B. H. Polyphenolic biflavonoids inhibit amyloid-beta fibrillation and disaggregate preformed amyloid-β fibrils. Biomol Ther (Seoul) 2020, 28, 145-151.

[111] Paul, A., Frenkel-Pinter, M., Escobar Alvarez, D., Milordini, G., Gazit, E., Zacco, E.&Segal, D. Tryptophan-galactosylamine conjugates inhibit and disaggregate amyloid fibrils of aβ42 and hiapp peptides while reducing their toxicity. Commun. Biol. 2020, 3, 484.

[112] Gautam, S., Karmakar, S., Batra, R., Sharma, P., Pradhan, P., Singh, J., Kundu, B.&Chowdhury, P. K. Polyphenols in combination with β-cyclodextrin can inhibit and

disaggregate α-synuclein amyloids under cell mimicking conditions: A promising therapeutic alternative. BBA - Proteins Proteom 2017, 1865, 589-603.

[113] Ahyayauch, H., Raab, M., Busto, J. V., Andraka, N., Arrondo, J.-L. R., Masserini, M., Tvaroska, I.&Goñi, F. M. Binding of β-amyloid (1–42) peptide to negatively charged phospholipid membranes in the liquid-ordered state: Modeling and experimental studies. Biophys. J. 2012, 103, 453-463.

[114] Shimanouchi, T., Onishi, R., Kitaura, N., Umakoshi, H.&Kuboi, R. Copper-mediated growth of amyloid β fibrils in the presence of oxidized and negatively charged liposomes. J. Biosci. Bioeng. 2011, 112, 611-615.

[115] Ryan, T. M., Roberts, B. R., McColl, G., Hare, D. J., Doble, P. A., Li, Q.-X., Lind, M., Roberts, A. M., Mertens, H. D. T., Kirby, N., Pham, C. L. L., Hinds, M. G., Adlard, P. A., Barnham, K. J., Curtain, C. C.&Masters, C. L. Stabilization of nontoxic aβ-oligomers: Insights into the mechanism of action of hydroxyquinolines in alzheimer's disease. J. Neurosci. 2015, 35, 2871-2884.

Chapter 4

Transferrin-Functionalized Liposomes for Alzheimer's Disease Therapy with Natural Compounds

4.1. Introduction

According to experimental and epidemiological studies, natural compounds consumption has been related to symptom improvements of various neurodegenerative illnesses, including AD [1, 2]. However, there is no solid proof that natural compounds prevent the development of AD or cure it. This has been mainly associated with the natural compounds' limitations such as low solubility, absorption, and bioavailability, *in vivo* instability, lack of specificity, high systemic clearance, and inability to cross the BBB, which prevent them from reaching the brain in effective concentrations [3].

Many innovative DDSs have attracted attention in the last decades for transporting drugs across the BBB, thus overcoming the above-referred limitations. Among them, liposomes have aroused particular interest for being one of the safest nanocarriers for human use [4]. The conjugation of Tf to the NPs' surface has been widely employed to enhance their transport across the BBB due to the overexpression of TfR in the endothelial cells of the BBB [5].

Hence, the present chapter aims to develop Tf-functionalized liposomes loaded with the natural compounds that showed successful *anti*-amyloidogenic properties in the presence of the neuronal cell membrane model – CA, GA, or VB12 – for AD therapy. Liposomes were produced and physicochemically characterized by various techniques. *In vitro* experiments were conducted to evaluate the ability of the CA, GA, or VB12 loaded into Tf-functionalized liposomes to prevent the Aβ fibrillation and disaggregate mature fibrils.

4.2. Materials and Methods

4.2.1. Materials

CA (purity>99%, MW 180), GA (purity≥99%, MW 170), VB12 (purity≥98%, MW 1355), holo-Tf human (purity≥98%, MW 80,000), N-(3-dimethylaminopropyl)-N′-ethylcarbodiimide hydrochloride (EDC, MW 192), ThT (MW 319), HFIP (purity≥99%, MW 168), and chloroform (purity ≥ 99%, MW 119) were acquired from Sigma-Aldrich (St. Louis, MO, USA). Methanol (purity ≥ 99%, MW 32) and ethanol absolute (purity≥99%, MW 46) were acquired from VWR International (Radnor, PA, EUA), while diethyl ether (purity≥99%, MW 74) was obtained from José Manuel Gomes dos Santos, Lda (Odivelas, Portugal). 1,2-distearoyl-sn-glycero-3-phosphocholine (DSPC, purity>99%, MW 790), CHOL (ovine wool, purity > 98%, MW 387), 1,2-distearoyl-sn-glycero-3-phosphoethanolamine-N-[methoxy(polyethylene glycol)-2000] (18:0 PEG2000 PE, purity > 99%, MW 2805), and 1,2-distearoyl-sn-glycero-3-phosphoethanolamine-N-[amino(polyethylene glycol)-2000] (DSPE-PEG2000 amine, purity > 99%, MW 2791) were purchased from Avanti Polar Lipids Inc. (Alabaster, AL, USA). Human amyloid-β peptide with 42 amino acid residues ($A\beta_{1-42}$, purity > 95%, MW 4514) and uranyl acetate dihydrate (purity > 99%, MW 424) were obtained from GenScript Biotech (Piscataway, NJ, EUA) and Electron Microscopy Sciences (Hatfield, PA, USA), respectively. Ultrapure water (Milli-Q Academic, Millipore, France) was used to prepare PBS (pH 7.4, 10 mM phosphate buffer, 2.7 mM potassium chloride, and 137 mM sodium chloride) purchased from VWR International (Radnor, PA, EUA).

4.2.2. Preparation of Liposomes

DSPC, CHOL, 18:0 PEG2000 PE, and DSPE-PEG2000 amine at a molar ratio of 52:45:3:0.06 were used to prepare liposomes. Distinct techniques were employed to prepare CA, GA, or VB12-loaded liposomes, including lipid film hydration, reverse phase evaporation, ethanol injection, and ethanol permeabilization. Unloaded liposomes were also prepared using the same methodologies as control.

4.2.2.1. Lipid Film Hydration

Lipids were dissolved in chloroform, which was evaporated under a nitrogen stream. The resulting dried lipid film was hydrated by adding 0.600 mL of CA, GA, or VB12 solution in PBS, at 4.0, 3.6, and 1.0 mM, respectively. The film was vortexed for 10 min to produce MLVs. To reduce the size of the vesicles and produce LUVs, the resulting suspension was sonicated for 40 minutes (1 min ON, 1 min OFF) in an ice-cold water bath using an ultrasonic processor UP400S (Hielscher, Germany) with an amplitude of 40% and ultrasonic frequency of 24 kHz. The natural compound solution was replaced by PBS to prepare unloaded liposomes.

4.2.2.2. Reverse-Phase Evaporation

The reverse-phase evaporation is a simple alternative technique to the lipid film hydration. Here, phospholipids are dissolved in a water-immiscible organic solvent. Then, a water-in-oil emulsion is created by brief sonication, and the organic solvents evaporated under reduced pressure to produce a semi-solid gel. The gel is subject to a vigorous mechanical agitation to reverse the water-in-oil into an oil-in-water emulsion containing LUVs and MLVs. Lower concentrations of phospholipids yield higher amounts of LUVs compared to MLVs. This process ensures high encapsulation rates due to the large volume: lipid ratio [6]. However, the use of high amounts of organic solvents, mechanical agitation, the possibility of the product containing solvent residues, and difficulty in scaling up remains its major limitations [7].

Here, lipids were dissolved in 0.600 mL of diethyl ether, and 0.050 mL of methanol was added to increase the lipids' solubility. 0.240 mL of a CA, GA, or VB12 solution in PBS at 10.0, 9.0, and 2.5 mM, respectively, was added dropwise to the organic phase. The resulting

two-phase system was sonicated for 5 min in a cold-water bath sonicator (ultrasonic cleaner, VWR, USA), resulting in a homogeneous opalescent dispersion. The mixture was placed on a 5 mL glass beaker under magnetic stirring (400 rpm) for 1 h at room temperature to allow the complete evaporation of the organic solvents, resulting in the formation of a viscous gel. PBS was added to the gel completing a final volume of 0.600 mL. The vesicles' size was reduced as described previously. Unloaded liposomes were developed by replacing the natural compound solution with PBS.

4.2.2.3. Ethanol Injection

The injection of organic solvents is widely used to produce liposomes. Here, phospholipids dissolved in an organic solvent, such as ethanol, are gradually injected into a warm aqueous solution of the molecule to be encapsulated, spontaneously forming liposomes. When ethanol is injected and dissolved in the water below a critical concentration, the phospholipids are forced to self-assemble in the aqueous phase and form liposomes. A higher concentration of phospholipids leads to an increase in the size, polydispersity, and lamellarity of liposomes. The main drawbacks of this technique are the heterogeneity of the population when compared to other methods [6]. Also, the exposure of the compounds to be encapsulated to organic solvents and high temperatures can affect the stability and biocompatibility of the liposomes [8]. However, the simplicity, rapidity, reproducibility, and ease of scaling up this technique make it a promising methodology for industry applications [9].

Here, lipids were dissolved in 0.120 mL of absolute ethanol. The resulting organic phase was injected in 0.600 mL of a CA, GA, or VB12 solution in PBS at 4.0, 3.6, and 1.0 mM, respectively, under magnetic stirring (400 rpm). The liposome suspension was kept under stirring for 1 h at room temperature to allow the complete evaporation of ethanol. The liposomes' size was reduced as described above. Unloaded liposomes were prepared by replacing the natural compound solution with PBS.

4.2.2.4. Ethanol Permeabilization

The ethanol permeabilization technique is a simple and rapid passive equilibration method that relies on adding molecules to preformed liposome in the presence of a permeability enhancer – ethanol. This permeability enhancer increases the lipid

bilayer permeability and, consequently, the drug diffusion through the lipid membrane without significantly affecting the NPs' structure [10].

Here, 0.219 mL of absolute ethanol containing CA, GA, or VB12 at 9.3, 8.4, and 2.3 mM, respectively, was added dropwise to liposomes (30% v/v) previously prepared by the lipid film hydration method followed by sonication under constant manual shaking. Samples were incubated at 37 °C for 1 h in an incubating microplate agitator under continuous stirring (350 rpm) (VWR, USA) to enhance the lipid bilayer's permeability. Samples were then placed under magnetic stirring (400 rpm) for 1 h at room temperature allowing the organic solvent to evaporate. Unloaded liposomes were prepared by replacing the natural compound solution in ethanol with pure ethanol.

4.2.3. Determination of Entrapment Efficiency and Loading Capacity

The entrapment efficiency and the loading capacity were determined by an indirect method, quantifying the amount of unencapsulated CA, GA, or VB12. The unencapsulated natural compound was separated from the natural compound-loaded liposomes using centrifugal filters (Amicon® Ultra 0.500 mL Centrifugal Filter Devices, 30 kDa, Merck, Germany). Briefly, 0.500 mL of sample was subjected to two consecutive centrifugation cycles at 14,500 rpm at room temperature for 30 min (MiniSpin®plus, Eppendorf, Germany). The concentrated solute containing natural compound-loaded liposomes was collected and stored at 4 ˚C for further analysis. The two filtrates containing free CA, GA, or VB12 were mixed and quantified by UV–Vis spectroscopy (Synergy 2 Multi-Mode Microplate Reader, BioTek Instruments, USA) at the wavelength of 282, 258, and 360 mm, respectively. The obtained absorbance value was correlated to the corresponding calibration curve. The entrapment efficiency (EE) was calculated by the following equation (Equation 4.1):

$$\text{EE (\%)} = \frac{\text{Total amount of natural compound (mg) - amount of free natural compound (mg)}}{\text{Total amount of natural compound (mg)}} \text{ x } 100$$

Equation 4.1

The loading capacity (LC) of the prepared liposomes was calculated as follows (Equation 4. 2):

$$\text{LC (\%)} = \frac{\text{Total amount of natural compound (mg) - amount of free natural compound (mg)}}{\text{Total amount of lipids (mg)}} \text{ x } 100$$

Equation 4.2

4.2.4. Functionalization of Liposomes with Transferrin

The liposomes' surface was modified with Tf, according to Pinheiro et al. [11]. Tf molecules were covalently coupled by their carboxyl groups to the amino group of DSPE-PEG2000 present on the liposomes' surface using EDC as a coupling agent. First, a Tf solution was prepared in PBS at 21 μM, and EDC was added at 100x molar excess. The mixture was stirred for 30 min at 500 rpm and at room temperature to activate the Tf's carboxyl groups. Free EDC was separated from the Tf-EDC using centrifugal filters (Amicon® Ultra 0.500 mL Centrifugal Filter Devices, 3 kDa, Merck, Germany) at 14,500 rpm at room temperature for 30 min. The concentrated solute was resuspended in PBS and mixed to liposomes at a molar ratio of 1:750 (Tf:liposome). The sample was incubated for 1 h at 4 °C and 500 rpm to form Tf-conjugated liposomes.

4.2.5. Determination of Transferrin Conjugation Efficiency

Unbound Tf was separated from the Tf-functionalized liposomes using centrifugal filters (100 kDa cutoff). The sample was subjected to two consecutive centrifugation cycles at 14,500 rpm and room temperature for 30 min. The concentrated solute containing Tf-conjugated liposomes was collected and stored at 4 ˚C for further analysis. To separate unbound Tf from released natural compound, the two filtrates were mixed and subjected to centrifugation using centrifugal filters (Amicon® Ultra 0.500 mL Centrifugal Filter Devices, 3 kDa, Merck, Germany). The free natural compound was quantified as previously described. Unbound Tf was then quantified using the PierceTM bicinchoninic acid (BCA) Protein Assay Kit (Thermo Fisher Scientific, USA). Here, the free Tf sample was incubated with the working reagent in a 96-well plate at 37 ˚C for 30 min. The absorbance of Tf was determined by UV−Vis spectroscopy (Synergy 2 Multi-Mode Microplate Reader, BioTek Instruments, USA) at the wavelength of 560 mm. The obtained absorbance value was correlated to the Tf's calibration curve, and the conjugation efficiency (CE) was determined according to the following equation (Equation 3.3):

$$\text{CE (\%)} = \frac{\text{Total amount of Tf (mg)- amount of free Tf (mg)}}{\text{Total amount of Tf (mg)}} \text{ x } 100 \qquad \text{Equation 3.3}$$

The number of Tf molecules per liposome was determined based on the number of lipids per liposome (N), which was estimated as follows (Equation 3.4):

$$N = \frac{4\,\pi\,(\frac{d}{2})^2 + 4\,\pi\,(\frac{d}{2} - h)^2}{a} \qquad \text{Equation 3.4}$$

where d is the diameter of the liposome, h is the thickness of the bilayer, and a is the lipid head group area.

4.2.6. Physicochemical Characterization of Liposomes

4.2.6.1. Dynamic Light Scattering

DLS was employed to physicochemically characterize the liposomes in terms of hydrodynamic diameter and PdI using a ZetaSizer Nano ZS (Malvern Instruments, UK). Liposomes were analyzed with a 633 nm red laser with a backscattering angle of 173° at 25 °C. The refractive index and viscosity of water (dispersant) were fixed at 1.330 and 0.8872 cP, respectively. The lipids' refractive index and absorption were set at 1.40 and 0, respectively. The obtained results were given as size distribution by intensity and result from 3 measurements of 12 runs each.

4.2.6.2. Electrophoretic light scattering

The zeta potential of the prepared liposomes was assessed by ELS using a ZetaSizer Nano ZS (Malvern Instruments, UK). Zeta potential values were obtained employing the Smoluchowski mathematical model. The dielectric constant, refractive index, and viscosity of the dispersant were set at 78.5, 1.330, and 0.8872 cP, respectively. The refractive index and absorption of the lipids were fixed at 1.40 and 0, respectively. Zeta potential values result from 5 measurements of 15 runs each. All the measurements were performed at 25°C.

4.2.6.3. Attenuated Total Reflection-Fourier Transform Infrared Spectroscopy

ATR-FTIR was used to confirm the lipids' functionalization with Tf, according to a prior work [12]. ATR-FTIR spectra were collected using an ALPHA-P spectrophotometer (Bruker Corporation, Billerica, MA, EUA). Succinctly, 2 µL of the concentrated solute

containing Tf, Tf-conjugated, or unconjugated liposomes were placed on the surface of the FTIR crystal. The water was removed using a nitrogen stream, and the ATR-FTIR spectra were recorded in the absorbance mode from 375 to 4000 cm^{-1} at 4 cm^{-1} resolution. The background spectrum was also collected and subtracted from the lipids' spectrum. ATR-FTIR spectra were obtained after 64 scans.

4.2.7. Stability of Liposomes at Storage Conditions

The stability of the prepared liposomes was investigated for two months at storage conditions (4 °C). The liposomes' stability was evaluated by variations of the hydrodynamic diameter, PdI, and zeta potential over time. The physicochemical properties of the NPs were assessed as described above. The samples were also subjected to visual observation to identify any occurrence of phase separation or flocculation, both indicating stability issues.

4.2.8. *In vitro* Natural Compound Release from Transferrin-Functionalized Liposomes

The *in vitro* release profile of CA, GA, or VB12 from the developed Tf-modified liposomes in simulated physiological conditions was studied using the cellulose dialysis membrane diffusion technique, as reported previously [13]. Before starting the drug release experiment, cellulose dialysis membranes (Float-A-Lyzer G2, CE, 10 kDa, SpectrumLabs, Los Angeles, CA, USA) were equilibrated with ultrapure water overnight and PBS for 1h at 4 °C. A known amount of CA, GA, or VB12-loaded Tf-liposomes was diluted in 1 mL of PBS and placed into the inner membrane. The outer space of the dialysis device was filled with 5 mL of PBS (10 mM, pH 7.4), ensuring the sink conditions. The dialysis device was continuously stirred at 250 rpm and 37 °C for 9 days. Aliquots of 300 μL were collected from the release medium at predetermined time points. The amount of released CA, GA, or VB12 was quantified by UV–Vis spectrophotometry (Synergy 2 Multi-Mode Microplate Reader, BioTek Instruments, USA) at the wavelength of 282, 258, and 360 mm, respectively, and correlated to the respective calibration curve. The natural compound release curve representing the percentage of CA, GA, or VB12 released over time (t) was plotted according to the following equation (Equation 3.5):

$$\text{Natural compound released (\%)} = \frac{\text{Amount of natural compound released at time t (mg)}}{\text{Amount of encapsulated natural compound (mg)}} \text{ x } 100$$

Equation 3.5

After absorbance measurements, the sample was returned to the release medium. Solutions of CA, GA, or VB12 in PBS were used as controls.

4.2.9. Anti-Amyloidogenic Properties of Transferrin-Functionalized Liposomes Loaded with Natural Compounds

4.2.9.1. Aβ Preparation

Stock solutions of $A\beta_{1-42}$ monomers and fibrils were prepared as described previously in section 3.2.3.

4.2.9.2. Thioflavin T Fluorescence Assay

The anti-amyloidogenic activity of CA, GA, or VB12-loaded Tf-functionalized liposomes was monitored by employing a well-established protocol [14]. Briefly, aggregation kinetics was evaluated by mixing CA, GA, or VB12-loaded Tf-liposomes to $A\beta_{1-42}$ monomers or fibrils (8 μM) in a 96-well plate (black, non-treated, flat bottom, UV-Star®). Respective negative controls in the absence of natural compound-loaded Tf-liposomes were also prepared. The anti-amyloidogenic activity of CA (800 μM), GA (800 μM), VB12 (160 μM), and unloaded Tf-liposomes were also assessed as positive controls. A ThT solution in PBS was added to the samples at a final concentration of 50 μM. The microplate was sealed to prevent evaporation and incubated for 5 h at 37 °C with continuous medium stirring. Fluorescence measurements were recorded every 30 s using a Synergy™ 2 Multi-Mode Microplate Reader (BioTek Instruments, Winooski, VT, USA) equipped with a 420/50 nm excitation filter and a 485/20 nm emission filter.

4.2.9.3. Kinetic Model of Aβ Fibril Formation

ThT fluorescence data were processed as described in section 3.2.5.

4.2.9.4. Transmission Electron Microscopy

Grids TEM were prepared as described in section 3.2.6.

4.2.10. Statistical Analysis

Results are given as the mean ± SD of at least three independent experiments. Student's t-tests with a 95% confidence interval were employed to assess significant differences between data. GraphPad Prism 8 software was used to analyze the data.

4.3. Results and Discussion

4.3.1. Transferrin-Functionalized Liposomes Loaded with Caffeic Acid

The results presented in this section are submitted for publication: *Andrade, S., Loureiro, J.A. & Pereira, M.C. Caffeic Acid-Loaded Liposomes Functionalized with Transferrin for Alzheimer's Disease Therapy. Submitted to Journal of Molecular Liquids.*

4.3.1.1. Physicochemical Characterization of Unloaded and CA-Loaded Liposomes

DSPC, CHOL, 18:0 PEG2000 PE, and DSPE-PEG2000 were the lipids selected to prepare liposomes since there is evidence of the safety of this particular DDS following repeated administration in wild-type mice [15]. NPs' physicochemical properties, including mean size, PdI, zeta potential, EE, and LC, play a significant role in how NPs perform biologically. Hence, four distinct methods for producing liposomes were employed to obtain the optimal formulation: lipid film hydration, reverse-phase evaporation, ethanol injection, and ethanol permeabilization. The physicochemical properties of the produced unloaded and CA-loaded liposomes are listed in Table 4.1.

Table 4.1. Physicochemical characterization of unloaded and CA-loaded liposomes. * Indicates a statistical difference between unloaded and CA-loaded liposomes ($p<0.05$).

Technique	Liposomes' formulation	Size (nm)	PdI	Zeta potential (mV)	EE (%)	LC (%)

Lipid film hydration	Unloaded LIP	111 ± 8	0.21 ± 0.02	-0.5 ± 1.7	-	-
	CA-loaded LIP	118 ± 10	0.27 ± 0.06	-2.4 ± 0.7	4 ± 2	0.7 ± 0.4
Reverse-phase evaporation	Unloaded LIP	125 ± 7	0.19 ± 0.02	-1.3 ± 1.3	-	-
	CA-loaded LIP	142 ± 6 *	0.24 ± 0.04 *	-1.3 ± 1.0	23 ± 4	3.0 ± 0.6
Ethanol injection	Unloaded LIP	139 ± 15	0.19 ± 0.02	-1.7 ± 0.5	-	-
	CA-loaded LIP	162 ± 9 *	0.20 ± 0.04	-1.6 ± 0.5	20 ± 1	2.7 ± 0.1
Ethanol permeabilization	Unloaded LIP	113 ± 4	0.19 ± 0.01	-1.7 ± 0.5	-	-
	CA-loaded LIP	119 ± 6	0.25 ± 0.03 *	-0.8 ± 1.1	17 ± 2	2.3 ± 0.2

The NPs' hydrodynamic diameter is a key property affecting their capacity to cross biological barriers, including the BBB, *in vivo* stability, blood circulation time, drug release, cell uptake, clearance, and toxicity. NPs larger than 200 nm have been described to be quickly cleared from the bloodstream by the lymphatic system. In contrast, NPs smaller than 50 nm have been associated with severe toxicity due to their increased surface area [16]. Additionally, 200 nm is the estimated maximum size for a NP to undergo RMT [17].

As shown in Table 4.1, all the produced formulations presented a mean size smaller than 200 nm regardless of the technique used to produce liposomes, thus being suitable for brain delivery. Additionally, Table 4.1 reveals that the size of unloaded and CA-loaded liposomes significantly depends ($p<0.05$) on the employed technique by the following order: ethanol injection = reverse-phase evaporation > ethanol permeabilization = lipid film hydration. Furthermore, the NPs' size was affected by the CA's encapsulation using reverse-phase evaporation and ethanol injection techniques ($p<0.05$). Both methods led to a significant increase in CA-loaded liposomes' sizes compared to unloaded NPs ($p<0.05$). This may be due to the higher EE obtained for these techniques compared to lipid film hydration and ethanol permeabilization methods, implying that more CA molecules are loaded into the liposomes.

The detailed examination of Table 4.1 also reveals that all formulations exhibit PDI values lower than 0.3, suggesting that the produced liposomes have homogenous diameters [18]. No significant differences in PdI values of unloaded liposomes were observed between the groups ($p>0.05$). However, encapsulating CA by reverse-phase evaporation and ethanol permeabilization led to an increase in PdI ($p<0.05$).

Another important factor to consider while designing NPs is their surface charge because it influences the NPs' toxicity and *in vivo* internalization rates. The liposomes' zeta

potential was assessed, and all formulations showed values close to 0 mV (Table 4.1), which is expected given the lipids composing the liposomes. In contrast to cationic NPs and highly concentrated anionic NPs, which can be harmful to the BBB, neutral NPs have a higher potential to cross the BBB without impacting its integrity [19]. Additionally, neutral NPs exhibit less protein adsorption, which results in longer circulation times [17]. As shown in Table 4.1, encapsulating CA did not modify the liposomes' zeta potential regardless of the liposome production technique ($p>0.05$).

Manufacturing procedures with less material loss, cheaper costs, and more environmentally friendly products are required to produce NPs efficiently. High EE and LC values are thus preferred. Table 4.1 shows that the EE and LC values depend on the method used to produce the liposomes ($p<0.05$) in the following order: reverse-phase evaporation = ethanol injection > ethanol permeabilization > lipid film hydration. This observation is consistent with previous evidence reporting that despite being the oldest and simplest technique to prepare liposomes, the thin-film hydration method leads to lower EE than the remaining techniques [7].

Based on the presented results, reverse-phase evaporation was selected to prepare CA-loaded liposomes for the following assays.

4.3.1.2. Functionalization of Liposomes with Tf

The surface of unloaded and CA-loaded liposomes was functionalized with Tf envisaging the dual-targeting strategy of the NPs to the BBB and neurons [20]. Holo-Tf was chosen over other Tf forms, such as apo-Tf, due its higher affinity for the TfR [21]. The liposomes' functionalization was achieved using EDC as a coupling agent. EDC activates the carboxyl groups of Tf through a carbodiimide-coupling reaction, allowing its covalent coupling of with the amino group of DSPE-PEG2000. Table 4.2 displays the physicochemical properties of the produced liposomes as well as the CE of Tf.

Table 4.2. Physicochemical characterization of unloaded and CA-loaded Tf-functionalized liposomes. * Denotes a statistical difference between unloaded and CA-loaded liposomes ($p<0.05$). # Indicates a statistical difference between unloaded Tf-liposomes and CA-loaded Tf-liposomes ($p<0.05$).

Formulation	Size (nm)	PdI	Zeta potential (mV)	EE (%)	LC (%)	CE (%)
Unloaded LIP	125 ± 7	0.19 ± 0.02	-1.3 ± 1.3	-	-	-
Unloaded Tf-LIP	129 ± 6	0.18 ± 0.01	-1.4 ± 1.0	-	-	31 ± 3
CA-loaded LIP	142 ± 6 *	0.24 ± 0.04 *	-1.3 ± 1.0	23 ± 4	3.0 ± 0.6	-
CA-loaded Tf-LIP	139 ± 9	0.20 ± 0.03	-0.9 ± 0.6	23 ± 4	3.1 ± 0.6	21 ± 1 #

As displayed in Table 4.2, the functionalization of both unloaded and CA-loaded liposomes with Tf did not impact the NPs' physicochemical properties ($p>0.05$). Furthermore, no CA was released in the functionalization process ($p>0.05$), with Tf-functionalized liposomes displaying an EE of 23 ± 4 %. This is consistent with previous studies that reported no drug release from lipid-based NPs at 4 °C [22, 23], the temperature at which the functionalization of liposomes was performed. In addition, Table 4.2 reveals that encapsulating CA into the liposomes decreased the CE from 31 ± 3 to 21 ± 1 % (<0.05). These values correspond to 100 ± 10 and 78 ± 3 molecules of Tf per liposome, amounts that enable NPs to cross the BBB by RMT [24]. This may be due to the presence of some CA molecules at the surface of the liposome, which may hinder the coupling of Tf with the amino group of DSPE-PEG2000. In fact, it was demonstrated in a previous study that CA has an affinity for the liposomes' lipid bilayer by establishing ion-dipole forces with the negative charge of the DMPC polar head [14]. Overall, CA Tf-functionalized liposomes exhibited suitable physicochemical properties for brain delivery.

ATR-FTIR was employed to confirm the lipids' functionalization with Tf. Figure 4.1 shows the ATR-FTIR spectra of non-functionalized and Tf-functionalized lipids, both in the absence and presence of CA. The ATR-FTIR spectrum of Tf is also presented for comparison purposes.

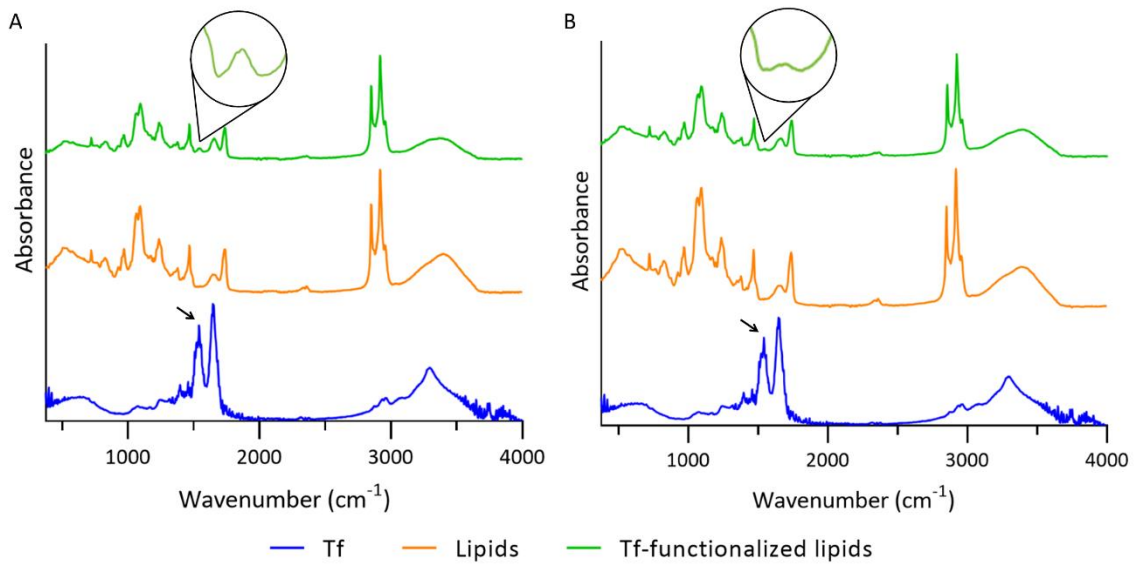

Figure 4.1. ATR-FTIR spectra of Tf (blue line), non-functionalized lipids (orange line), and Tf- functionalized lipids (green line) in the A) absence and B) presence of CA.

The ATR-FTIR spectrum of Tf (blue line) displayed in Figure 4.1 shows two major peaks at 1647 (amine I) and 1541 cm^{-1} (amine II). These bands correspond, respectively, to the C=O stretching vibrations and N-H bending vibrations found in the peptide bonds between the amino acids of Tf [25]. Both peaks can be seen in Tf-functionalized lipids (green line), regardless of the CA encapsulation, in contrast to non-functionalized lipids (orange line), which lack the amine I peak. Moreover, Figure 4.1 reveals that the intensity of the amine II peak in the presence of CA (Figure 4.1 B) is less than in the absence of the natural compounds (Figure 4.1 A), probably due to the lowest CE attained for CA-loaded liposomes. These results confirm the successful functionalization of the lipids with Tf, regardless of the CA encapsulation.

4.3.1.3. Physical Stability of Liposomes at Storage Conditions

The stability of NPs at storage conditions continues to be a major restriction to their commercialization. It is mandatory to ensure that the NPs' physicochemical properties do not change during storage since variations in these characteristics imply changes in the liposomes' structure [26]. Therefore, the produced liposomes' physical stability was periodically evaluated at 4 °C for 2 months. Figure 4.2 shows the mean size, PdI, and zeta

potential of unloaded and CA-loaded liposomes, both with and without Tf functionalization over storage time.

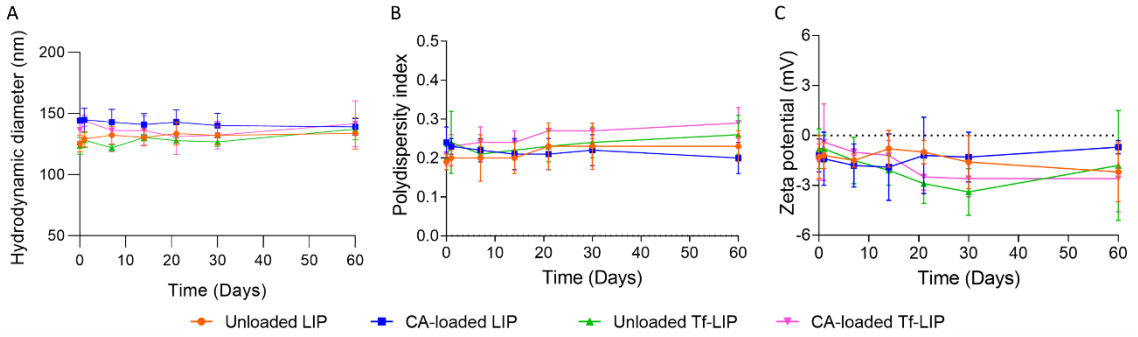

Figure 4.2. Physicochemical characterization of unloaded (orange), CA-loaded (blue), Tf-functionalized (green), and CA-loaded Tf-functionalized liposomes (pink) stored for 2 months at 4 °C.

As presented in Figure 4.2, no significant variations in the measured physicochemical properties of all liposomal formulations were observed over the storage period at 4 ˚C ($p>0.05$). No creaming, flocculation, or phase separation was visible in any of the formulations. These findings indicate that the liposomes remain stable for 2 months under storage conditions, regardless of CA loading and NPs functionalization with Tf.

4.3.1.4. *In vitro* Release of CA

The effectiveness of a DDS is greatly influenced by the drug release profile. The sustained release of drugs is desired to maintain the drug concentration in plasma at therapeutic levels for an extended period. Thereby, optimal drug therapeutic efficacy can be achieved while minimizing adverse effects [27]. Thus, the *in vitro* release of CA from the produced Tf-functionalized liposomes under simulated physiological conditions (37 °C, PBS, pH 7.4, 10 mM) was investigated and compared to free CA. Figure 4.3 displays the obtained release profiles.

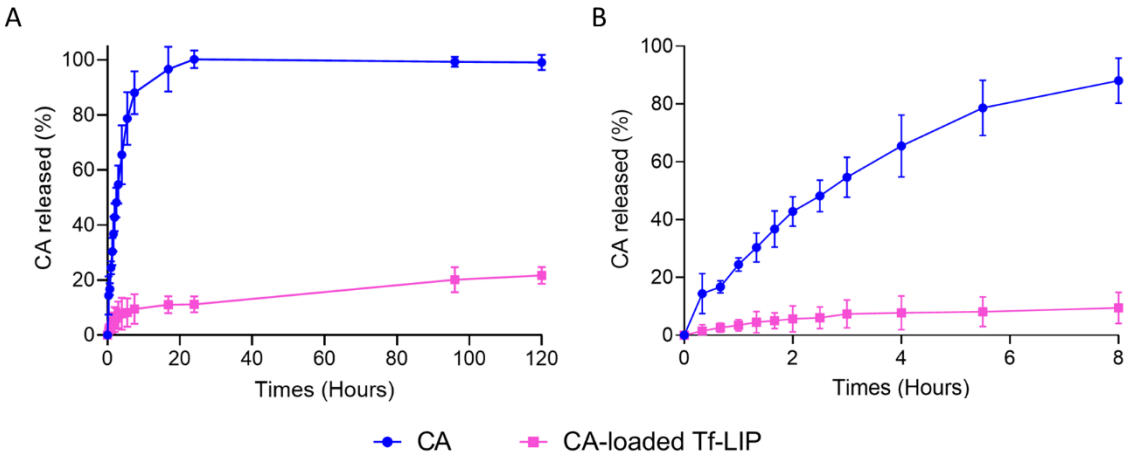

Figure 4.3. A) *In vitro* release profiles of free CA (blue) and CA-loaded Tf-functionalized liposomes (pink) at 37 °C in PBS (pH 7.4, 10 mM) over 120 h. B) shows the *in vitro* release profiles in the first 8 h.

As depicted in Figure 4.3, the *in vitro* release of CA from the Tf-functionalized liposomes (pink data) exhibits a sustained profile. In contrast to the control group (free CA) (blue data), which was completely released in 24 hours, Tf-functionalized liposomes only released 11 ± 3 % of CA over this time (pink data) ($p<0.05$). As shown in Figure 4.3 B, CA molecules started to release from Tf-functionalized liposomes immediately, achieving 8% of CA release in the first 4 h. This phenomenon is frequently ascribed to the desorption of molecules that have been adsorbed at the liposomes' surface [28]. After this burst release, a slower and controlled CA release is observed, with about 14% of the natural compounds being released until the end of the experiment. These results are in line with the liposomal dispersions' biphasic release patterns [29].

Since CA is poorly soluble in water, it is expected to be kept in the liposomes' phospholipid bilayer instead of released to the release medium. This is supported by Andrade et al. (2021) findings, which revealed the CA's ability to partition from the aqueous medium to the liposomes' lipid bilayer. Previous data also suggest that the presence of PEG and Tf molecules at the NPs' surface blocks the drug diffusion to the release medium [30, 31]. It is thus expected that CA molecules retained in the liposomes' lipid bilayer will be further released in the target site in a controlled and sustained manner due to the liposomes' degradation [32].

4.3.1.5. Anti-Amyloidogenic Activity of CA-Loaded Liposomes Functionalized with Transferrin

4.3.1.5.1. Inhibition of Aβ Fibril Formation

The therapeutic efficacy of the developed brain targeted-DDS in inhibiting the $A\beta_{1-42}$ fibrillation was investigated through a ThT fluorescence assay combined with a kinetic model of amyloid fibril formation. ThT is a benzothiazole dye that displays enhanced fluorescence after binding to amyloid fibrils. ThT fluorescence assay is widely employed for amyloid fibril detection and quantification since there is a direct correlation between the intensity of ThT fluorescence and the extent of amyloid fibrils [14].

To this end, Aβ monomers were incubated with CA, unloaded Tf-functionalized liposomes, and CA-loaded Tf-functionalized liposomes for 2 h at 37 °C, and the ThT fluorescence was recorded. The results of the ThT fluorescence assay are shown in Figure 4.4.

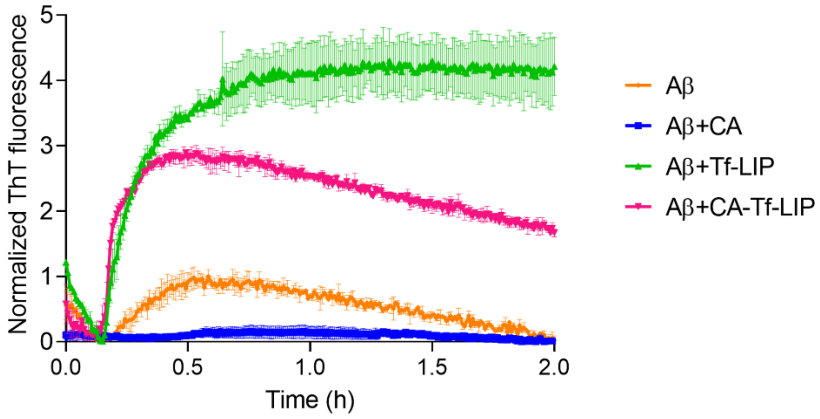

Figure 4.4. Normalized ThT fluorescence of Aβ1−42 (orange data) as a function of time (h) upon incubation with CA (blue data), Tf-functionalized liposomes (green data), and CA-loaded Tf-functionalized liposomes (pink data).

The kinetic curves corresponding to Aβ in the absence and presence of unloaded and CA-loaded Tf-functionalized liposomes exhibit a typical sigmoidal pattern, as depicted in Figure 4.4, which has been seen in earlier investigations [12]. Each kinetic curve starts with a low ThT fluorescence intensity, implying the absence of Aβ fibrils. In this stage, often called the lag phase, Aβ monomers aggregate to form oligomers. Oligomers then aggregate into Aβ fibrils, a process known as the elongation phase. In this phase, a gradual increase is

observed as the fibrils form, followed by the stationary phase, characterized by a plateau when all Aβ peptides are assembled into fibrils.

The kinetic parameters for each of the ThT curves were obtained by fitting Equations 6 and 7 to the data and are presented in Table 4.3.

Table 4.3. Kinetic parameters calculated by fitting Equations 3.6 and 3.7 to the ThT data. * Signifies a statistical difference compared to the control (Aβ) ($p<0.05$). # Indicates a statistical difference between unloaded and CA-loaded Tf-functionalized liposomes ($p<0.05$).

Kinetic Parameters	Aβ	Aβ + CA	Aβ + Tf-LIP	Aβ + CA-Tf-LIP
t_{lag} (h)	0.18 ± 0.02	n.d.	0.07 ± 0.01 *	0.14 ± 0.01 *,#
$t_{1/2}$ (h)	0.30 ± 0.02	n.d.	0.27 ± 0.02	0.19 ± 0.01 *,#
k (h^{-1})	16 ± 1	n.d.	10 ± 1 *	39 ± 4 *,#
Max. Fluorescence	0.9 ± 0.1	n.d.	4.4 ± 0.1 *	2.7 ± 0.1 *,#

n.d. not determined

Free CA significantly modified the kinetic curve of $Aβ_{1-42}$, as shown in Figure 4.4. No significant increase in the ThT fluorescence signal was observed after incubating Aβ monomers with CA ($p>0.05$) (blue data). Moreover, the ThT intensity remained constant throughout the experiment ($p>0.05$), indicating that CA completely inhibits the Aβ fibril formation. Comparable effects were reported previously [14].

Figure 4.4 also reveals that unloaded Tf-functionalized liposomes significantly impacted the formation of Aβ fibrils (green data). From Table 4.3, it can be seen that the NPs significantly reduced the lag phase time compared to Aβ from 0.18 ± 0.02 to 0.07 ± 0.01 h ($p<0.05$), inferring that unloaded Tf-functionalized liposomes accelerate the transition of Aβ monomers to oligomers. Furthermore, unloaded Tf-functionalized liposomes significantly decreased the elongation rate from 16 ± 1 to 10 ± 1 h^{-1} ($p<0.05$), implying that the unloaded NPs slow the transition from oligomers to fibrils. Table 4.3 also reveals that the maximum ThT fluorescence significantly increased by approximately 5-folds compared to untreated Aβ (orange data) ($p<0.05$), suggesting that unloaded Tf-functionalized liposomes increase substantially the amount of fibrils. The findings are in accordance with

previous reports demonstrating that lipid-based NPs, including liposomes, promote the Aβ fibril formation by acting as aggregation nuclei [11, 23, 33].

Additionally, it is evident from Figure 4.4 that CA-loaded Tf-functionalized liposomes also altered the Aβ's fibrillation kinetic (pink data). CA-loaded NPs significantly increased the lag phase time compared to unloaded Tf-functionalized liposomes (green data) ($p<0.05$), implying that the presence of CA in the NPs decelerate the transition of Aβ monomers to oligomers. In addition, a significant increase in the elongation rate was observed compared to untreated Aβ (orange data) ($p<0.05$), thus decreasing the time needed for half of the maximum ThT fluorescence intensity to be reached ($p<0.05$). Moreover, CA-loaded Tf-functionalized liposomes significantly reduced the maximum fluorescence intensity by approximately 1.6-fold compared to unloaded NPs ($p<0.05$). Despite CA-loaded Tf-functionalized liposomes accelerating the transition of Aβ oligomers to fibrils, the amount of fibrils formed is significantly lower than in the absence of the natural compound. It can thus be concluded that the CA released during the ThT fluorescence assay (2 h) is enough to contradict the nucleation effect of the unloaded Tf-functionalized liposomes. Predictably, the ability of the developed DDS to prevent the formation of Aβ fibrils could be even higher *in vivo* due to the release of CA molecules that remain retained in the liposomes' lipid bilayer.

TEM was used to examine the morphology of Aβ following 2 h of incubation at 37 °C in the presence of CA, unloaded, and CA-loaded Tf-functionalized liposomes (Figure 4.5). This high-resolution imaging method is frequently used to gather in-depth information about the shape, size distribution, and structural details of amyloid fibrils and prefibrillar species. Without CA (Figure 4.5 A), Aβ formed thin and long fibrils. In turn, in the presence of the natural compound, Aβ mainly formed small structures, although few fibrils can also be observed (Figure 4.5 B). Figures 4.5 C and D confirm the presence of fibrils after incubating Aβ with unloaded and CA-loaded liposomes, respectively. No major differences in the fibrils' morphology were observed between the groups.

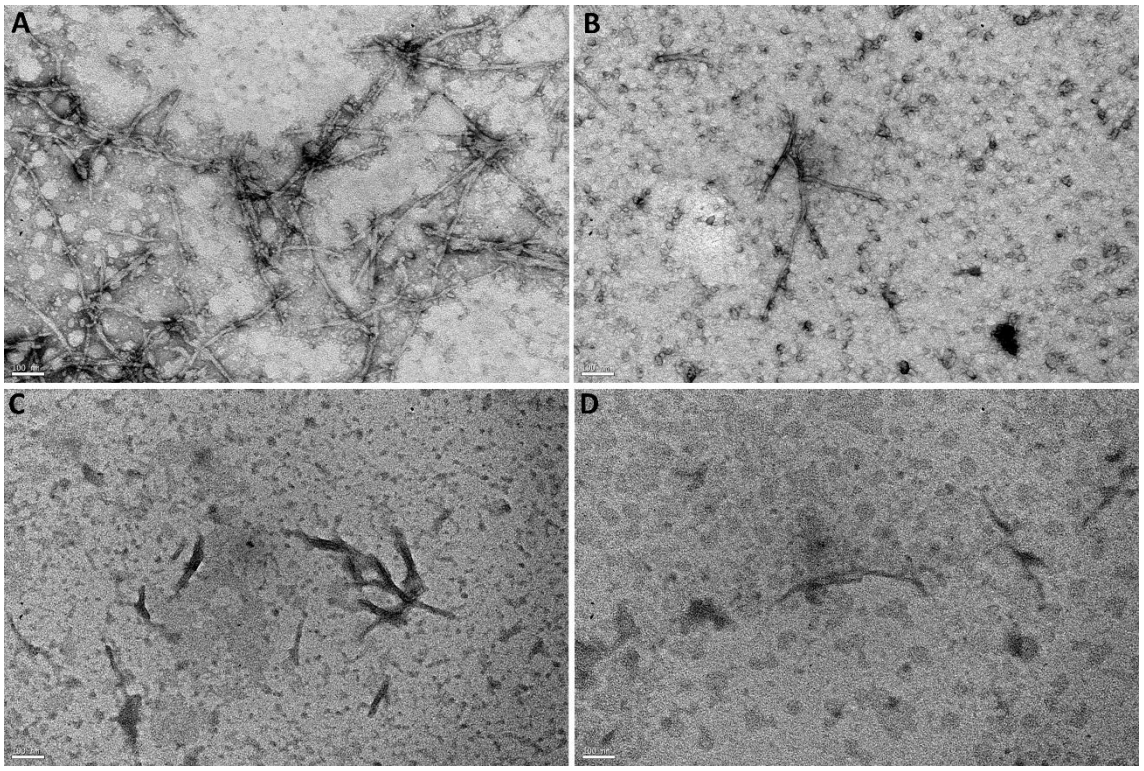

Figure 4.5. TEM images of A) Aβ1−42 incubated with B) CA, C) Tf-functionalized liposomes, and D) CA-loaded Tf-functionalized liposomes for 2 h at 37 °C. Scale bars correspond to 100 nm.

4.3.1.5.2. Disaggregation of Mature Aβ Fibrils

The therapeutic efficacy of the developed brain targeted-DDS in disaggregating preformed $A\beta_{1-42}$ fibrils was investigated through a ThT fluorescence assay. For this purpose, mature fibrils were produced by incubating Aβ peptide for 1 h at 37 °C. The fibrils were then incubated with CA, unloaded, and CA-loaded Tf-functionalized liposomes for 1 h at 37 °C while recording the ThT fluorescence. Figure 4.6 displays the entire set of normalized ThT fluorescence data, and Table 4.4 summarizes the Aβ fibril content after incubating preformed fibrils with CA, unloaded, and CA-loaded Tf-functionalized liposomes.

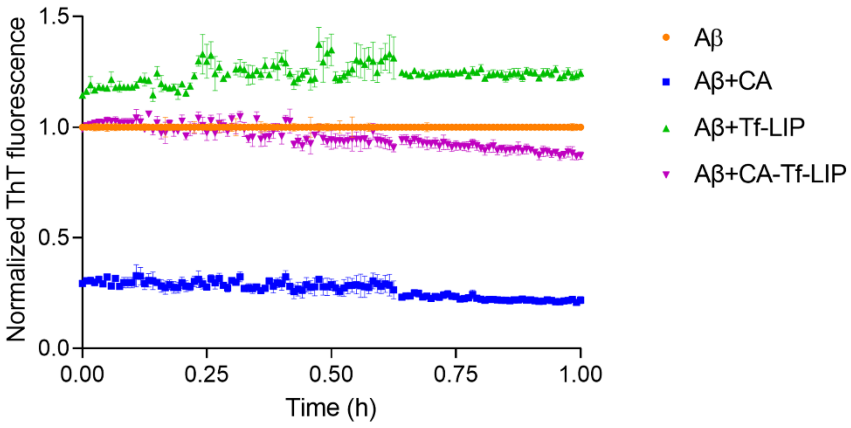

Figure 4.6. Normalized ThT fluorescence of mature Aβ1−42 fibrils (orange data) as a function of time (h) upon incubation with CA (blue data), Tf-functionalized liposomes (green data), and CA-loaded Tf-functionalized liposomes (pink data).

Table 4.4. Percentage of $A\beta_{1-42}$ fibrils disaggregation upon incubation with CA, unloaded, and CA-loaded Tf-functionalized liposomes for 1 h at 37 °C, determined from ThT data. * Indicates a statistical difference compared to untreated Aβ fibrils ($p<0.05$). # Implies a statistical difference between the beginning and end of the assay ($p<0.05$). § Indicates a statistical difference between unloaded and CA-loaded Tf-liposomes ($p<0.05$).

	Aβ Fibril content (%)		
Time (h)	**Aβ + CA**	**Aβ + Tf-LIP**	**Aβ + CA-Tf-LIP**
0	29 ± 1 *	114 ± 1 *	99 ± 1 *, §
1	22 ± 2 *,#	125 ± 2 *,#	87 ± 2 *,#, §

Adding CA, unloaded, or CA-loaded Tf-functionalized liposomes to preformed fibrils significantly affected the fibril content, as displayed in Figure 4.6. CA (blue data) led to an immediate decrease in the ThT fluorescence signal ($p<0.05$) of about 71 %, which increased to 78% after 1 h of incubation at 37 °C ($p<0.05$) (Table 4.4). These results validate the CA's ability to disaggregate Aβ fibrils, as previously observed [14].

Figure 4.6 further shows that unloaded Tf-functionalized liposomes significantly increased the ThT fluorescence signal following their addition to Aβ fibrils (green data) compared to untreated Aβ fibrils (orange data) ($p<0.05$). As shown in Table 4.4, unloaded NPs led to a rapid rise in the fibril content of approximately 14%, which increased to 25%

after 1 h of incubation at 37 °C ($p<0.05$). Encapsulating CA into the Tf-functionalized liposomes (pink data) considerably contradicted the amyloidogenic effect of the unloaded NPs (green data). CA-loaded Tf-functionalized liposomes did not modify the ThT fluorescence intensity compared to untreated Aβ fibrils immediately after their incubation (orange data) ($p>0.05$). However, the ThT signal decreased to 87% after 1 h of incubation, implying a reduction of 13% in the fibril content, probably due to the CA release from the NPs. These findings validate the ability of the developed brain-targeted DDS to disrupt mature fibrils.

The morphology of Aβ fibrils following their incubation with CA, Tf-functionalized liposomes, and CA-loaded Tf-functionalized liposomes for 1 h at 37 °C was also investigated by TEM. Figure 4.7 A shows the presence of long and thin fibrils when those were incubated alone. No discernible differences in the fibrils' morphology were observed between the groups. However, when CA was incubated with Aβ fibrils, shorter structures were detected, and fewer fibrils were noticed in the sample (Figure 4.7 B), validating the CA's capacity to disrupt mature Aβ fibrils.

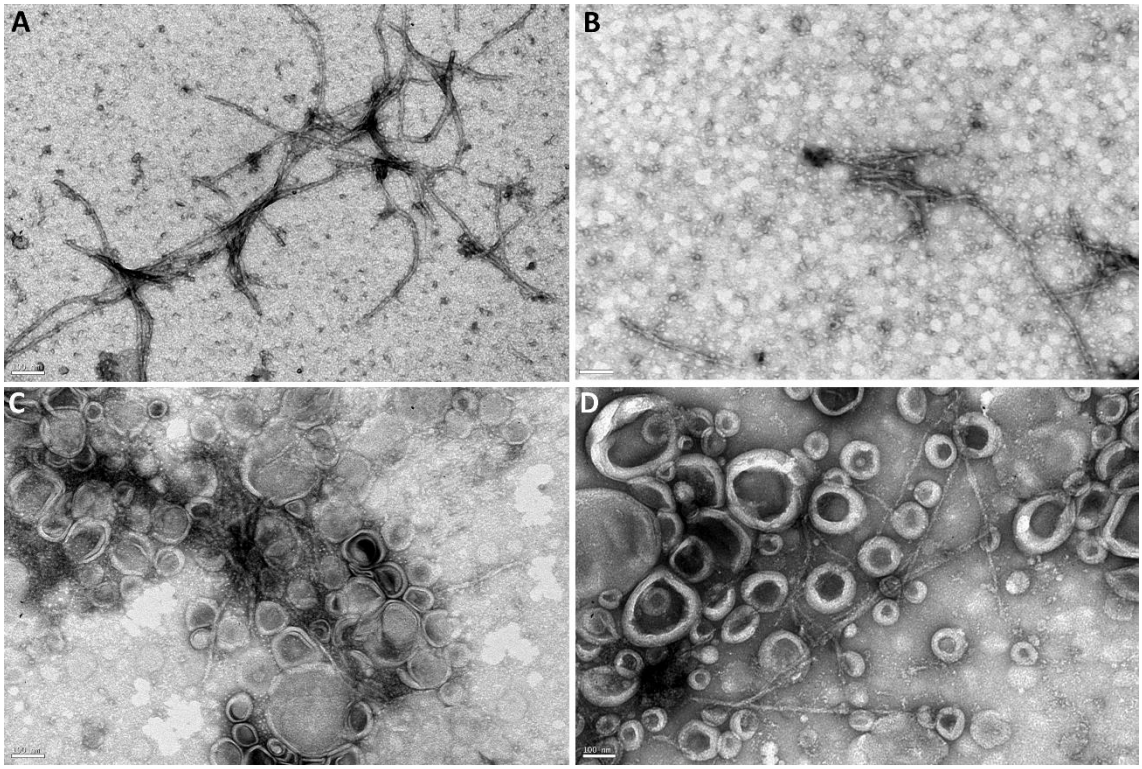

Figure 4.7. TEM images of A) Aβ fibrils after 1 h of incubation at 37 °C with B) CA, C) Tf-functionalized liposomes, or D) CA-loaded Tf-functionalized liposomes. Scale bars correspond to 100 nm.

4.3.2. Transferrin-Functionalized Liposomes Loaded with Gallic Acid

The content of this section is published in: *Andrade, S., Loureiro, J.A. & Pereira, M.C. (2022) Transferrin-Functionalized Liposomes for the Delivery of Gallic Acid: A Therapeutic Approach for Alzheimer's Disease. Pharmaceutics, 14(10), 2163.*

4.3.2.1. Physicochemical Characterization of Unloaded and GA-Loaded Liposomes

GA-loaded liposomes were produced using distinct techniques, including lipid film hydration, reverse phase evaporation, ethanol injection, and ethanol permeabilization, to obtain a formulation with the best physicochemical properties for brain delivery purposes. The liposomes' composition included DSPC, CHOL, 18:0 PEG2000 PE, and DSPE-PEG2000 amine at a molar ratio of 52:45:3:0.06, which was maintained regardless of the technique since these particular NPs proved to be safe after administering intravenously 10 doses over 3 weeks to adult wild-type mice [15] (Chapter 5). The physicochemical properties of the unloaded and GA-loaded liposomes produced using the mentioned procedures are presented in Table 4.5.

Table 4.5. Physicochemical properties of unloaded and GA-loaded liposomes, including hydrodynamic diameter, PdI, zeta potential, EE, and LC.

Technique	Liposomes' formulation	Size (nm)	PdI	Zeta potential (mV)	EE (%)	LC (%)
Lipid film hydration	Unloaded LIP	117 ± 6	0.17 ± 0.03	-2.3 ± 0.6	-	-
	GA-loaded LIP	112 ± 4	0.16 ± 0.02	-2.2 ± 0.1	12 ± 2	0.7 ± 0.1
Reverse-phase Evaporation	Unloaded LIP	129 ± 10	0.17 ± 0.04	-0.7 ± 1.0	-	-
	GA-loaded LIP	126 ± 10	0.18 ± 0.02	-0.4 ± 0.8	29 ± 3	1.7 ± 0.2
Ethanol injection	Unloaded LIP	163 ± 4	0.20 ± 0.03	-1.9 ± 0.5	-	-
	GA-loaded LIP	150 ± 12	0.21 ± 0.07	-1.2 ± 0.4	11 ± 4	0.6 ± 0.2
Ethanol permeabilization	Unloaded LIP	145 ± 2	0.19 ± 0.01	-0.8 ± 0.4	-	-
	GA-loaded LIP	147 ± 5	0.16 ± 0.03	-1.7 ± 0.1	15 ± 4	0.9 ± 0.3

According to Table 4.5, all formulations present mean hydrodynamic diameters larger than 100 nm and smaller than 200 nm, making them appropriate for brain delivery [16, 17]. The technique used to produce liposomes appears to significantly affect their size ($p<0.05$) in the following order: lipid film hydration < reverse-phase evaporation < ethanol permeabilization < ethanol injection. Furthermore, no significant variations in the NPs' size were observed following GA encapsulation, regardless of the employed methodology ($p>0.05$).

Table 4.5's comprehensive analysis further demonstrates that all formulations have PdI values below 0.2 [18]. No significant differences in PdI values of liposomes were observed regardless of the technique used for the NPs production and GA encapsulation ($p>0.05$).

The surface charge of a NP is another key physicochemical property affecting its biodistribution, toxicity, and internalization rates [19]. Neutral NPs are characterized by longer circulation times due to the lower protein adsorption and capacity to cross the BBB without compromising its integrity [17]. Thus, the surface charge of all produced liposomes was investigated, and all formulations displayed zeta potential values close to 0 mV (Table 4.5), which is expected considering the lipids composing the liposomes. No significant variations in the liposomes' zeta potential were noticed regardless of the technique used for the NPs production and GA encapsulation ($p>0.05$).

Another important parameter to consider when developing DDS is the EE. EE depends on the properties of both drug and NPs, including the drug's molecular weight and solubility, NPs size, and drug-NPs chemical interactions, among others [34]. According to Table 4.5, the EE and LC values are influenced by the liposome production technique ($p<0.05$) in the following sequence: reverse-phase evaporation > lipid film hydration = ethanol injection = ethanol permeabilization. Gomez et al. (2019) [35] reported similar findings when encapsulating the antibiotic vancomycin hydrochloride into liposomes by distinct techniques. Higher EE was obtained using reverse-phase evaporation, while lipid film hydration showed the lowest values. For this reason, reverse-phase evaporation was used to produce unloaded and GA-loaded liposomes in the following experiments.

4.3.2.2. Functionalization of Liposomes with Tf

GA-loaded liposomes were produced by reverse-phase evaporation and functionalized with Tf, envisaging the dual-targeting of GA to the BBB and neuronal cells. EDC was used as a coupling agent to functionalize the NPs by activating the Tf's carboxyl groups through a carbodiimide-coupling reaction. This allows the covalent coupling of activated Tf with DSPE-PEG2000 amine's amino group. The physicochemical properties of unloaded and GA-loaded liposomes, before and after Tf functionalization, are presented in Table 4.6.

Table 4.6. Physicochemical properties of unloaded and GA-loaded liposomes, without and with Tf functionalization. * Implies a statistical difference between GA-loaded liposomes before and after Tf functionalization ($p<0.05$).

Formulation	Size (nm)	PdI	Zeta potential (mV)	EE (%)	LC (%)	CE (%)
Unloaded LIP	129 ± 10	0.17 ± 0.04	-0.7 ± 1.0	-	-	-
Unloaded Tf-LIP	132 ± 4	0.15 ± 0.02	-1.3 ± 0.5	-	-	35 ± 3
GA-loaded LIP	126 ± 10	0.18 ± 0.02	-0.4 ± 0.8	29 ± 3	1.7 ± 0.2	-
GA-loaded Tf-LIP	131 ± 9	0.16 ± 0.02	-0.8 ± 1.0	31 ± 6	1.8 ± 0.4	26 ± 3 *

As shown in Table 4.6, the physicochemical properties of unloaded or GA-loaded liposomes were not affected by the functionalization with Tf ($p>0.05$), with both formulations exhibiting mean sizes of 130 nm, PdI values lower than 0.2, and zeta potential values close to 0 mV. Moreover, no significant variations in the EE and LC were observed before and after the NPs' functionalization ($p>0.05$), implying that no GA was released during the process. This is in line with earlier research revealing that storing lipid-based NPs at 4 °C, the temperature at which the liposomes' functionalization was executed, prevents drug leakage [22, 23]. Table 4.6 further shows that the CE of GA-loaded liposomes is significantly lower than unloaded NPs ($p<0.05$). This may be explained by the presence of GA molecules at the liposomes' surface, which may hamper the covalent coupling between activated Tf and DSPE-PEG2000 amine. This hypothesis is supported by Andrade et al. (2019) outcomes that demonstrated that the GA establishes electrostatic interactions with the phospholipids' polar head [2]. The CE values in Table 4.6 translate into 119 ± 10 of

Tf molecules per unloaded liposomes and 86 ± 11 per GA-loaded liposomes. Both values fall within the range of Tf molecules per NP needed to cross the BBB by RMT [24]. The obtained results confirm thus that the produced GA-loaded Tf-functionalized liposomes show appropriate physicochemical properties for brain delivery.

ATR-FTIR was used to validate the lipids' functionalization with Tf molecules. ATR-FTIR spectra of unloaded and GA-loaded liposomes, without and with Tf functionalization, are illustrated in Figure 4.8. For comparison, the ATR-FTIR spectrum of Tf is also provided.

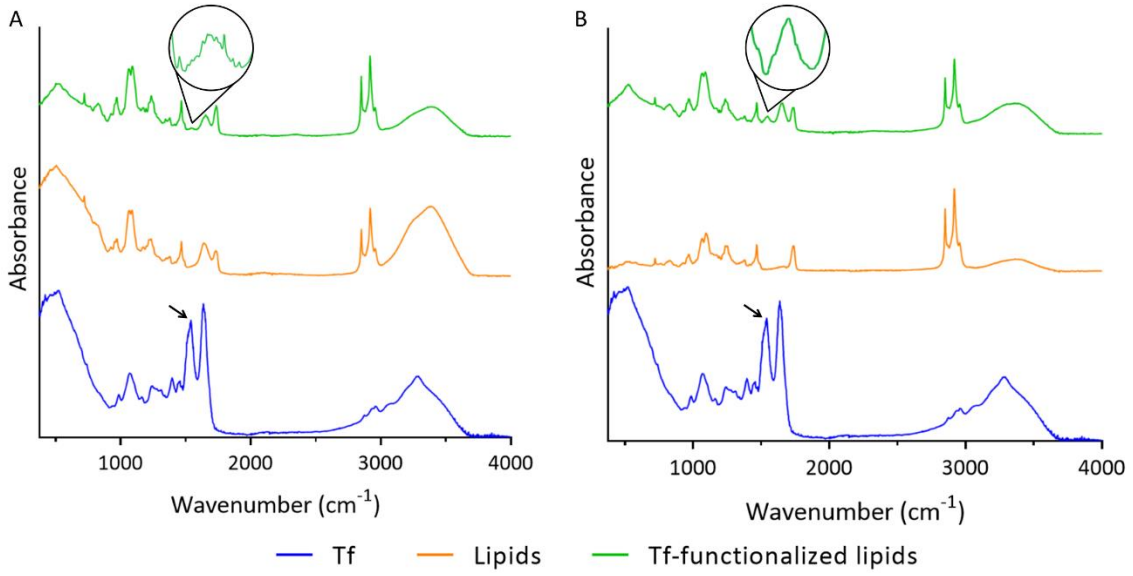

Figure 4.8. ATR-FTIR spectra of Tf (blue line), non-functionalized lipids (orange line), and Tf- functionalized lipids (green line) in the A) absence and B) presence of GA.

Two major bands in the ATR-FTIR spectrum of Tf can be observed in Figure 4.8 (blue data). The peak at 1636 cm^{-1} is assigned to the amine I vibrations, while the band at 1540 cm^{-1} corresponds to amine II. These major peaks are ascribed to the C=O stretching and N-H bending vibrations, respectively, present in the peptide bonds between Tf's amino acids [25]. In contrast to non-functionalized lipids (orange data), which lack the amine II peak, Tf-functionalized lipids (green data) present both peaks at the same wavenumber as Tf (blue data). Similar ATR-FTIR spectra were obtained in the presence of GA (Figure 4.8 B). The presence of the amino II peak at 1540 cm^{-1} in the ATR-FTIR spectra of Tf-functionalized lipids in the absence and presence of GA can thus be assigned to the successful functionalization of the lipids with Tf.

4.3.2.3. Physical Stability of Liposomes at Storage Conditions

One of the potential barriers to the use of liposomes in therapeutic applications is their lipids' physical and chemical instability. The long-term storage of liposomes can cause phospholipids' degradation, which can in turn induce changes in liposomes' permeability, structure, and drug retention. Storing liposomal formulations in the aqueous form is typically preferred over lyophilization and rehydration since these procedures result in a variation in the NPs' size and drug leakage. Doxil® and Onivyde® are commercially available liposomal formulations stored in the fluid state [36]. Thus, the physical stability of the produced liposomal formulations was investigated at storage conditions (4 °C) for 2 months. The mean diameter, PdI, and zeta potential of the unloaded and GA-loaded liposomes, before and after Tf functionalization, were periodically recorded since variations in the liposomes' physicochemical properties suggest changes in their structure [26]. The results are shown in Figure 4.9.

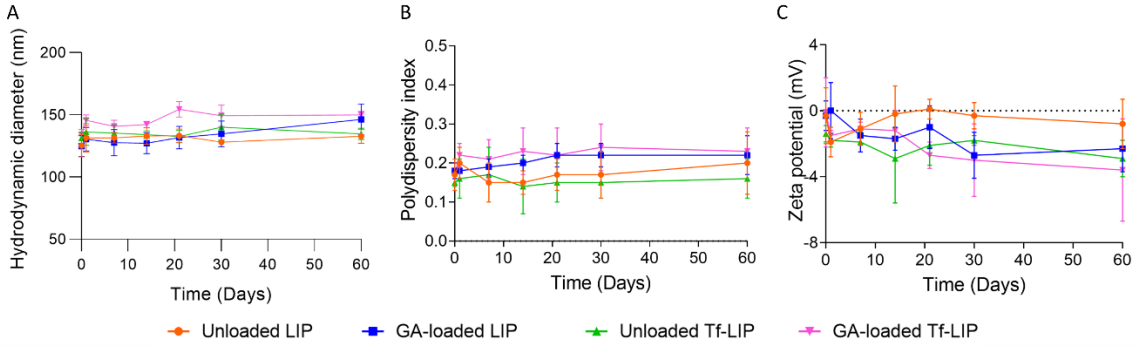

Figure 4.9. Physicochemical properties of unloaded (orange), GA-loaded (blue), Tf-functionalized (green), and GA-loaded Tf-functionalized liposomes (pink) stored at 4 °C for 2 months.

The findings presented in Figure 4.9 A show that the mean size of unloaded liposomes, before and after Tf functionalization, and GA-loaded liposomes remained constant over the experiment ($p>0.05$). The size of GA-loaded Tf-functionalized liposomes increased significantly ($p<0.05$) from 131 ± 9 nm to 150 ± 3 nm, corresponding to an increase of 15%. This rise can be attributed to some adjustments in the liposomes' structure. Moreover, no significant variations in the PdI (Figure 4.9 B) and zeta potential (Figure 4.9 C) of all formulations were detected over 2 months at 4 °C ($p>0.05$). The visual observation of the samples revealed no signs of phase separation, flocculation, or creaming. According to these

results, all formulations remained stable for 1 month under storage conditions, regardless of GA encapsulation or liposomes' functionalization.

4.3.2.4. *In vitro* Release of GA from Tf-Functionalized Liposomes

The *in vitro* release of GA from the Tf-functionalized liposomes was investigated under simulated physiological conditions (37 °C, PBS, pH 7.4, 10 mM) using the dialysis bag technique. The *in vitro* release of free GA was also attained for comparison purposes. The results are displayed in Figure 4.10.

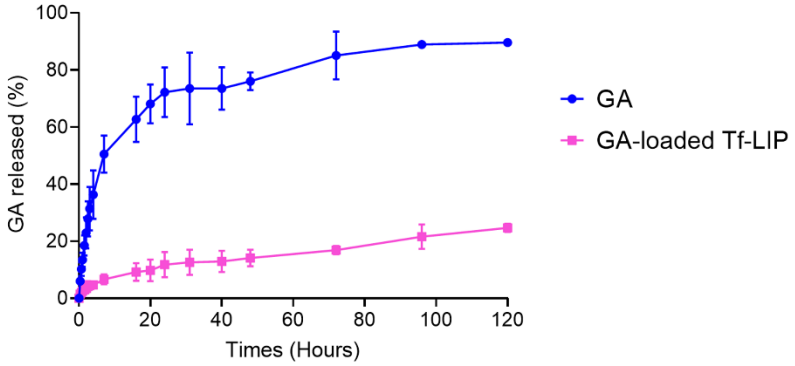

Figure 4.10. A) *In vitro* release profile of GA from Tf-functionalized liposomes (pink data) at 37 °C in PBS (pH 7.4, 10 mM) for 120 h. Blue data shows the *in vitro* release profile of free GA.

As shown in Figure 4.10, the *in vitro* release profile of GA from the Tf-functionalized liposomes (pink data) follows a sustained tendency, unlike free GA (blue data). While 25 ± 2% of GA was released from the NPs after 120 h, free GA reached a plateau after 96 h, with 90 ± 1 % of molecules being released in this period ($p<0.05$). About 12 ± 4 % of GA was released from the Tf-functionalized liposomes in the first 24 h. The remaining 13% were released in the following 4 days. This initial burst release followed by a slower and controlled release was previously observed [29], and it has been attributed to the desorption of adsorbed molecules at the NP's surface [28]. This particular biphasic release pattern allows most of the compound to reach the target site [32]. Similar *in vitro* drug release profiles from liposomes have previously been reported [37, 38].

Since GA has limited solubility in water, most GA molecules are expected to remain within the phospholipid bilayer of the Tf-functionalized liposomes instead of being released

into the release medium. This hypothesis is supported by previous evidence [2], which demonstrated that GA has a higher affinity for the liposomes' bilayer than for the aqueous medium. The same authors also verified that GA is preferentially located in the hydrophobic region of the lipid membrane [2]. In addition to the GA's properties, also the presence of PEG and Tf molecules at the liposomes' surface hinders the drug diffusion to the release medium [30, 31]. Once NPs have reached the target site, it is expectable that the remaining encapsulated GA will be released in a controlled and sustained manner as the liposomes are degraded [32]. The prepared DDS present thus an appropriate release profile for the brain delivery of GA.

4.3.2.5. Anti-Amyloidogenic Activity of GA-Loaded Liposomes Functionalized with Transferrin

4.3.2.5.1. Inhibition of Aβ Fibril Formation

The therapeutic potential of the developed brain-targeted DDS to prevent AD was investigated. For this purpose, the ability of GA-loaded Tf-functionalized liposomes to inhibit the $A\beta_{1\text{-}42}$ aggregation was assessed using a ThT fluorescence assay, a widely employed protocol to monitor amyloid fibril formation. This experiment is based on the ThT's ability to emit fluorescence when binding to amyloid fibrils. Scientists established a direct relationship between ThT fluorescence intensity and the amount of amyloid fibrils [14].

In this assay, Aβ monomers were incubated with GA, unloaded, and GA-loaded Tf-functionalized liposomes for 5 h at 37 °C. ThT fluorescence intensities were continuously recorded and are displayed in Figure 4.11. Equations 6 and 7 were applied to the obtained ThT data to calculate the kinetic parameters of each group, which are shown in Table 4.7.

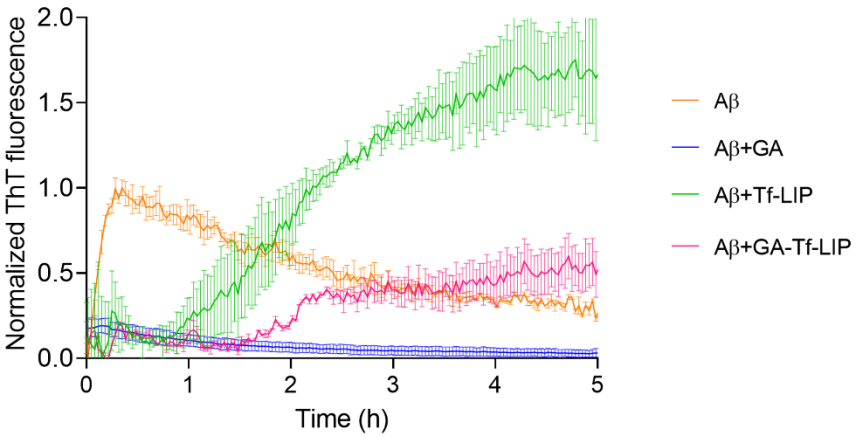

Figure 4.11. Normalized ThT fluorescence of Aβ1−42 (orange data) as a function of time (h) upon incubation with GA (blue data), Tf-functionalized liposomes (green data), and GA-loaded Tf-functionalized liposomes (pink data).

Table 4.7. Kinetic parameters calculated by fitting Equations 4.6 and 4.7 to the ThT data. * Indicates a statistical difference compared to Aβ ($p<0.05$). # Indicates a statistical difference between unloaded and GA-loaded Tf-functionalized liposomes ($p<0.05$).

Kinetic Parameters	Aβ	Aβ + GA	Aβ + Tf-LIP	Aβ + GA-Tf-LIP
t_{lag} (h)	0.015 ± 0.002	n.d.	0.9 ± 0.4 *	1.4 ± 0.03 *
$t_{1/2}$ (h)	0.10 ± 0.01	n.d.	2.0 ± 0.5 *	2.2 ± 0.3 *
k (h^{-1})	22.7 ± 0.6	n.d.	1.9 ± 0.1 *	4.9 ± 3.4 *
Max. Fluorescence	0.9 ± 0.1	n.d.	1.7 ± 0.3 *	0.5 ± 0.2 *,#

n.d. not determined

Figure 4.11 depicts typical sigmoidal curves for the kinetics of Aβ in the absence (orange data) and presence of unloaded (green data) and GA-loaded Tf-functionalized liposomes (pink data). At the beginning of each curve, the fluorescence emitted by ThT is low, suggesting the presence of few Aβ fibrils in the samples. Aβ monomers gather to form oligomers in this phase, frequently referred to as the lag phase. In the next phase, termed the elongation phase, oligomers group together to form Aβ fibrils. The formation of the fibrils is found to cause a progressive rise in the ThT fluorescence intensity in this phase, followed by the stationary phase, which is marked by a plateau after all of the Aβ peptides have been assembled into fibrils.

As shown in Figure 4.11, the Aβ fibrillation kinetic time course (orange data) was considerably modified by adding GA to the Aβ monomers (blue data). No discernible rise in the ThT fluorescence signal was seen ($p>0.05$) (blue data), suggesting that GA entirely prevents the formation of Aβ fibrils. Instead, after 5 h of incubation, GA caused a slight reduction in the ThT signal ($p<0.05$). This can be due to the GA's ability to disrupt existing fibrils from the examined sample. Similar outcomes have previously been reported [14].

Figure 4.11 further shows that the formation of Aβ fibrils was dramatically influenced by unloaded Tf-functionalized liposomes (green data). Table 4.7 reveals that the empty

liposomes dramatically extended the lag phase duration compared to Aβ from 0.015 ± 0.002 h (approximately 1 min) to 0.9 ± 0.4 h (about 54 min) ($p<0.05$), suggesting that the presence of NPs inhibit the conversion of Aβ monomers to oligomers. Unloaded Tf-functionalized liposomes also appear to impede the transition from oligomers to fibrils since they dramatically decreased the elongation rate compared to untreated Aβ from 22.7 ± 0.6 to 1.9 ± 0.1 h^{-1} ($p<0.05$). As a result, the time needed to reach 50% of the maximum ThT fluorescence intensity increased by 20 folds. However, the maximal ThT fluorescence almost doubled in the presence of unloaded Tf-functionalized liposomes than in the absence ($p<0.05$), suggesting that the NPs increase the number of fibrils formed. The results are consistent with other studies showing that lipid-based NPs, including liposomes, promote the Aβ fibril formation [11, 23, 33].

The Aβ's fibrillation kinetics was also impacted by the presence of GA-loaded Tf-functionalized liposomes (pink data), as depicted in Figure 4.11. Similar to unloaded NPs, GA-loaded NPs also substantially lengthened the lag phase time compared to untreated Aβ from 0.015 ± 0.002 h (approximately 1 min) to 1.4 ± 0.03 h (about 84 min) ($p<0.05$), suggesting that the DDS slows the conversion of Aβ monomers to oligomers. Additionally, a substantial reduction in elongation rate was seen in comparison to untreated Aβ (orange data) from 22.7 ± 0.6 h^{-1} to 4.9 ± 3.4 h^{-1} ($p<0.05$), which lengthened the time required to attain half of the maximal ThT fluorescence intensity by 22 times ($p<0.05$). These results indicate that the developed DDS inhibits the Aβ oligomers to fibrils transition. According to Table 4.7, GA-loaded Tf-functionalized liposomes also dramatically lowered the maximum ThT fluorescence intensity compared to untreated Aβ from 0.9 ± 0.1 to 0.5 ± 0.2 ($p<0.05$), implying a reduction of around 56% in the number of fibrils formed. Moreover, the presence of GA in the Tf-functionalized NPs significantly decreased the ThT signal compared to unloaded NPs from 1.7 ± 0.3 to 0.5 ± 0.2 ($p<0.05$), suggesting that the natural compound released so far is enough to prevent the nucleation effect of the empty NPs. Thus, the presented results validate the therapeutic potential of the developed brain-targeted DDS to delay the onset of AD.

The ability of the developed brain-targeted DDS to prevent fibril formation was also investigated by TEM. This widely employed technique offers detailed information on the amyloid aggregates' structure, size distribution, and structural characteristics [45]. Figure 4.12 shows the TEM images of Aβ incubated with GA, unloaded, and GA-loaded NPs for 5 h at 37 °C. After incubation, untreated Aβ formed several thin and long fibrils (Figure 4.12 A).

However, the presence of GA significantly prevented fibril formation as fewer Aβ fibrils were present in the sample (Figure 4.12 B). Instead, numerous small structures are observed, confirming the GA's anti-aggregation properties. As expected by ThT data, Aβ fibrils were also seen when Aβ was incubated with unloaded (Figure 4.12 C) and GA-loaded NPs (Figure 4.12 D). However, fewer fibrils were observed in the presence of GA-loaded Tf-functionalized liposomes (Figure 4.12 D) compared to untreated Aβ (Figure 4.12 A), thus validating the DDS's ability to prevent fibril formation.

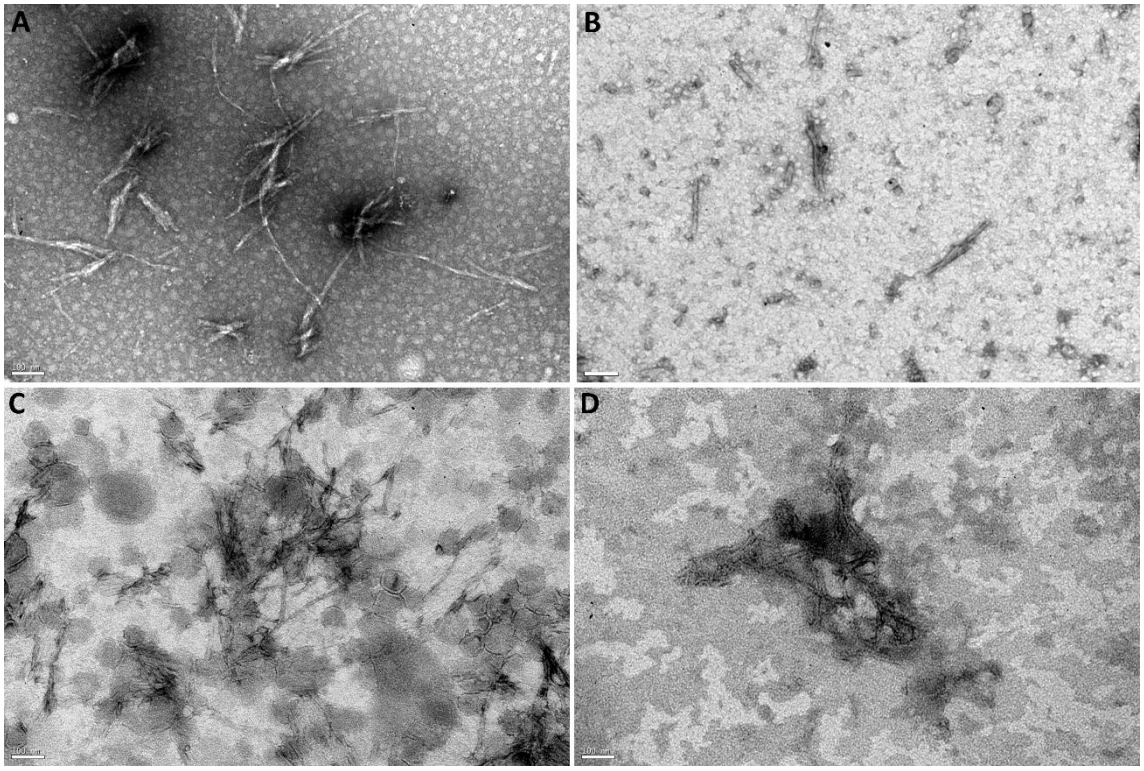

Figure 4.12. TEM images of A) Aβ1−42 incubated with B) GA, C) Tf-functionalized liposomes, and D) GA-loaded Tf-functionalized liposomes for 5 h at 37 °C. Scale bars correspond to 100 nm.

4.3.2.5.2. Disaggregation of Mature Aβ Fibrils

The therapeutic potential of the developed brain-targeted DDS to treat AD was studied. For this purpose, the capability of GA-loaded Tf-functionalized liposomes to disaggregate mature fibrils was evaluated using a ThT fluorescence assay. In this experiment, Aβ fibrils were incubated with GA, unloaded, and GA-loaded Tf-functionalized liposomes for 3 h at 37 °C while the ThT fluorescence signals were recorded. The results are displayed in Figure 4.13. Table 4.8 presents the amount of Aβ fibrils after their incubation

with GA, unloaded, and GA-loaded Tf-functionalized liposomes at the beginning and end of the experiment.

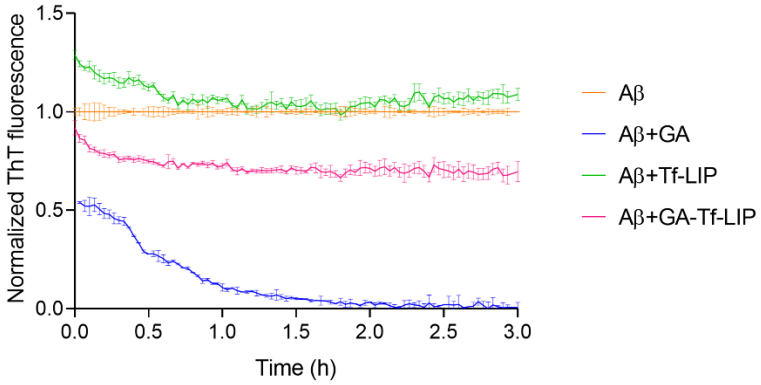

Figure 4.13. Normalized ThT fluorescence of mature Aβ1−42 fibrils (orange data) as a function of time (h) upon incubation with GA (blue data), Tf-functionalized liposomes (green data), and GA-loaded Tf-functionalized liposomes (pink data).

Table 4.8. Amount of $A\beta_{1-42}$ fibrils upon their incubation with GA, unloaded, and GA-loaded Tf-functionalized liposomes for 3 h at 37 °C. * Indicates a statistical difference compared to untreated Aβ fibrils ($p<0.05$). # Indicates a statistical difference between the beginning and end of the experiment ($p<0.05$). § Indicates a statistical difference between unloaded and GA-loaded Tf-liposomes ($p<0.05$).

	Aβ Fibril content (%)		
Time (h)	**Aβ + GA**	**Aβ + Tf-LIP**	**Aβ + GA-Tf-LIP**
0	54 ± 5 *	129 ± 2 *	92 ± 4 §
3	1 ± 1 *,#	109 ± 3 #	70 ± 5 *,#, §

The Aβ fibrils' content was significantly impacted by whether GA (blue data), unloaded (green data), or GA-loaded Tf-functionalized liposomes (pink data) were added, as shown in Figure 4.13. The ThT fluorescence signal was immediately reduced after adding GA to the fibrils by around 46% ($p<0.05$). As shown in Table 4.8, ThT fluorescence gradually decays over time until reaching a 99% drop after 3h of incubation. These results support earlier findings that GA can disrupt Aβ fibrils [14].

Additionally, Figure 4.13 demonstrates that the addition of unloaded NPs (green data) considerably boosted the ThT fluorescence signal in comparison to untreated Aβ fibrils

(orange data) ($p<0.05$). According to Table 4.8, unloaded Tf-functionalized liposomes immediately raised the fibril content by around 29 % ($p<0.05$), which decreased by 20% after 3 h of incubation at 37 °C ($p<0.05$). Adding GA to the NPs (pink data) significantly contradicted the unloaded NPs' amyloidogenic action (green data) ($p<0.05$). No significant variations in the fibril content were observed immediately after adding GA-loaded Tf-functionalized liposomes to Aβ fibrils ($p>0.05$). However, after 3 h of incubation, the ThT fluorescence intensity dropped about 30% compared to untreated Aβ fibrils ($p<0.05$) and 39% compared to unloaded NPs ($p<0.05$). The data, therefore, support the therapeutic potential of the produced brain-targeted DDS to treat AD.

The Aβ's morphology after incubating fibrils with GA, unloaded, and GA-loaded Tf-functionalized liposomes for 3 h at 37 °C was examined by TEM (Figure 4.14). Numerous slender and lengthy fibrils were seen when Aβ fibrils were incubated alone (Figure 4.14 A). However, the presence of GA significantly reduced the number of fibrils (Figure 4.14 B). The structures observed in Figure 4.14 B appear shorter than untreated Aβ fibrils (Figure 4.14 A), thus validating the GA's ability to disaggregate preformed Aβ fibrils. Furthermore, the presence of unloaded (Figure 4.14 C) did not affect the fibrils' morphology. However, GA-loaded liposomes (Figure 4.14 D) appear to disrupt the fibrils as many fragmented as small structures are noticed compared to untreated Aβ fibrils (Figure 4.14 A), thus confirming the therapeutic potential of the developed brain-targeted DDS to treat AD.

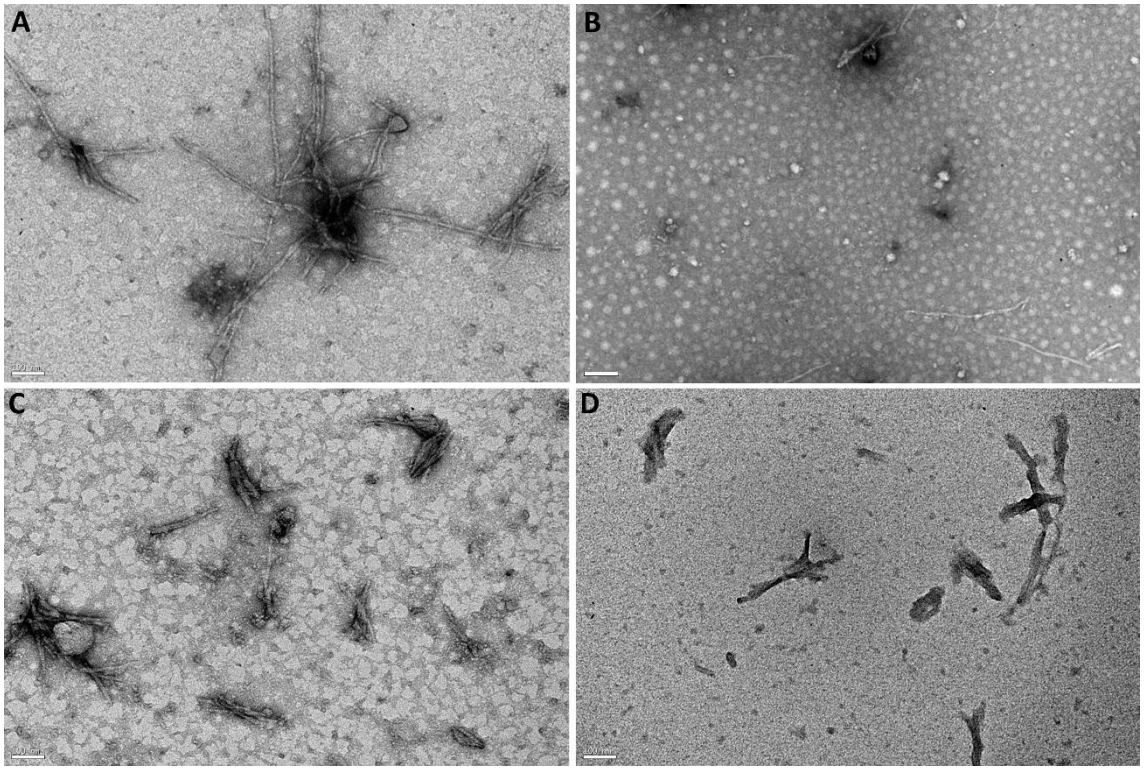

Figure 4.14. TEM images of A) Aβ fibrils incubated with B) GA, C) Tf-functionalized liposomes, or D) GA-loaded Tf-functionalized liposomes for 3 h at 37 °C. Scale bars are 100 nm.

4.3.3. Transferrin-Functionalized Liposomes Loaded with Vitamin B12

The content of this section is published in: *Andrade, S., Ramalho, M.J., Loureiro, J.A. & Pereira, M.C. (2022) Transferrin-Functionalized Liposomes Loaded with Vitamin VB12 for the Alzheimer's Disease Therapy. International Journal of Pharmaceutics, 122167.*

4.3.3.1. Physicochemical Characterization of Unloaded and VB12-Loaded Liposomes

In this study, liposomes composed of DSPC, CHOL, 18:0 PEG2000 PE, and DSPE-PEG2000 amine were produced. Aiming to find the adequate formulation, three different techniques of liposome production were evaluated – lipid film hydration, ethanol injection, and ethanol permeabilization. Table 4.9 summarizes the physicochemical properties of the unloaded and VB12-loaded liposomes produced by the referred techniques.

Table 4.9. Physicochemical characterization of unloaded and VB12-loaded liposomes in terms of hydrodynamic diameter, polydispersity index (PdI), zeta potential, encapsulation efficiency, and loading capacity. * Implies a statistical difference between unloaded and VB12-loaded liposomes ($p<0.05$).

Technique	Liposomes' formulation	Size (nm)	PdI	Zeta potential (mV)	EE (%)	LC (%)
Lipid film hydration	Unloaded LIP	114 ± 5	0.18 ± 0.02	-2.5 ± 0.5	-	-
	VB12-loaded LIP	116 ± 3	0.18 ± 0.02	-1.1 ± 0.1 *	14 ± 4	7 ± 2
Ethanol injection	Unloaded LIP	160 ± 11	0.20 ± 0.01	-3 ± 2	-	-
	VB12-loaded LIP	176 ± 9	0.21 ± 0.01	-1.3 ± 0.4	24 ± 4	12 ± 2
Ethanol permeabilization	Unloaded LIP	134 ± 11	0.19 ± 0.04	-2.4 ± 0.3	-	-
	VB12-loaded LIP	135 ± 10	0.19 ± 0.05	-1.5 ± 0.7 *	27 ± 5	14 ± 2

As revealed in Table 4.9, unloaded liposomes exhibited a mean diameter lower than 200 nm regardless of the preparation methodology. In addition, the encapsulation of VB12 in the liposomes did not affect their size ($p>0.05$). It can also be observed that the size of the liposomes significantly depends ($p<0.05$) on the production technique by the following order: ethanol injection > ethanol permeabilization > lipid film hydration. These results demonstrate that all VB12-loaded formulations present suitable sizes for brain delivery. Furthermore, all formulations presented PdI values lower than 0.2 (Table 4.9), with no significant differences between the groups ($p>0.05$), suggesting that the lipid vesicles have homogenous sizes and, therefore, are valid for delivery purposes [39].

The zeta potential of liposomes was determined, and all formulations showed a zeta potential close to 0 mV (Table 4.9), which is expected due to the nature of the lipids used in liposome production. From Table 4.9, it can also be noticed that the encapsulation of VB12 into the liposomes through the lipid film hydration and the ethanol permeabilization techniques led to a significant decrease ($p<0.05$) in the liposomes' zeta potential. A slight increase in the NPs' zeta potential following VB12 encapsulation by the ethanol injection technique was also noticed. This finding could suggest that some VB12 molecules are located at the liposomes' surface. Since 99% of VB12 molecules are positively charged at pH 7.4 [40], the cationic species are expected to interact with the DSPC polar head's negative charge, therefore increasing the NPs' surface charge.

For NPs to be efficiently produced, a manufacturing process with reduced material loss, lower costs, and more sustainable products is necessary. Therefore, high EE and LC values are desirable. From Table 4.9, it is possible to observe that the EE and LC values depend on the liposome production technique. The EE and LC through the ethanol permeabilization and ethanol injection techniques showed significantly higher values ($p<0.05$) than those obtained through the lipid film hydration. Slightly higher EE and LC values were observed using the ethanol permeabilization technique than the ethanol injection. The ethanol permeabilization technique is a simple and rapid passive equilibration method that relies on adding molecules to preformed liposome in the presence of a permeability enhancer – ethanol. This permeability enhancer increases the lipid bilayer permeability and consequently the drug diffusion through the lipid membrane without significantly affecting the NPs structure. Liposomes prepared using passive equilibration methods were found to have higher EE values for extremely water-soluble molecules [10].

Therefore, based on all the physicochemical characteristics of the formulations, ethanol permeabilization was the technique selected to prepare VB12-loaded liposomes for the following experiments.

4.3.3.2. Functionalization of Liposomes with Tf

The unloaded liposomes' surface was modified with Tf envisaging the dual-targeting strategy of the DDS to the BBB and neurons [20]. Holo-Tf was selected for the liposomes' surface functionalization rather than other Tf forms, such as apo-Tf, because of its higher affinity for TfR [21]. The covalent coupling of Tf with the amino group of DSPE-PEG2000 was achieved by a carbodiimide-coupling reaction where EDC activates the Tf carboxyl groups. The VB12 was then loaded into the Tf-functionalized liposomes through the ethanol permeabilization technique. The physicochemical characterization of the prepared liposomes and the Tf's CE are presented in Table 4.10.

Table 4.10. Physicochemical characterization of unloaded and VB12-loaded transferrin (Tf)-functionalized liposomes. * Indicates a statistical difference between unfunctionalized and Tf-functionalized liposomes ($p<0.05$).

Formulation	Size (nm)	PdI	Zeta potential (mV)	EE (%)	LC (%)	CE (%)
Unloaded LIP	134 ± 11	0.19 ± 0.04	-2.4 ± 0.3	-	-	-
VB12-loaded LIP	135 ± 10	0.19 ± 0.05	-1.5 ± 0.7	27 ± 5	14 ± 2	-
Unloaded Tf-LIP	142 ± 19	0.19 ± 0.02	-0.5 ± 0.3 *	-	-	31 ± 4
VB12-loaded Tf-LIP	153 ± 17	0.15 ± 0.04	-0.4 ± 0.3 *	15 ± 2 *	8 ± 1 *	

As shown in Table 4.10, the functionalization of unloaded liposomes with Tf did not affect the NPs size and PdI ($p>0.05$), with the Tf-liposomes exhibiting a mean diameter of 142 ± 19 nm and a PdI value of 0.19 ± 0.02. A slight increase was observed in the liposomes' zeta potential following liposome modification with Tf ($p<0.05$). The CE was determined to be 31 ± 4 %, corresponding to 122 ± 16 Tf molecules per liposome, an amount that allows liposomes to cross the BBB efficiently [28]. Overall, the produced unloaded Tf-modified liposomes showed proper physicochemical properties for brain delivery.

The functionalization of lipids with Tf was confirmed by FTIR. The spectra of Tf, unmodified lipids, and Tf-modified lipids are depicted in Figure 4.15.

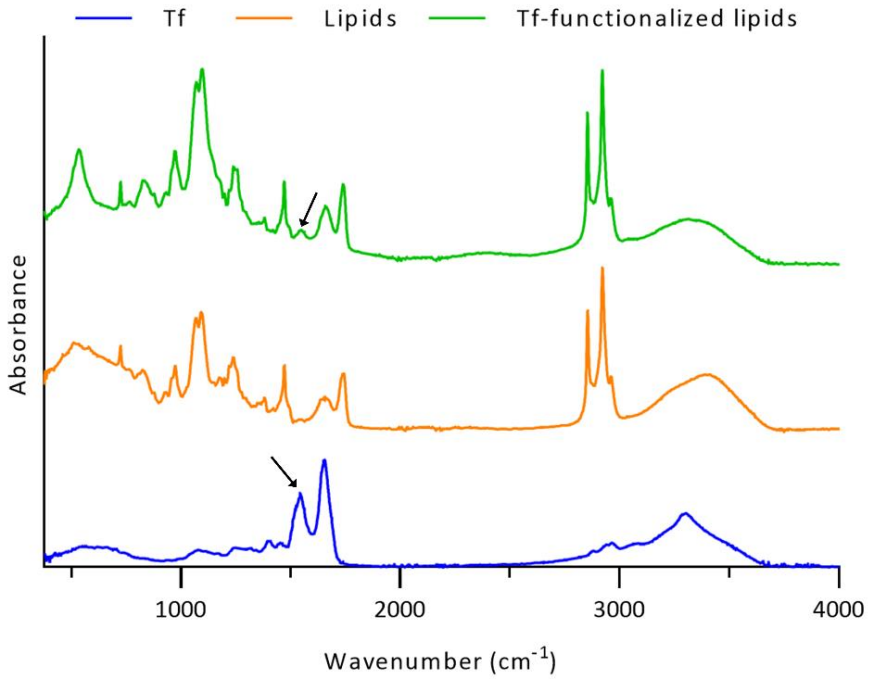

Figure 4.15. ATR-FTIR spectra of Tf (blue line), unmodified lipids (orange line), and Tf-modified lipids (green line).

From Figure 4.15, it is possible to identify two prominent peaks in the Tf control sample at 1648 (amine I) and 1543 cm^{-1} (amine II) (blue line). These bands are assigned to C=O and N-H bending stretching vibrations present in the peptide bonds between amino acids of Tf, respectively [25]. Likewise, Tf-functionalized lipids (green line) exhibit the same peaks, unlike unmodified lipids (orange line) that do not display the amine II peak, indicative of the successful functionalization of liposomes with Tf.

Following the lipids' modification, VB12 was loaded into the liposomes by the ethanol permeabilization technique, which did not affect the physicochemical properties of the NPs ($p>0.05$) (Table 4.10). However, EE significantly decreased from 27 ± 5 % to 15 ± 2 % ($p<0.05$) with the liposome surface modification, suggesting that Tf molecules hinder the diffusion of VB12 through the liposomes' lipid bilayer. Accordingly, the LC decreased from 14 ± 2 % to 8 ± 1 % following liposome functionalization ($p<0.05$) due to the decrease in the amount of encapsulated VB12 (Table 4.10).

4.3.3.3. Physical Stability of Liposomes at Storage Conditions

The physical stability of the produced liposomes was assessed at storage conditions (4 °C) for 2 months. The mean hydrodynamic diameter, PdI, and zeta potential of unloaded and VB12-loaded liposomes, with and without Tf functionalization, were periodically evaluated and are displayed in Figure 4.16.

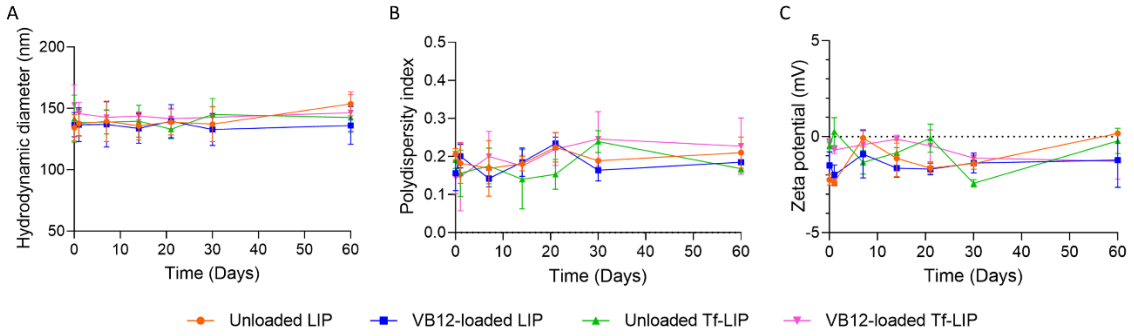

Figure 4.16. Physicochemical characterization of unloaded liposomes (orange), VB12-loaded liposomes (blue), Tf-functionalized liposomes (green), and VB12-loaded Tf-functionalized liposomes (pink) over 2 months at 4 °C.

From Figure 4.16, it is possible to observe that the evaluated physicochemical parameters of all liposomal formulations remained constant over 2 months at 4 °C ($p>0.05$). Visually, all formulations presented the same homogeneous appearance, without creaming, flocculation, or phase separation. These results suggest that the NPs are stable under storage conditions regardless of the encapsulation of VB12 and the liposome functionalization with Tf.

4.3.3.4. *In vitro* Release of VB12

The *in vitro* release of VB12 from the prepared Tf-functionalized liposomes was studied under simulated physiological conditions (37 °C, PBS, pH 7.4, 10 mM) and compared to free VB12. The obtained release profiles are presented in Figure 4.17.

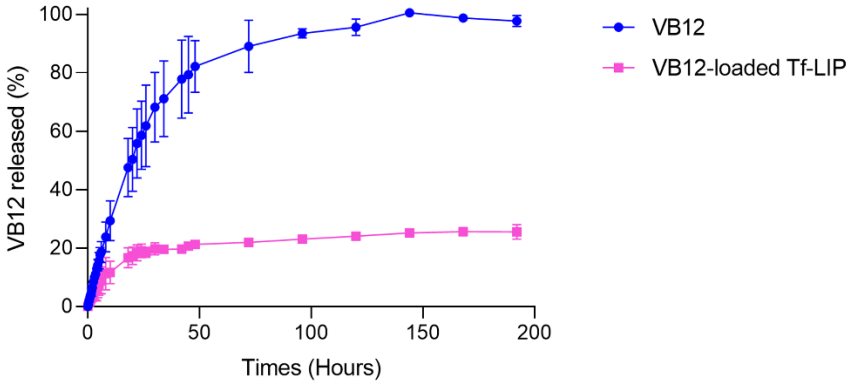

Figure 4.17. *In vitro* release profiles of free VB12 (blue) and VB12-loaded Tf-functionalized liposomes (pink) at 37 °C in PBS (pH 7.4, 10 mM).

As noticed in Figure 4.17, the *in vitro* release of VB12 from the Tf-functionalized liposomes presented a sustained profile. Similar *in vitro* drug release profiles from liposomes were reported before [37, 38]. Unlike VB12 from the control group (blue data), which was released entirely in 144 h, liposomes released 25 ± 2 % of VB12 in this period (pink data) ($p<0.05$). A rapid release was verified in the first 6 h, with about 9% of VB12 released. This initial fast release can be attributed to the desorption of the VB12 adsorbed molecules to the liposomes' surface [41], which agrees with the zeta potential measurements (Table 4.9). Then, a slower and controlled release is noted, with 16% of molecules released in the next 6 days. Since VB12 is a water-soluble molecule, it is expected to be mainly retained in the liposomes' aqueous core, which hinders its release through the phospholipid bilayer. Evidence revealed that the presence of PEG and Tf molecules at the NPs' surface also hinders the drug diffusion to the release medium [30, 31]. This ensures minimal cargo leakage before reaching the target site [32]. It is expected that the VB12 molecules retained in the aqueous core of liposomes will be released later in the target site in a controlled and sustained manner due to the NPs degradation [32]. The *in vivo* degradation of liposomes occurs due to the direct action of lipases that catalytically degrade lipids, causing membrane permeabilization and vesicle dissolution [42].

Sustained drug release is needed to ensure the prolonged plasma concentration of drugs at therapeutic levels. Hence, optimal therapeutic efficacy can be obtained while reducing the side effects of drugs [27]. Overall, these results indicate that Tf-functionalized liposomes maintain a sustained release of VB12 for 9 days in simulated physiological conditions, thus being a suitable nanocarrier for delivering VB12.

4.3.3.5. Anti-Amyloidogenic Activity of VB12-Loaded Tf-Functionalized Liposomes

4.3.3.5.1. Inhibition of Aβ Fibril Formation

The ability of the VB12-loaded Tf-functionalized liposomes to inhibit the $A\beta_{1-42}$ fibril formation was evaluated to assess the potential of the developed DDS to prevent AD. A ThT fluorescence assay combined with a kinetic model of amyloid fibrillation was employed in this study [14]. For this purpose, Aβ monomers and VB12-loaded Tf-functionalized liposomes were incubated at 37 °C for 2 h. The aggregation kinetics of Aβ in the presence and absence of free VB12 and unloaded Tf-functionalized liposomes were also recorded for comparison purposes. Figure 4.18 displays the complete sets of normalized ThT fluorescence kinetic curves.

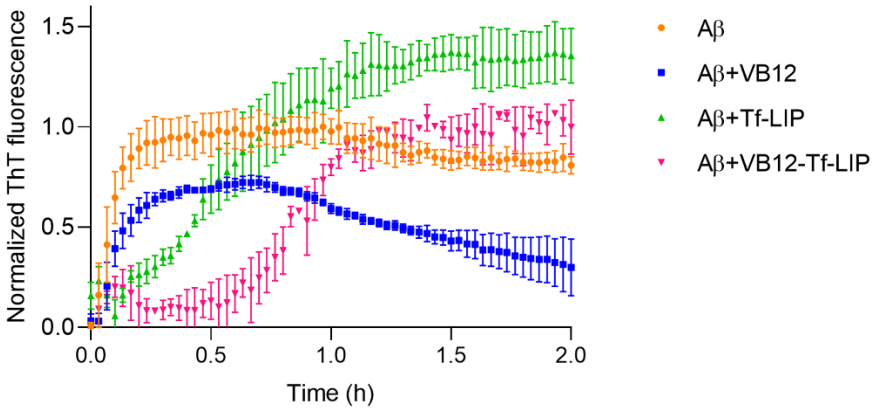

Figure 4.18. Normalized ThT fluorescence of $A\beta_{1-42}$ (orange circle) as a function of time (h) upon incubation with VB12 (blue square), Tf-functionalized liposomes (green triangle), and VB12-loaded Tf-functionalized liposomes (pink inverted triangle).

As shown in Figure 4.18, all kinetic curves follow a typical sigmoidal pattern, as observed in prior studies [12]. ThT emits a low fluorescence intensity at the start of each kinetic, indicating that the samples contain few β-sheet structures. Aβ monomers assemble into oligomers during this phase, also known as the lag phase. Then, ThT fluorescence signal increases due to the formation of Aβ fibrils, a process designed elongation phase. The plateau is observed when all molecules aggregate into fibrils (stationary phase).

Fitting Equations 6 and 7 to the data yielded the kinetic parameters for all ThT curves listed in Table 4.11.

Table 4.11. Kinetic parameters were calculated by fitting Equations 3.6 and 3.7 to the ThT data. *p<0.05 indicates a statistical difference compared to the control (Aβ).

Kinetic Parameters	Aβ	Aβ + VB12	Aβ + Tf-LIP	Aβ + VB12-Tf-LIP
t_{lag} (h)	0.02 ± 0.01	0.03 ± 0.01	0.07 ± 0.06	0.58 ± 0.15 *
$t_{1/2}$ (h)	0.08 ± 0.02	0.10 ± 0.03	0.50 ± 0.01 *	0.84 ± 0.03 *
k (h^{-1})	38 ± 4	27 ± 7	5 ± 1 *	8 ± 4 *
Max. Fluorescence	0.9 ± 0.1	0.68 ± 0.01 *	1.3 ± 0.2 *	1.0 ± 0.1

As seen in Figure 4.18, free VB12 had a considerable effect on Aβ's fibrillation kinetics. When Aβ was incubated with VB12, no significant differences were observed in the lag phase time compared to the control (Table 4.11) ($p>0.05$), implying that VB12 does not affect the transition of Aβ monomers to oligomers. VB12 also did not change the elongation rate nor the time needed to achieve half of the maximum fluorescence intensity ($p>0.05$), suggesting that VB12 does not affect the transition from Aβ oligomers to mature fibrils. However, VB12 significantly reduced the maximum fluorescence intensity by approximately 26% ($p<0.05$) compared to untreated Aβ, inferring a reduction in the fibril content, as reported in our previous work [43].

Figure 4.18 also shows a significant impact of unloaded Tf-functionalized liposomes on the Aβ's fibrillation kinetics. Table 4.11 indicates that the NPs did not affect the lag phase time, i.e., the monomers-to-oligomers transition, compared to the control ($p>0.05$). However, liposomes significantly increased the time needed for 50% of the maximum fluorescence intensity to be obtained ($p<0.05$) by a factor of 6, resulting in a significantly lower fibril elongation rate ($p<0.05$). In addition, liposomes led to a significant increase of about 36% in the maximum fluorescence intensity ($p<0.05$). These results suggest that despite slowing down the transition of Aβ oligomers to fibrils, the amount of fibrils formed is significantly higher in the presence of Tf-functionalized liposomes. It is widely recognized that liposomes catalyze the Aβ fibrillation process by acting as aggregation nuclei [33]. Other types of lipid-based NPs have been shown to increase the Aβ fibril content [11, 23].

VB12-loaded Tf-functionalized liposomes also influenced the Aβ aggregation process, as displayed in Figure 4.18. VB12-loaded Tf-functionalized liposomes increased significantly the time needed for monomers to aggregate into oligomers compared to untreated Aβ ($p<0.05$), from 1.4 min to 34.7 min (Table 4.11). The DDS also substantially impacted the elongation rate, which was reduced by 5 times ($p<0.05$). Consequently, the time required to reach 50% of the maximal fluorescence intensity has increased by 11 folds compared to the control ($p<0.05$), thus indicating that VB12 slows down the oligomers-to-fibrils transition. In addition, no significant differences were observed in the maximum ThT fluorescence signal between Aβ in the presence and absence of VB12-loaded liposomes ($p>0.05$). However, when comparing the effect of VB12-loaded liposomes to unloaded liposomes, it is possible to conclude that VB12 induces a significant reduction of about 31% in the fluorescence intensity, suggesting that the amount of vitamin released so far is enough to contradict the nucleation effect of the liposomes. Since most of the VB12 molecules are kept in the aqueous core of liposomes, it is expected that the DDS's ability to prevent the Aβ fibrillation *in vivo* would be further enhanced due to the release of the remaining VB12 molecules.

The morphology of the ThT end-point products after 2 h of incubation was observed by TEM (Figure 4.19). Untreated Aβ (Figure 4.19 A) shows fibrils with typical lengths varying between 100 and 700 nm. Moreover, it is possible to observe that these fibrils present a left-handed β-sheet twist, as reported in previous studies [44]. No discrepancies in the morphology of the fibrils were noticed in the absence and presence of VB12 (Figure 4.19 B), Tf-functionalized liposomes (Figure 4.19 C), or VB12-loaded Tf-functionalized liposomes (Figure 4.19 D).

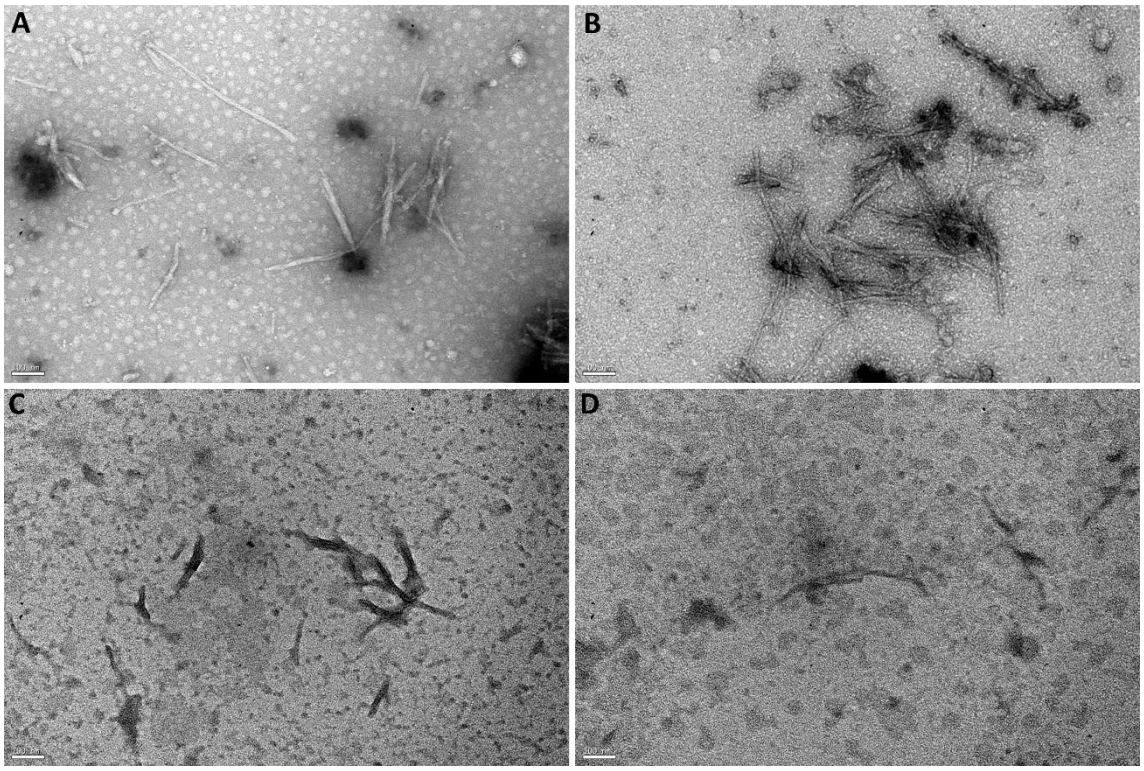

Figure 4.19. TEM images of A) control Aβ or incubated with B) VB12, C) Tf-functionalized liposomes or D) VB12-loaded Tf-functionalized liposomes. Scale bars correspond to 100 nm.

4.3.3.5.2. Disaggregation of Mature Aβ Fibrils

The ability of the VB12-loaded Tf-functionalized liposomes to disaggregate mature $A\beta_{1\text{-}42}$ fibrils was evaluated to assess the capacity of the developed DDS to treat AD. To this end, preformed Aβ fibrils and VB12-loaded Tf-functionalized liposomes were incubated at 37 °C for 2 h. For comparison, ThT fluorescence signals of Aβ in the presence and absence of free VB12 and unloaded Tf-functionalized liposomes over time were also recorded. The complete set of normalized ThT fluorescence data is shown in Figure 4.20. Table 4.12 displays the percentage of Aβ fibrils content after incubating preformed fibrils with VB12, unloaded Tf-functionalized liposomes, and VB12-loaded Tf-functionalized liposomes at the beginning and end of the experiment.

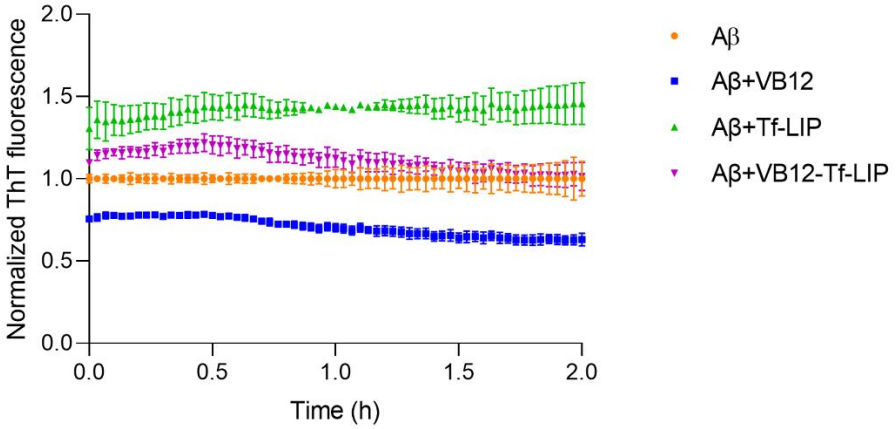

Figure 4.20. Normalized ThT fluorescence of preformed $A\beta_{1-42}$ (orange circle) as a function of time (h) upon incubation with VB12 (blue square), Tf-functionalized liposomes (green triangle), and VB12-loaded Tf-functionalized liposomes (pink inverted triangle).

Table 4.12. Percentage of $A\beta_{1-42}$ fibrils disaggregation upon incubation with VB12 for 2h at 37 °C, determined from ThT data. * $p<0.05$ indicates a statistical difference compared to untreated Aβ fibrils. # $p<0.05$ implies a statistical difference between the beginning and end of the assay.

	Aβ Fibril content (%)		
Time (h)	Aβ + VB12	Aβ + Tf-LIP	Aβ + VB12-Tf-LIP
0	76 ± 1 *	131 ± 13 *	110 ± 1 *
2	63 ± 4 *, #	146 ± 13 *	101 ± 8

Figure 4.20 shows that adding free VB12 after the fibrillation process was completed resulted in an instantaneous drop in the ThT fluorescence signal (blue data) compared to untreated Aβ fibrils (orange data) ($p<0.05$). About 24% of Aβ fibrils were disrupted as soon as VB12 was added (Table 4.12). After 2 h of incubation at 37 °C, this value increased significantly to 37% ($p<0.05$). These results agree with our previous study [40], confirming the VB12's ability to disaggregate preformed Aβ fibrils.

It is also visible from Figure 4.20 that unloaded Tf-functionalized liposomes significantly altered the ThT fluorescence intensities immediately upon their addition to Aβ fibrils (green data) compared to untreated Aβ fibrils (orange data) ($p<0.05$). Table 4.12 reveals that unloaded liposomes led to a significant increase in the fibril content of around 31%, which remained constant throughout the assay ($p>0.05$). Adding VB12 to Tf-

functionalized liposomes (pink data) contradicted their amyloidogenic effect considerably ($p<0.05$). As shown in Table 4.12, VB12-loaded Tf-functionalized liposomes increased the fibrils amount significantly by about 10% compared to untreated fibrils ($p<0.05$). However, this increase was significantly lower than the one caused by the unloaded liposomes ($p<0.05$), probably due to the interaction of the fibrils with the VB12 molecules present at the liposomes' surface. A slight decrease in the ThT fluorescence signal of about 9% is observed after 2 h of incubation at 37 °C, which may be caused by the sustained VB12 release. At the end of the ThT fluorescence assay, no significant difference in the fibril content was observed between fibrils incubated in the absence (orange data) and the presence of VB12-loaded Tf-functionalized liposomes (pink data) ($p>0.05$). It is expected that the developed DDS's ability to disaggregate mature fibrils *in vivo* will be enhanced by the complete VB12 release.

Figure 4.21 shows the TEM images of the ThT end-point products after 2 h of incubation. No apparent variations in the morphology of fibrils were observed between the groups. However, when VB12 was added to the Aβ fibrils, in addition to fibrils, many short and disintegrated structures were noted, thus corroborating the VB12's ability to disaggregate preformed $A\beta_{1-42}$ fibrils.

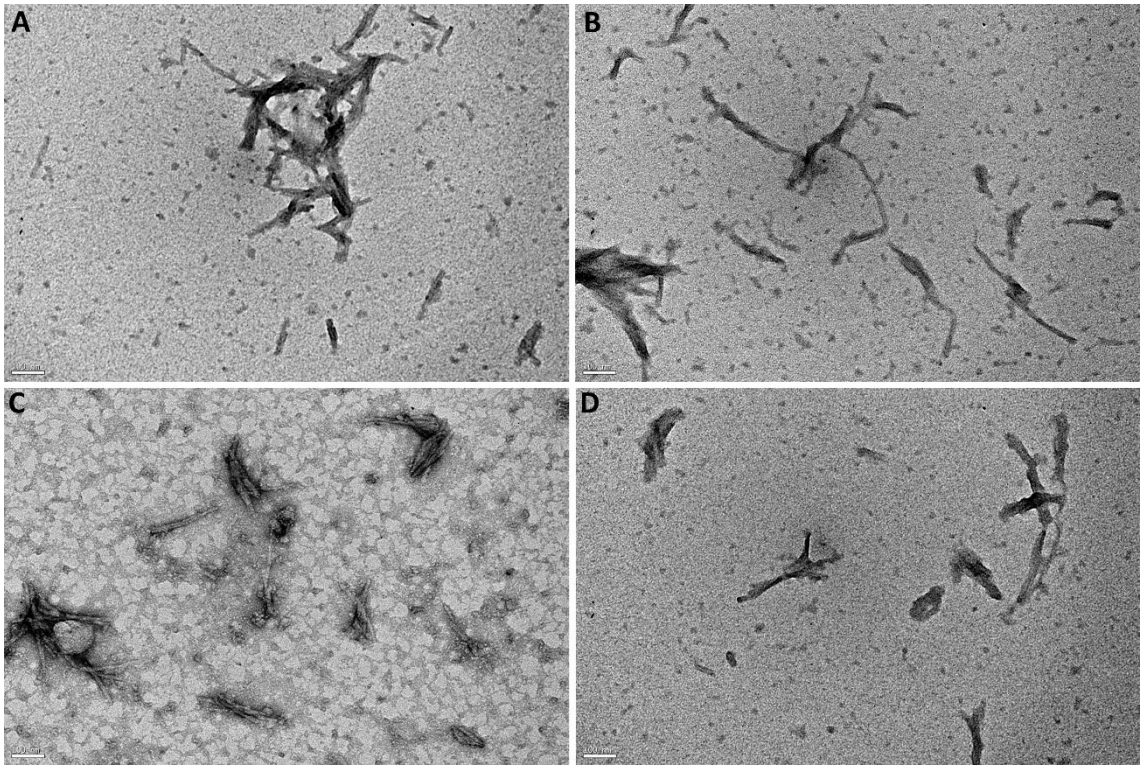

Figure 4.21. TEM images of A) control Aβ fibrils or incubated with B) VB12, C) Tf-functionalized liposomes, or D) VB12-loaded Tf-functionalized liposomes. Scale bars correspond to 100 nm.

4.4. Conclusion

This chapter aimed to develop CA, GA, and VB12-loaded liposomes functionalized with Tf to prevent and treat AD. Different techniques for liposome production were tested to find the formulation with the best physicochemical characteristics, including hydrodynamic diameter, PDI, zeta potential, EE, and LC. All formulations exhibited mean sizes smaller than 200 nm and neutral zeta potentials, being suitable for drug delivery purposes. The liposomes' surface was successfully modified with Tf to improve the brain delivery of the natural compounds. The NPs were stable for 1 month under storage conditions and maintained a sustained release of the compounds for an extended period.

The ability of the developed DDSs to inhibit the Aβ fibrillation and disaggregate preformed fibrils was evaluated. First, the results revealed that unloaded liposomes act as aggregation nuclei. However, their ability to promote Aβ fibril formation was significantly contradicted by the encapsulation of the three compounds. CA-loaded Tf-functionalized liposomes decelerated the monomers-to-oligomers transition and decreased the number of fibrils formed by approximately 1.6-fold compared to unloaded liposomes. However, the proposed DDS still presents some fibrillation activity compared to untreated Aβ.

The DDS for GA was able to reverse the harmful effect of unloaded liposomes and slowed the conversion of Aβ monomers-to-oligomers and oligomers-to-fibrils compared to untreated Aβ. Furthermore, GA-loaded liposomes reduced the number of fibrils formed by approximately 56%, compared with the control.

In turn, the DDS for VB12 was capable of slowing down the oligomers-to-fibrils transition compared to untreated Aβ. However, no significant differences were observed in the number of fibrils formed.

Concerning the disaggregation activity of the proposed DDSs, the three natural compounds were capable of reverting the amyloidogenic properties of unloaded liposomes.

Compared to untreated Aβ fibrils, the NPs containing CA and GA were responsible for a reduction of 13% and 30%, respectively, in the fibril content. No significant difference in the amount of fibrils was observed after the incubation of fibrils with VB12-loaded liposomes. Thus, from the brain-targeted liposomes produced, the DDS containing GA has stronger anti-amyloidogenic effects than the other systems and thus, could be the most effective approach for AD therapy.

References

[1] Talebi, M., Kakouri, E., Talebi, M., Tarantilis, P. A., Farkhondeh, T., İlgün, S., Pourbagher-Shahri, A. M.&Samarghandian, S. Nutraceuticals-based therapeutic approach: Recent advances to combat pathogenesis of alzheimer's disease. Expert review of neurotherapeutics 2021, 21, 625-642.

[2] Andrade, S., Ramalho, M. J., Loureiro, J. A.&Pereira, M. C. Interaction of natural compounds with biomembrane models: A biophysical approach for the alzheimer's disease therapy. Colloids Surf., B 2019, 180, 83-92.

[3] Ramalho, M. J., Andrade, S., Loureiro, J. A.&Pereira, M. C. Nanotechnology to improve the alzheimer's disease therapy with natural compounds. Drug delivery and translational research 2020, 10, 380-402.

[4] Guimarães, D., Cavaco-Paulo, A.&Nogueira, E. Design of liposomes as drug delivery system for therapeutic applications. International Journal of Pharmaceutics 2021, 601, 120571.

[5] Tashima, T. Smart strategies for therapeutic agent delivery into brain across the blood–brain barrier using receptor-mediated transcytosis. Chemical and Pharmaceutical Bulletin 2020, 68, 316-325.

[6] Andrade, S., Ramalho, M. J., Loureiro, J. A.&Pereira, M. C. Techniques to produce liposomes for the emerging market of nano-based formulations. 2020,

[7] Maja, L., Željko, K.&Mateja, P. Sustainable technologies for liposome preparation. The Journal of Supercritical Fluids 2020, 165, 104984.

[8] Akbarzadeh, A., Rezaei-Sadabady, R., Davaran, S., Joo, S. W., Zarghami, N., Hanifehpour, Y., Samiei, M., Kouhi, M.&Nejati-Koshki, K. Liposome: Classification, preparation, and applications. Nanoscale research letters 2013, 8, 1-9.

[9] Charcosset, C., Juban, A., Valour, J.-P., Urbaniak, S.&Fessi, H. Preparation of liposomes at large scale using the ethanol injection method: Effect of scale-up and injection devices. Chemical engineering research and design 2015, 94, 508-515.

[10] Wehbe, M., Malhotra, A., Anantha, M., Roosendaal, J., Leung, A. W. Y., Plackett, D., Edwards, K., Gilabert-Oriol, R.&Bally, M. B. A simple passive equilibration method for loading carboplatin into pre-formed liposomes incubated with ethanol as a temperature dependent permeability enhancer. Journal of Controlled Release 2017, 252, 50-61.

[11] Pinheiro, R. G. R., Granja, A., Loureiro, J. A., Pereira, M. C., Pinheiro, M., Neves, A. R.&Reis, S. Quercetin lipid nanoparticles functionalized with transferrin for alzheimer's disease. European Journal of Pharmaceutical Sciences 2020, 148, 105314.

[12] Andrade, S., Loureiro, J. A.&Pereira, M. C. Influence of in vitro neuronal membranes on the anti-amyloidogenic activity of gallic acid: Implication for the therapy of alzheimer's disease. Archives of Biochemistry and Biophysics 2021, 711, 109022.

[13] Ramalho, M. J., Loureiro, J. A., Coelho, M. A.&Pereira, M. C. Factorial design as a tool for the optimization of plga nanoparticles for the co-delivery of temozolomide and o6-benzylguanine. Pharmaceutics 2019, 11, 401.

[14] Andrade, S., Loureiro, J. A.&Pereira, M. C. Caffeic acid for the prevention and treatment of alzheimer's disease: The effect of lipid membranes on the inhibition of aggregation and disruption of aβ fibrils. International Journal of Biological Macromolecules 2021, 190, 853-861.

[15] Andrade, S., Loureiro, J. A., Ramirez, S., Catumbela, C. S. G., Soto, C., Morales, R.&Pereira, M. C. Multi-dose intravenous administration of neutral and cationic liposomes in mice: An extensive toxicity study. Pharmaceuticals 2022, 15, 761.

[16] Hoshyar, N., Gray, S., Han, H.&Bao, G. The effect of nanoparticle size on in vivo pharmacokinetics and cellular interaction. Nanomedicine (Lond) 2016, 11, 673-692.

[17] Ceña, V.&Játiva, P. Nanoparticle crossing of blood–brain barrier: A road to new therapeutic approaches to central nervous system diseases. Nanomedicine 2018, 13, 1513-1516.

[18] Danaei, M., Dehghankhold, M., Ataei, S., Hasanzadeh Davarani, F., Javanmard, R., Dokhani, A., Khorasani, S.&Mozafari, M. Impact of particle size and polydispersity index on the clinical applications of lipidic nanocarrier systems. Pharmaceutics 2018, 10, 57.

[19] Saraiva, C., Praça, C., Ferreira, R., Santos, T., Ferreira, L.&Bernardino, L. Nanoparticle-mediated brain drug delivery: Overcoming blood–brain barrier to treat neurodegenerative diseases. Journal of controlled release 2016, 235, 34-47.

[20] Kawabata, H. Transferrin and transferrin receptors update. Free Radical Biology and Medicine 2019, 133, 46-54.

[21] Lao, B. J., Tsai, W.-L. P., Mashayekhi, F., Pham, E. A., Mason, A. B.&Kamei, D. T. Inhibition of transferrin iron release increases in vitro drug carrier efficacy. Journal of Controlled Release 2007, 117, 403-412.

[22] Yucel, C., De Gim, Z.&Yilmaz, S. Development of cisplatin-loaded liposome and evaluation of transport properties through caco-2 cell line. Turk. J. Pharm. Sci 2016, 13, 95-108.

[23] Loureiro, J. A., Andrade, S., Duarte, A., Neves, A. R., Queiroz, J. F., Nunes, C., Sevin, E., Fenart, L., Gosselet, F., Coelho, M. A. N.&Pereira, M. C. Resveratrol and grape extract-loaded solid lipid nanoparticles for the treatment of alzheimer's disease. Molecules 2017, 22, 1-16.

[24] Visser, C. C., Stevanović, S., Voorwinden, L. H., Bloois, L. v., Gaillard, P. J., Danhof, M., Crommelin, D. J. A.&Boer, A. G. d. Targeting liposomes with protein drugs to the blood–brain barrier in vitro. European Journal of Pharmaceutical Sciences 2005, 25, 299-305.

[25] Piraux, h., Hai, J., Gaudisson, T., Merah, S., Gazeau, F., Chahine, J.&Hémadi, M. Transferrin-bearing maghemite nano-constructs for biomedical applications. Journal of Applied Physics 2015, 117, 17A336.

[26] Salem, H. F., Kharshoum, R. M., Mahmoud, M., Azim, S. A.&Ebeid, E.-Z. M. Development and characterization of a novel nano-liposomal formulation of alendronate sodium loaded with biodegradable polymer. Ars Pharmaceutica (Internet) 2018, 59, 9-20.

[27] Yadav, D., Sandeep, K., Pandey, D.&Dutta, R. K. Liposomes for drug delivery. J Biotechnol Biomater 2017, 7, 276.

[29] Hua, S. Comparison of in vitro dialysis release methods of loperamide-encapsulated liposomal gel for topical drug delivery. International journal of nanomedicine 2014, 9, 735-744.

[30] Liu, Y., Gao, D., Zhang, X., Liu, Z., Dai, K., Ji, B., Wang, Q.&Luo, L. Antitumor drug effect of betulinic acid mediated by polyethylene glycol modified liposomes. Materials science and engineering: C 2016, 64, 124-132.

[31] Ramalho, M. J., Bravo, M., Loureiro, J. A., Lima, J.&Pereira, M. C. Transferrin-modified nanoparticles for targeted delivery of asiatic acid to glioblastoma cells. Life Sciences 2022, 296, 120435.

[32] Liu, P., Chen, G.&Zhang, J. A review of liposomes as a drug delivery system: Current status of approved products, regulatory environments, and future perspectives. Molecules 2022, 27, 1372.

[33] Andrade, S., Loureiro, J. A.&Pereira, M. C. The role of amyloid β-biomembrane interactions in the pathogenesis of alzheimer's disease: Insights from liposomes as membrane models. ChemPhysChem n/a,

[34] Sharma, G., Parchur, A. K., Jagtap, J. M., Hansen, C. P.&Joshi, A., Chapter 8 - hybrid nanostructures in targeted drug delivery, in Hybrid nanostructures for cancer theranostics, R. Ashok Bohara and N. Thorat, Editors. 2019, Elsevier. p. 139-158.

[35] Gonzalez Gomez, A., Syed, S., Marshall, K.&Hosseinidoust, Z. Liposomal nanovesicles for efficient encapsulation of staphylococcal antibiotics. ACS omega 2019, 4, 10866-10876.

[36] Doi, Y., Shimizu, T., Ishima, Y.&Ishida, T. Long-term storage of pegylated liposomal oxaliplatin with improved stability and long circulation times in vivo. International Journal of Pharmaceutics 2019, 564, 237-243.

[37] Haghiralsadat, F., Amoabediny, G., Helder, M. N., Naderinezhad, S., Sheikhha, M. H., Forouzanfar, T.&Zandieh-Doulabi, B. A comprehensive mathematical model of drug release kinetics from nano-liposomes, derived from optimization studies of cationic pegylated liposomal doxorubicin formulations for drug-gene delivery. Artificial Cells, Nanomedicine, and Biotechnology 2018, 46, 169-177.

[38] Rodrigues, B. d. S., Kanekiyo, T.&Singh, J. Nerve growth factor gene delivery across the blood–brain barrier to reduce beta amyloid accumulation in ad mice. Molecular Pharmaceutics 2020, 17, 2054-2063.

[39] Danaei, M., Dehghankhold, M., Ataei, S., Hasanzadeh Davarani, F., Javanmard, R., Dokhani, A., Khorasani, S.&Mozafari, M. R. Impact of particle size and polydispersity index on the clinical applications of lipidic nanocarrier systems. Pharmaceutics 2018, 10, 57.

[40] Andrade, S., Loureiro, J. A.&Pereira, M. C. Vitamin b12 inhibits aβ fibrillation and disaggregates preformed fibrils in the presence of synthetic neuronal membranes. ACS Chemical Neuroscience 2021, 12, 2491-2502.

[41] Miao, Z. L., Deng, Y. J., Du, H. Y., Suo, X. B., Wang, X. Y., Wang, X., Wang, L., Cui, L. J.&Duan, N. Preparation of a liposomal delivery system and its in vitro release of rapamycin. Experimental and therapeutic medicine 2015, 9, 941-946.

[42] Mumtaz Virk, M.&Reimhult, E. Phospholipase a2-induced degradation and release from lipid-containing polymersomes. Langmuir 2018, 34, 395-405.

[43] Alam, P., Siddiqi, M. K., Chaturvedi, S. K., Zaman, M.&Khan, R. H. Vitamin b12 offers neuronal cell protection by inhibiting aβ-42 amyloid fibrillation. Int. J. Biol. Macromol. 2017, 99, 477-482.

[44] Close, W., Neumann, M., Schmidt, A., Hora, M., Annamalai, K., Schmidt, M., Reif, B., Schmidt, V., Grigorieff, N.&Fändrich, M. Physical basis of amyloid fibril polymorphism. Nature communications 2018, 9, 1-7.

Chapter 5

in vivo Toxicity of Liposomes

The results of this section are published in: *Andrade, S., Loureiro, J.A., Ramirez, S., Catumbela, C.S.G., Soto, C., Morales, R., Pereira, M.C. (2022). Multi-Dose Intravenous Administration of Neutral and Cationic Liposomes in Mice: An Extensive Toxicity Study. Pharmaceuticals, 15, 761.*

5.1. Introduction

The poor pharmacokinetics, reduced bioavailability, and high toxicity of most therapeutic molecules are some of the aspects that decrease their therapeutic efficacy. Such limitations can be overcome using delivery systems to protect molecules from degradation and direct them to the desired target site [1].

Despite the several advantages related to the use of liposomes as delivery systems, they have some drawbacks that restrict their therapeutic potential. While liposomes have been successfully used to reduce the toxicity of therapeutic agents, the vesicles themselves can induce toxicity. Dozens of *in vivo* studies have described the toxicity associated with the administration of one or just a few doses of cationic liposomes [2-4]. However, these reports lack information regarding the long-term toxicity, which is crucial considering the therapeutic regime of several pathologies, such as chronic diseases, that require the repeated administration of therapeutic agents to ensure sustained drug levels for extended periods [5].

Thereby, this chapter aims to provide more details on the liposomes toxicity after repeated doses. This is the first prolonged systemic toxicity study by intravenously administering 10 doses of neutral and cationic liposomes to wild-type mice over 3 weeks. Bare NPs were tested without any targeting ligand to focus this study on evaluating the nanocarriers' toxicity upon repeated administration. Lipid vesicles were characterized physicochemically in terms of hydrodynamic diameter, PdI, and zeta potential. The long-term stability at storage conditions was also evaluated for over 4 months. Mice mortality, variations in body weights (BW), glucose levels, motor abilities, microscopic urinalyses, liposome-blood interaction, and organ weight and morphology were assessed to evaluate potential liposome-induced toxic effects. Histopathological examinations were also performed, and liver injury markers in blood were quantified.

5.2. Materials and Methods

5.2.1. Materials

DSPC (MW 790), CHOL (MW 387), 2-distearoyl-sn-glycero-3-phosphoethanolamine-N-[amino(polyethylene glycol)-2000] (ammonium salt) (DSPE-PEG(2000) amine, MW 2791) and 1,2-dioleoyl-3-trimethylammonium-propane (chloride salt) (DOTAP, MW 699) were purchased from Avanti Polar Lipids, Inc. (USA). Chloroform was obtained from Sigma-Aldrich (EUA). PBS (10X, pH 7.0-7.2, 0.067 M) was acquired from GE Healthcare Life Sciences (HyClone™, USA). Heparin (sodium salt, 1,000 units/mL) was purchased from Sagent (USA).

5.2.2. Preparation of Liposomes

Neutral liposomes were produced by the thin-film hydration method by sonication [6]. Briefly, DSPC, CHOL, and DSPE-PEG(2000)amine were dissolved in chloroform at a molar ratio of 52:45:3. Then, the organic solvent was evaporated under a nitrogen stream. The produced film was hydrated with PBS at 37 °C (66 mM). To reduce the size, the suspension was sonicated for 40 minutes (1-minute ON, 1-minute OFF, 40% of amplitude) in an ice bath using an ultrasonic processor UP400S (Hielscher, Germany).

Cationic liposomes were also produced by the thin-film hydration method followed by extrusion [7]. DOTAP and CHOL (molar ratio 85:15) were dissolved in chloroform, and a thin lipid film was obtained after the evaporation of the organic solvent under a nitrogen stream. The dried lipid film was hydrated with PBS at 37 °C (17 mM) and vortexed for 10 minutes. To reduce the vesicles' size, the suspension was extruded eleven times through Nuclepore™ track-etch polycarbonate membranes with a pore size of 100 nm.

5.2.3. Experimental Animals, Grouping, and Dosing Regime

Thirty-three adult female wild-type mice (C57Bl6) aged between 3-4 months were obtained from Jackson's laboratories (Bar Harbor, USA). Only female mice were used in the present study to avoid possible variability of the results induced by sex differences. Five mice were housed per polypropylene ventilated cage in a room at 22 °C, humidity (40-60%) and a 12/12 h light/dark cycle. Animals were fed with standard mice pellet feed and water ad libitum in the animal facility of the Center for Laboratory Animal Medicine and Care (CLAMC) at UTHealth (Houston, TX, USA). Mice were housed for 48h before starting the experiments. The animal protocol was reviewed and approved by the Animal Welfare Committee (AWC) of the University of Texas Health Science Center at Houston (UTHealth) (approval number AWC-19-0061). All the experiments were performed according to the institutional guidelines.

The animals were randomly distributed into three groups receiving either vehicle (PBS), neutral or cationic liposomes (11/group). All groups received 10 doses of 200 μL over 3 weeks (administrations held on Mondays, Wednesdays, and Fridays). The doses and duration of treatment were selected according to previous studies [8, 9].

5.2.4. Animal Survival, Clinical Observation, Body Weight, and Glucose Levels

Mice were examined daily for clinical signs of toxicity and mortality. The clinical observation included changes in fur, eyes, mucous membranes, lacrimation, and unusual breathing patterns. The BW was recorded before each administration and necropsy. Glucose levels were measured before the first injection and at euthanasia and monitored weekly.

5.2.5. Behavioral Tests

5.2.5.1. Rotarod Test

First created in 1957 by Dunham and Miya, the rotarod test is currently one of the most used behavior tests to test the neuromuscular coordination of rodents [10]. This behavioral test allows concluding on the toxicity of drugs or materials since toxicity in commonly accompanied by modifications in the motor coordination, reducing the time that the animals remain in the rotarod apparatus.

The rotarod equipment consists of a circular rod, spinning at a constant or increasing speed (Figure 5.1). Vertical separators are used to separate each animal, which allow to test simultaneously several animals. The sensitivity of this test can be influenced by some factors, such as the type of rod (smooth or grooved), that need to be considered when designing the experiment or comparing results from distinct studies. Also, in continuous studies, some mice/rats learn that fall is safe and therefore, fall quickly after placed on the rotarod. These animals are the minority and usually removed from the data as outliers [11].

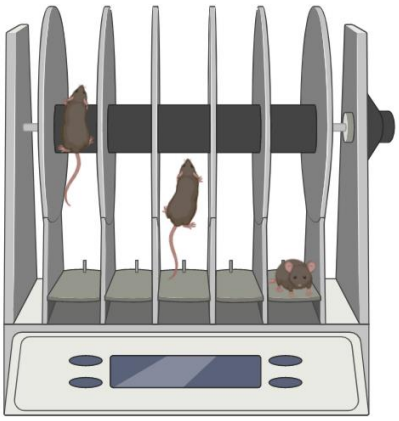

Figure 5.1. Schematic representation of a rotarod test.

The training and test can be performed at a constant or increasing speed, depending on the animal model and the experimental design. Tests conducted at increasing speeds avoid intensive training. The rodent is typically trained to stay on the rod at a reduced and constant rotation speed. The mouse/rat is repositioned each time it falls or changes its direction. Then, the animal is tested on the moving rotarod, which starts at a slow speed and increases the rotation speed at a fixed rate until the equipment reaches a speed at which the

animal falls [12]. The time the mouse takes to fall is considered the endpoint of the experiment. The experiment is recorded three times before the animal returns to its home cage [11]. Control animals can stay on the rotarod for longer than animals with some neurotoxicity [13].

In this study, the rotarod test was performed before the injections and 24 h after the last administration to detect any defects in motor coordination. Following an accelerated speed test protocol, mice were placed into a rotating rod (Med Associates Inc., Fairfax, USA), and the latency to fall was recorded. Succinctly, mice were placed on the rotarod apparatus, rotating at an increasing speed from 4 to 40 rpm, in a trial of 300 seconds. The latency to fall of 3 trials was recorded. A rest interval of 120 seconds between each trial was employed to avoid the animals' fatigue. Two successive animal rotations clinging to the rotarod were registered as latency to fall measurement. Before the first experiment, mice were helped to stay in the correct position for 30 seconds at a constant speed of 4 rpm, to avoid false positives of animals turning, falling, or jumping.

5.2.5.2. Forelimb Grip Strength Test

Distinct techniques, both invasive and non-invasive, have been proposed in the last decades to measure the muscle strength of rodents. Invasive procedures include the in-situ measure of muscle force, while the non-invasive ones include the *in vivo* measurement of muscular strength. Among these methods, the grip strength test presents advantages such as the greatest convenience and lower stress-induced to the animal [14]. Therefore, the grip strength test has been commonly used to evaluate rodents' limb motor and neuromuscular function, as well as neurobehavioral toxicity. This test determines the maximum force performed by an animal. Thus, significant variations in grip strength suggest motor neurotoxicity. The grip strength test is usually complemented with the rotarod test since an animal with low muscle strength will show a low score on the rotarod test [15].

The equipment to perform this experiment consists of a grasping bar horizontally oriented and connected to a force sensor, as illustrated in Figure 5.2. The animal is handled by the tail and positioned in the grid. Instinctively, the animal grabs the grid. It is then pulled back in the horizontal direction. The force exerted by the animal just before it drops the grip is recorded.

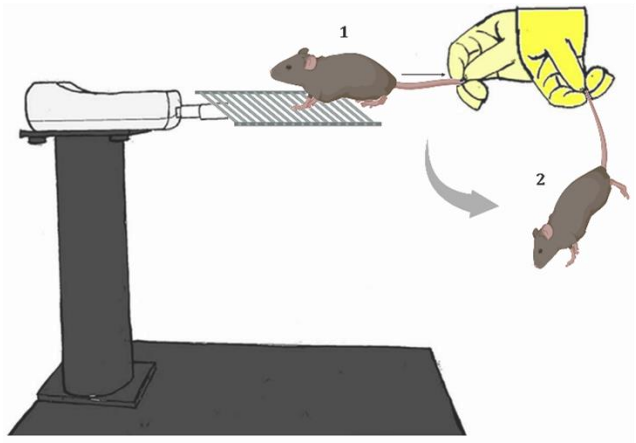

Figure 5.2. Schematic representation of a grip strength test. 1 and 2 represent the initial and final position of the animal, respectively.

However, this technique presents some disadvantages, such as the variation between animals of the same group, the motivation of the animal, as well as the variation in the scientist procedure. It is recommended to perform a reduced number of repetitions in each session, and each session to be interspaced to avoid the animal learning and consequent disinterest in the test. In fact, when the test is performed repeatedly, the animals learn the procedure, lose interest and stop resisting [14].

In this chapter, defects in rodents' limb motor and neuromuscular function were evaluated using a forelimb grip strength test. This test was performed before starting the injections and 48 h post-treatment, allowing an interval rest of 24 h from the rotarod test to avoid mice fatigue. A grip strength meter grid was manufactured to perform this experiment. Concisely, mice were held by the tail and placed horizontally over the grid until the animal forepaws cling. The animals were smoothly pulled back by the tail, and the maximal grip strength value displayed on the screen was recorded. A constant velocity was applied to ensure the repeatability of the test. This procedure was repeated 9 times, with a rest time of 120 seconds every 3 measurements. The forelimb grip strength values were recorded as the average of the 9 measurements.

5.2.6. Microscopic Urinalysis

In the morning following the last administration, three animals from each group were randomly chosen, and urine was collected for microscopic urinalysis. The microscopic

examination was performed using a DMI6000B microscope (Leica, Buffalo Grove, USA). Briefly, a 10 µL drop of urine was placed on a glass microscope slide and covered with a coverslip. The presence of microscopic elements such as red and white blood cells, epithelial cells, casts, crystals, bacteria, yeast, and clumps was analyzed.

5.2.7. *in vitro* Interaction between Blood and Liposomes

The blood was collected by cardiac puncture after being euthanized by CO_2 inhalation. Blood samples (200 µL) were mixed with 200 µL of DSPC:CHOL:PEG(2000) amine and DOTAP:CHOL LUVs (1:1 v/v). A control sample was prepared containing an identical volume of PBS. Blood turbidity changes, clot formation, and hemolysis were examined macroscopically. Then, blood smears of the mixtures (30 µL) were performed and observed using a DMI6000B microscope (Leica, Buffalo Grove, IL, USA).

5.2.8. Acute *in vivo* Interaction between Blood and Liposomes

A group of mice was injected with a single dose of DOTAP:CHOL LUVs. Animals were euthanized by an overdose of anesthesia, and the blood was collected by cardiac puncture. Animals injected with PBS were subjected to the same procedure and used as controls. Blood smears from both animal groups (30 µL) were performed and observed using a DMI6000B microscope (Leica, Buffalo Grove, IL, USA). The effect of a single dose of positively charged liposomes on the morphology of RBCs was evaluated.

5.2.9. Prolonged *in vivo* Study to Assess the Interaction between Blood and Liposomes

After administering 10 doses of PBS, DSPC:CHOL:PEG(2000) amine, and DOTAP:CHOL LUVs, the surviving animals were euthanized 120 h after the last injection via CO_2 inhalation followed by cardiac puncture to collect the blood. Three blood samples (30 µL) of each group were randomly selected to perform blood smears. The morphology of RBCs was analyzed using a DMI6000B microscope (Leica, Buffalo Grove, IL, USA).

5.2.10. Necropsy, Organ Weight, and Morphology

Necropsy was performed immediately after euthanasia. Here, each animal's brain, lungs, liver, kidneys, and spleen were excised and examined macroscopically to identify possible signs of toxicity. The organs were washed with PBS, placed on an absorbent paper for a few seconds, and the absolute organ weight was determined. The dimensions of the organs were also recorded using an automatic digital caliper (Neiko, Wenzhou, China). For further histopathological studies, the organs were placed in a 10% neutral buffered formalin solution. The blood samples from cardiac punctures were collected into Eppendorf tubes containing sodium heparin as an anticoagulant. Blood samples were centrifuged at 3,000 rpm for 15 minutes to collect the serum. Plasma samples were frozen in liquid nitrogen and then stored at -80°C until used for the liver injury assessment.

5.2.11. Histopathological Examinations

Histology is one of the many branches of biology that aims to study biological tissues' anatomy at a microscopic level. After the tissue extraction, samples must be processed before they can be observed under the microscope. Figure 5.3 shows sample preparation's main steps, which include fixation, dehydration, clearing, embedding, sectioning, and staining [16].

Figure 5.3. Schematic representation of the main steps of tissue processing.

After animal death and tissue extraction, samples must be fixed, i.e., preserved to maintain their structure, avoiding autolysis (self-destruction by enzymes) and tissue damage. The organ is immersed in a chemical fixative, usually formaldehyde. The chemical fixative diffuses through the tissue and reacts with amino acids producing reactive groups, which combine and form methylene bridges (crosslinks). As a result, the rigidity of the tissue increases, and the enzymes are inactivated, preventing tissue degradation. The recommended fixative volume is 50 to 100 times higher than the tissue volume [17].

Once the tissue is fixed, it needs to be treated to allow its cutting into thin sections required for microscopic observation. To cut the tissue, the sample must first be embedded in paraffin wax. However, wax is insoluble in water; therefore, samples need to be dehydrated before adding paraffin wax. Thus, dehydration consists of immersing the sample in a series of ethanol solutions at increasing concentrations until reaching pure ethanol to replace the water in the tissue. After dehydrating the tissue, ethanol is replaced by a clearing solution to clear the sample and prepare it for embedding. Xylene is the most used solvent to replace ethanol since they are miscible.

To preserve the tissue morphology and mechanically support the sample during the sectioning step, tissues must be infiltrated with an embedding medium, typically paraffin. In this step, the tissue is embedded in liquid paraffin (at 60 °C), which is cooled at room temperature until solidifying. Once the tissue is embedded, it is stable for several years at room temperature.

After embedding, the tissue is cut into thin sections (5 to 20 microns) using a microtome. To smooth out any wrinkles, the sections are positioned in a water bath at 37 °C for some minutes. Then, the sections are placed on the microscope slide and dried overnight to improve the adhesion. After that, the samples can be stored for many years.

To assist in the microscopic visualization, samples are stained to confer contrast and make tissue components visibly conspicuous. Most staining solutions are aqueous, so the wax must be dissolved and replaced with water (rehydration) to stain the sections. The sections are passed through xylene and then in a series of ethanol solutions at decreasing concentrations until reaching pure water. Once stained, the section is dehydrated and placed in xylene. A mounting medium is added, and a coverslip is placed on the top of the microscope slide to stabilize and protect the sample.

In this study, major organs were stored in 3.7% formaldehyde, paraffin-embedded, and sliced at 10 μm for hematoxylin-eosin staining following routine protocols [18]. Briefly, after deparaffinization and rehydration, tissue slices were stained with hematoxylin solution for 5 minutes in a dark container and rinsed with distilled water. Next, sections were stained with eosin solution for 30 seconds, followed by dehydration with alcohol and clearing with xylene. The mounted sections were visualized under light microscopy, and histopathological evaluation was performed for spleen, lung, liver, and kidney tissues. Stained slices were observed at low- and high-power magnifications (10X and 40X, respectively) using a Leica DMI6000 B microscope (Leica Microsystems, Buffalo Grove, IL). Representative photomicrographs were taken with a digital camera (DFC310FX Leica™). Low- and high-power magnifications were used to qualitatively analyze the cell type content in the red pulp of the spleen, the micromorphological integrity, the presence of granuloma formation, and the extent of cellular infiltration exhibited by lungs, livers, and kidneys.

5.2.12. Quantification of Liver Injury Markers in Blood

The levels of two established liver injury biomarkers, aspartate aminotransferase (AST) and alanine aminotransferase (ALT) were measured via diagnostic enzyme assay kits (Teco Diagnostics, Anaheim, CA) in blood plasma, according to the manufacturer's protocol. ALT and AST activity was determined by measuring the rate of oxidation of NADH throughout an enzymatic reaction sequence at a specific wavelength (340 nm) using a SpectraMax® iD3 Multi-Mode Microplate Reader.

5.2.13. Statistical Analysis

All the results are expressed as mean ± SD. The statistical analysis of data was performed using student's t-tests, with a confidence interval of 95%. Results whose p-values ≤ 0.05 were considered significantly different. Statistical analysis and data presentation were completed using Prism 8 (GraphPad Software Inc. La Jolla, CA, USA).

5.3. Results and Discussion

5.3.1. Physicochemical Characterization of Liposomes

The physicochemical properties of the neutral and cationic LUVs were evaluated in terms of hydrodynamic diameter, PdI, and zeta potential values, as shown in Table 5.1. While neutral liposomes exhibited a hydrodynamic diameter of 139 ± 13 nm, the cationic liposomes showed a significantly smaller average of 112 ± 3 nm ($p<0.05$) (Table 5.1). Such difference may be related to the distinct composition of the liposomes [19].

Table 5.1. Physicochemical properties of neutral and cationic liposomes in terms of hydrodynamic diameter, PdI, and zeta potential.

Liposomes	Composition	Hydrodynamic diameter (nm)	PdI	Zeta potential (mV)
Neutral	DSPC:CHOL:DSPE-PEG(2000) amine	139 ± 13	0.22 ± 0.02	-1 ± 1
Cationic	DOTAP:CHOL	112 ± 3	0.13 ± 0.01	33 ± 2

It has been reported that the efficacy of a delivery system is closely related to the size of NPs since this property can affect the *in vivo* stability, blood circulation time, agent release, cell uptake, clearance, and toxicity of NPs. NPs larger than 200 nm have revealed to be quickly cleared from the bloodstream by the lymphatic system [20]. However, nanocarriers too small have been connected to higher toxicity as the NP surface area increases. Thus, an optimal diameter of around 100 nm has been identified as particles around that size have shown decreased toxicity [1]. Such evidence proved that the produced formulations have mean sizes valid for delivery applications.

The size distribution of NPs was evaluated by assessing the PdI of formulations. All formulations presented PdI values lower than 0.2 (Table 5.1), suggesting that the lipid suspensions have homogenous sizes and therefore, are valid for delivery purposes [21]. However, the neutral liposomes showed PdI values significantly higher than the cationic liposomes ($p<0.05$), probably due to the different techniques used to reduce the size of the vesicles. This data goes in line with a report by Ong et al. demonstrating that extruded liposomes present smaller PdI values than sonicated liposomes [22].

The surface charge of NPs is another key property to consider when designing delivery systems since it affects nanocarriers' *in vivo* internalization rate and toxicity. As expected, neutral LUVs showed a zeta potential close to zero mV while cationic LUVs exhibited a zeta potential of 33 ± 2 mV (Table 5.1).

Liposome stability remains a major limitation for their clinical application. For that reason, it is crucial to ensure their stability during the production process, and the duration of the experiments since NPs tend to aggregate to attain a thermodynamically favorable state. Hence, a long-term stability study of the produced liposomes was performed at storage conditions (4 °C) over 4 months (Figure 5.4). Variations in some of these characteristics suggest that the structure of NPs is altered over time, which may be linked with the loss of their stability and potential activities [23]. From Figure 5.4, it is possible to observe that the physicochemical properties of the neutral liposomes remained constant ($p>0.05$) for at least 4 months when stored at 4 ˚C in the buffered medium. Moreover, while neutral LUVs exhibited a mean d/d0 value of approximately 1.1 over the 4 months study period, cationic vesicles presented a value of 3.9 at the experimental endpoint, indicating NPs aggregation. The d/d0 value represents the ratio between the mean diameter of the NPs at each time point and the initial mean diameter, being an indicator of size variation [24]. However, the physicochemical properties of DOTAP:CHOL vesicles were not significantly changed over the first month of storage. After this time, cationic liposomes exhibited a mean diameter above 200 nm and a PdI over 0.4.

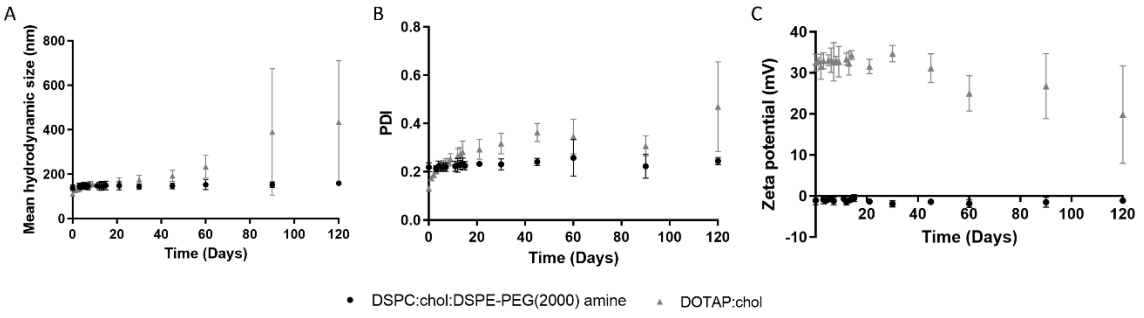

Figure 5.4. Physicochemical characterization of liposomes over 4 months.

5.3.2. Mice Survival and Clinical Observations

The survival curves of mice repeatedly exposed to the different liposomes are shown in Figure 5.5. No mortality was registered among mice exposed to repeated doses of neutral liposomes, thus overlapping the survival curve of the control group (treated with PBS).

However, a significant mortality rate was observed in mice treated with cationic liposomes, with an average of 27% mortality immediately after the first injection. Moreover, the mortality rate increased to 36% after the second injection. From the sixth to the tenth administration, mice treated with cationic liposomes displayed a survival rate of 55%. These results are in accordance with Chien et al. (2005) [9], which observed a 33% mortality rate after injecting three doses of cationic liposomes to male BALB/c mice. Despite the mortality observed in mice exposed to cationic liposomes, none exhibited alterations in fur appearance, eyes, sleep cycles, salivation, defecation, food and water intake, or other visible signs.

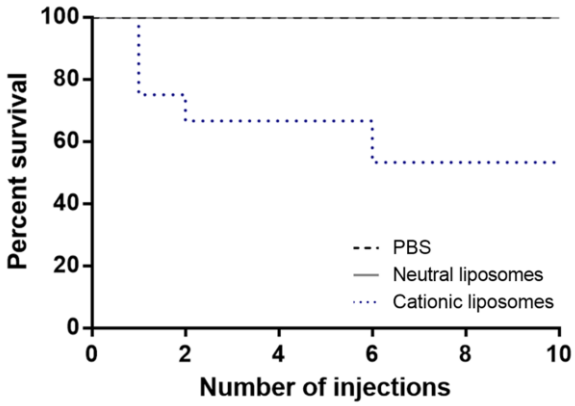

Figure 5.5. Effect of the repeated administration of PBS, neutral and cationic liposomes on mice survival.

5.3.3. Bodyweight

BW is frequently recorded in toxicology studies since variations over 20% can be linked with toxic effects [25]. Thus, the mice's BW was recorded before each administration and euthanasia (Table S5.1 of the Supplementary Material). At the baseline, the PBS, neutral liposomes, and cationic liposomes groups showed an average BW of 21.6 ± 1.3, 21.6 ± 1.4, and 21.2 ± 0.8, respectively, with no significant differences between the liposomes-treated and control mice ($p>0.05$). The mice's BW remained stable until the end of the experiment ($p>0.05$). Similar findings were obtained by Knudsen et al. (2015) [8] after administering a single dose of cationic liposomes to male Han Wistar rats.

5.3.4. Glucose Levels

Blood glucose represents another extensively used indicator in toxicological studies since variations in glucose levels are an established toxicity surrogate. Importantly, fluctuations in blood glucose concentrations can induce secondary toxic events, including glial toxicity, oxidative stress, and inflammatory processes [26]. Thus, the glucose levels of mice treated with repeated doses of PBS, neutral- and cationic- lipid vesicles were monitored weekly and are shown in Figure S5.1 (Supplementary Material). Before starting the injection of LUVs, control, neutral and cationic groups exhibited glucose levels of 135 ± 14, 126 ± 8, and 140 ± 10 mg/dL, respectively, with no significant differences between groups ($p>0.05$). No significant variations were observed over the experiment in neutral and cationic liposomes-treated mice compared with the control group ($p>0.05$), which is in concordance with a previous study [8].

5.3.5. Behavioral Tests

Behavioral monitoring is a sensitive way to assess the nervous system toxicosis induced by a tested drug or material [27]. In fact, variations in the behavioral responses of animals may be related to the impairment of sensory, motor, and cognitive aspects. The rotarod test is currently one of the most used behavior tests where the neurotoxicity or effect of a compound on animal behavior can be evaluated [10]. By monitoring the time rodents remain in the rotarod, motor coordination and balance defects can be detected [13]. Therefore, the rotarod test was performed before starting the NPs injection and 24 h-post-treatment. To complement the rotarod test, a forelimb grip strength test was performed 48 h post-treatment to evaluate the limb motor and neuromuscular function of experimental and control rodents [15]. The results of the rotarod and grip strength tests are shown in Figures 5.6 A and B, respectively.

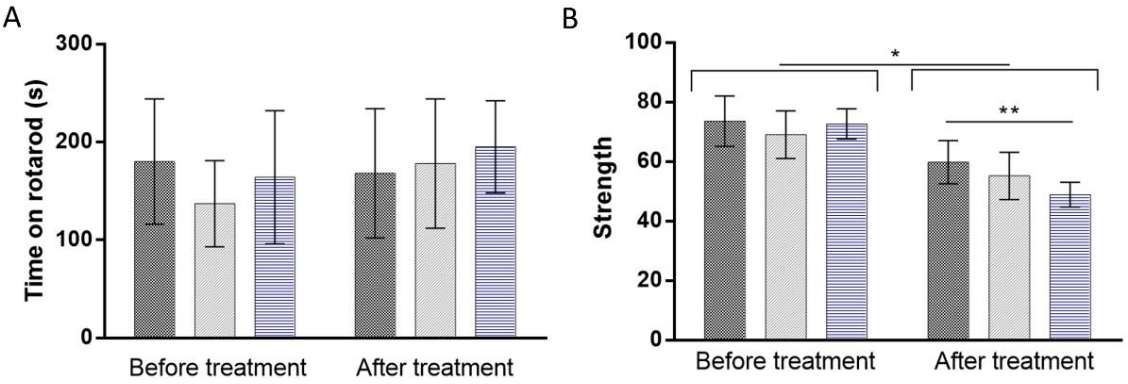

Figure 5.6. Effect of multi-dose administration of PBS (dark gray), neutral (light gray), and cationic liposomes (blue) on A) rotarod and B) grip strength performance. *p<0.05, **p<0.01.

Concerning the rotarod test (Figure 5.6 A), no significant variation in the latency to fall from the rotarod apparatus was detected after the repeated administration of both neutral and cationic vesicles compared to the control group (p>0.05). These data suggest the absence of motor dysfunction due to liposome treatments. However, grip strength data (Figure 5.6 B) revealed a significant reduction of the maximal muscle strength of mice after the repeated injection of PBS, neutral and cationic liposomes (p<0.05). Although variations on the maximal peak force may indicate motor neurotoxicity, the decreased grip strength of the control group suggests a lack of interest in the trial, potentially due to the excessive manipulation associated with repeated injections. Alternatively, rodents may get used to the manipulation, reducing their willingness to execute the task. Regardless, the repeated administration of cationic liposomes significantly declined the forelimb peak force values of mice by around 9.1% compared to the control group (p<0.01), suggesting that these particular vesicles induce harmful effects on limb motor and neuromuscular function of mice.

5.3.6. Microscopic Urinalysis

The microscopic examination of urine is another common procedure to detect possible toxicity signals. Urinalysis identifies abnormal solutes, cells, casts, crystals, organisms, or particulate matter that may indicate some renal or systemic pathology. Figure S5.2 (Supplementary Material) shows the microscopic urinalysis of mice after the prolonged treatment of PBS, neutral or positively charged liposomes. The urine of healthy animals or patients usually contains several chemicals that can be found in the form of crystals, and so, a small number of urine crystals become clinically irrelevant. However, the presence of abnormal crystals may indicate renal dysfunction. Some usually present crystals (triple phosphate) are pointed by black arrows in Figure S5.2 (Supplementary Material). In contrast, evidence of hippuric acid crystals was identified in the urine of mice treated with neutral liposomes.

In addition to crystals, some endothelial cells are also commonly present in the urine of healthy individuals. Red arrows in Figure S5.2 (Supplementary Material) depict some of these cells. However, other cell types are not expected to be found in urine, and thus, their presence is acknowledged as an indicator of health issues. An example of this are red blood cells (RBCs). When present in urine, RBCs are indicative of a disease condition known as hematuria. Figure S5.2 C (blue arrows) indicates some of the numerous RBCs present in the urine of mice treated with cationic LUVs, indicating damage at this level. Notably, hematuria was absent in the urine of the control and neutral liposome groups. Importantly, the RBCs identified in the cationic LUVs-treated mice's urine exhibited an unusual form with a spiked cell membrane, characteristic of acanthocytes [28]. This abnormal kind of RBCs possesses some spikes of varying lengths and widths irregularly located on the cell surface, as shown by the green arrows in Figure S5.2 D.

5.3.7. Liposomes-Blood Interaction

Before reaching target tissues or cells, liposomes injected intravenously first interact with blood components [29]. Thus, after observing a 27% mortality rate caused by the first injection of DOTAP:CHOL LUVs, an *in vitro* LUVs-blood interaction study was performed to identify the possible cause of such immediate deaths. Figure 5.7 shows blood samples from untreated mice mixed with PBS, neutral or cationic liposomes. It is possible to observe that positively charged liposomes induced noticeable changes in blood, substantially increasing its turbidity and inducing coagulation (Figure 5.7 C). In contrast, neither the increase of the turbidity nor the formation of clots was verified when PBS and neutral liposomes were mixed with blood (Figures 5.7 A and B). Confirming the previous observations, a microscopic analysis of blood smears suggests that RBCs agglutinate in the presence of cationic liposomes (Figure S5.3 of Supplementary Material). These findings are in line with Senior's report [30], which also detected the increase in turbidity and the formation of clot-like mass upon the incubation of cationic liposomes with rat plasma. Furthermore, the authors revealed that the extent of plasma-liposomes interactions depends on the concentration of the phospholipid positive charge [30].

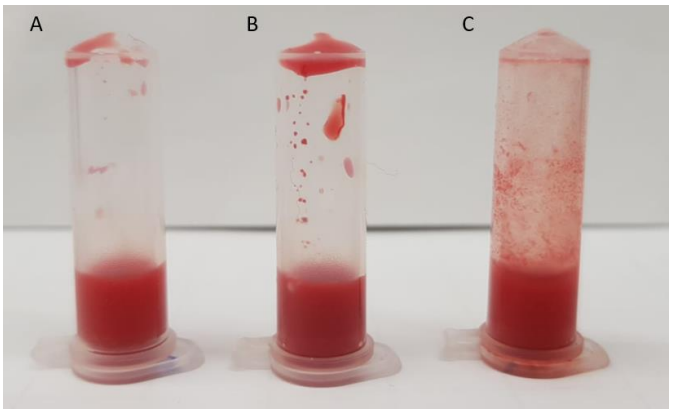

Figure 5.7. *Ex vivo* blood-liposome interaction. Blood from non-treated mice was mixed with either A) PBS, B) neutral, or C) cationic liposomes.

The acute interaction between blood components and liposomes was also assessed *in vivo* by intravenously injecting one dose of DOTAP:CHOL LUVs into mice. Fresh blood was collected, and a blood smear was performed to evaluate possible alterations in RBCs morphology. The microscopic analysis of the blood smears of these mice shows that, after a single administration, positively charged liposomes induce morphological changes in RBCs (Figure S5.4 of Supplementary Material). Specifically, RBCs transitioned from a regular spherical shape (Figure S5.4 A of Supplementary Material) to irregular structures involving either fusiform (acuminocytes) (Figure S5.4 B of Supplementary Material, red arrows) or teardrop forms (dacrocytes) (Figure S5.4 B of Supplementary Material, blue arrows).

While numerous acuminocytes and dacrocytes were observed after a single dose of DOTAP:CHOL LUVs (Figure S5.4 B of Supplementary Material), such variations were less evident after repeated administration of cationic liposomes (Figure 5.8 C). Instead, several fragmented RBCs (commonly called schistocytes) were identified in the blood smears of mice from the cationic liposomes group (Figure 5.8 C, black arrows). Such structures are smaller than usual RBCs and typically irregularly shaped, and result from hemolysis (Figure 5C, red arrow). Hemolysis of erythrocytes caused by the interaction with cationic liposomes was previously observed *in vitro* [30]. No irregular structures were noticed in the groups treated with PBS (Figure 5.8 A) and neutral liposomes (Figure 5.8 B).

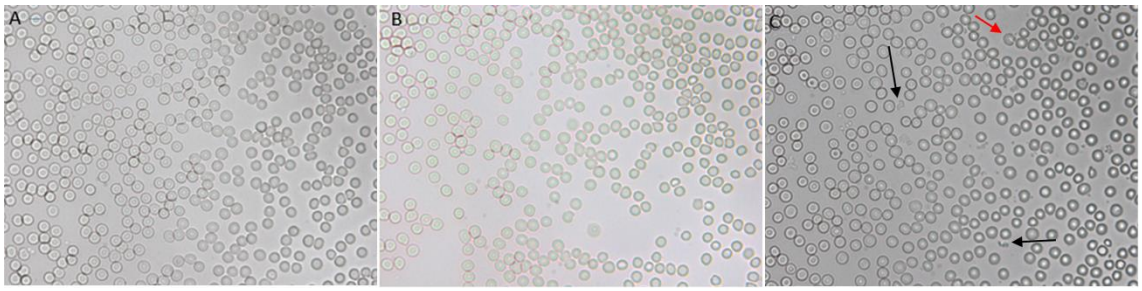

Figure 5.8. *In vivo* cationic liposomes-blood interaction. Microscopic images of blood smears from mice treated with A) PBS, B) neutral, and C) cationic liposomes. Images obtained at a 40X magnification.

Moreover, high variability in the size of RBCs was observed, a condition called anisocytosis (Figure S5.5 of Supplementary Material). Anisocytosis was quantified by assessing the RBC's mean width and the SD of the gaussian distributions from the red cell distribution width (RDW) histograms using the Measure Tool of the ImageJ software (National Institutes of Health, Bethesda, MD, USA). Details on these results are shown in Figure S5.5 (Supplementary Material) and Table 5.2. Overall, these findings suggest that neutral liposomes do not alter RDW compared to RBCs derived from control mice (Figure S5.5, gray and black lines and bars). However, repeated injections of positively charged LUVs significantly affect RDW (Figure S5.5, blue lines and bars). Actually, the data presented in Table 5.2 reveals a reduction in the average width of RBCs, likely due to the presence of several microcytic RBCs (erythrocytes smaller than usual). As expected, the cationic group displayed the largest SD (Table 2), suggesting a more significant size variability of RBCs, i.e., anisocytosis [31]. This information is relevant as it explains the toxicity exerted by cationic liposomes. The fact that RBCs in mice treated with cationic liposomes are less and smaller indicates a loss of RBCs. Consequently, two events should be occurring in these mice: i) the faster production of RBCs to compensate low levels results in smaller RBCs due to the high demand for hemoglobin; and ii) larger RBCs also appear to compensate the loss.

Table 5.2. Effect of the repeated administration of PBS, neutral and cationic liposomes on the mean width of red blood cells (RBCs).

	PBS group	Neutral group	Cationic group
Mean width of RBCs (pixel)	44.7 ± 2.6	44.6 ± 2.6	43.4 ± 3.1

The surface charge as been pointed as a determining factor affecting the NPs hemocompatibility [32]. Han et al. (2012) [33] revealed that the electrostatic interactions between cationic NPs and the erythrocyte membrane cause erythrocyte agglutination. The functionalization of the NPs surface with negatively charged groups reduced the erythrocyte aggregating effects of the NPs [33]. In turn, Zhao et al. (2011) revealed that modifying the liposomes surface with PEG molecules may shade the positive charge of the NPs, thus avoiding the toxic blood-liposomes interactions [34].

5.3.8. Organ Weight and Morphology

The comparison of the organ weight between substance-treated and control groups is extensively used to assess harmful effects [35]. In fact, organ weight is one of the most sensitive markers of toxicity since organ damage does not always translate into modifications in its morphology [36]. The absolute weight of the brain, lung, liver, kidney, and spleen was recorded at necropsy (Figure 5.9 A). The brain, liver, and kidney weight and size of mice treated with neutral and cationic liposomes did not significantly change compared to the control group ($p>0.05$). However, a significant reduction of the absolute lung weight was observed in mice treated with cationic LUVs-treated. Interestingly, the absolute weight of the spleen significantly increased in both liposome-treated groups. This variation was accompanied by an increase in the spleen dimensions in both liposomes-treated groups ($p<0.05$) (Figure 5.9 B). No major macroscopic changes were observed in the brain, lung, liver, kidney, or spleen after the repeated administration of liposomes.

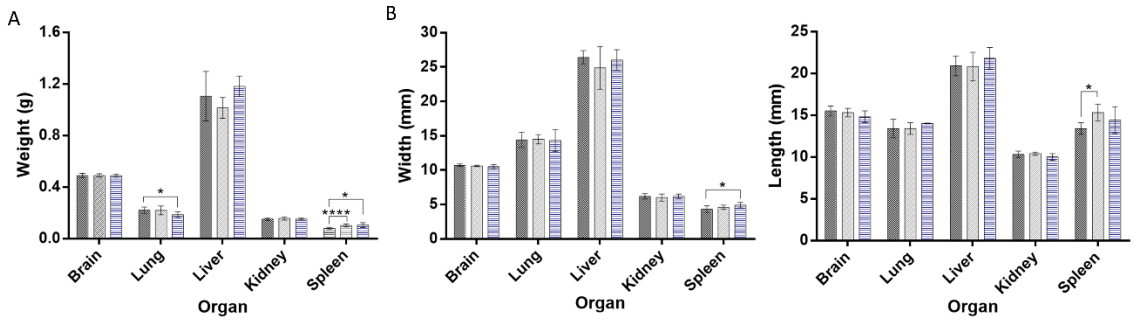

Figure 5.9. A) Absolute organ weight, B) organ width, and C) organ length of mice treated with repeated doses of PBS (dark gray), neutral (light gray), and cationic (blue) liposomes. *$p<0.05$, ****$p<0.0001$.

5.3.9. Histopathological Examination

Histopathological studies of several tissues, including liver, lung, kidney, and spleen, were performed. While no alterations were noticed in the tissues of neutral LUVs-treated mice, the histopathological examination revealed that cationic liposomes induce alterations at the hematological level and inflammatory components. The spleen revealed extravascular hematopoiesis observed as diffuse hyperplasia of the red pulp (Figure S5.6 of Supplementary Material). In addition, an evident enrichment in megakaryocytes (Figure 5.10 C, blue arrowhead) was observed in the spleen of mice treated with cationic liposomes compared with animals challenged with neutral liposomes or PBS. While some extra-medullar hematopoiesis is normal in rodents (especially in mice), an increase in this feature may result from induced hematotoxicity. The presence of hemosiderin (brown pigment) (Figure 5.10 C, red arrowhead) in the spleens of cationic liposomes treated mice may result from hemolytic anemia [37]. It is conceivable that since these are non-PEGylated liposomes, the NPs are recognized relatively fast by the spleen due to binding to proteins such as immunoglobulins, complement proteins and apolipoproteins [8]. Supporting these observations, the lungs of mice treated with cationic liposomes also showed a large population of brown pigmented alveolar macrophages (Figure 5.10). This could be explained by the high levels of damaged RBCs induced by cationic liposomes. These results agree with the modification of the morphology observed in both organs (Figure 5.9). Similar findings have been found after the acute administration of cationic nanoparticles [8, 38]. Increased DNA damage in both lung and spleen after a single administration of cationic liposomes was observed in a previous study [8]. Moreover, cationic liposomes have been associated with dose-dependent toxicity and pulmonary inflammation. Dokka et al. (2000) demonstrated that cationic liposomes induces the generation of reactive oxygen species in lung cells causing inflammation and toxicity [3].

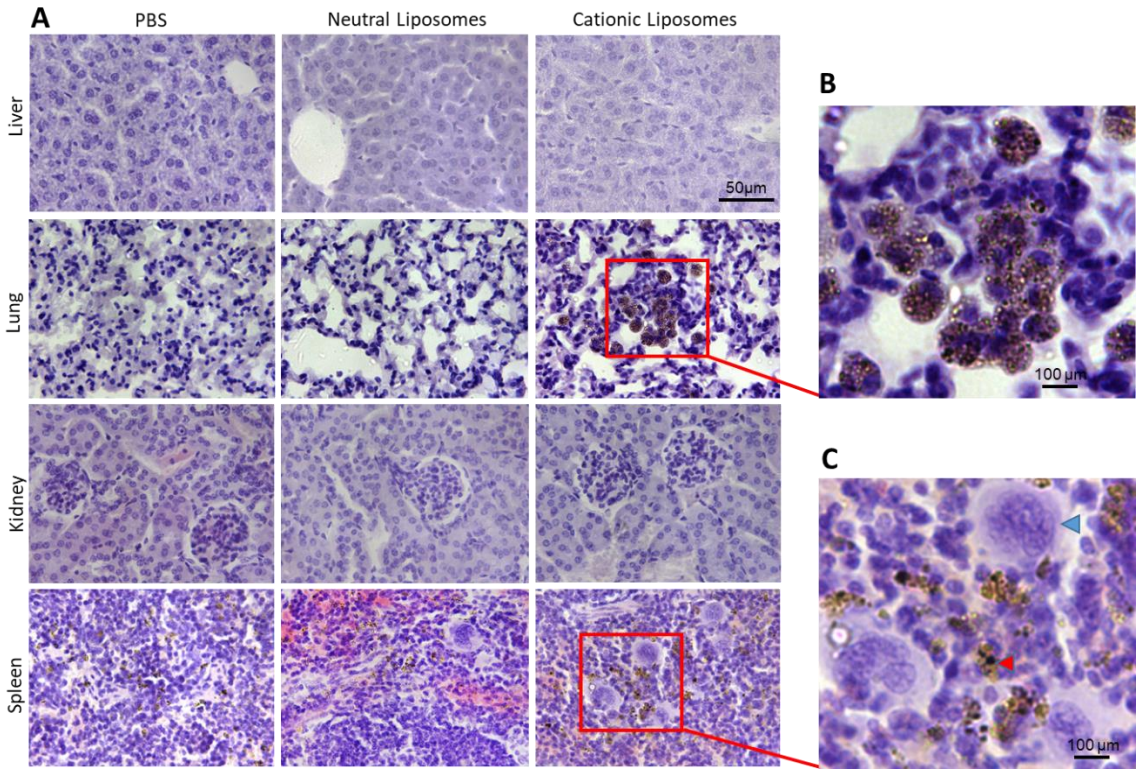

Figure 5.10. A) Histopathological analysis of liver, lung, kidney, and spleen from mice treated with PBS, neutral or cationic liposomes (bar depicts 50 µm) (10X magnification). B) Magnification of a lung area from mice treated with cationic liposomes displaying brown pigment (hemosiderin) contained within alveolar macrophages. C) Magnification of a spleen area from mice treated with cationic liposomes depicting brown pigmentation (hemosiderin, red arrowhead), and megakaryocytes (blue arrowhead). Bar in B) and C) represent 100 µm (40X magnification).

Importantly, the above-mentioned alterations are in line with the anisocytosis observed in blood smears (Figure S5.3 of Supplementary Material), the increased hematuria characterized by the presence of shape-altered RBCs in the urine of mice treated with cationic liposomes (Figure S5.2 of Supplementary Material), and the agglutination of fresh blood induced by cationic liposomes *in vitro* (Figure 5.7). No evident alterations were observed in the liver and kidneys (Figures S5.6 and S5.7 of Supplementary Material).

5.3.10. Serum Biochemistry

The liver is the organ that processes most of the substances introduced into the organism. As such, toxic compounds or molecules may exert their toxicity at the liver level.

To explore potential liver-induced toxicity, alterations in the levels of liver proteins such as AST and ALT were assessed in the blood of experimental and control mice. In agreement with the data presented in Figure 5.10, no changes in AST and ALT levels were found between any of the groups included in this study (Figure 5.11). These data suggest that the liver is not critically damaged by liposomes and support the idea that the toxicity induced by cationic liposomes is mainly associated with RBCs.

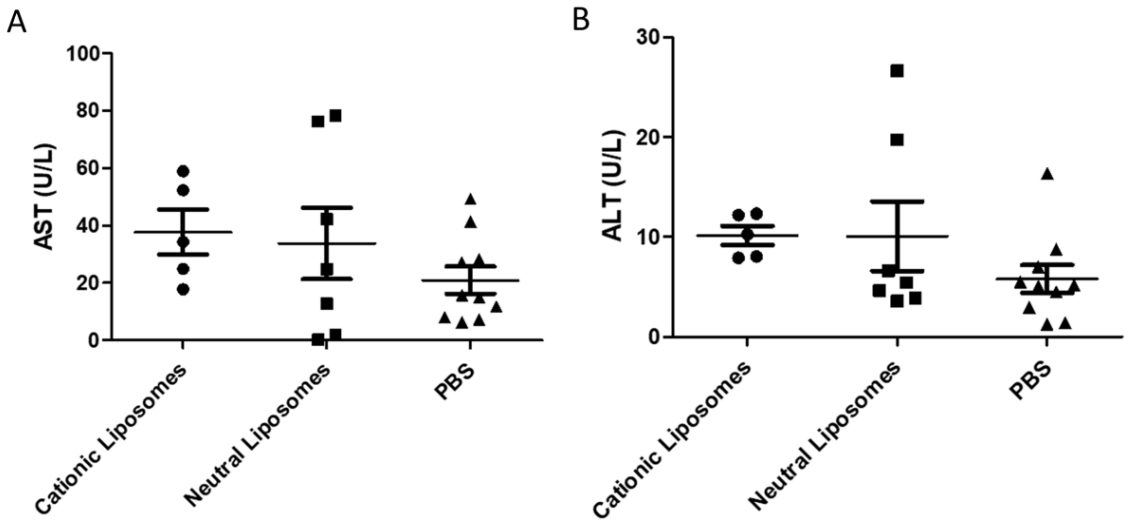

Figure 5.11. Plasma levels of A) aspartate aminotransferase (AST) and B) alanine aminotransferase (ALT) in the blood of mice treated with either PBS (triangles), neutral (squares), or cationic liposomes (circles).

5.4. Conclusion

This study thoroughly characterized the potential toxicity of neutral liposomes after repeated intravenous administrations in rodents. The neutral liposomes' toxicity was compared with that of traditional cationic liposomes. The results show that neutral liposomes did not induce animal mortality or alterations in the evaluated parameters including bodyweight and glucose levels. Moreover, no indicators of toxicity were observed through the rotarod and grip strength tests, microscopic urinalysis, and blood cells morphology analysis. Histopathological studies were performed, and no alterations were noticed in the tissues of neutral liposomes-treated mice. Cationic liposomes were toxic, evidenced by a 45% lethality. According to the data, the toxicity induced by the repeated

administration of the cationic liposomes appears to be associated with the adverse interactions of the lipid vesicles with anionic serum macromolecules. Importantly, this study highlights the safety of neutral liposomes and support their use as drug shuttles, even when repeated doses of a therapeutic agent are needed to be administered for optimal effects.

References

[1] Ramalho, M. J., Andrade, S., Loureiro, J. A.&do Carmo Pereira, M. Nanotechnology to improve the alzheimer's disease therapy with natural compounds. Drug delivery and translational research 2019, 1-23.

[2] Li, Y., Cui, X.-L., Chen, Q.-S., Yu, J., Zhang, H., Gao, J., Sun, D.-X.&Zhang, G.-Q. Cationic liposomes induce cytotoxicity in hepg2 via regulation of lipid metabolism based on whole-transcriptome sequencing analysis. BMC Pharmacology and Toxicology 2018, 19, 43.

[3] Dokka, S., Toledo, D., Shi, X., Castranova, V.&Rojanasakul, Y. Oxygen radical-mediated pulmonary toxicity induced by some cationic liposomes. Pharmaceutical Research 2000, 17, 521-525.

[4] Yu, J., Zhang, H., Li, Y., Sun, S., Gao, J., Zhong, Y., Sun, D.&Zhang, G. Metabolomics revealed the toxicity of cationic liposomes in hepg2 cells using uhplc-q-tof/ms and multivariate data analysis. Biomedical Chromatography 2017, 31, e4036.

[5] Singh, A. P., Biswas, A., Shukla, A.&Maiti, P. Targeted therapy in chronic diseases using nanomaterial-based drug delivery vehicles. Signal transduction and targeted therapy 2019, 4, 1-21.

[6] Andrade, S., Ramalho, M. J., Loureiro, J. A.&Pereira, M. C. Interaction of natural compounds with biomembrane models: A biophysical approach for the alzheimer's disease therapy. Colloids Surf B Biointerfaces 2019, 180, 83-92.

[7] Andrade, S., Loureiro, J. A.&Pereira, M. C. Vitamin b12 inhibits aβ fibrillation and disaggregates preformed fibrils in the presence of synthetic neuronal membranes. ACS Chemical Neuroscience 2021, 12, 2491-2502.

[8] Knudsen, K. B., Northeved, H., Kumar Ek, P., Permin, A., Gjetting, T., Andresen, T. L., Larsen, S., Wegener, K. M., Lykkesfeldt, J., Jantzen, K., Loft, S., Møller, P.&Roursgaard, M. In vivo toxicity of cationic micelles and liposomes. Nanomedicine: Nanotechnology, Biology and Medicine 2015, 11, 467-477.

[9] Chien, P.-Y., Wang, J., Carbonaro, D., Lei, S., Miller, B., Sheikh, S., Ali, S. M., Ahmad, M. U.&Ahmad, I. Novel cationic cardiolipin analogue-based liposome for efficient DNA and small interfering rna delivery in vitro and in vivo. Cancer gene therapy 2005, 12, 321-328.

[10] Dunham, N. W.&Miya, T. S. A note on a simple apparatus for detecting neurological deficit in rats and mice *. Journal of the American Pharmaceutical Association (Scientific Edition) 1957, 46, 208-209.

[11] Mann, A.&Chesselet, M.-F., Chapter 8 - techniques for motor assessment in rodents, in Movement disorders (second edition), M.S. LeDoux, Editor. 2015, Academic Press: Boston. p. 139-157.

[12] Rustay, N. R., Wahlsten, D.&Crabbe, J. C. Influence of task parameters on rotarod performance and sensitivity to ethanol in mice. Behavioural Brain Research 2003, 141, 237-249.

[13] Sills, G. J.&Brodie, M. J., Antiepileptic drugs | preclinical drug development in epilepsy, in Encyclopedia of basic epilepsy research, P.A. Schwartzkroin, Editor. 2009, Academic Press: Oxford. p. 97-103.

[14] Takeshita, H., Yamamoto, K., Nozato, S., Inagaki, T., Tsuchimochi, H., Shirai, M., Yamamoto, R., Imaizumi, Y., Hongyo, K., Yokoyama, S., Takeda, M., Oguro, R., Takami, Y., Itoh, N., Takeya, Y., Sugimoto, K., Fukada, S.-i.&Rakugi, H. Modified forelimb grip strength test detects aging-associated physiological decline in skeletal muscle function in male mice. Scientific Reports 2017, 7, 42323.

[15] Nevins, M. E., Nash, S. A.&Beardsley, P. M. Quantitative grip strength assessment as a means of evaluating muscle relaxation in mice. Psychopharmacology 1993, 110, 92-96.

[16] Trigiano, R. N., Malueg, K. R.&Graham, E. T., Histological techniques, in Plant tissue culture concepts and laboratory exercises. 2018, Routledge. p. 45-53.

[17] Dey, P., Fixation of histology samples: Principles, methods and types of fixatives, in Basic and advanced laboratory techniques in histopathology and cytology. 2018, Springer Singapore: Singapore. p. 3-17.

[18] Duran-Aniotz, C., Moreno-Gonzalez, I., Gamez, N., Perez-Urrutia, N., Vegas-Gomez, L., Soto, C.&Morales, R. Amyloid pathology arrangements in alzheimer's disease brains modulate in vivo seeding capability. Acta neuropathologica communications 2021, 9, 1-13.

[19] Garbuzenko, O., Barenholz, Y.&Priev, A. Effect of grafted peg on liposome size and on compressibility and packing of lipid bilayer. Chemistry and Physics of Lipids 2005, 135, 117-129.

[20] Hoshyar, N., Gray, S., Han, H.&Bao, G. The effect of nanoparticle size on in vivo pharmacokinetics and cellular interaction. Nanomedicine (Lond) 2016, 11, 673-692.

[21] Danaei, M., Dehghankhold, M., Ataei, S., Hasanzadeh Davarani, F., Javanmard, R., Dokhani, A., Khorasani, S.&Mozafari, M. R. Impact of particle size and polydispersity index on the clinical applications of lipidic nanocarrier systems. Pharmaceutics 2018, 10, 57.

[22] Ong, S. G. M., Chitneni, M., Lee, K. S., Ming, L. C.&Yuen, K. H. Evaluation of extrusion technique for nanosizing liposomes. Pharmaceutics 2016, 8, 36.

[23] Ramalho, M. J., Loureiro, J. A., Coelho, M. A.&Pereira, M. C. Factorial design as a tool for the optimization of plga nanoparticles for the co-delivery of temozolomide and o6-benzylguanine. Pharmaceutics 2019, 11, 401.

[24] Ramalho, M. J., Loureiro, J. A., Gomes, B., Frasco, M., Coelho, M.&Pereira, M. C., presented at 2015 IEEE 4th Portuguese Meeting on Bioengineering (ENBENG). Plga nanoparticles for calcitriol delivery, 2015.

[25] Lim, H.-S., Seo, Y. S., Ryu, S. M., Moon, B. C., Choi, G.&Kim, J.-S. Two-week repeated oral dose toxicity study of mantidis ootheca water extract in c57bl/6 mice. Evidence-Based Complementary and Alternative Medicine 2019, 2019, 6.

[26] Quincozes-Santos, A., Bobermin, L. D., de Assis, A. M., Gonçalves, C.-A.&Souza, D. O. Fluctuations in glucose levels induce glial toxicity with glutamatergic, oxidative and inflammatory implications. Biochimica et Biophysica Acta (BBA) - Molecular Basis of Disease 2017, 1863, 1-14.

[27] Council, N. R., Toxicity testing: Strategies to determine needs and priorities. 1984: National Academies Press.

[28] Heine, G. H., Sester, U., Girndt, M.&Köhler, H. Acanthocytes in the urine: Useful tool to differentiate diabetic nephropathy from glomerulonephritis? Diabetes care 2004, 27, 190-194.

[29] Ishida, T., Harashima, H.&Kiwada, H. Interactions of liposomes with cells in vitro and in vivo: Opsonins and receptors. Current drug metabolism 2001, 2, 397-409.

[30] Senior, J. H., Trimble, K. R.&Maskiewicz, R. Interaction of positively-charged liposomes with blood: Implications for their application in vivo. Biochimica et Biophysica Acta (BBA) - Biomembranes 1991, 1070, 173-179.

[31] Lippi, G., Cervellin, G.&Sanchis-Gomar, F. Red blood cell distribution width: A marker of anisocytosis potentially associated with atrial fibrillation. World journal of cardiology 2019, 11, 292.

[32] de la Harpe, K. M., Kondiah, P. P., Choonara, Y. E., Marimuthu, T., du Toit, L. C.&Pillay, V. The hemocompatibility of nanoparticles: A review of cell–nanoparticle interactions and hemostasis. Cells 2019, 8, 1209.

[33] Han, Y., Wang, X., Dai, H.&Li, S. Nanosize and surface charge effects of hydroxyapatite nanoparticles on red blood cell suspensions. ACS applied materials & interfaces 2012, 4, 4616-4622.

[34] Zhao, W., Zhuang, S.&Qi, X.-R. Comparative study of the in vitro and in vivo characteristics of cationic and neutral liposomes. International journal of nanomedicine 2011, 6, 3087.

[35] Michael, B., Yano, B., Sellers, R. S., Perry, R., Morton, D., Roome, N., Johnson, J. K.&Schafer, K. Evaluation of organ weights for rodent and non-rodent toxicity studies: A review of regulatory guidelines and a survey of current practices. Toxicologic pathology 2007, 35, 742-750.

[36] Piao, Y., Liu, Y.&Xie, X. Change trends of organ weight background data in sprague dawley rats at different ages. Journal of toxicologic pathology 2013, 26, 29-34.

[37] Suttie, A. W. Histopathology of the spleen. Toxicologic pathology 2006, 34, 466-503.

[38] Mendonca, M. C. P., Radaic, A., Garcia-Fossa, F., da Cruz-Hofling, M. A., Vinolo, M. A. R.&de Jesus, M. B. The in vivo toxicological profile of cationic solid lipid nanoparticles. Drug Deliv Transl Res 2020, 10, 34-42.

Chapter 6

Concluding Remarks

Despite the efforts of the pharmaceutical and research sectors, AD remains incurable, imposing the demand for new effective strategies. The exact mechanisms that cause AD are still debated, but it is widely accepted that senile plaques composed of Aβ fibrils in the patients' brains are associated with the disease. Preventing the Aβ aggregation or disaggregating mature Aβ fibrils are thus viable therapeutic options for preventing or treating AD, respectively. Because most synthetic chemotherapeutics have side effects, researchers have focused on natural compounds since their consumption has been associated with several health benefits. In the first part of this work, three natural compounds – CA, GA, and VB12– have been identified as promising molecules for AD therapy, both by inhibiting the Aβ fibril formation and disaggregation of mature fibrils in the presence of *in vitro* neuronal cell membranes.

However, natural compounds present some limiting characteristics, such as low bioavailability and the low ability to cross the BBB, which hinder the development of effective therapies. To overcome these issues, the delivery of natural products by targeting nanocarriers has aroused great interest, improving the therapeutic activity of these molecules. Thus, in the second part of this work, three Tf-functionalized liposomes were proposed for the brain-targeted delivery of CA, GA, and VB12. The developed DDS showed suitable properties for brain delivery and strong anti-amyloidogenic properties, thus promising for AD therapy.

Despite their numerous advantages, NPs have some drawbacks that restrict their therapeutic potential. While NPs have been successfully used to decrease the drugs' toxicity, NPs themselves can induce toxicity. Therefore, in the last part of this work, the *in vivo* toxicity of the developed unloaded liposomes was investigated and compared to the well-known cationic liposomes. Ten doses of neutral and cationic liposomes were intravenously administered to wild-type mice over 3 weeks. The data encourage using the developed neutral liposomes as safe nanocarriers to transport the selected natural compounds, even when repetitive administrations are needed.

Future *in vivo* studies with transgenic animal models of AD are necessary to validate the therapeutic efficacy of the three developed brain-targeted DDSs for AD therapy.

Supplementary Material

Table S3.1. Physicochemical characterization of LUVs comprised of DMPC:CHOL:SM:PS [65:15:10:10] (5 mM).

Hydrodynamic diameter (nm)	PdI	Zeta potential (mV)
147 ± 2	0.06 ± 0.03	-12 ± 1

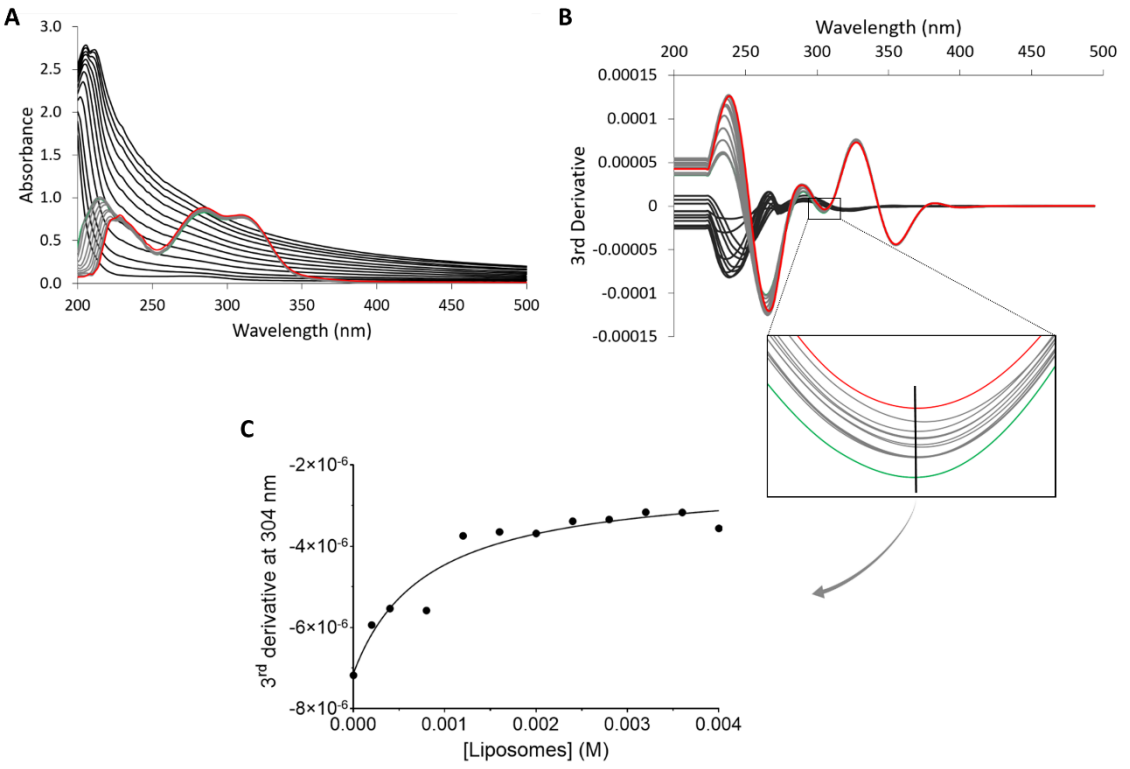

Figure S3.1. A) Absorbance spectra of liposomes at increasing concentrations (0 to 4000μM) in the absence (black lines) and presence of CA (100μM) (gray lines) (after subtraction of liposomes' contribution). Green lines represent the absorption spectrum of CA in the absence of LUVs. Red lines show the absorption spectrum of CA in the presence of LUVs at 4000 μM. B) shows the 3rd derivative spectra and C) the curve attained by plotting Equation 3.9 to the 3rd derivative spectrum at 304 nm.

Table S3.2. Physicochemical characterization of liposomes composed of DMPC:CHOL:SM:PS [65:15:10:10] (5 mM).

Hydrodynamic diameter (nm)	PdI	Zeta potential (mV)
143 ± 5	0.05 ± 0.02	-12 ± 1

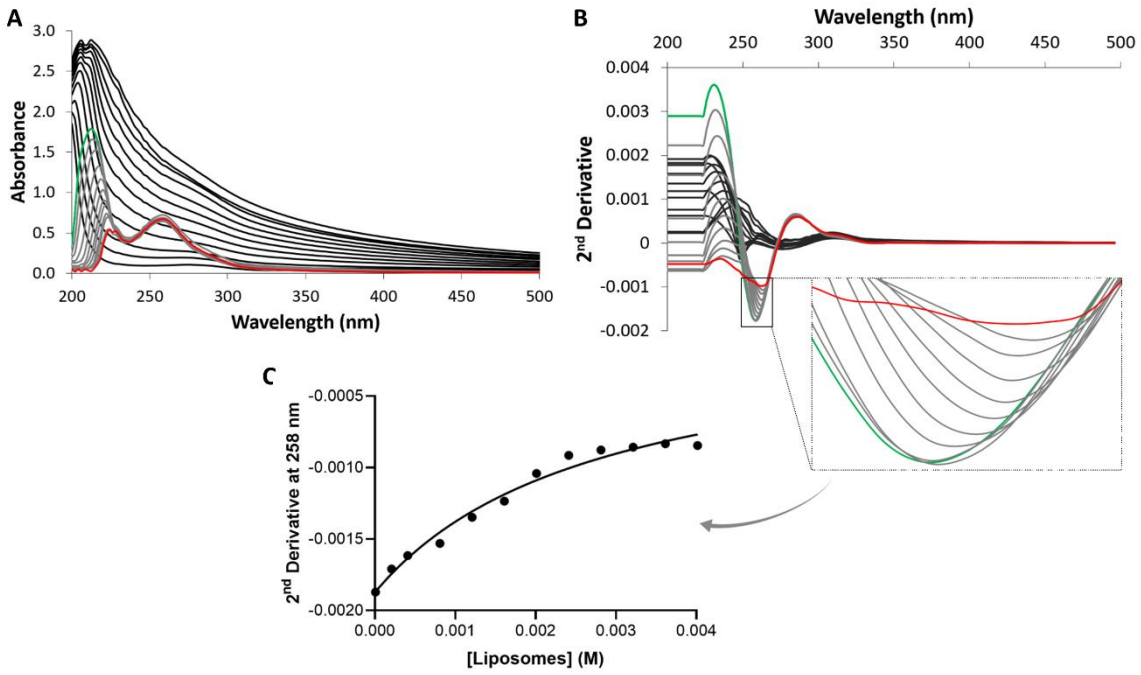

Figure S3.2. A) Black and gray lines correspond to the absorbance spectra of liposomes at increasing concentrations (0 to 4000μM) in the absence and presence of GA (100μM), respectively, following controls subtraction. Green lines show the GA's absorption spectrum in the absence of liposomes, while red lines indicate the absorption spectrum of GA in the presence of LUVs at maximum concentration. B) 2nd Derivative spectra. C) Curve resulting from the fit of the Equation 3.9 on the 2nd derivative spectrum at 258 nm.

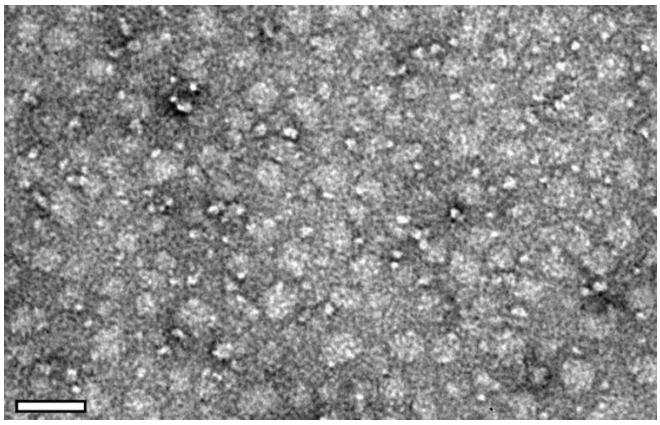

Figure S3.3. Negatively stained TEM image of $A\beta_{1-42}$ monomers (8 μM) in PBS. Scale bars indicate 100 nm.

Table S3.3. Physicochemical characterization of liposomes composed of DMPC:CHOL:SM:PS [65:15:10:10] (5 mM). Data are expressed as the mean ± SD (n = 3).

Hydrodynamic diameter (nm)	PdI	Zeta potential (mV)
140 ± 4	0.05 ± 0.01	-12.3 ± 0.4

Table S5.1. Effect of the repeated administration of PBS, neutral and cationic liposomes on mice body weight.

	Body weight (g)		
Injection	**PBS group**	**Neutral group**	**Cationic group**
1	21.6 ± 1.3	21.6 ± 1.4	21.2 ± 0.8
2	21.9 ± 1.4	20.4 ± 1.3	21.4 ± 0.4
3	21.6 ± 1.5	21.5 ± 1.1	21.0 ± 0.6
4	21.5 ± 1.4	21.3 ± 1.1	21.0 ± 0.6
5	21.6 ± 1.4	21.0 ± 1.0	21.4 ± 0.6
6	21.3 ± 1.4	21.0 ± 1.1	20.9 ± 0.6
7	21.5 ± 1.5	21.0 ± 1.1	21.1 ± 0.4
8	21.9 ± 1.7	21.6 ± 1.1	21.8 ± 0.6
9	21.8 ± 1.4	21.5 ± 1.1	21.8 ± 0.7
10	21.8 ± 1.9	21.3 ± 1.0	21.7 ± 0.5
End	21.9 ± 1.7	21.5 ± 1.0	21.5 ± 0.8

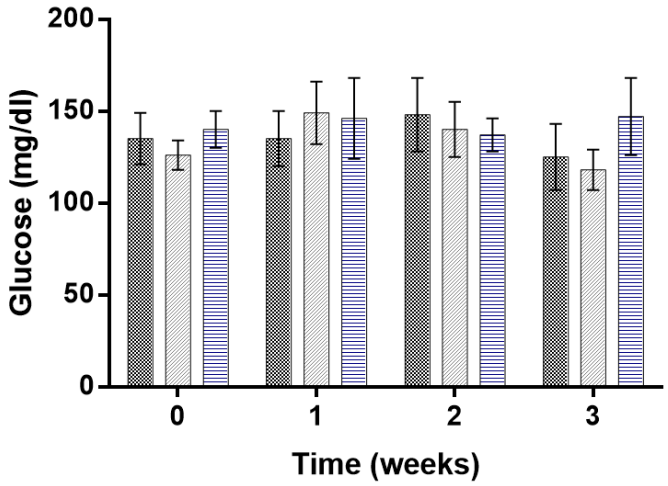

Figure S5.1. Effect of the repeated administration of PBS (dark gray), neutral (light gray), and cationic liposomes (blue) on blood glucose levels.

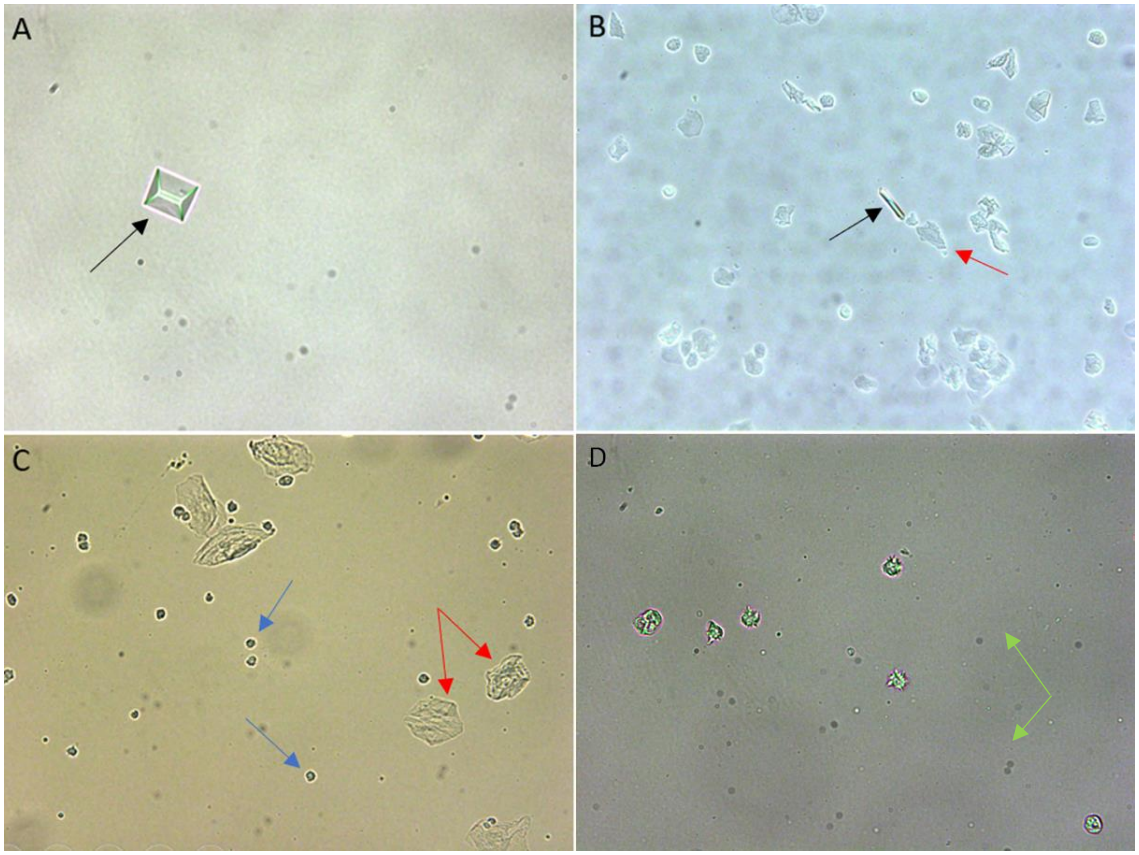

Figure S5.2. Microscopic urinalysis of mice treated with cationic and neutral liposomes. Urine from mice subjected to repeated doses of PBS (A), neutral liposomes (B), and cationic liposomes (C and D) were evaluated under the microscope. Magnifications used in each panel are A) 40X, B) 10X, C) 20X, D) 40X. Black arrows: triple phosphate crystals; blue arrows: RBCs; red arrows: endothelial cells.

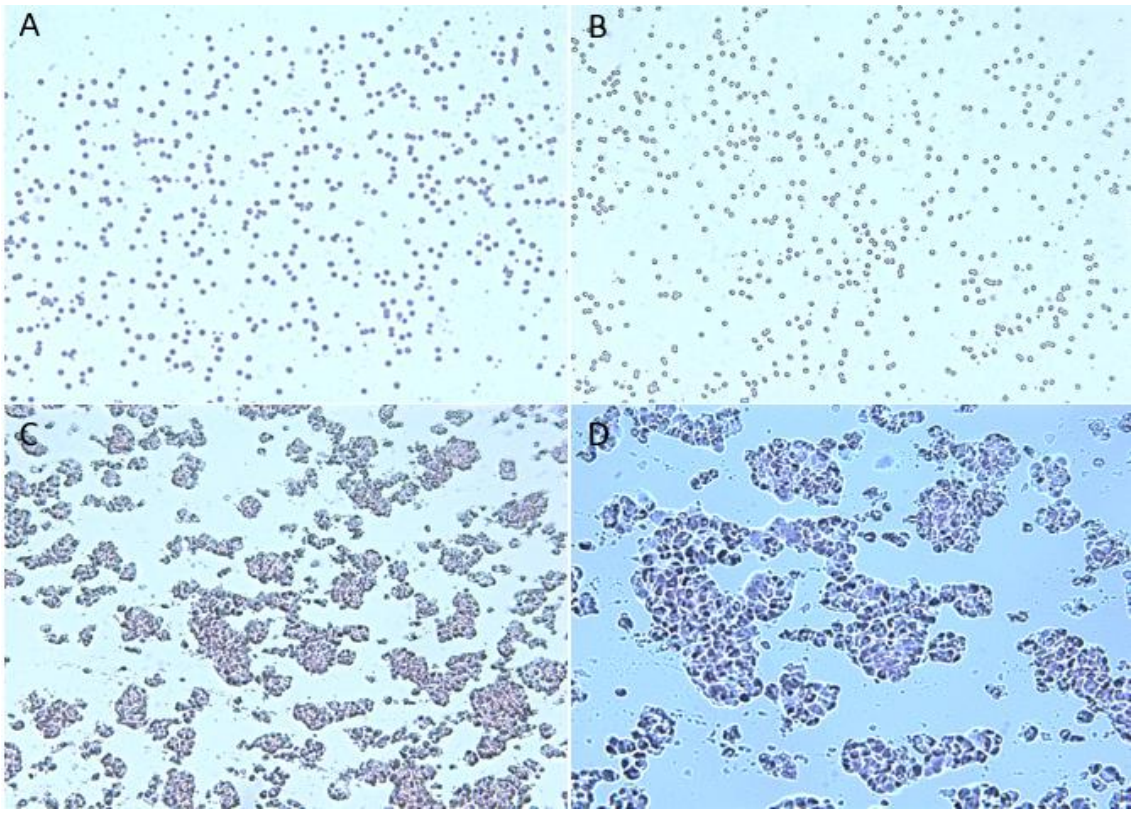

Figure S5.3. Microscopic images of blood smears after mixing blood and liposomes ex vivo. Blood samples from the experiment described in Figure 7 were checked under the microscope. Panels represent mouse blood mixed with PBS (A), neutral liposomes (B), and cationic liposomes (C and D). Magnifications used in each panel are as follows: A) 10X, B) 10X, C) 10X, D) 20X.

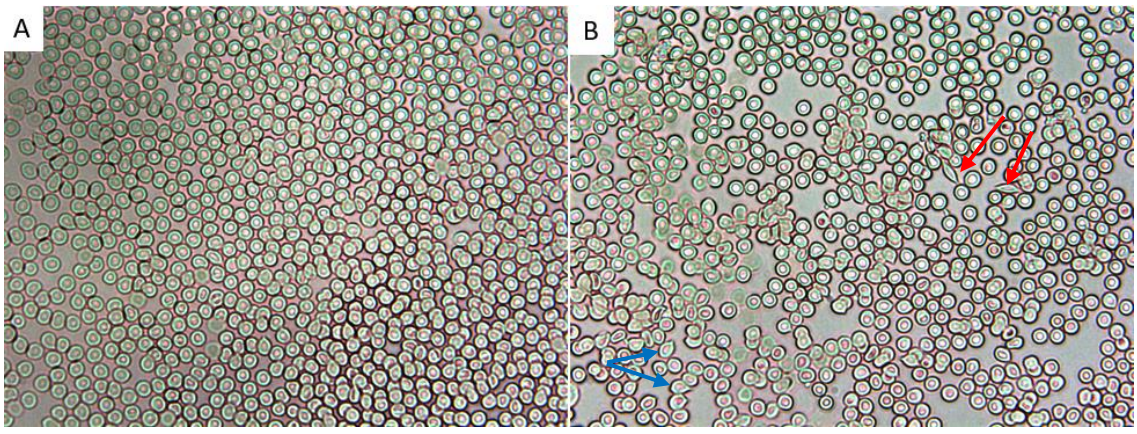

Figure S5.4. Acute in vivo cationic liposomes-blood interaction. Microscopic images of blood smears before (A) and after (B) injecting one dose of DOTAP:CHOL LUVs into mice. Images in this figure were obtained at a 40X magnification. Blue arrows represent dacrocytes, and red arrows depict acuminocytes.

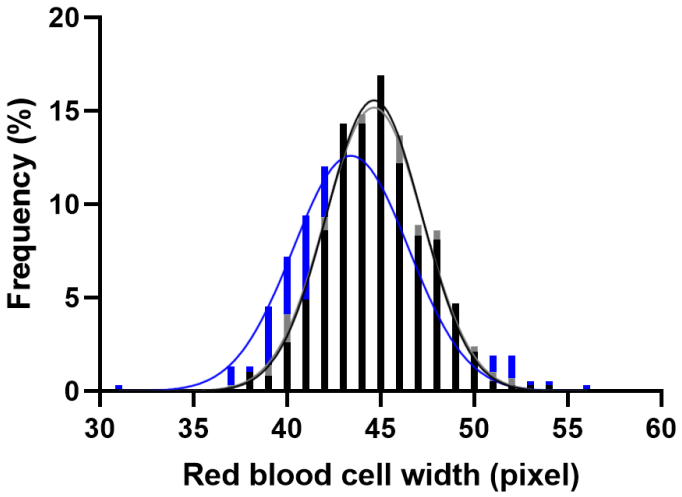

Figure S5.5. Effect of prolonged administration of PBS (black), neutral (gray), and cationic liposomes (blue) on the red blood cell distribution width (RDW). Data corresponds to the frequency distribution of RBCs width measured in pixels in a blood smear as an indicator of anisocytosis.

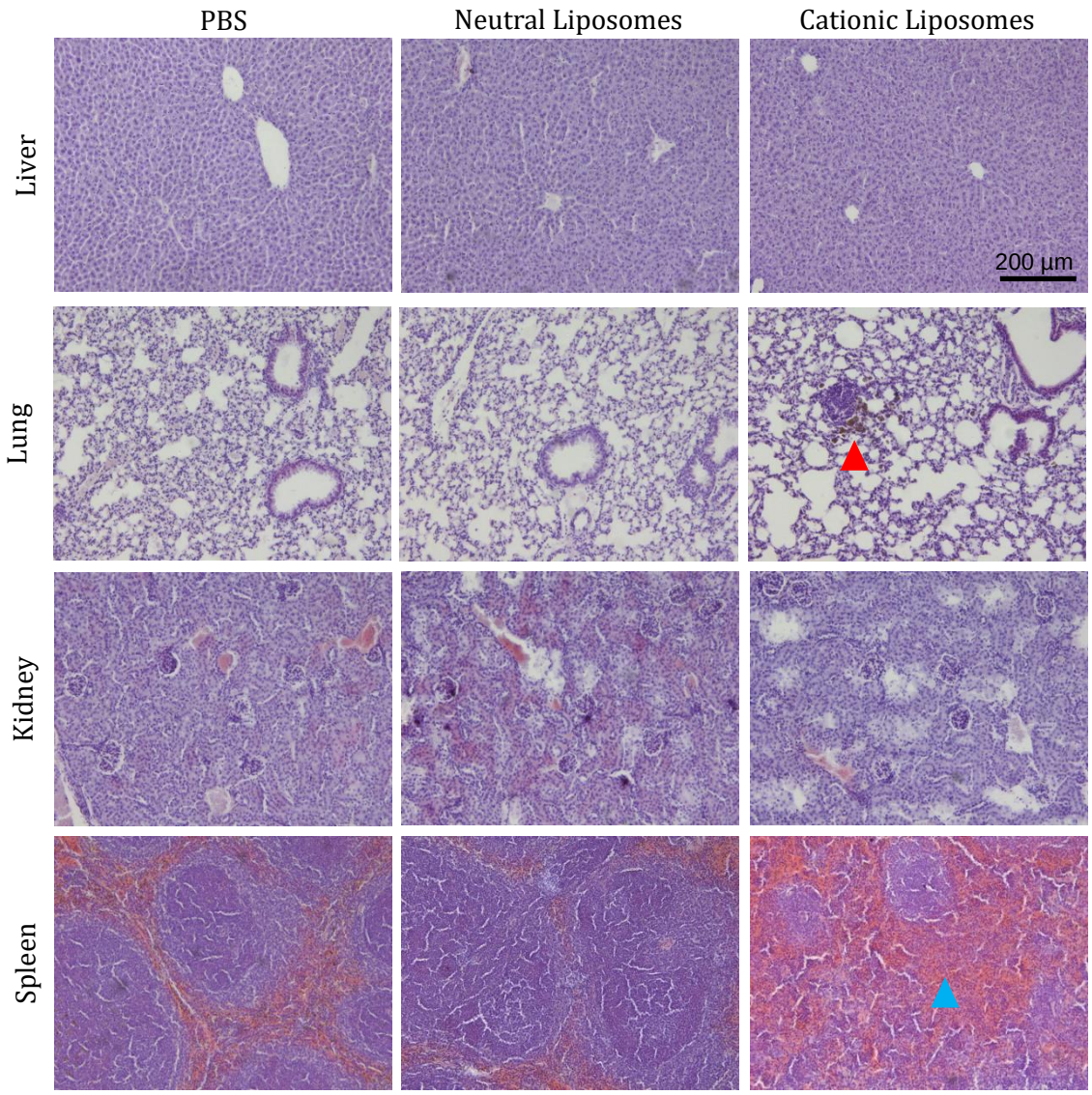

Figure S5.6. Histopathological analysis of liver, lung, kidney, and spleen at low power magnification. A comparison between different experimental groups after treatment shows the presence of brown pigmented cells only in animals treated with cationic liposomes (red arrowhead). In spleens of mice treated with cationic liposomes, an increased area of the red pulp (blue arrowhead) was observed. Images in this figure were obtained at a 10X magnification.